



Swansea University
Prifysgol Abertawe

The Generation of Solar Fuels in Deep Eutectic Solvents

**A dissertation submitted to the Faculty of Science and Engineering at
Swansea University**

for the fulfilment of the degree of Doctor of Philosophy

October 2022

Michael Allan

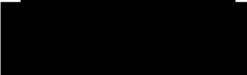
Supervisor: Dr. Moritz Kuehnel

Copyright: The Author, Michael Allan, 2023

Distributed under the terms of a Creative Commons Attribution 4.0
License (CC BY).


Declarations

This work has not previously been accepted in substance for any degree and is not being concurrently submitted in candidature for any degree.

Signed.. 


Date..... 31/10/2022

This thesis is the result of my own investigations, except where otherwise stated. Other sources are acknowledged by footnotes giving explicit references. A bibliography is appended.

Signed.... 


Date..... 31/10/2022

I hereby give consent for my thesis, if accepted, to be available for photocopying and for inter-library loan, and for the title and summary to be made available to outside organisations.

Signed.... 

Date..... 31/10/2022

The University's ethical procedures have been followed and, where appropriate, that ethical approval has been granted.

Signed.... 

Date..... 31/10/2022

For Connel

Acknowledgements

This thesis, and indeed the man I am today, would not have been possible without some incredibly special people.

Firstly, to my supervisor Dr. Moritz Kuehnel, who has persevered through immeasurable difficulties and has shown an unmeasured amount of dedication and commitment to my research project. I could not have asked for a more passionate and intelligent supervisor.

To my parents James and Maureen Allan, who have given me every opportunity and supported me through every peak and pitfall of my academic career. Their love and support knows no bounds. I hope to make you proud in everything I do.

To my friends and colleagues who I have had the pleasure of knowing during my time in Swansea of which there are too many to name. To Ben F, Chiara, Natalia, Katie, Ben J, Marc, Kadie, Denise, Ariana, Yue, Natasha, Saul, Luis, and Maite. You made coming to the lab every day a joy. A special thank you to Martina Salerno, who has been the greatest company in the short time I have known her. I will miss our coffees and our chats together.

To Dr. Mariolino Carta, Dr. James Ryan, Dr. Francisco Martin-Martinez, Dr. Martin Gill, Professor Simon Bott, and Dr. Marcella Bassetto, who have provided me with guidance, wisdom, lots of insightful (and some not so insightful) conversations. A special thank you to James and Fran who assisted me during the latter stages of my project. I am truly grateful.

To my friends in Swansea, especially James R, Ben C, Hywel, Annie, James T, Craig, Sev, and Martyn, with who have I have shared countless memorable moments. Thank you for your support, friendship, for all the wonderful memories, and for providing me with a life outside of academia. A special thank you to Alex Dearden who I met on my first day at Swansea as a lonely postgraduate, and who has provided me with 4 years of fun, friendship, and floods of great times. Truly the greatest friend one could ask for. YJB.

To my friends back home – Katie, Sarah, Clare Louise, Stephen and Carlie, Fiona, Zak, Matthew, Chris, and Aisling. Everything I have done is because of your love and support. Words will always fail to describe how much you mean to me. Through the good times and bad, you have been there. I hope you will be with me for whatever comes along.

To my best friend Callum. Your friendship is everything. You have shown me there is much more to life, and that life is better with you in it. I am grateful for you every single day.

To Bruce Springsteen and Brian Fallon, who will never read this thesis. Your music has helped and moulded me in ways I cannot comprehend. I am who I am because of your music. I hope to carry you with me on many more journeys.

“Walk tall, or baby don’t walk at all.”

Glossary of Terms

AM = Air mass

AQY = Apparent quantum yield

CB = Conduction Band

ChCl = Choline chloride

CN = Carbon Nitride

CV = Cyclic Voltammetry

DCDA = Dicyandiamide

DES = Deep eutectic solvent

DR-UV = Diffuse Reflectance Ultraviolet Spectroscopy

DSSC = Dye-sensitised solar cell

eV = electron volt

EY = Eosin Y

FT-IR = Fourier transform infrared spectroscopy

GC = Gas chromatography

GISS = Goddard Institute for Space Studies

HBA = Hydrogen bond acceptor

HBD = Hydrogen bond donor

IL = Ionic liquid

MFC = Mass flow controller

MV = Methyl viologen

MWCNT = Multi-walled carbon nanotube

NHE = Normal Hydrogen Electrode

PEC = photoelectrochemical cell

PV-E = Photovoltaic electrolysis

PXRD = Powdered X-ray diffraction

ROS = Reactive oxygen species

SCE = Saturated Calomel Electrode

SED = Sacrificial electron donor

STH = Solar-to-hydrogen

TEOA = triethanolamine

VB = Valence band

Abstract

New reaction systems that can efficiently convert solar energy into fuels is of major scientific importance to aid in alleviating the global use of fossil fuels. Hydrogen is viewed as the ideal solar fuel as it can be used in a clean carbon free energy cycle. Research into reaction systems which can evolve hydrogen with the help of photocatalysts and sunlight mostly focuses on material development, with not a lot of thought given to the reaction solvent, even though the solvent is in constant contact with the photocatalytic components.

This thesis focuses on deep eutectic solvents (DESs) as alternative reaction media for photocatalytic hydrogen evolution. Type III DESs based on choline chloride are favourable solvents due to their cost, ease of preparation, stability, and low toxicity. While DESs have found some uses in the literature, they have never been investigated as reaction media for photocatalytic hydrogen evolution. The work presented herein shows that tuning of the solvent media is key to controlling solar hydrogen production at heterogenous and homogenous photocatalysts. By varying water content of the solvents, the results show that DESs can compete with standard aqueous solutions in terms of photocatalytic solar fuel generation, and under some conditions, catalysts show greater activity in DESs compared to conventional aqueous solutions. Through the use of co-catalytic Pt, sacrificial electron donors and a redox mediator, the H₂ evolution performance in DESs can be better understood to maximise hydrogen production activity.

This thesis also shows that DESs are effective as reaction media for aerobic hydrogen production. The motivation behind aerobic hydrogen evolution lies in the fact that solar hydrogen production systems need to exhibit photocatalytic activity in the presence of oxygen, but to date tests on many photocatalytic systems in aerobic conditions is unknown, and those catalysts which show tolerance to oxygen are typically much lower than their inert counterpart. The work in this thesis shows that DESs allow photocatalysts which are inactive in the presence of oxygen to be photocatalytically active in atmospheric levels of oxygen. In fact, in some cases over 90% of original activity can be retained simply through solvent choice, versus 8% in water. This increase in activity under air results from the fact that DESs possess

lower rates of oxygen diffusion and concentration relative to water, and it is electrochemically determined that through lowering of the diffusion coefficient and concentration of oxygen in the solution, the hydrogen evolution activity can be increased through a supposed decrease in competing oxygen reduction. This is also demonstrated through solvent engineering of aqueous solvents, and electrochemical measurements show that increase in the salinity of water can aid in increasing aerobic hydrogen evolution through a lowering of diffusion and concentration of oxygen.

Finally, from knowing that solvent tuning can aid in increasing the photocatalytic activity, natural hydrogenase enzymes are tested for their photocatalytic hydrogen production in both inert and aerobic conditions. The work presented shows that choice and tuning of the solvent aids in increasing the activity of the hydrogenase in conjunction with a TiO₂ light absorber. The increase in activity of performance in aerobic conditions in DESs relative to water again results from the lowering of the diffusion and concentration of dissolved oxygen. The presence of DESs again aids in increasing hydrogen production and it is thought this is the first demonstration of photocatalytic hydrogenase activity in organic media. In some reaction systems with DES, the performance of the enzyme exceeds water. This again can be explained electrochemically, whereby hydrogenases at a working electrode show good proton reduction currents in DESs. The electroanalytical technique of microwire chronoamperometry probes the proton diffusion and concentration in the DESs, with the difference in performance of the photocatalytic performance between the solvents rationalised. It is proposed that the hydrogen bonding network in the DESs aids in increasing the mobility solutions, with the activity of the hydrogenase affected by the solvent environment.

This work shows that DESs are viable reaction media for the photocatalytic hydrogen production reaction and shows a new alternative of enabling highly efficient oxygen tolerance of catalysts, and that reaction conditions can be systematically and rationally tuned to aid in the increase of solar fuel production.

Table of Contents

Chapter 1

Introduction

1. Energy	7
1.01. Outlook	7
1.02. Solar Energy and Air Mass.....	8
1.1. Photosynthesis.....	9
1.1.1 Natural Photosynthesis.....	9
1.1.2. Artificial Photosynthesis for Solar Water Splitting	11
1.2. Principles of Particulate Photocatalysis for Solar Water Splitting and Hydrogen Evolution.....	14
1.2.1. Photocatalysts.....	14
1.2.2. Quantum Yield.....	16
1.2.3. Co-Catalysis.....	17
1.2.4. Photocatalytic Hydrogen Evolution.....	19
1.2.5. Solar to Fuel Devices	20
1.2.6. Principles of Hydrogen Evolution	25
1.2.7. Sacrificial Electron Donors for Solar Hydrogen Evolution.....	27
1.3.1. TiO ₂	28
1.3.2. Carbon Nitrides.....	30
1.3.3. Functionalised Carbon Nitride – NCN-CN _x	32
1.4. Homogenous Photocatalysts for Solar Fuel Production	34
1.4.1. Eosin Y	34
1.5. Project Aims	35
1.6. References.....	37

Chapter 2

Deep Eutectic Solvents as Viable Reaction Media for Solar-Driven Hydrogen Production

2. Introduction.....	40
2.1. Deep Eutectic Solvents and ILs.....	40
2.2. Origin of Deep Eutectic Solvent Synthesis.....	41
2.3. Properties and Behaviour of Type III DESs.....	43
2.5. Results	46
2.5.1. Characterisation of NCN-functionalised Carbon Nitride.....	46

2.5.2. Quantification of Photocatalytic H ₂ Production – Gas Chromatography Calibration and Experimental Setup	49
2.5.3. Photocatalytic H ₂ Evolution in H ₂ O with NCN-CN _x	50
2.5.4. Photocatalytic H ₂ Evolution in Reline-based Solvents with NCN-CN _x	52
2.5.5. Photocatalytic H ₂ Evolution in Glyceline-based Solvents with NCN-CN _x	58
2.5.6. Photocatalytic H ₂ Evolution in Ethaline-based Solvents with NCN-CN _x	62
2.5.7. Photocatalytic H ₂ Evolution in DESs in the Absence of TEOA.....	64
2.5.8. Homogenous Photocatalytic H ₂ Evolution in DESs with Eosin Y.....	66
2.6. Discussion	69
2.7. Conclusions.....	70
2.8. Materials and Methods	72
2.9. References.....	75

Chapter 3

Deep Eutectic Solvents as a Reaction Medium for Aerobic Hydrogen Evolution

3.1. Introduction	78
3.2. Principles of O ₂ Reduction.....	78
3.3. O ₂ Tolerant Photocatalysis.....	80
3.4. Methods of Oxygen-Tolerant Photocatalysis.....	82
3.5. Results	86
3.5.1. Solar Hydrogen Evolution of NCN-CN _x Photocatalyst in Aerobic Conditions	86
3.5.2. Investigating Solvent Effects on Photocatalytic Properties.....	91
3.5.3. Simultaneous Determination of Diffusion Coefficient and Concentration of Oxygen in DESs.	97
3.5.4. Rationalising Oxygen Tolerance from a Mechanistic Perspective	104
3.6. Discussion	106
3.7. Conclusions.....	109
3.8. Methods and Materials	110
3.9. References.....	113

Chapter 4

Augmenting Performance of Hydrogenase Enzymes for Photocatalytic Hydrogen Evolution via Solvent Tuning

4. Introduction.....	116
4.1. Co-catalysts and Enzymes	116
4.2. H ₂ ase Chemistry	117
4.3. [NiFeSe]-H ₂ ases	119
4.4. The Experimental O ₂ Tolerance of [NiFeSe]-H ₂ ase.....	122

4.5. Results	124
4.5.1 H ₂ Evolution Performance by [NiFeSe]-H ₂ ase – TiO ₂ in Water	124
4.5.2. H ₂ Evolution Performance by [NiFeSe]-H ₂ ase – TiO ₂ in Reline.....	125
4.5.3. H ₂ Evolution Performance by [NiFeSe]-H ₂ ase – TiO ₂ in Ethaline.....	127
4.5.3. H ₂ Evolution Performance by [NiFeSe]-H ₂ ase – TiO ₂ in Glyceline	129
4.5.4 Oxygen Tolerance of [NiFeSe]-H ₂ ase – TiO ₂ in DESs	132
4.5.5. Proton Mobility in DESs – Rationalising Enzymatic Performance.....	137
4.5.6. Electrochemical Studies of a [NiFeSe]-H ₂ ase Electrode in the Presence of Glyceline	144
4.6. Discussion	145
4.7. Conclusion.....	148
4.8. Materials and Methods	149
4.9. References.....	153

Chapter 5

Summary and Outlook

5.1. Thesis Summary	157
5.2. Outlook.....	159
5.3. References.....	161

Chapter 1

Introduction

1. Energy

1.01. Outlook

The production and supply of renewable energy to meet global demands is arguably the most important scientific task facing humanity in the 21st century. Energy demands continue to increase with an increasing global population to meet food production and transportation with most of the world's energy supply coming from the consumption of fossil fuels (oil, natural gas, and coal). Other areas of vast consumption include manufacturing and construction, with energy needed to power plants and factories for production.¹ (Figure 1.01a). However, the consumption of non-renewable energy sources leads to the production of greenhouse gases, namely CO₂. Greenhouse gases, when emitted into the atmosphere, trap heat and cause a warming of the planet's surface. According to the International Energy Agency, as of 2021 global energy-related CO₂ emissions reached 31.5 gigatonnes.² The rise in temperature from sustained greenhouse gas emission has caused the earth's land and ocean average temperature to rise by approximately 0.2 °C per decade since 1980, reaching an all-time high in 2020 (Figure 1.01b).³ To help combat energy crises, research into renewable sources of energy production has greatly increased. As a result, renewable energy use has increased globally from various sources, namely solar energy, wind energy, hydropower, and biomass.⁴⁻⁸ Of these sources, the most abundant source is the sun – more energy from the sun strikes the earth surface in 90 minutes (1.2×10^{17} kWh) than the entire global energy consumption in one year, with the 2022 annual estimate set to be 5.8×10^{20} J.⁹ Theoretically solar energy has the capacity to sustain all the earth's global energy requirements, and so using this vast, abundant, and natural resource is an incredibly favourable approach to help alleviate climate and energy challenges.

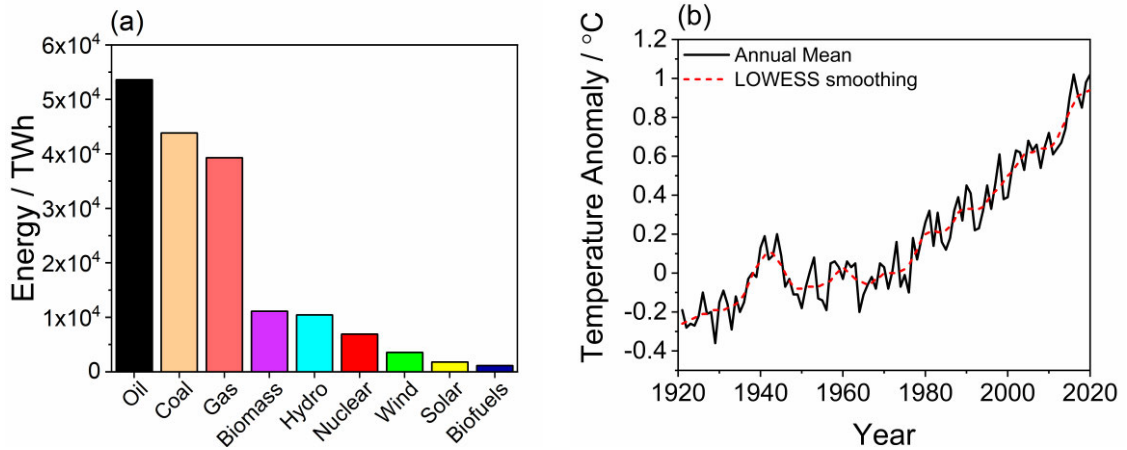


Figure 1.01. (a) Sources of global energy in Terawatt-hours. Adapted from REF 1. (b) Change in global surface temperature from 1921 to 2021. The black line shows the annual mean temperature difference from the average temperatures recorded between 1951 to 1980. The red line is the locally weighted scatterplot smoothing of the moving average of temperatures. Data adapted from NASA's Goddard Institute for Space Studies (GISS) from REF 3.

1.02. Solar Energy and Air Mass

Solar energy is the radiation emitted from the sun that can be captured and used as a source of power for electricity or to promote chemical reactions. The radiation emitted from the sun covers most of the electromagnetic spectrum, with sunlight at the Earth's surface composed of UV light (3-5%), visible light (42-43%) and infrared (52-55%), although the intensity of sunlight and the solar spectrum depends on the path length through the Earth's atmosphere.¹⁰ Figure 1.02 shows standard solar spectra of various air masses used to co-ordinate international standards.^{11, 12} Air mass is defined as a coefficient describing the optical path length through the Earth's atmosphere - solar radiation i.e., light energy travelling through the atmosphere experiences different levels of scattering and attenuation depending on the amount of atmosphere.¹³ The coefficient used to characterise air mass is a measurement relating to the amount of atmosphere interfering with the emitted energy.¹³ The greater the coefficient, the greater the attenuation of solar energy. Air mass is dependent on the Sun's elevation path and so varies with time. An air mass coefficient of 1.5 is conventionally used as this value represent the overall yearly average for solar research facilities, solar cells, and other solar devices in mid-

latitude countries, such as those in Europe, China, Japan, and the United States of America.¹³

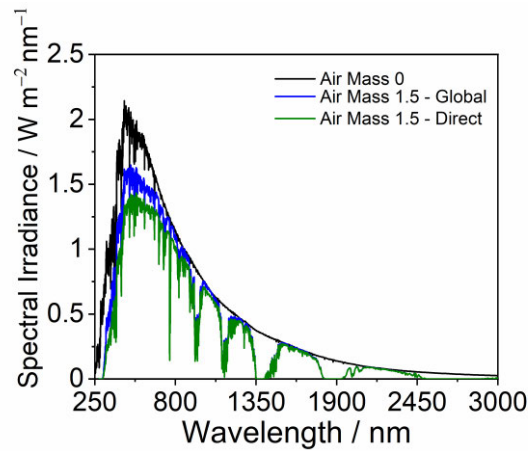


Figure 1.02. Solar spectrum of air mass coefficients equal to 0 (black trace), 1.5 Global, used as a standard for flat plate solar panels, and 1.5 Direct which includes

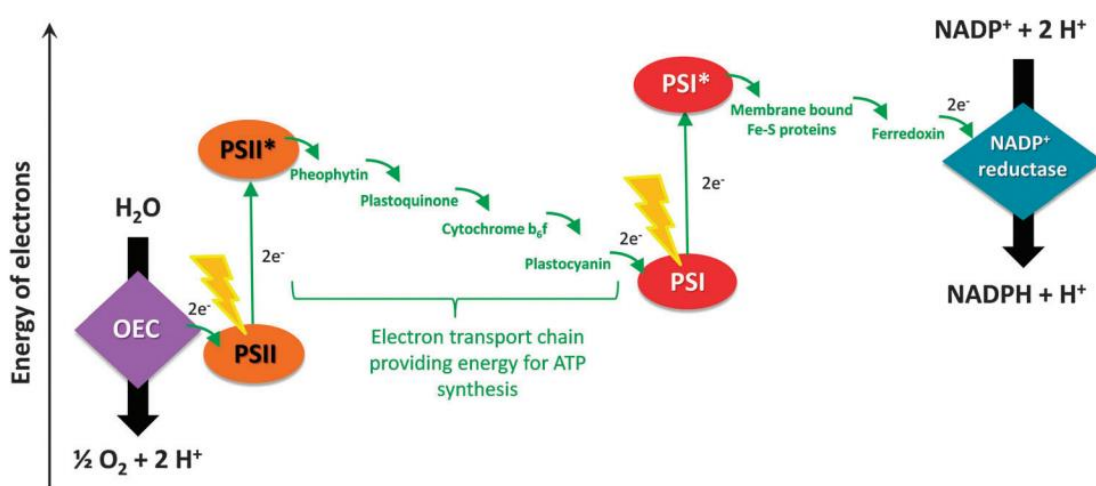
While vastly abundant, solar energy is intrinsically diurnal due to the rotation of the Earth. Different countries are subject to different amounts of sunlight, and sunlight itself is only experienced in most countries for a few hours a day. Therefore, capturing and storing the Sun’s energy for use is an important consideration for upscaling solar power. The capture, conversion, and storage of sunlight to a different energy exists and is performed by plants in a process called *photosynthesis*.

1.1. Photosynthesis

1.1.1 Natural Photosynthesis

Photosynthesis is the process by which plants and some other organisms convert sunlight into chemical energy in the form of chemical bonds. Carbon dioxide and water are converted into glucose and oxygen through light driven processes. Light reactions in natural photosynthesis occur *via* electron transfer in a stepwise process to provide enough potential energy for water splitting. In this process, water is oxidised to produce oxygen and protons, with the resultant electrons pumped

through a light absorbing photosystem to a higher energy state. The high-energy photoexcited electron can then be used to generate bio-reducing agents such as NADPH for further bioreactions. The separation of the photoexcited electron from the manganese calcium oxide cluster located in the light absorber PSII is so structured that the quantum efficiency of charge separation is near unity i.e., each photo-excited electron is used in a chemical process. The electron pathway and charge separation is highlighted in Scheme 1.01.¹⁴



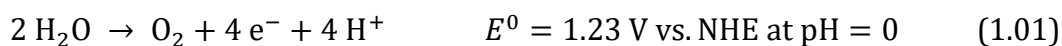
Scheme 1.01. Depiction of electron pathway and fate during natural photosynthesis. Here, OEC is the oxygen evolution complex, PSII is photosystem II, PSI is photosystem I, and NADP⁺ is the nicotinamide adenine dinucleotide phosphate co-factor. Reprinted with permission from REF 14. Copyright 2014, Royal Society of Chemistry

The spatial charge separation achieved in natural photosynthesis, even in low light intensities, results from ultrafast transport of electrons through reaction centres found in plants and, through the use of a series of co-factors, can shuttle electrons through an energy cascade to achieve rapid charge separation.¹⁵ This process of electron shuttling using co-factors can produce quantum efficiencies of >90% even in low light intensities. This can be thought of converting sunlight into a “wireless current”, whereby the anodic charge is used to generate oxygen from the oxidation of water with the associated release of four protons.⁵ The cathodic charge of this current reduces protons through the conversion of NADP to NADPH. This process is known to be “thermodynamically uphill”, however the charge separation energy is great enough to act as a driving force for the redox processes performed by the

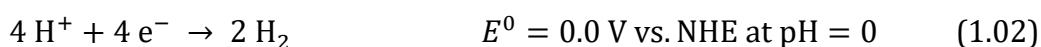
system. It should be noted that production of charges and transfer of electrons can only arise in the presence of light.

1.1.2. Artificial Photosynthesis for Solar Water Splitting

Artificial photosynthesis aims to emulate natural photosynthesis with man-made devices and materials. In an artificial photosynthesis system sunlight is absorbed and the energy converted in the form of chemical bonds to create a solar fuel. Scheme 1.02 highlights the key processes of an artificial photosynthetic procedure for water splitting.¹⁶ Light energy aids in exciting an electron from a low energy to a higher energy, rendering both a positive charge carrier (positive hole) and a negative charge carrier (excited electron). These charge carriers can perform oxidation and reduction reactions, respectively. In the case of solar hydrogen generation from water, water is oxidised to protons and molecular oxygen at the positive hole. The reaction for this process is shown in the following equation, with the necessary energy needed to perform the reaction quoted as a potential versus the normal hydrogen electrode (NHE):

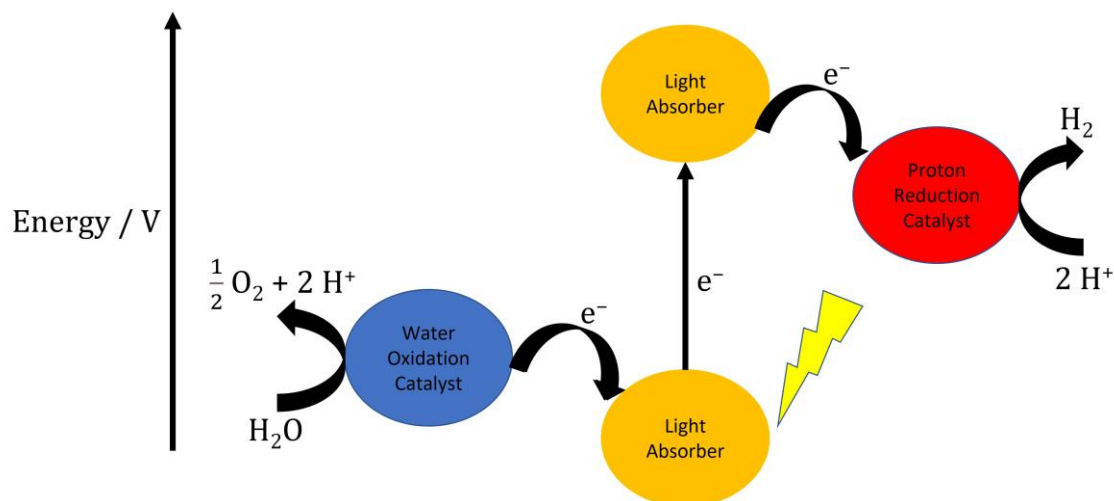


The protons generated from the water oxidation process are subsequently reduced to hydrogen:



The development of devices and materials is research intensive in the area of solar fuels. Both scalability and efficiency need to be high to enable the acceptance and conversion of a large amount of sunlight to develop viable alternatives to the combustion of fossil fuels.¹⁷ Hydrogen produced directly from sunlight is viewed as the ideal alternative to fossil fuels due to molecular hydrogen's high gravimetric energy density of approximately 120 megajoules per kilogram (MJ kg^{-1}), almost three times greater than that of petrol (46 MJ kg^{-1}).¹⁸ Moreover, the only by-product of the combustion of hydrogen is water which allows the possibility of the creation

of a carbon free energy cycle. Solar hydrogen production from water has gained immense attention as a low-cost, low-energy consuming, and environmentally friendly process.



Scheme 1.02. Depiction of electron pathway and fate during artificial photosynthesis for solar hydrogen production. Schematic adapted from REF 16.

Hydrogen as a fuel should be considered for global implications, with the overall purpose of hydrogen to serve as an alternative fuel to those based on carbon. The hydrogen economy refers to the shift away from conventional industries' dependence on carbon to a more environmentally friendly fuel. However, the large-scale use of hydrogen as a fuel should be considered greatly. While hydrogen is viewed favourably due to its high gravimetric energy density as previously mentioned, it possesses an intrinsically low volumetric energy density resulting from its low molecular size. The volumetric energy density of gaseous hydrogen is 8 MJ L^{-1} at atmospheric pressure, which is vastly lower than that of petrol (32 MJ L^{-1}) and even methanol (17.5 MJ L^{-1}).¹⁹ Figure 1.03 shows the volumetric and gravimetric energy densities of selected fuels, which highlights the higher volumetric energy density of hydrogen as a liquid in comparison to a high-pressure gaseous form. The low energy density of hydrogen means that it can be very expensive to transport over long distances. Nonetheless, a number of possible options are available to overcome this hurdle, including compression, liquefaction or incorporation of the hydrogen into larger molecules that can be more readily transported as liquids.

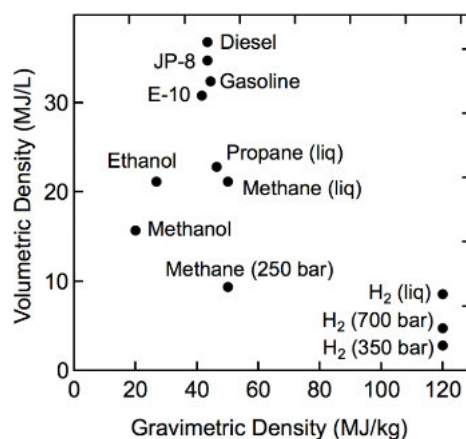


Figure 1.03. Volumetric energy densities (y-axis) and gravimetric energy densities (x-axis) of select fuels. Note the increase in volumetric energy density of liquid hydrogen over its gaseous counterparts. Original figure found in REF 19

Hydrogen in industry is often used for the synthesis of important chemicals, mainly ammonia (for fertilisers, or itself as a fuel) in the Haber-Bosch process, the synthesis of methanol, and for the refining of petroleum.²⁰ As of 2020, the majority of hydrogen is produced from the steam reforming reaction, whereby water reacts with methane to produce syngas – a combination of carbon monoxide and hydrogen (Equation 1.03).²¹



As this method of producing hydrogen comes from natural gas, renewable methods of hydrogen production and storage should be investigated. Today, hydrogen is conventionally stored as a gas or liquid for mobile and stationary applications. Hydrogen at high pressures has only 15% of the energy density of gasoline, so storing the equivalent amount of energy at a vehicle refuelling station would require nearly seven times the space.²² Electrical batteries offer a solution to energy storage issues, but the operation of batteries requires large amounts of stored energy for electrical grids, and there exists no infrastructure with the battery capacity to store and use electricity we use for power purposes.^{23, 24} For road transport and small-scale devices, batteries are much more competitive in terms of energy storage due to the cost and efficiencies associated with modern batteries.²⁵ Despite this, hydrogen fuel cells, where hydrogen and oxygen react to produce water and energy,

are viewed as more beneficial than combustion-based technologies used in power plants and vehicles as they can convert the chemical energy in hydrogen as the fuel directly to electrical energy with efficiencies in excess of 60%, in addition to much lower emissions in comparison to combustion engines.²⁶ Moreover due to the versatility of the uses of hydrogen, renewable sources of hydrogen would possess important implications for large scale industrial applications and may even be considered as a fuel for long-haul transportation.

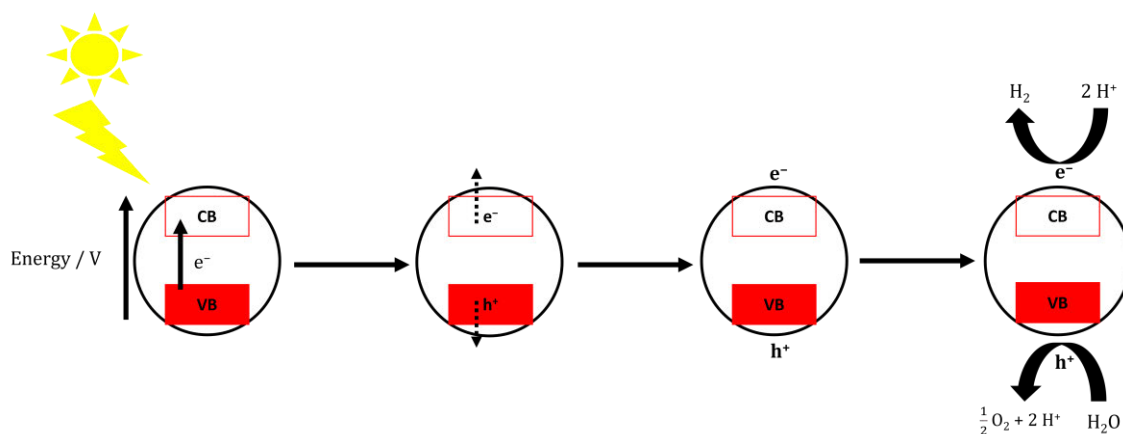
Hydrogen therefore is appealing due to its versatility as a feedstock for important chemicals such as ammonia and methanol, and as a fuel itself if the hydrogen can be produced in a clean manner. Fuel cells provide an efficient way of utilising hydrogen as a fuel to generate electricity, but for the purposes of industrial applications such as transport and as a power source for power plant operation, hydrogen should be able to be produced and stored on a large scale. Photocatalysis offers an idealised method of producing hydrogen, and a major focus of this thesis is the means and methods of performing and analysing photocatalytic hydrogen evolution.

1.2. Principles of Particulate Photocatalysis for Solar Water Splitting and Hydrogen Evolution

1.2.1. Photocatalysts

The light absorbing materials capable of generating charge carriers to perform redox processes are called *photocatalysts*. Photocatalysts differentiate themselves from typical thermal catalysts in that the sites and sources of chemical reactions occurring at the catalyst are finite and short lived, which determines the efficiency of the system. Photocatalysts employed for solar fuel generation include light absorbing dyes, as is the case in natural photosynthesis, but the most widely utilised materials are semiconductors. Semiconductors possess an electronic structure suited for photocatalytic procedures, as electrons in a low-lying energy band – called the valence band (VB) – can be excited to a higher energy state in the conduction band (CB) of the material.²⁷ The process to convert solar energy to chemical energy in the form of chemical bonds using semiconductors is a multistep process and

begins with the absorption of photons. Incident photons possessing an energy equal to or greater than the energy bandgap, E_g , of the semiconductor can produce excited electrons and positive holes. These photogenerated electrons in the CB and positive holes in the VB must then migrate to the surface where they can perform reduction and oxidation process, respectively. This process is summarised in Scheme 1.03.²⁸



Scheme 1.03. Steps in the photocatalytic reaction processes, showcasing electron and hole generation and subsequent migration.

Some considerations must be made when selecting photocatalysts for water splitting. The energy level of the VB maximum must lie at a more positive potential than the energy required for water oxidation (1.23 V vs. NHE at pH = 0), while the energy level of the CB minimum must be more negative than the energy required for proton reduction (0.0 V vs. NHE at pH = 0).²⁹ Only a few materials are known that possess bands at such energy levels as well as a favourable bandgap that is capable of absorbing photons with energy in the visible region ($\lambda \geq 400$ nm). It is also important to note the consequences of solar light utilisation in terms of energy levels and bandgaps. By lowering the bandgap and the subsequent energy of incident photons, the photocatalyst is able to use more of the solar spectrum increasing photocatalytic performance through the generation of more charge carriers. Utilising as much of the solar spectrum is necessary as photogenerated charge carriers are prone to recombination in the bulk of the material, with the energy lost as heat or radiation, producing a hindered quantum yield.³⁰

1.2.2. Quantum Yield

The measure of a chosen photocatalyst's performance can be determined by the *quantum yield*, Φ . In photocatalysis, the quantum yield is the number of catalytic events occurring resulting from the number of absorbed photons:

$$\Phi = \frac{\text{number of photochemical events}}{\text{number of absorbed photons}} \quad (1.03)$$

The quantum yield can be determined for numerous photochemical events, such as reactant disappearance (for photocatalytic dye degradation), product formation (in the production of solar fuels) and light emission (in fluorescence). For photocatalytic processes, quantum efficiency defines the number of electrons involved in the reaction of a species (e.g., proton reduction to H₂) versus the total number of incident photons from a light source. Variations in parameters between reaction systems, such as light intensity and temperature, means it is often difficult to compare performances in reaction systems. In addition, the number of absorbed photons is difficult to determine because of light scattering factors. Therefore, *apparent quantum yield* (AQY) at a known monochromatic wavelength is often used. For solar hydrogen evolution, the AQY is calculated from:³¹

$$\text{AQY (\%)} = \frac{\text{number of reacted electrons}}{\text{number of incident photons}} \quad (1.04)$$

$$\text{AQY (\%)} = \frac{(2 \times \text{number of H}_2 \text{ molecules produced})}{\text{number of incident photons}} \quad (1.05)$$

For semiconductors to be considered for solar driven water splitting, limiting the charge recombination rate is a key step in improving the efficiency of the system. Surface sites of photocatalysts may not be suitable to accommodate redox processes, as the binding energies of reactants to photocatalyst particles may not be favourable.³²

Photocatalytic water splitting also suffers from low efficiency due to thermodynamic considerations. The theoretical energy needed to fully split water

into its constituents is 1.229 V, with a Gibbs free energy of +237 kJ mol⁻¹, signalling a thermodynamically uphill reaction. In addition, a major factor that needs to be considered for water splitting reaction systems is overpotential, meaning the energy input necessary for water oxidation to occur often exceeds the 1.23 V threshold. Overpotential often results from kinetic challenges in reaction systems - depending on the particle in question, the formation of products may be kinetically hindered. More energy is often needed to migrate reactants to and from the particle surface. As such, research is often done in limiting overpotential through the addition of co-catalysts.

1.2.3. Co-Catalysis

To aid in lowering the energy necessary to realise solar fuel generation, co-catalysts are often employed. Co-catalysts used in photocatalytic solar fuel production are typically transition metals and serve multiple purposes. They act as alternative, more favourable active sites for catalytic reactions, as the binding energies are often lower for substrates on the co-catalyst surface. Co-catalysts are used as they lower the activation energy necessary to facilitate the redox processes occurring on the photocatalyst (Figure 1.04).³¹ The lowering of the activation energy allows for the chemical reactions to occur more quickly. In addition, in a photocatalytic reaction, co-catalysts can increase activity by “trapping” excited electrons at the conduction band. Essentially the co-catalyst acts as an electron sink, with its ability to harvest electrons largely determined by its work function.³³ The work function is the minimum energy needed to remove electrons from the surface of a solid to a point outside the solid surface. The work function is a property of the surface of solids and is typically higher for those metals which create strong electrical contacts.³⁴ The work function of metal co-catalysts has to be higher than that of the semiconductor to act as an efficient electron trap, with larger work functions corresponding to a lower Fermi level (Figure 1.05).³³ Some light absorbers are able to form Schottky barriers at the light absorber – co-catalyst interface. The Schottky barrier is a junction which aids in charge separation as the barrier prevents recombination of photogenerated holes and electrons, allowing the respective charge carriers to carry out redox reactions.^{35, 36}

Early work by Trassati showed a “volcano plot” for exchange current density (the rate of electron flow through a given area at reversible potentials) for the proton reduction reaction as a function of the binding energy of hydrogen atoms on the metal surface.³⁷ A low binding energy results from an insufficient overlap between metal orbitals and adsorbed atoms, creating weak bonds, while the opposite is true of high binding energies. In addition, low exchange current densities are indicative of insufficient electron flow from the metal to hydrogen – therefore a high exchange current density is favoured. Materials at the tip of the volcano plot act as the best cocatalysts as they possess the optimal binding energies for atom adsorption and desorption. As a result, Pt is often used in conjunction with semiconductors due to its negligible overpotential and fast reaction kinetics.³⁸

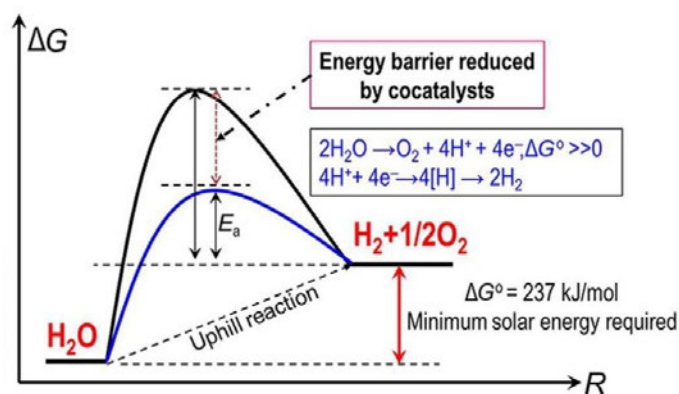


Figure 1.04. Schematic showing of the function of cocatalysts in lowering the activation energy in photocatalytic overall water splitting. Reprinted with permission from REF 31. Copyright 2017, Elsevier Publishing.

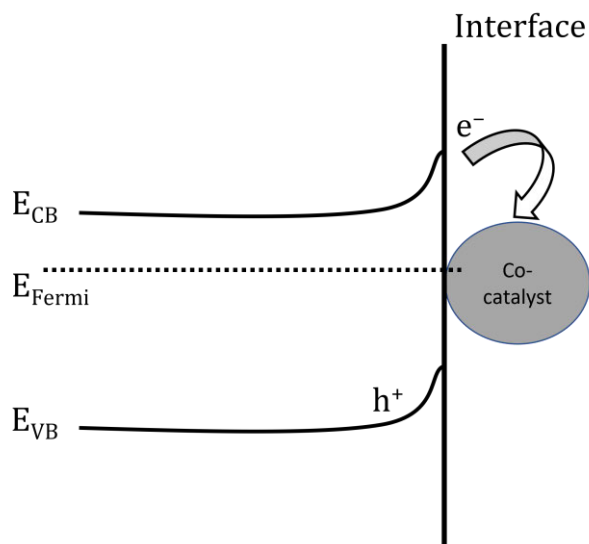


Figure 1.05. Depiction of photoexcited electron migrating to co-catalyst through the semiconductor – co-catalyst interface. The electron migrates to the co-catalyst in a lower lying energy state through the barrier.

1.2.4. Photocatalytic Hydrogen Evolution

In terms of solar fuel production, photocatalytic hydrogen evolution resulting from water splitting is viewed as a favourable means of tackling large scale energy crises. This is due from the simplicity of the system in that photocatalyst particles can act as light absorbers and the source of charge carriers to perform the necessary redox processes, not to mention a more scalable approach versus photovoltaic powered electrolysis (PV-E) and photoelectrochemical (PEC) processes.³⁹ PV-E processes are known to produce the best solar-to-hydrogen (STH) efficiency however are hindered in their applicability due to cost.³¹ Photocatalytic systems can simply be expanded, particularly those based on powdered semiconductors, provided the materials used in a large-scale system are cheap, readily available, and non-toxic.⁴⁰

It is estimated that hydrogen produced by particulate photocatalysts, assuming a STH efficiency of 5% to 10%, will cost 1.5 – 3.5\$ kg⁻¹.²² STH is defined by the output energy as hydrogen over incident solar light energy:^{39, 41, 42}

$$\text{STH} = \frac{(\text{mmol H}_2 \text{ s}^{-1}) \times 237000 \text{ J mol}^{-1}}{(100 \text{ mW cm}^{-2}) \times (\text{area}) \text{ cm}^2} \quad (1.06)$$

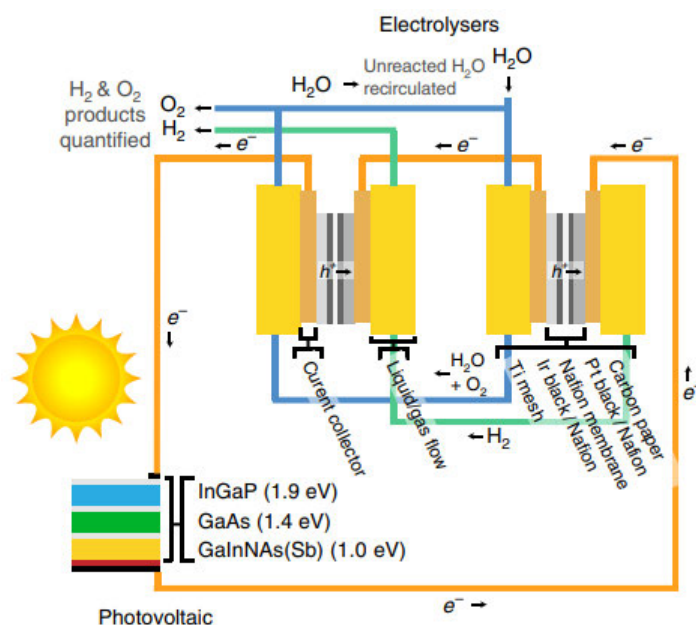
The STH efficiency is derived from the chemical energy of produced hydrogen (1.23 eV or 237 kJ mol⁻¹) divided by the solar energy input on the process, determined from the light intensity and the area of interest.³⁴ The costs associated with a STH efficiency of 5% to 10% align with the United States Department of Energy's goal to achieve H₂ production costs of 1\$ kg⁻¹ by 2030 to obtain a favourable economic alternative to non-renewable energy.⁴³

Despite the potential, generating hydrogen from sunlight *via* photocatalysis has not reached the efficiency required for industrial scale practical applications. The limitations can arise from multiple factors, including the use of photocatalyst, the choice of co-catalyst, and the susceptibility of the reaction system to be damaged through the presence of unwanted side products. For example, in photocatalytic water splitting oxygen is inherently produced as a product, which can become reactive and form reactive oxygen species (ROs) when reduced by photoexcited electrons. Thus, further research into the design and development of efficient photocatalytic hydrogen evolution systems are vital. Materials employed for solar hydrogen evolution should be considered based on their scalability, availability, and cost in addition to their practical ability.

1.2.5. Solar to Fuel Devices

The development, testing, and creation of solar to fuel devices is currently research intensive. As discussed, the aim of such research is to mimic plants, whereby sunlight is absorbed and the solar energy converted so that chemicals may be produced which can be used as fuels. The fuel produced in question would then ideally be harvested and utilised for energy purposes, such as a fuel cell, to power devices and infrastructure. In the past several decades, water splitting driven by sunlight has been investigated via various approaches to enhance the energy efficiency and cost effectiveness of the process. Photovoltaic devices to create hydrogen seems appealing as they can be coupled to an electrolyser, which performs the water splitting process to generate oxygen at an anode. Protons generated from water oxidation then migrate through a proton exchange membrane (PEM) and react with electrons at a cathode to evolve hydrogen. An example of such a device is shown in Scheme 1.04, whereby a multi-junction photovoltaic cell generates

photoexcited electrons which travel through an external circuit to the electrolyser. The device shown was capable of obtaining STH values of over 30%, using a InGaP/GaAs/GaInNAsSb triple-junction solar cell.⁴⁴

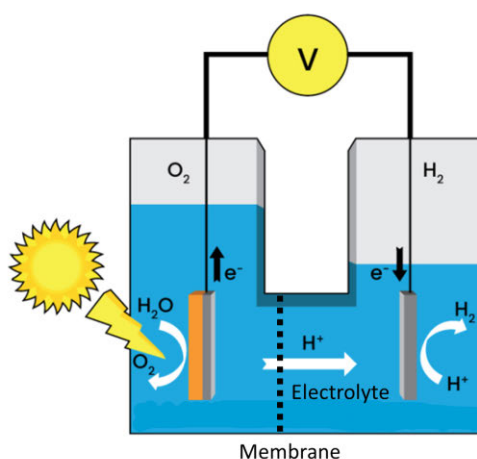


Scheme 1.04. Depiction of a PV-E system which highlights the bandgaps of the components used as the solar cell, the pathway of the photogenerated electrons to the cathode chamber of an electrolyser. Water is fed into the anode where it is oxidised, and the protons move across a PEM to the cathode, where they are subsequently reduced to H₂ gas. The gas produced can then be quantified. Reprinted with permission from REF 44, Copyright 2016, Springer Nature.

Reported values for STH efficiencies for PV-E devices are typically lower than solar to electricity PV efficiencies, resulting from poor matching of the current-voltage curves of the PV and the electrolyser.^{44, 45} This discrepancy in efficiency can be overcome by coupling multiple PV cells to electrolysers to optimize the match between the voltage characteristics of these device components.^{46, 47} This allowed STH efficiencies of 28% using a PV-E setup to evolve hydrogen in alkaline electrolysers with a triple-junction InGaP/InGaAs/Ge cell.⁴⁸ Systems such as these currently produce the best STH efficiencies but are highly limited in their application. This is a result of resistances in solution and mass transport in the liquid phase due to long ion transport distances. In PV-E systems, addition of the large amounts of supporting electrolyte, a high concentration of pH buffer reagents, and

circulation of the electrolyte solution are needed to minimize the solution resistances and overpotentials.⁴⁹⁻⁵¹

Direct photoelectrolysis of water is another method of solar to hydrogen production. This process involves a photoelectrochemical (PEC) cell, which consists of a photoelectrode (typically a photoanode) immersed in an aqueous electrolyte, an external circuit and a counter electrode to complete redox processes. Rather than coupling the light absorbing component to an electrolyser, PEC cells allow for the production of hydrogen through the integration of solar absorption and water splitting into a two-component assembly, where oxidation and reduction processes can occur.^{52, 53} (Scheme 1.05.)

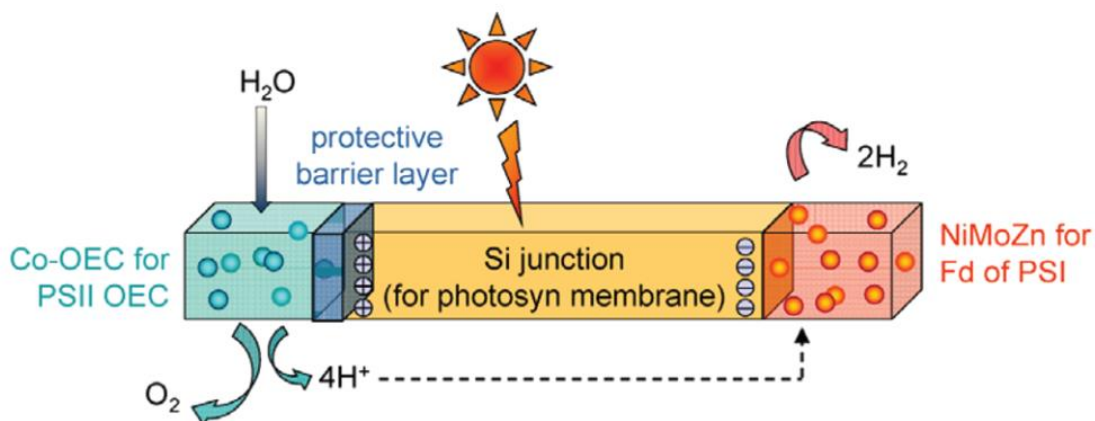


Scheme 1.05. Depiction of a photoelectrochemical cell for water splitting. A photoanode absorbs light to generate photoexcited electrons - these electrons migrate through an external circuit to a typically metal cathode, where protons are reduced. Protons migrate to the cathode through a PEM, and hydrogen can be evolved. The hydrogen evolved can then be harvested and stored for energy purposes. Original schematic found in REF 53.

For hydrogen to be produced using a PEC cell, multiple components need to be considered. First, the photoelectrode should be a semiconducting material with an appropriate bandgap, where the VB and CB lie at energy levels below the oxidation potential of water and above the reduction potential of protons, respectively. The semiconductor material in the photoelectrode must be capable of absorbing sunlight of an appropriate wavelength to generate electrons and holes. Moreover, the electrolyte solution should be conductive to allow for the mobility of protons. Protons migrate through a PEM, which is semi-permeable to protons as well as acting as an electronic insulator and reaction barrier.⁵⁴ This aims to prevent the mixing of hydrogen and oxygen to increase the STH efficiency.

Semiconductors for photoelectrodes are an area of great research, with many metal-based materials having been tested for PEC water splitting including CdS, Cu₂O, ZnO, and Fe₂O₃.⁵⁵⁻⁵⁸ Of the emerging materials, BiVO₄ offers improved STH efficiency and can achieve up to 80% of its theoretical STH efficiency.⁵⁹ It should be noted however, that the improvements in performance arise from delicate tuning of the material, including surface modifications as well as coupling to WO₃ to aid in increasing performance.⁶⁰ In addition, most photoelectrodes suffer from a decrease in STH efficiency as a result poor long-term stability and poor charge separation at the semiconductor-electrolyte interface. Moreover, a dual component setup requires careful design of each component to achieve tangible results.

A direct means of solar to fuel production lies in close replication to the mechanism in plants – the artificial leaf.⁶¹ The artificial leaf copies natural photosynthesis by possessing an oxygen evolving component as well as a proton reducing component to evolve hydrogen, a schematic of which is shown in Scheme 1.06.



Scheme 1.06. Schematic showing the process in an artificial leaf, composed of both a water oxidation and proton reduction site. The charges made available for oxidation and reduction are created through the excitation of a Si semiconductor. Reprinted with permission from REF 61 Copyright 2012, American Chemical Society

For the artificial leaf to efficiently evolve hydrogen careful consideration must be given to the water oxidation catalyst, which is a Co-based catalyst composed of Co and O, with Co shown to be in both a +2 and +4 oxidation state.⁶² The Co(IV) centre is responsible for water oxidation and operates at low overpotentials and has near 100% faradaic efficiency highlighting the selectivity of the catalyst for O₂ production from water.⁶³ The Co-OEC is immersed in water containing phosphate, and the activity of the catalyst notably decreases in the absence of phosphate.⁶⁴ The hydrogen evolving component of the artificial leaf is an alloy composed of Ni, Mo, and Zn which is formed from electrodeposition.⁶⁵ The “leaf” can also be constructed with triple junction amorphous Si.⁶⁶ This triple junction is shown to produce greater performance for water splitting, as the three PVs are able to absorb more light to generate more voltage for the reactions at the anodic and cathodic components.

While the artificial leaf shows good photoelectrocatalytic performance for the overall water splitting reaction, the STH efficiency is still much lower than that obtained from PV-E and PEC setups, and when scaled up is likely to lose even more efficiency due to Ohmic resistance. More efficient PVs than Si may allow for an increase in the hydrogen-producing capabilities of the artificial leaf.

An emerging technology which possesses great appeal for direct hydrogen production from sunlight due to its cost and accessibility is a photocatalytic solar panel. In the panel is a particulate photocatalyst and water. When the photocatalyst

is irradiated, hydrogen and oxygen gas can be produced simultaneously on light absorbing catalyst particles in close proximity to each other – this mitigates the aforementioned issues with solution resistances and concentration overpotentials, as no supporting electrolyte is necessary.⁶⁷ Planar photocatalyst sheets for solar-to-hydrogen reactions can be made by drop casting the photocatalyst onto a glass substrate. Notably upon irradiation, the activities of a planar photocatalyst sheet and a conventional powdered suspension show similar levels of activity and produce hydrogen and oxygen in stoichiometric amounts over long periods of irradiation.⁶⁷ Moreover, a 1 m × 1 m planar catalyst sheet with varying depths of water as a feedstock did not diminish the gas detection allowing for the production of gaseous products to easily be released from the panel structure to an outlet. A photocatalyst panel of this type needs to be carefully engineered to avoid accumulation of explosive quantities of hydrogen and oxygen gas, as the flammability of hydrogen can occur at as little as 4%.⁶⁸ Work also showed that, while the STH efficiency is lower than a PV-E system, the AQY of the photocatalyst is near 60%, showing that a high number of photons are actually used in the generation of photoexcited electrons for proton reduction. The STH efficiency can be improved by choosing semiconducting materials with narrower bandgaps to access more of the solar spectrum, and to produce more charge carriers for chemical processes.

The beauty of a construction utilising planar panels containing catalysts lies in the simplicity and cost. Cost analysis has shown that photocatalytic water splitting offers a scalable and cost-feasible means for the production of hydrogen from sunlight.⁶⁹ While scaling up measures are being attempted, devices need further research to improve the spatial separation of hydrogen and oxygen produced on a photocatalyst particle, as well as finding suitable materials which are capable of performing photocatalytic water splitting. Research should also focus on novel reaction conditions for the photocatalyst to aid in realising idealised systems for the scalable production of hydrogen.

1.2.6. Principles of Hydrogen Evolution

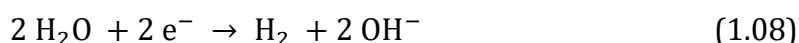
Currently, there is an abundance of known photocatalytic materials capable of absorbing solar light to generate charge carriers at potentials required for the reduction of protons to hydrogen. These photocatalysts operate under the basic mechanism of operation. Sequentially:²⁸

- i) Photons possessing energy greater than the bandgap energy of the photocatalyst are absorbed
- ii) Electrons are excited from the VB to the higher energy CB, creating an electron / hole pair
- iii) The photoexcited carriers must then separate and migrate to the surface
- iv) Redox reactions involving the migrated charge carriers are then carried out

If the electron / hole pair cannot sufficiently separate, the absorbed light energy is lost as heat energy or radiation when electrons and holes recombine in the bulk of the semiconductor. Electrons that do participate in the reduction of protons to hydrogen can react in acidic conditions:



Or in basic conditions as follows:



In acidic conditions protons are reduced by excited electrons in the CB / co-catalyst, however this can only occur if the energy level at the CB possesses an energy potential more negative (more reducing) than the reduction potential of protons (0.0 V vs. the normal hydrogen electrode NHE at pH = 0). Oxidation at the VB can only occur if the VB possesses an energy more positive (more oxidising) than the oxidation potential of the species in question (for H₂O, the oxidation potential = 1.23 V vs. NHE at pH = 0). As a result, the theoretical bandgap of a material performing simultaneous water oxidation and proton reduction is 1.23 V. This energy corresponds to a photon with a wavelength of ~1000 nm according to the following calculation. Given that 1 electron volt (eV) = 1.60 × 10⁻¹⁹ joules:

$$E = h\nu \quad (1.09)$$

$$E = \frac{hc}{\lambda} \quad (1.10)$$

$$\lambda = \frac{hc}{E} \quad (1.11)$$

$$\lambda = \frac{(6.626 \times 10^{-34} \text{ J s}) \times (3.0 \times 10^8 \text{ m s}^{-1})}{1.97 \times 10^{-19} \text{ J}} \quad (1.12)$$

$$\lambda = 1009 \text{ nm}$$

where E is the energy of a photon, h is Planck's constant, ν is frequency, c is the speed of light, λ is the wavelength. However, to account for thermal and kinetic losses associated with the reduction and oxidation processes at the photocatalyst, semiconductors should possess bandgaps greater than 1.6 eV to effectively split water, corresponding to a wavelength of around 776 nm.⁴¹ In addition, to aid in increasing the separation of charge carriers, semiconductors should possess a smaller particle size – as photocatalyst particles shrink in size there exists fewer grain boundaries in the bulk material and so recombination of charge carriers is limited in the bulk as they have less time to recombine.^{28,70} By also creating smaller particles, the time for charge carriers to migrate to the surface is shortened which also prevents recombination.⁷¹

1.2.7. Sacrificial Electron Donors for Solar Hydrogen Evolution

Due to the thermodynamically uphill nature associated with the overall water splitting reaction, it is often favourable to investigate half reactions of the water splitting process. This can be done using *sacrificial reagents*.⁷² Sacrificial reagents are used to increase activity for redox processes – sacrificial electron acceptors are reduced from excited electrons at the CB, while sacrificial electrons donors (SEDs) are oxidised at the VB. For solar hydrogen generation, SEDs are often used in reaction systems to quench photogenerated positive holes in the VB. By quenching the photogenerated positive holes, charge recombination is prevented, allowing the

free electrons to migrate and reduce protons to hydrogen. Primarily, the role of the SED is to disregard the oxidation step of overall water splitting, isolating the reduction half reaction and increasing photocatalytic hydrogen evolution activity of the system.⁷³

SEDs are used as they are much easier to oxidise than H₂O resulting from their more negative oxidation potential relative to the VB of semiconductors. Common organic electron donors are based on amines, alcohols, and carboxylic acids such as ascorbic acid and lactic acid. The choice of electron donor is important for reaction systems as their oxidation potential is highly dependent on pH, and the activity of solar hydrogen evolution associated with semiconductors can vary depending on the choice of sacrificial reagent.⁷⁴

1.3. Semiconductors for solar hydrogen evolution

1.3.1. TiO₂

In the 1970s, Fujishima and Honda used a PEC cell consisting of a TiO₂ photoanode, a Pt counter electrode, and a source of UV irradiation to successfully decompose water into oxygen and hydrogen.⁷⁵ However, this system suffers from low efficiency, with a quantum yield of less than 1%. Nevertheless, TiO₂ has been extensively studied in the literature, and has been used in multiple studies as a model photocatalyst owing to its availability, low cost, low toxic nature, and its stability.⁷⁶

TiO₂ exists in a variety of crystalline phases, the most common of which are anatase, rutile, and brookite.⁷⁷ Each phase possesses its own unique crystal structure, and the electronic, physical, and optical properties differ between TiO₂ phases, with anatase and rutile the most widely researched phases.⁷⁸ The difference in lattice structure (Figure 1.03) between anatase and rutile results in different densities and band structures.^{71, 79, 80} Anatase TiO₂ possesses a bandgap of 3.2 eV while rutile TiO₂ has a bandgap of 3.0 eV. The difference in electronic band structure affects photon absorption and consequently redox reactivity occurring at the VBs and CBs.^{81, 82} Despite its larger bandgap, anatase TiO₂ is known to be more active for

photocatalytic processes, as rutile TiO_2 exhibits a slower rate of transport of photogenerated charge carriers to the material surface.⁸³ Research has also suggested that rutile TiO_2 tends to possess a lower surface adsorption capacity, meaning substrates are not as favourably bound to rutile surfaces in comparison to anatase.^{84, 85} Moreover, photogenerated charge carriers in anatase TiO_2 have a lifetime an order of magnitude greater than rutile, enhancing the probability of excited electrons and holes participating in chemical reactions at the surface sites of the semiconductor.⁸⁶⁻⁸⁸

Commercial TiO_2 powder is often a mixture of anatase TiO_2 and rutile TiO_2 . This phase mixing is also thought to contribute to photocatalytic activity, as the photoexcited electrons can transfer between anatase and rutile surface sites, promoting charge separation.^{86, 87} It has also been demonstrated that the surface states relating to oxygen vacancies in commercial TiO_2 can aid photocatalytic reactions upon irradiation, due to the electron transfer from anatase surface states to rutile.⁸⁹

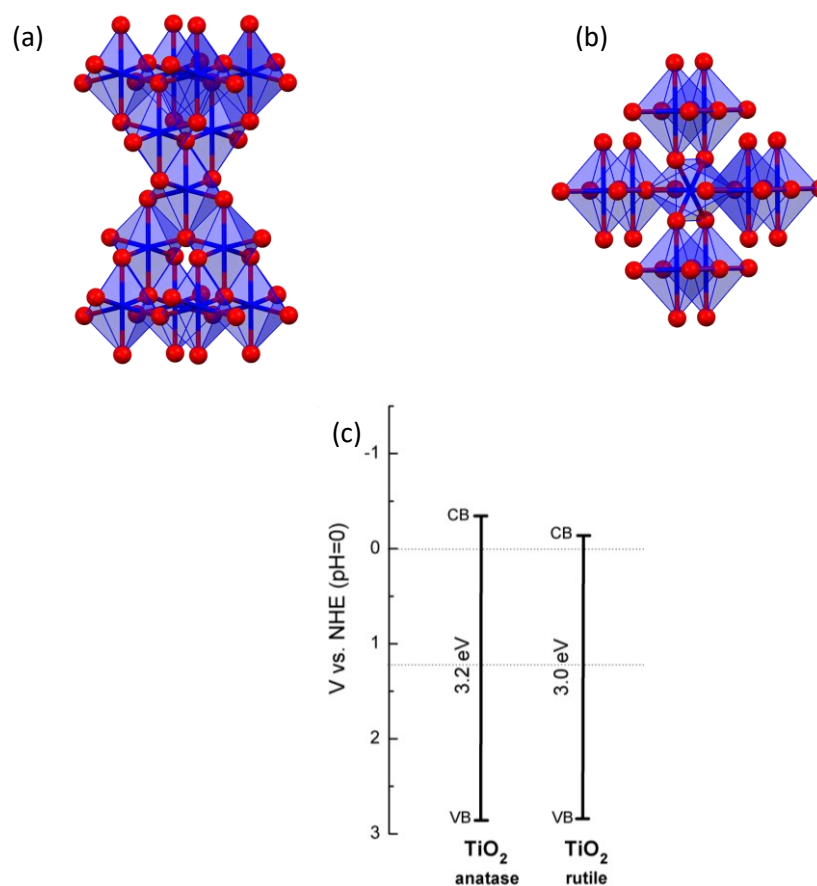


Figure 1.06. Crystalline structure of (a) anatase TiO₂ and (b) rutile TiO₂. Titanium atoms are blue and oxygen atoms are red. (c) Depiction of band gap energies and positions of anatase TiO₂ and rutile TiO₂ vs. normal hydrogen electrode (NHE). Reprinted with permission from REF 82. Copyright 2015, Springer Nature

TiO₂ suffers from issues hindering its function as a viable photocatalyst for solar fuel production. These issues include its large bandgap, which limits absorption to strictly high energy photons.⁸⁰ TiO₂ also exhibits rapid charge recombination, whereby photoexcited charge carriers fail to separate, preventing them from partaking in redox processes on the photocatalyst.⁹⁰ Strategies to overcome these problems have been extensively researched, such as doping with both metals and non-metals, increasing crystallinity (and subsequently charge carrier separation) through annealing, introducing trapping layers through defect introduction, and many more.⁹¹⁻⁹⁷ Systems utilising TiO₂ should consider its viability and applicability for solar fuel production due to these modifications required to enhance performance.

1.3.2. Carbon Nitrides

Carbon nitrides (CNs) are organic compounds composed of carbon and nitrogen. In the literature, CNs are often referred to as a series of polymeric compounds synthesised from thermal poly-condensation of nitrogen rich organic compounds. CNs synthesised in this manner can exist as different allotropes – “melon” is a linear allotrope of CN consisting of tri-s-triazines, interconnected via secondary nitrogen atoms. The most well-known and utilised allotrope of CN is graphitic carbon nitride, which is often termed g-C₃N₄. g-C₃N₄ was first used as a photocatalyst for water splitting under visible light in 2009 by Antonietti and co-workers,⁹⁸ and has since been researched extensively as a metal-free heterogenous semiconductor for solar fuel production, degradation of organic dyes and drugs, even bone regeneration and fracture healing.⁹⁹⁻¹⁰⁶

g-C₃N₄ possesses a bandgap typically around 2.7 eV with the CB lying at a potential of -1.1 V vs. NHE and the VB at +1.6 V vs. NHE, meaning the energy levels of the bands are suitable to perform solar water splitting (Figure 1.07).¹⁰⁷⁻¹⁰⁹ CNs also have the desired benefit of being easy to synthesise. They can be synthesised from the

pyrolysis of nitrogen rich organic precursors such as melamine, dicyandiamide, and urea, as shown in Scheme 1.04.¹⁰⁹ g-C₃N₄ is considered the most stable allotrope of CN under ambient conditions and when the aforementioned precursors are synthesised *via* thermal polycondensation, a material composed of two-dimensional sheets composed of tri-s-triazine subunits connected *via* tertiary amines in a layered graphitic nature is produced.

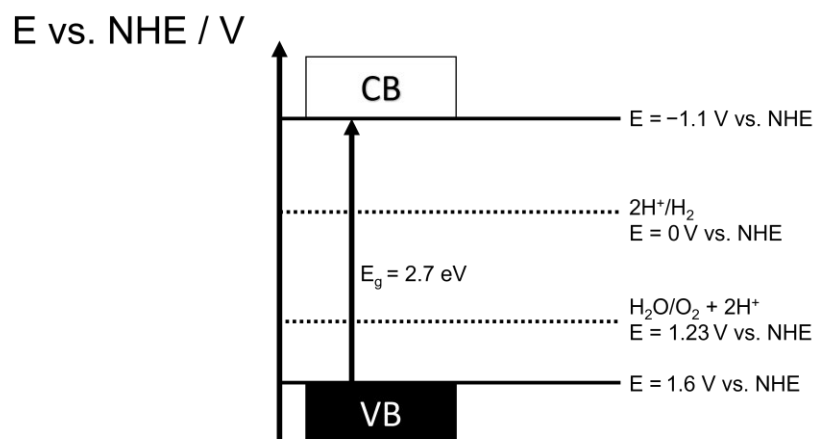
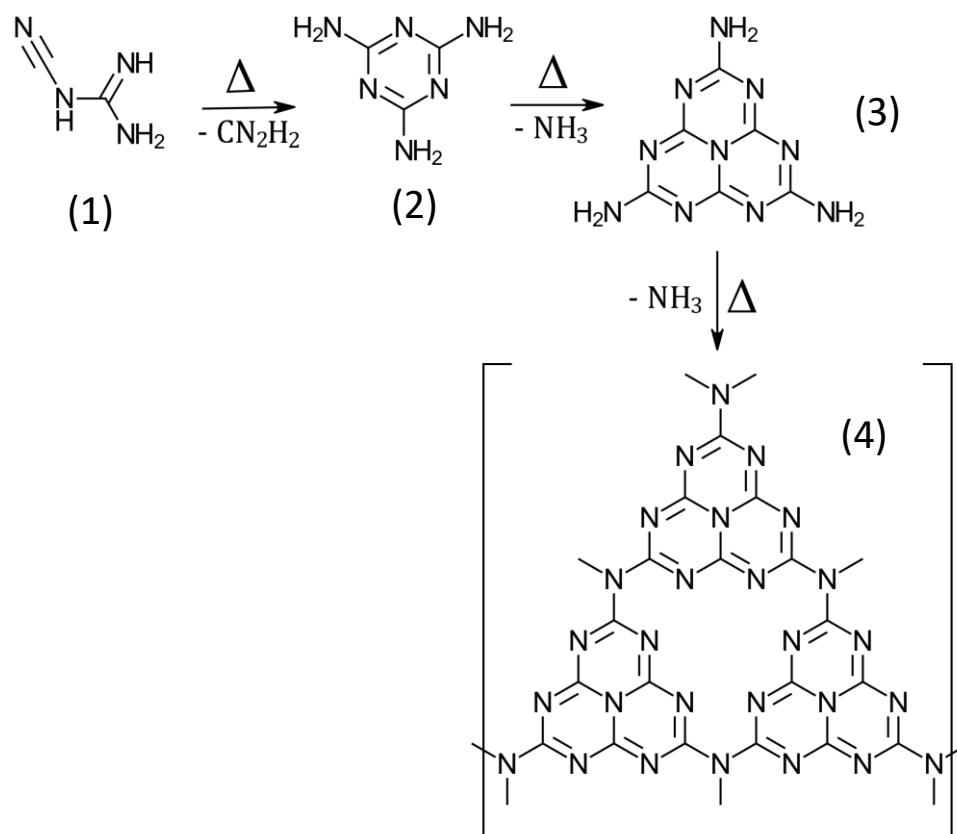


Figure 1.07. Depiction of band gap energies and positions of g-C₃N₄ relative to water oxidation and proton reduction energies vs. normal hydrogen electrode at pH = 0.

The choice of precursor can affect both the physical and electronic properties of the resulting semiconductor when synthesised. For example, g-C₃N₄ synthesised from dicyandiamide (DCDA) has a higher surface area ($11 \text{ m}^2 \text{ g}^{-1}$) than g-C₃N₄ synthesised from melamine ($9 \text{ m}^2 \text{ g}^{-1}$), but both precursors yield semiconductors with similar absorption profiles and bandgaps.^{110, 111} On the other hand, urea-derived g-C₃N₄ possesses a large surface area ($31 \text{ m}^2 \text{ g}^{-1}$) but shows an absorption edge closer to the UV region, limiting its visible light absorption capabilities.¹¹² All g-C₃N₄ materials show some absorption in the visible region greatly expanding their viability as photocatalysts compared to TiO₂ as they can absorb a greater number of photons. These properties make g-C₃N₄ a model photocatalyst. While the synthesis and mechanism for its synthesis is speculated, the proposed thermal polycondensation reaction to produce g-C₃N₄ semiconductor is shown in Scheme 1.07.^{108, 111}



Scheme 1.07. Proposed synthesis pathway of $g\text{-C}_3\text{N}_4$ (4) from dicyandiamide (1). Melamine (2) and the heptazine melem (4) are known as intermediates in the thermal polycondensation process. Varying temperatures are reported for the syntheses of $g\text{-C}_3\text{N}_4$.¹⁰⁹

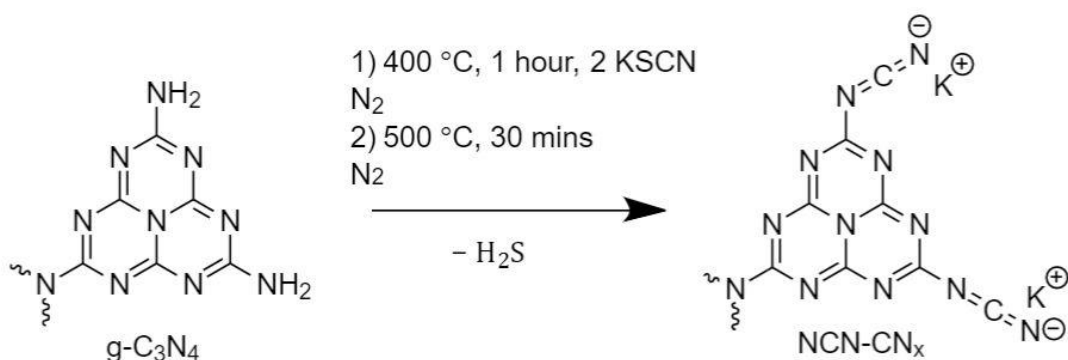
Despite its favourable properties, as-prepared $g\text{-C}_3\text{N}_4$ materials often exhibit low photocatalytic activity mostly resulting from a rapid photogenerated charge recombination rate. Photoexcited holes and electrons in $g\text{-C}_3\text{N}_4$ often exhibit short lifetimes owing to the poor crystallinity associated with its amorphous graphitic structure. Most focus on improving the photocatalytic performance of $g\text{-C}_3\text{N}_4$ materials is on enhancing this charge carrier generation through introduction of dopants, and through increasing the absorption edge of the semiconductor above 460 nm.^{113, 114} Functionalising and nanostructuring $g\text{-C}_3\text{N}_4$ is viewed as a favourable means to aid in increasing activity.

1.3.3. Functionalised Carbon Nitride – NCN-CN_x

When carbon nitride based semiconductors are synthesised, the stoichiometry of C : N is not exactly C_3N_4 as a result of incomplete condensation of amino groups at

terminal edge sites. Edge sites of semiconductor particles are decisive for photocatalytic activity as they are the active sites where redox processes occur. Chemical modification of edge sites provides an interesting means to alter the performance of carbon nitride photocatalysts.

It has been shown that functionalising the *s*-heptazine subunits of the carbon nitride polymer with cyanamide ($-N=C=N^-$) moieties can aid in enhancing co-catalyst binding to the photocatalyst surface and improve charge separation.¹¹⁵ Individual heptazine units are the locations of excitons - the bound state of an electron-hole pair which are attracted to each other by the electrostatic Coulomb force; as such, improving charge separation on heptazine oligomers is a desirable means of improving performance of the semiconducting materials for photocatalytic redox processes. By treating bulk $g\text{-C}_3\text{N}_4$ with KSCN, edge sites with amine residues can selectively react to generate $-N=C=N^-$ groups as shown in Scheme 1.08.¹¹⁵ Functionalising in this manner allows for the generation of an accumulation of electrons in the CB of the material upon irradiation in the presence of an efficient reductant. The electrons can also become trapped in other states in the material where they can reside indefinitely. This “reduced state” is observable by eye as a colour change of the material occurs from yellow to turquoise blue when irradiated.^{115, 116} This colour change is thought to occur through the presence of band-edge excitons inducing state-filling or through a depletion of ground state carriers to the excited state.



Scheme 1.08. Proposed reaction scheme for the formation of NCN-CN_x from the edge sites in $g\text{-C}_3\text{N}_4$.¹¹⁵

NCN-CN_x serves to function as a more active photocatalyst than conventional g-C₃N₄ and due to its facile synthesis and high performance for proton reduction has attracted attention in recent years for applications in photocatalysis reactions.

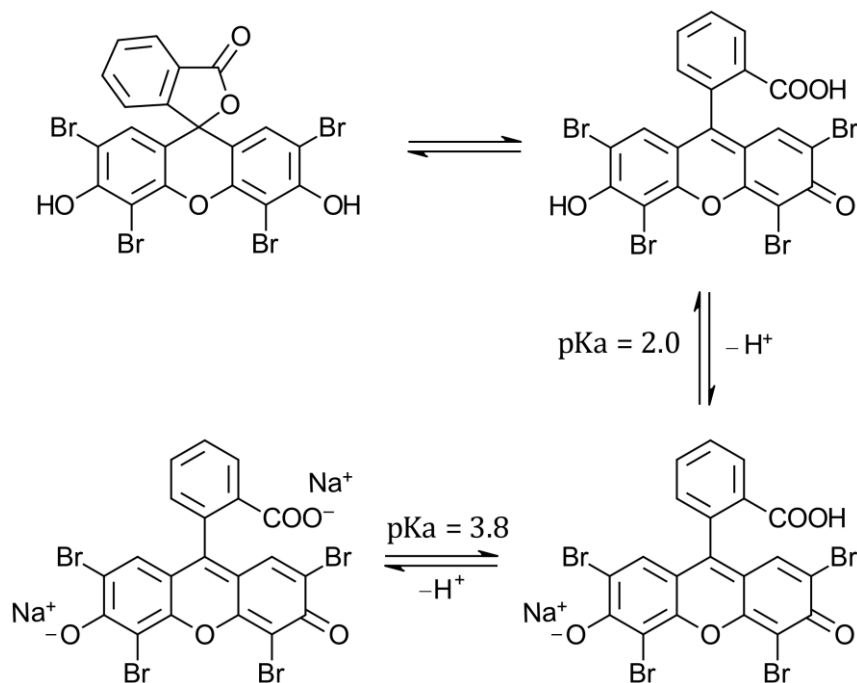
1.4. Homogenous Photocatalysts for Solar Fuel Production

1.4.1. Eosin Y

While particulate semiconductors are typically used as light absorbers for photocatalytic purposes, organic molecules can also fulfil the necessary prerequisites for the conversion of light energy into chemical energy. These organic molecules are convenient as they possess properties which are tunable through their syntheses. Of these, xanthene dyes are highly appealing due to their ease of preparation and cost. Eosin Y is a xanthene derivate which is used as a dye and has also found use as a light absorber in photocatalytic solar fuel reactions.¹¹⁷⁻¹¹⁹

Eosin Y (2', 4', 5', 7'-tetrabromofluorescein, EY) is a well-known and well-studied photoabsorber which features a very prominent absorption of light giving it a notable red colour when dissolved in water. Photochemically, EY is well understood – when excited by visible light, EY undergoes intersystem crossing from a singlet to a low energy triplet state allowing the molecule to become more reducing and oxidising in comparison to its ground state.^{120, 121} The lifetime of the excited triplet state is around 24 μs and shows notable absorption at 539 nm.^{122, 123} The energy between the ground state and triplet state is known to be 1.89 eV, and so possesses a much smaller HOMO – LUMO gap than most conventional semiconductors applied for photocatalytic purposes. The redox potentials of the excited state can be estimated from the standard redox potentials of the ground state, determined by cyclic voltammetry, and the triplet excited state energy.^{119, 120} Despite its favourable absorption properties and small HOMO – LUMO energy gap, EY is known to have limitations. EY suffers from an inherently low stability - when irradiated with visible light in the presence of molecular O₂, photoexcited electrons from EY react to form singlet O₂ which can react with EY and induce a discolouration of the dye, with the

absorbance dramatically decreased after only three hours irradiation.^{124, 125} In the absence of molecular O₂, EY undergoes debromination when irradiated with visible light, which affects the absorption properties of the dye, lowering the absorption in the visible and UV region.¹²⁵ As such, considerations should be made to the reaction setup when using EY, particularly an inert atmosphere.



Scheme 1.09. Acid-base behaviour of Eosin Y and the formation of the disodium salt Na₂EY. Schematic based on original scheme found in REF 112.

Eosin Y and indeed other fluorescein dyes are subject to different photochemical behaviours based on the pH of the solution. Scheme 1.09 shows the pK_a values at which Eosin Y becomes deprotonated and can attain a state in which the molecule becomes photocatalytically active.¹¹⁰ At low pH values, Eosin Y adopts a spirocyclic structure which breaks the aromaticity of the xanthenoid π-system. Typically, a higher pH is required to realise the dibasic form of Eosin Y and enable an increase in photocatalytic performance.

1.5. Project Aims

While the principles and underlying mechanisms of photocatalytic solar fuel production are well understood and have been researched extensively, the

literature largely fails to address a key component of photocatalysis – the solvent. Solvent effects on photocatalysis have gone unexplored in the literature despite the fact that catalytic systems – the photocatalyst, sacrificial reagents, and co-catalysts are in constant contact with the reaction medium. Typically, H₂ evolution is performed in aqueous conditions with the semiconductor powder suspended *in situ*. Homogenous light absorbers are dissolved prior to irradiation. The aims of this project are to investigate a new type of solvent – deep eutectic solvents (DESs) – and their effect on photocatalytic hydrogen production.

In chapter 2, DESs are introduced as competitive media with aqueous solutions. The DESs investigated show that stability and performance is not affected using certain photocatalysts in DESs – the efficiency of photocatalytic H₂ production by select materials and select dyes will also be discussed and rationalised.

In chapter 3, properties of DESs are exploited to enable highly efficient and stable O₂ tolerant H₂ evolution. The chemical properties of DESs will be explored electrochemically and applying the factors which enable DESs to be tolerant to O₂ in aqueous solutions. A mechanistic understanding of O₂ tolerance will be discussed and how fully O₂ tolerant photocatalytic hydrogen production may be possible.

Chapter 4 shows how DESs can also enhance the H₂ evolution activity of co-catalytic hydrogenases. A [NiFeSe] hydrogenase is used in conjunction with a TiO₂ light absorber to highlight the strength of DESs as reaction media for solar H₂ production. DESs and their properties will again be analysed electrochemically to understand the increase in performance, and the aerobic H₂ evolution by the enzyme, which conventionally is applied in anaerobic conditions, can also be augmented and tuned through solvent design.

1.6. References

1. BP, Statistical Review of World Energy, <https://www.bp.com/en/global/corporate/energy-economics/statistical-review-of-world-energy.html>, (accessed April 2022).
2. International Energy Agency, Global Energy Review 2021, <https://www.iea.org/reports/global-energy-review-2021>, (accessed April 2022)
3. N. J. L. Lenssen, G. A. Schmidt, J. E. Hansen, M. J. Menne, A. Persin, R. Ruedy and D. Zyss, *J. Geophys. Res. Atmos.*, 2019, **124**, 6307-6326.
4. H. B. Gray, *Nature Chem.*, 2009, **1**, 7-7.
5. N. S. Lewis and D. G. Nocera, *Proc. Natl. Acad. Sci. U.S.A.*, 2006, **103**, 15729-15735.
6. V. Nelson and K. Starcher, *Wind Energy: Renewable Energy and the Environment*, CRC Press, Florida, 2018.
7. Darmawi, R. Sipahutar, S. M. Bernas and M. S. Imanuddin, *Renew. Sust. Energ. Rev.*, 2013, **17**, 213-215.
8. M. F. Kuehnel and E. Reisner, *Angew. Chem. Int. Ed.*, 2018, **57**, 3290-3296.
9. The World Counts, <https://www.theworldcounts.com/challenges/climate-change/energy/renewable-energy-resources>, (accessed April 2022).
10. National Renewable Energy Laboratory, <https://www.nrel.gov/grid/solar-resource/spectra.html>, (accessed June 2022).
11. PVEducation, <https://www.pveducation.org/pvcdrom/appendices/standard-solar-spectra>. (accessed June 2022)
12. National Renewable Energy Laboratory, <https://www.nrel.gov/grid/solar-resource/spectra-am1.5.html>, (accessed June 2022).
13. C. A. Gueymard, D. Myers and K. Emery, *Sol. Energy*, 2002, **73**, 443-467.
14. S. Berardi, S. Drouet, L. Francàs, C. Gimbert-Suriñach, M. Guttentag, C. Richmond, T. Stoll and A. Llobet, *Chem. Soc. Rev.*, 2014, **43**, 7501-7519.
15. G. R. Fleming, G. S. Schlau-Cohen, K. Amarnath and J. Zaks, *Faraday Discuss.*, 2012, **155**, 27-41.
16. Y. Tachibana, L. Vayssieres and J. R. Durrant, *Nat. Photonics*, 2012, **6**, 511-518.
17. N. Armaroli, V. Balzani, *Energy for a Sustainable World: From the Oil Age to a Sun-Powered Future*, Wiley-VCH, Weinheim, 2010
18. W. Zhao, Z. Chen, X. Yang, X. Qian, C. Liu, D. Zhou, T. Sun, M. Zhang, G. Wei, P. D. Dissanayake and Y. S. Ok, *Renew. Sust. Energ. Rev.*, 2020, **132**, 110040.
- 19.
19. J. Yang, H. Yan, X. Zong, F. Wen, M. Liu and C. Li, *Proc. R. Soc. A: Math. Phys. Eng. Sci.*, 2013, **371**, 20110430.
20. S. Zhu and D. Wang, *Adv. Energy Mater.*, 2017, **7**, 1700841.
21. L. Zhang, N. Ding, J. Wu, K. Iwasaki, L. Lin, Y. Yamaguchi, Y. Shibayama, J. Shi, H. Wu, Y. Luo, K. Nakata, D. Li, X. Wang, A. Fujishima and Q. Meng, *Catal. Sci. Technol.*, 2018, **8**, 3846-3852.
22. A. Kudo and Y. Miseki, *Chem. Soc. Rev.*, 2009, **38**, 253-278.
23. R. Li and C. Li, in *Adv. Catal.*, ed. C. Song, Academic Press, Massachusetts, 2017, vol. 60, ch. 4 1pp. 1-57.
24. W. Bi, X. Li, L. Zhang, T. Jin, L. Zhang, Q. Zhang, Y. Luo, C. Wu and Y. Xie, *Nat. Commun.*, 2015, **6**, 8647.
25. J. Yang, D. Wang, H. Han and C. Li, *Acc. Chem. Res.*, 2013, **46**, 1900-1909.
26. B. Ofuonye, J. Lee, M. Yan, C. Sun, J.-M. Zuo and I. Adesida, *Semicond. Sci. Technol.*, 2014, **29**, 095005.
27. S. Du, X. Lin, C. Li, G. Li, B. Zheng, Y. Liu, H. Xu and P. Fang, *Chem. Eng. J.*, 2020, **389**, 124431.

28. S. M. Sze, Kwok K. Ng., *Physics of Semiconductor Devices*, John Wiley and Sons, New Jersey, 3rd edn, 2006, vol. 1, ch. 4 pp. 197-240.
29. S. Trasatti, *J. Electroanal. Chem. Interfacial Electrochem.* 1972, **39**, 163-184.
30. B. Han and Y. H. Hu, *Energy Sci. Eng.*, 2016, **4**, 285-304.
31. T. Takata and K. Domen, *ACS Energy Lett.*, 2019, **4**, 542-549.
32. T. Setoyama, T. Takewaki, K. Domen and T. Tatsumi, *Faraday Discuss.*, 2017, **198**, 509-527.
33. Q. Wang and K. Domen, *Chem. Rev.*, 2020, **120**, 919-985.
34. M. Qureshi and K. Takanabe, *Chem. Mater.*, 2017, **29**, 158-167.
35. Office of Energy Efficiency and Renewable Energy, <https://www.energy.gov/eere/fuelcells/articles/hydrogen-shot-introduction>, (accessed July 2022)
70. Q. Li, B. Guo, J. Yu, J. Ran, B. Zhang, H. Yan and J. R. Gong, *J. Am. Chem. Soc.*, 2011, **133**, 10878-10884.
71. R. Marschall, *Adv. Funct. Mater.*, 2014, **24**, 2421-2440.
72. Y. Pellegrin and F. Odobel, *C. R. Chim.*, 2017, **20**, 283-295.
73. E. A. Kozlova and V. N. Parmon, *Russ. Chem. Rev.*, 2017, **86**, 870-906.
74. U. Pal, S. Ghosh and D. Chatterjee, *Transition Met. Chem.*, 2012, **37**, 93-96.
75. A. Fujishima and K. Honda, *Nature*, 1972, **238**, 37-38.
76. J. Schneider, M. Matsuoka, M. Takeuchi, J. Zhang, Y. Horiuchi, M. Anpo and D. W. Bahnemann, *Chem. Rev.*, 2014, **114**, 9919-9986.
77. Q. Guo, C. Zhou, Z. Ma and X. Yang, *Adv. Mater.*, 2019, **31**, 1901997.
78. S. Nosheen, F. S. Galasso and S. L. Suib, *Langmuir*, 2009, **25**, 7623-7630.
79. A. N. Yoshio Nosaka, *Introduction to Photocatalysis: From Basic Science to Applications*, Royal Society of Chemistry, Cambridge, 2016.
90. M. Janczarek and E. Kowalska, *Catalysts*, 2017, **7**, 317.
81. Y. Liu, Z. Li, M. Green, M. Just, Y. Y. Li and X. Chen, *J. Phys. D: Appl. Phys.*, 2017, **50**, 193003.
82. Y. Mi and Y. Weng, *Sci. Rep.*, 2015, **5**, 11482.
83. T. Luttrell, S. Halpegamage, J. Tao, A. Kramer, E. Sutter and M. Batzill, *Sci. Rep.*, 2014, **4**, 4043.
84. J. Zhang, P. Zhou, J. Liu and J. Yu, *Phys. Chem. Chem. Phys.*, 2014, **16**, 20382-20386.
85. M. Xu, Y. Gao, E. M. Moreno, M. Kunst, M. Muhler, Y. Wang, H. Idriss and C. Wöll, *Phys. Rev. Lett.*, 2011, **106**, 138302.
86. T. Ohno, K. Sarukawa, K. Tokieda and M. Matsumura, *J. Catal.*, 2001, **203**, 82-86.
87. J. M. Kesselman, G. A. Shreve, M. R. Hoffmann and N. S. Lewis, *J. Phys. Chem.*, 1994, **98**, 13385-13395.
88. M. A. Fox and M. T. Dulay, *Chem. Rev.*, 1993, **93**, 341-357.
89. L. Jing, S. Li, S. Song, L. Xue and H. Fu, *Sol. Energy Mater. Sol. Cells*, 2008, **92**, 1030-1036.
90. R. Qian, H. Zong, J. Schneider, G. Zhou, T. Zhao, Y. Li, J. Yang, D. W. Bahnemann and J. H. Pan, *Catal. Today*, 2019, **335**, 78-90.
91. Z. Cui, M. Zhao, X. Que, J. Wang, Y. Xu, M. N. Ghazzal, C. Colbeau-Justin, D. Pan and W. Wu, *ACS Omega*, 2021, **6**, 27121-27128.
92. K. Shirai, G. Fazio, T. Sugimoto, D. Selli, L. Ferraro, K. Watanabe, M. Haruta, B. Ohtani, H. Kurata, C. Di Valentin and Y. Matsumoto, *J. Am. Chem. Soc.*, 2018, **140**, 1415-1422.
93. B. Dong, T. Liu, C. Li and F. Zhang, *Chin. Chem. Lett.*, 2018, **29**, 671-680.
94. O. Teruhisa, M. Takahiro and M. Michio, *Chem. Lett.*, 2003, **32**, 364-365.
95. A. Zaleska, *Recent Pat. Eng.*, 2008, **2**, 157-164.
96. P. S. Basavarajappa, S. B. Patil, N. Ganganagappa, K. R. Reddy, A. V. Raghu and C. V. Reddy, *Int. J. Hydrogen Energy*, 2020, **45**, 7764-7778.

97. Z. Youssef, L. Colombeau, N. Yesmurzayeva, F. Baros, R. Vanderesse, T. Hamieh, J. Toufaily, C. Frochot, T. Roques-Carmes and S. Acherar, *Dyes Pigm.*, 2018, **159**, 49-71.
98. X. Wang, K. Maeda, A. Thomas, K. Takanahe, G. Xin, J. M. Carlsson, K. Domen and M. Antonietti, *Nat. Mater.*, 2009, **8**, 76-80.
99. G. Liao, Y. Gong, L. Zhang, H. Gao, G.-J. Yang and B. Fang, *Energy Environ. Sci.*, 2019, **12**, 2080-2147.
100. J. Lin, W. Tian, H. Zhang, X. Duan, H. Sun and S. Wang, *Energy Fuels*, 2021, **35**, 7-24.
101. J. Wu, Y. Xie, Y. Ling, Y. Dong, J. Li, S. Li and J. Zhao, *Front Chem*, 2019, **7**, 649.
102. K. K. Das, S. Patnaik, S. Mansingh, A. Behera, A. Mohanty, C. Acharya and K. M. Parida, *J. Colloid Interface Sci.*, 2020, **561**, 551-567.
103. Z. Wan, G. Zhang, X. Wu and S. Yin, *Appl. Catal. B: Environ.*, 2017, **207**, 17-26.
104. W. K. Darkwah and K. A. Oswald, *Nanoscale Res. Lett.*, 2019, **14**, 234.
105. K. Prakash, P. S. Kumar, P. Latha, K. Saravanakumar and S. Karuthapandian, *J. Inorg. Organomet. Polym. Mater.*, 2018, **28**, 268-278.
106. J. N. Tiwari, Y.-K. Seo, T. Yoon, W. G. Lee, W. J. Cho, M. Yousuf, A. M. Harzandi, D.-S. Kang, K.-Y. Kim, P.-G. Suh and K. S. Kim, *ACS Nano*, 2017, **11**, 742-751.
107. S. C. Yan, S. B. Lv, Z. S. Li and Z. G. Zou, *Dalton Trans.*, 2010, **39**, 1488-1491.
108. X. Wang, K. Maeda, A. Thomas, K. Takanahe, G. Xin, J. M. Carlsson, K. Domen and M. Antonietti, *Nat. Mater.*, 2009, **8**, 76-80.
109. S. Cao, J. Low, J. Yu and M. Jaroniec, *Adv. Mater.*, 2015, **27**, 2150-2176.
110. S. C. Yan, Z. S. Li and Z. G. Zou, *Langmuir*, 2009, **25**, 10397-10401.
111. G. Zhang, J. Zhang, M. Zhang and X. Wang, *J. Mater. Chem.*, 2012, **22**, 8083-8091.
112. Y. Zhang, J. Liu, G. Wu and W. Chen, *Nanoscale*, 2012, **4**, 5300-5303.
113. H. J. Kong, D. H. Won, J. Kim and S. I. Woo, *Chem. Mater.*, 2016, **28**, 1318-1324.
114. G. Liu, P. Niu, C. Sun, S. C. Smith, Z. Chen, G. Q. Lu and H.-M. Cheng, *J. Am. Chem. Soc.*, 2010, **132**, 11642-11648.
115. V. W.-h. Lau, I. Moudrakovski, T. Botari, S. Weinberger, M. B. Mesch, V. Duppel, J. Senker, V. Blum and B. V. Lotsch, *Nat. Commun.*, 2016, **7**, 12165.
116. W. Yang, R. Godin, H. Kasap, B. Moss, Y. Dong, S. A. J. Hillman, L. Steier, E. Reisner and J. R. Durrant, *J. Am. Chem. Soc.*, 2019, **141**, 11219-11229.
117. Y. Li, C. Xie, S. Peng, G. Lu and S. Li, *J. Mol. Catal. A: Chem.*, 2008, **282**, 117-123.
118. L. Wang, H. Zhao, Y. Chen, R. Sun and B. Han, *Opt. Commun.*, 2016, **370**, 122-126.
119. T. Lazarides, T. McCormick, P. Du, G. Luo, B. Lindley and R. Eisenberg, *J. Am. Chem. Soc.*, 2009, **131**, 9192-9194.
120. V. Srivastava and P. P. Singh, *RSC Adv.*, 2017, **7**, 31377-31392.
121. V. R. Batistela, D. S. Pellosi, F. D. de Souza, W. F. da Costa, S. M. de Oliveira Santin, V. R. de Souza, W. Caetano, H. P. M. de Oliveira, I. S. Scarminio and N. Hioka, *Spectrochim. Acta. A. Mol. Biomol. Spectrosc.*, 2011, **79**, 889-897.
122. A. Penzkofer, A. Beidoun and M. Daiber, *J. Lumin.*, 1992, **51**, 297-314.
123. A. Penzkofer, A. Beidoun and S. Speiser, *Chem. Phys.*, 1993, **170**, 139-148.
124. L. S. Herculano, L. C. Malacarne, V. S. Zanuto, G. V. B. Lukasiewicz, O. A. Capeloto and N. G. C. Astrath, *J. Phys. Chem. B*, 2013, **117**, 1932-1937.
125. A. Alvarez-Martin, S. Trashin, M. Cuykx, A. Covaci, K. De Wael and K. Janssens, *Dyes Pigm.*, 2017, **145**, 376-384.

Chapter 2

Deep Eutectic Solvents as Viable Reaction Media for Solar-Driven Hydrogen Production

2. Introduction

2.1. Deep Eutectic Solvents and ILs

Deep eutectic solvents (DESs) have emerged as a new, alternative class of green solvents.¹ DESs were first realised in a pioneering study by Abbott *et al.*, whereby solid choline chloride ($T_m \approx 302 \text{ }^\circ\text{C}$) was mixed in certain molar ratios with solid urea ($T_m \approx 133 \text{ }^\circ\text{C}$) to produce mixtures with their melting points lower than both the substituents. One such mixture – choline chloride : urea in a 1 : 2 molar ratio produce a room temperature liquid with $T_m \approx 12 \text{ }^\circ\text{C}$.² The phase diagram of this mixture is shown in Figure 2.01.³

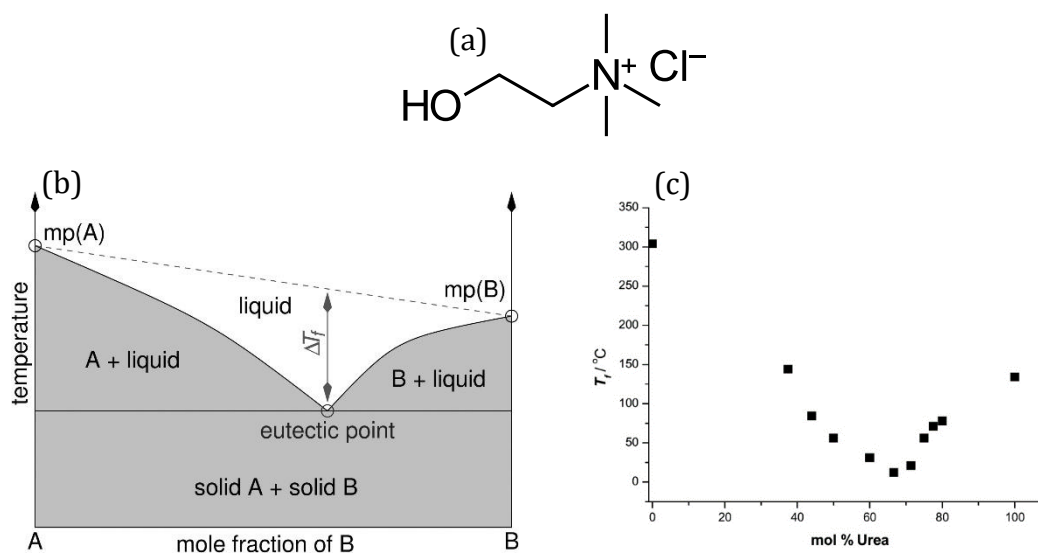


Figure 2.01. (a) Chemical structure of choline chloride, one of the most common hydrogen bond acceptor components used to make DESs. Choline chloride acts as a Lewis base, facilitating hydrogen bonding through the chloride ion. (b) Schematic representation of a eutectic point on a two-component phase diagram, showing the change in freezing point, ΔT_f as a function of the composition. Reprinted with permission from REF 3.

Eutectic mixtures of two constituents which induce this changing in melting point to make novel liquids economically accessible as solvents are commonly called DESs. DESs are often seen as a branch of ionic liquids (ILs) as they have very similar characteristics – like ILs, DESs possess high thermal stabilities, low vapour pressure, are non-volatile, and have tunable polarities.⁴ However there are distinct differences in the properties of ILs and DESs. While the term “ionic liquid” generally refers to solvents which are composed solely of ions, and was first used in the literature to describe chloroaluminate based ionic fluids.⁵ Tetrafluoroborate and acetate moieties have gradually replaced the chloroaluminate species in ILs, as this was found to produce liquids with enhanced stability towards air and moisture.⁶ Stability has been shown to further increase with the use of more hydrophobic anions.⁷ Even though the study of ILs is research intensive, many problems remain with their use. These include, but are not limited to, their difficulty of synthesis, purification, their toxicity, and their lack of biodegradability.⁴

DESs share properties with ILs, particularly physical properties as those noted above, but also share the property of being tunable solvents which can be customised to generate a reaction environment to facilitate particular chemical reactions. Components of DESs can also be ionic, such as the choline cation. However, DESs do differ from conventional ILs in a variety of ways.

2.2. Origin of Deep Eutectic Solvent Synthesis

DESs have the benefit over ILs of being much easier to synthesise. A DES can be described by the general formula:³



where Cat^+ refers to the primary cation of, typically, an ammonium, phosphonium or sulfonium salt, X^- is typically a halide anion, and z is the molar equivalent of a Lewis or Brønsted acid Y . In this formula, z is the number of Y molecules that interact with the X^- anion. Most DESs to date have been based on quaternary ammonium

salts, particularly choline chloride. However, DESs generally fall into four categories, which are shown in Table 2.01.³

Table 2.01. General Formula for the Classification of DESs.³

DES Type	General Formula
Type I	$\text{Cat}^+\text{X}^{-z}\text{MCl}_x$
Type II	$\text{Cat}^+\text{X}^{-z}\text{MCl}_x \times y\text{H}_2\text{O}$
Type III	$\text{Cat}^+\text{X}^{-z}\text{RZ}$
Type IV	$\text{MCl}_x + \text{RZ}$

Here, M refers to a metal ion, with DESs shown to have been made with ZnCl_2 , SnCl_2 , FeCl_2 and FeCl_3 , and even InCl_3 .⁸⁻¹¹ Type I DESs are typically produced from the combination of these metal salts with imidazolium salts, particularly 1-ethyl-3-methylimidazolium chloride.^{9, 12, 13} Even though these DESs have been studied and made, their melting point is not appropriate to be considered as conventional solvents, as the melting point is far above room temperature. The range of DESs has been increased through the use of the hydrated form of the metal salts – the low cost of hydrated metal salts and their stability towards air and moisture allows the DESs formed from these species to be more widely considered.

Type III DESs formed from choline chloride (ChCl) are the most widely studied and often thought to be the most practical DESs. ChCl can form a variety of solvents with melting points below room temperature, increasing the scope, and applicability of DESs for more general use. Mixing choline chloride in certain molar ratios with selected hydrogen bond donors (HBDs), and after simply applying moderate heat to the two components, eutectic mixtures are formed. The HBD species can bond to the chloride ion via hydrogen bonding which causes a lowering of the lattice energy, with a stronger interaction of the halide ion to the HBD causing a higher ΔT_m i.e., the magnitude of the interaction between ChCl and the HBD dictates ΔT_m . The interaction of urea as a HBD bonding to the chloride anion in ChCl is shown in Figure 2.02.¹⁴

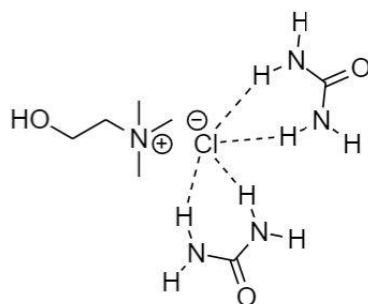


Figure 2.02. Proposed structure of choline chloride, with two urea molecules bonded to the chloride anion of choline chloride.¹⁴

2.3. Properties and Behaviour of Type III DESs.

It is thought that, due to the above formulations, more than 10^6 DESs can be made when combined in the appropriate molar ratios.³ Due to the sheer number of DESs already studied and the span of possible solvents, it is best to limit focus to a select type. Type III DESs represent the ideal solvents for a multitude of reasons. As they are almost always metal free, type III DESs are considered non-toxic as shown from environmental toxicity studies.¹⁵ In addition, they can be easily prepared from cheap readily available precursors.¹⁶ The possible combination of hydrogen bond acceptors (HBAs) which are halide salts, such as choline chloride, with the vast combination of HBDs available make DESs highly tunable and functionable, with selected DESs summarised in Table 2.02.^{2, 17-19}

Table 2.02. Freezing point of a selection of DESs formed from choline chloride (ChCl) and the respective hydrogen bond donors (HBDs) with molar ratios

Halide Salt	HBD	HBD Melting Point / °C	Salt : HBD Molar Ratio	DES T _f / °C	Ref
ChCl	Urea	134	1 : 2	12	2
ChCl	Glycerol	17.8	1 : 2	n/a	15
ChCl	Ethylene Glycol	-12.9	1 : 2	n/a	15
ChCl	1-methyl urea	93	1 : 2	29	15
ChCl	Malonic acid	134	1 : 1	10	15
ChCl	MgCl ₂ ·6H ₂ O	116	1 : 2	16	17
ChCl	Phenylpropionic acid	48	1 : 1	20	15
ChCl	Acrylic acid	14	1 : 1.6	-4	16

Simply changing the HBD component in a type III DES composed of ChCl can alter the physical properties of the solvents in question. In fact, even changing molar ratios of HBA : HBD have shown to induce variations in properties. For example, Hayyan et al. analysed properties of ChCl : glucose at varying molar ratios, showing that a change in molar composition resulted in the change of pH, refractive index, and surface tension of the solvent.²⁰ However not all ratios result in providing the true eutectic composition upon mixing, and so it is more prudent to study DESs at the true eutectic composition.

The nature of hydrogen bonding in ChCl based DESs is expected to be the main driving force behind the depression of melting points that occurs during DES formation.^{21, 22} The choice of HBD, as well as the molar composition of the DES can alter the hydrogen bonding profile of the solvent. Work by Ozturk et al. found an increase in density was observed when glycerol was used as a HBD over ethylene glycol, even when both HBDs were used in the same molar ratios.²³ The increase in density was attributed to glycerol's intrinsically larger molar mass, as it contains an additional CHOH group, i.e. one more hydroxyl group compared to ethylene glycol. As such, it is reasoned that the addition of ChCl to make the ChCl : glycerol DES disturbs the hydrogen bonding network of pure glycerol to create a "density minimum" at the eutectic composition. However, addition of ChCl to ethylene glycol is thought to increase hydrogen bonding compared to pure ethylene glycol to create a "density maximum."⁴ This is significant as, despite the fact that glycerol and ethylene glycol are chemically similar and both induce deep freezing point depressions, it highlights the different hydrogen bonding mechanism between the DESs. This difference was further augmented by Stefanovic et al., whose computational work with ChCl and urea, glycerol, and ethylene glycol showed that nanoscale hydrogen bonding networks between the chloride ion and the HBD differ significantly.²¹ ChCl : urea exhibits a well-established hydrogen bond network between the salt and hydrogen bond donor, leading to a larger melting point depression. This extensive hydrogen bond network in ChCl : urea also leads to substantially higher viscosity compared to ChCl : glycerol and ChCl : ethylene glycol, and particularly compared to water. Some of the physical properties of the DESs

mentioned here are presented in Table 2.03.^{17, 21, 24} These studies show that hydrogen bonding manifestation in the three solvents in question is different, but not any less important.

Table 2.03. Physical properties of DESs based on ChCl at 298 K. Data taken from REFS 15, 19, 22

Salt	HBD	Viscosity	Density	Surface Tension	Conductivity
(Molar equivalent)	(Molar equivalent)	cP	g cm⁻¹	mN m⁻¹	mS cm⁻¹
ChCl (1)	Urea (2)	632	1.24	52	0.75
ChCl (1)	Glycerol (2)	376	1.12	55.8	1.05
ChCl (1)	Ethylene Glycol (2)	36	1.18	49	7.61

DESs possess interesting properties as a result of the choice of HBA and HBD with notable change in viscosity. The viscosity of DESs allows for exciting chemical and physical properties, with a primary research area being redox-flow batteries arising from their ionic conductivities.²⁵ The origin of this difference derives from hole theory.^{26, 27} Hole theory assumes that ionic material, when melted, contains holes which arise from the fluctuations in local density – these holes are said to be of random size and undergo constant flux. These holes are responsible for the viscosity of DESs. Importantly DESs display different sizes of vacant sites depending on the size of the components – studies have shown that for ChCl : reline, ChCl : ethaline and ChCl : glycerol, the choline cation diffuses slower than the associated HBD which is a reflection on the molecular size and weight.²⁸ Increasing temperatures can cause a weaker interaction between the chloride anion and the HBD which can aid in lowering viscosities to provide DESs with more applicability. Free volumes in DESs can also be increased through simply altering the HBD which can lead to a decrease in viscosity and aid to increase conductivity. Studies have also shown the effect of water on the viscosities of DESs, noting that increasing the water content decreases viscosity for the DESs tested.²⁹

By simply changing components of a DES, physical and chemical properties can be altered and allow solvents to be applied for purposes in place of conventional solvents. For example, some type III DESs have found use as electrolytes in dye-sensitised solar cells (DSSCs). Electrolytes are necessary to facilitate the function of DSSCs to aid in the mobility of redox active species to complete the chemical

circuit.³⁰ Interest lies in the development of nonaqueous electrolytes that are non-volatile with high thermal and electrochemical stability with the first use of DESs as electrolytes in these systems was formulated by Jhong et al., using a ChI : glycerol-based DES. The work noted an increase in the diffusion coefficient of the redox active species used in the solar powered system, as well as an increase in the ionic conductivity compared to those systems employing ILs as electrolytes when a small amount of water was added (15 wt. %). While the overall conversion efficiency was lower further studies featuring DESs as electrolytes in DSSC systems include the understanding of DES structures inside a slit pore, small-scale setups mimicking small-scale DSSCs,³¹ and studying the effect of surfactant additives for aqueous DES electrolytes in DSSCs.³² Research like this paves the way for further investigation as DESs as viable electrolytes in renewable power generation systems.

This chapter aims to showcase the viability of DESs as reaction media for solar hydrogen evolution, which has never been a purpose for DESs to date. Heterogenous and homogenous photocatalysts were tested in three common DESs: choline chloride : urea 1 : 2, called reline, choline chloride : glycerol 1 : 2, called glyceline, and choline chloride : ethylene glycol 1 : 2, called ethaline. The performance of the photocatalysts in varying conditions of these solvents for solar-driven H₂ production was assessed by gas chromatography in an inert atmosphere and were compared to a conventional aqueous solution commonly used to test photocatalysts.

2.5. Results

2.5.1. Characterisation of NCN-functionalised Carbon Nitride

NCN-functionalised carbon nitride (NCN-CN_x) was synthesised according to a procedure in the literature and subsequently characterised.³³ FT-IR spectroscopy showed a notable peak at 2180 cm⁻¹, which is indicative of a notable N=C=N stretch. (Figure 2.03). This peak does not appear in the IR spectrum recorded of g-C₃N₄. Diffuse reflectance UV-vis spectroscopy was used to measure the optical absorption profile of the synthesised yellow materials.

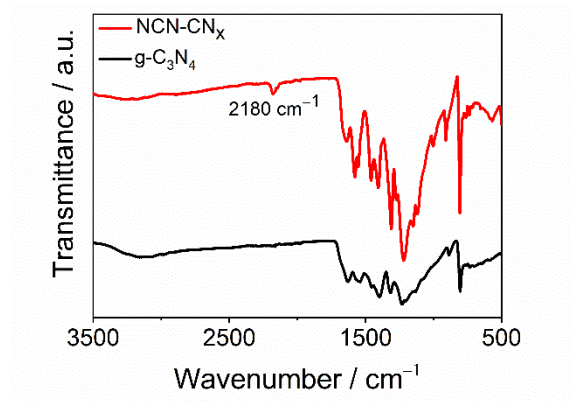


Figure 2.03. FT-IR spectrum of as-synthesised NCN-CN_x and g-C₃N₄.

The Kubelka-Munk transformation of the reflectance spectra of the as-synthesised g-C₃N₄ and NCN-CN_x powders shown in Figure 2.04 indicates a slight difference between spectra of the g-C₃N₄ and NCN-CN_x powders, in that the absorption edge in the NCN-CN_x spectrum is slightly greater, which indicates that the NCN-CN_x material is capable of absorbing more photons. Tauc plots produced from the Kubelka-Munk absorption indicate that both materials possess a similar bandgap, with both g-C₃N₄ and NCN-CN_x possessing a bandgap of approximately 2.7 eV indirect bandgaps, which is in line with previously obtained values.³⁴ (REF). (See Materials and Methods for more information on bandgap determination).

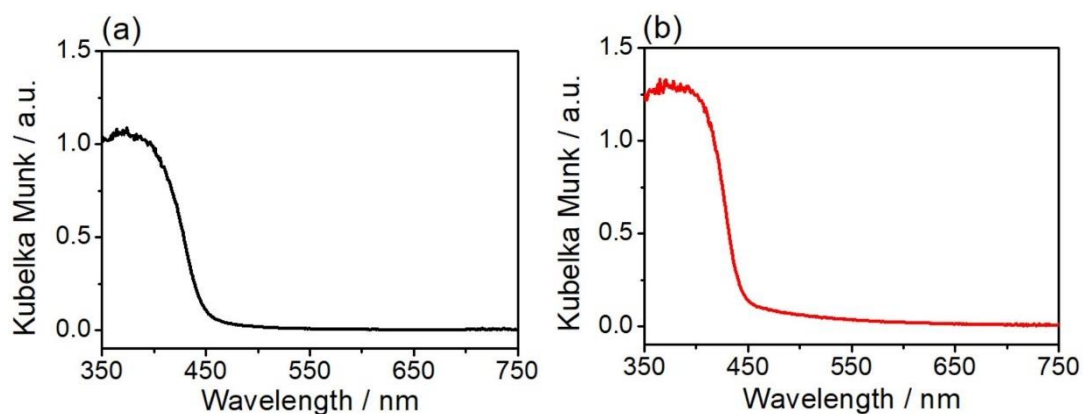


Figure 2.04. (a) Kubelka Munk function obtained from diffuse reflectance UV-Vis spectrum of g-C₃N₄ and (b) Kubelka Munk function obtained from diffuse reflectance UV-vis spectrum of NCN-CN_x

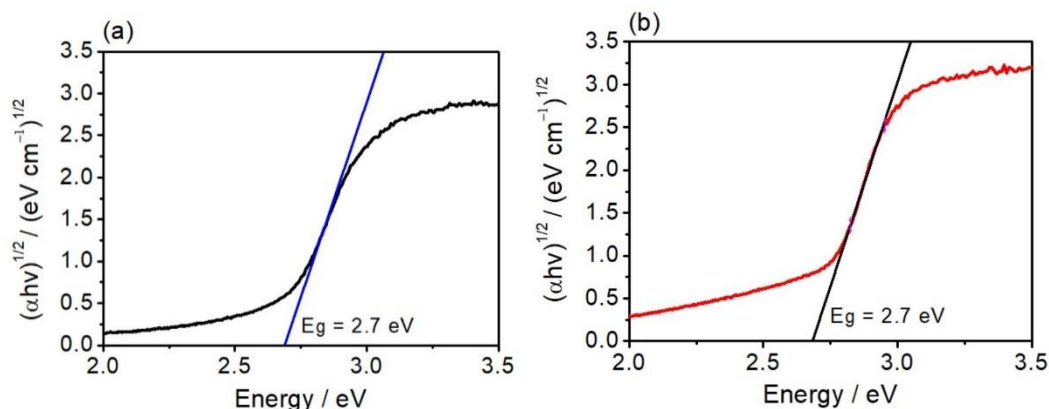


Figure 2.05. (a) Tauc plot (black trace) of $g\text{-C}_3\text{N}_4$ and extrapolation of linear tangent of Tauc plot (blue trace) which shows optical bandgap = 2.7 eV (b) Tauc plot (red trace) of NCN-CN_x and extrapolation of linear tangent of Tauc plot (red trace) which shows optical bandgap = 2.7 eV

Powder X-ray diffraction was used to examine structural differences between the samples. The large peak present in both diffractograms appearing at $\sim 28^\circ 2\theta$ arises from the (0 0 2) plane – in $g\text{-C}_3\text{N}_4$ this has a $d = 3.35 \text{ \AA}$, corresponding to the interlayer spacing between the graphitic layers. The (1 0 0) plane causes the diffraction at $12.5^\circ 2\theta$ correlating to the distance between heptazine units ($d = 6.7 \text{ \AA}$). Meanwhile, in NCN-CN_x the distance between layers in the materials is shorted to $d = 3.18 \text{ \AA}$, causing the peak to appear at a slightly higher 2θ value. (Figure 2.06). These patterns are in line with materials previously synthesised and reported.³³

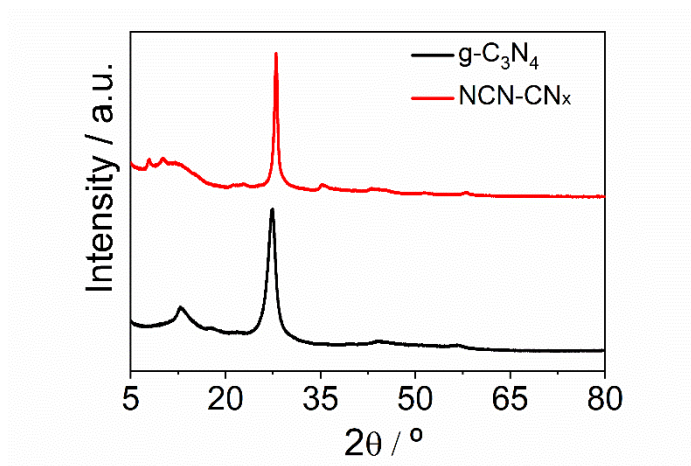


Figure 2.06. Powder X-Ray diffraction of $g\text{-C}_3\text{N}_4$ and NCN-CN_x

2.5.2. Quantification of Photocatalytic H₂ Production – Gas Chromatography Calibration and Experimental Setup

The principal method for determining H₂ evolution performance was gas chromatography. Sample conditions were analysed using gas chromatography by injecting 2 mL of the sample headspace periodically. Headspace gas was continuously transported to the GC using nitrogen as a purge gas from mass flow controllers (MFCs) without recirculation. The samples themselves were subject to constant solar irradiation and were thermostatically controlled by placing the samples in a water bath with a fixed temperature at 40 °C (see Materials and Methods for full experimental setup).

The gas chromatograph (GC) was calibrated using calibration gas with a concentration of 2000 ppm H₂ in CO₂. Calibration gas flowing into a glass vial from and MFC was diluted with a known volume of N₂ gas from another MFC. The flow rate of the MFCs was varied to produce different concentrations of H₂ for calibration, with the chosen calibration concentrations set as 2000 ppm, 1400 ppm, 1200 ppm, 1000 ppm, 800 ppm, 500 ppm, 400 ppm, 200 ppm and 100 ppm. This allowed a calibration curve to be produced which allowed an area under a chromatographic peak to be converted to a concentration of H₂ using the following relationship:

$$\text{Area of peak} = M \times \text{H}_2 \text{ concentration (ppm)} + C \quad (2.02)$$

$$\text{H}_2 \text{ concentration (ppm)} = \frac{\text{Area of integral} - C}{M} \quad (2.04)$$

where M and C are the calibration coefficients determined from the calibration curve. This allows any chromatograph with a detectable peak corresponding to H₂ to be converted to a concentration. An example of a calibration curve is given in Figure 2.07.

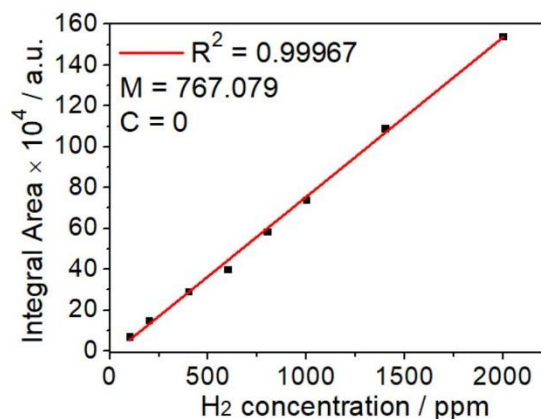


Figure 2.07. Example of calibration curve used for the calculation of H₂ concentration from any peak area from an obtained chromatogram. The calibration coefficients M and C are used in determining the H₂ concentration.

The rate of H₂ evolution in $\mu\text{mol h}^{-1}$ was calculated from chromatographs using the H₂ concentration, the flow rate of the N₂ purge gas and the molar volume according to the following equation:

$$\text{H}_2 \text{ rate } (\mu\text{mol h}^{-1}) = \text{Flow rate } (\text{mL h}^{-1}) \times \frac{\text{H}_2 \text{ concentration (ppm)}}{\text{molar volume } (\text{L mol}^{-1}) \times 1000} \quad (2.05)$$

The total H₂ in μmol can then be calculated assuming a constant H₂ rate at the point of injection of the sample headspace from the previous calculated total H₂ amount:

$$\text{Total H}_{2T_2} (\mu\text{mol}) = \text{Total H}_{2T_1} (\mu\text{mol}) + (T_2 - T_1) \times \text{H}_2 \text{ rate}_{T_2} \quad (2.06)$$

where T₂ and T₁ are the times of the sample injection and rate_{T₂} is the rate of H₂ evolution determined at T₂. Control of the flow rate was done automatically by the MFCs, which regulate the flow of N₂ purge gas accurately.

2.5.3. Photocatalytic H₂ Evolution in H₂O with NCN-CN_x

Photocatalytic H₂ evolution by NCN-CN_x was first investigated in an aqueous environment, using a TEOA buffer at pH 7.0 as a solution and co-catalytic Pt (See Materials and Methods for full experimental information).

In the presence of the redox mediator methyl viologen dichloride (MV²⁺), and using a Pt co-catalyst (from H₂PtCl₆) under simulated solar light at an intensity equating 1

sun (AM 1.5G), Pt/NCN-CN_x produced 10.2±4.0 μmol_{H2} after 14 hours irradiation. In the absence of MV²⁺, Pt/NCN-CN_x produced 86.1±5.4 μmol_{H2} with a maximum production rate of 13.0±1.4 μmol_{H2} h⁻¹ (Figure 2.08). Atypically, a decrease in performance is observed when a redox mediator is added – this may be explained by the binding of co-catalytic Pt to the NCN-CN_x surface. Pt in H₂PtCl₆ is in a +4 oxidation state (Pt⁴⁺) and can be photochemically reduced by excited electrons to become deposited on the light absorber surface *in situ*. It has been previously reported that H₂ evolution can be suppressed in the presence of methyl viologen when good electron transfer exists between the light absorber (in this case, NCN-CN_x) and the hydrogen evolution co-catalyst.³⁵ The suppression in activity arises from the competition between photogenerated electrons transferring either to the co-catalyst or to the methyl viologen redox mediator. If the attachment and electronic coupling between the surface of the light absorber and H₂ evolution co-catalyst is proficient, electrons will be transferred to the co-catalyst for proton reduction. The addition of a redox mediator to such a system will compete with protons for the chemical reduction process. It could be visibly observed that, upon irradiation, the reduced MV²⁺ species, MV^{•+}, accumulates in the reaction samples. This indicates the insufficiency of available electrons for proton reduction, as the electrons are taken up by the mediator. In addition, this MV^{•+} species possesses a deep blue colour which attenuates the incoming photons. As the number of photons available to the light absorber are diminished resulting from an accumulation of MV^{•+}, the production of charge carriers is also diminished, and so the number of electrons available for proton reduction is reduced, thus lowering the H₂ evolution performance. This phenomenon is highlighted in Figure 2.09 below.

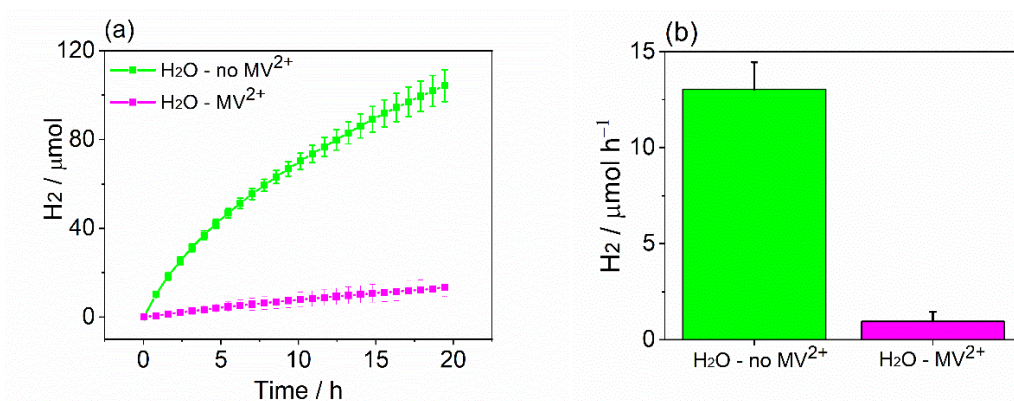


Figure 2.08. (a) Cumulative photocatalytic H₂ generation at Pt/NCN-CN_x in water. (b) Maximum H₂ evolution rate at Pt/NCN-CN_x in water. Conditions: NCN-CN_x (2.0 mg), H₂PtCl₆ (0.05 mg Pt) in 2.0 mL water (0.4 M TEOA, pH 7); with or without MV²⁺ (2 mM); AM 1.5G, 1 sun, 40 °C, constant N₂ purge.

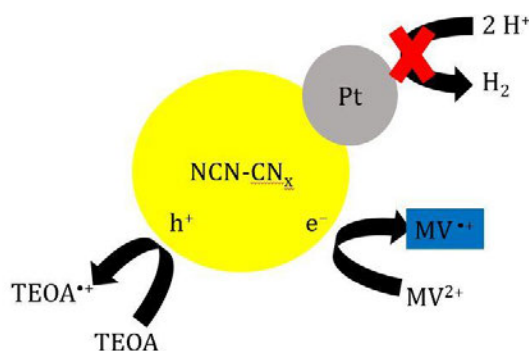


Figure 2.09. Proposed schematic mechanism of photocatalytic methyl viologen reduction versus proton reduction in H₂O on a carbon nitride catalyst with Pt as a co-catalyst in the presence of TEOA as a sacrificial electron donor.

2.5.4. Photocatalytic H₂ Evolution in Reline-based Solvents with NCN-CN_x

To probe optimal reaction conditions for DESs, three well-known and well-studied DESs were investigated as a medium for solar hydrogen evolution using NCN-CN_x as the photocatalyst. Reline was synthesised by mixing choline chloride with urea in a 1:2 molar ratio according to a conventional procedure in the literature.² NCN-CN_x was placed in a 2.0 mL reline solution, containing 0.1 mL TEOA (0.4 M) and 50 μL of colloidal Pt (2.5 wt.% Pt in water) and MV²⁺ (2 mM). After 15 hours, the Pt/NCN-CN_x catalyst produced 0.91±0.2 μmol_{H₂} (Figure 2.10).

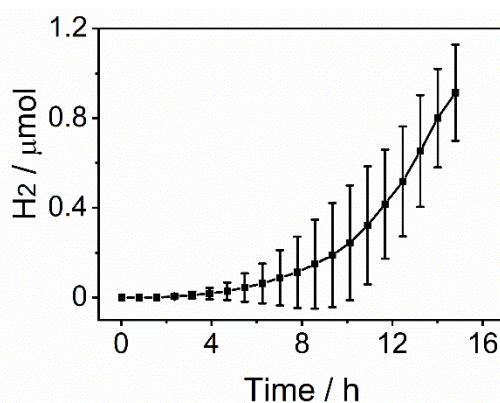


Figure 2.10. Cumulative photocatalytic H₂ production by Pt/NCN-CN_x in DES solution with 2.5% vol. H₂O from colloidal Pt solution. Conditions: NCN-CN_x (2.0 mg), Pt colloids (0.05 mg, 0.05 mL), TEOA (0.4 M), MV²⁺ (2 mM) in reline (2.0 mL), AM 1.5G, 1 sun, 40 °C, constant N₂ purge.

It was found that adding H₂O to the reaction solution increased the photocatalytic performance. This is believed to result from the higher availability of protons to the reaction surface. In addition, it is known that an increase in the water content of DESs lowers viscosity and so may allow for greater diffusion in the reaction media.³⁶

To evaluate the effect of the DESs on H₂ production, the water concentration in the DES reline was varied in a series of reactions without modification of the catalyst or the TEOA concentration. In an 82.5% volume (% vol.) reline solution, in the presence of MV²⁺, Pt/NCN-CN_x showed a maximum rate of H₂ evolution of 17.9±1.7 μmol_{H2} h⁻¹, with a total H₂ production of 138.3±2.6 μmol_{H2} after 14 hours irradiation. In a 77.5% vol. reline solution, Pt/NCN-CN_x produced 160.8±15.9 μmol_{H2}, while the photocatalyst in a 62.5% vol. reline solution showed similar performance with 166.0±7.0 μmol_{H2} observed after 14 hours irradiation.

As the water content is increased further and the DES concentration is decreased, the H₂ evolution decreased notably. Pt/NCN-CN_x in 50% vol. reline produced 70.1±17.8 μmol_{H2} while only 0.2±0.1 μmol_{H2} was observed in 37.5% vol. reline and a similar performance for H₂ production was observed in 25% vol. reline with 0.2±0.1 μmol_{H2} detected after 14 hours. In a solution without reline, containing H₂O and TEOA only without any pH adjustment, no H₂ was detected. This may be explained by the tendency of DESs to obtain properties resembling more traditional aqueous solutions as the water content exceeds 50% and so activity of proton reduction again competes with methyl viologen reduction on the Pt co-catalyst.³⁷ The reaction profile for the photocatalyst in these solvents is presented in the Figure 2.11.

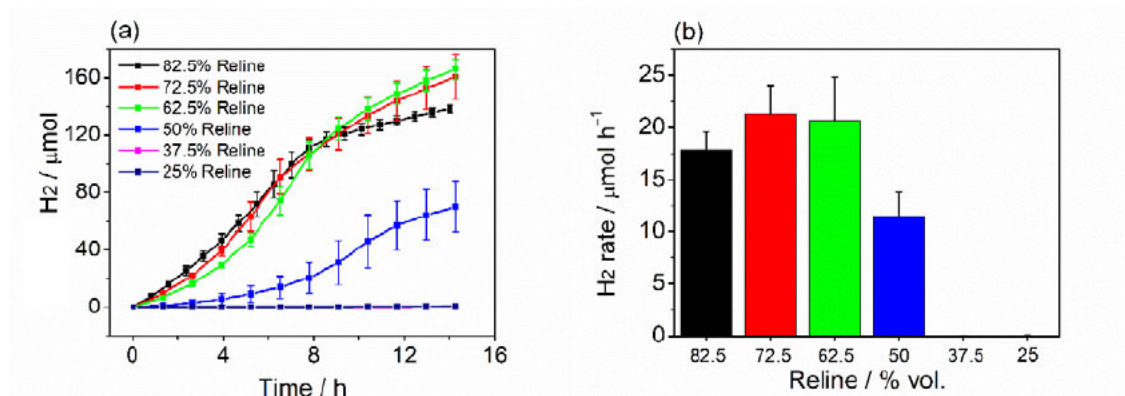


Figure 2.11. Photocatalytic H₂ generation at Pt/NCN-CN_x in reline with varying %vol. using H₂O. (a) cumulative H₂ generation and (b) maximum H₂ production rate. Conditions: NCN-CN_x (2.0 mg) H₂PtCl₆ (0.05 mg Pt), MV²⁺ (2.0 mM), TEOA (0.4 M), 2.0 mL, AM 1.5G, 1 sun, 40 °C, constant N₂ purge.

When no redox mediator is used, there is a notable difference in the H₂ evolution trends for the reline-based solutions. As the reline concentration is decreased from 82.5% vol to 72.5% vol., 62.5% vol and 50% vol., the total H₂ produced by Pt/NCN-CN_x was found to be 43.2±3.7 μmol_{H₂}, 36.4±3.2 μmol_{H₂}, 38.0±3.4 μmol_{H₂}, and 36.6±12.2 μmol_{H₂} respectively (Figure 2.12). As the reline concentration is decreased even further and the solution becomes more aqueous based, there is no notable increase or difference in H₂ evolution performance. It can be inferred from this data that lowering the reline DES concentration in the solution does not alter the performance or the stability of the photocatalyst. The total H₂ produced by the Pt/NCN-CN_x photocatalyst in the presence of the reline DES are highlighted in Table 2.04.

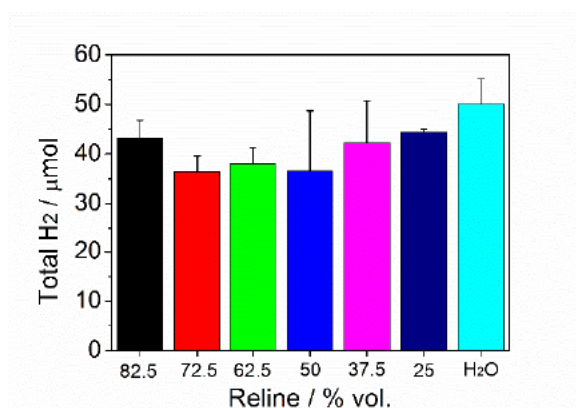


Figure 2.12. Total photocatalytic H₂ generation at Pt/NCN-CN_x in various % vol. of reline in the absence of a redox mediator. Conditions: NCN-CN_x (2.0 mg), H₂PtCl₆ (0.05 mg Pt), TEOA (0.4 M), 2.0 mL, AM 1.5G, 1 sun, 14.3 h irradiation time, 40 °C, constant N₂ purge.

Table 2.04. Photocatalytic H₂ generation by Pt/NCN-CN_x in reline-based solutions and H₂O in inert conditions with Total H₂ values after 14 h irradiation. Conditions: NCN-CN_x (2.0 mg), H₂PtCl₆ (0.05 mg Pt) in 2.0 mL, 0.4 M TEOA, AM 1.5G, 1 sun, 40 °C, purge gas at 4 mL min⁻¹.

		With added MV ²⁺		Without added MV ²⁺	
Reline % vol.	H ₂ O % vol.	Max. H ₂ Rate μmol h ⁻¹	Total H ₂ μmol	Max. H ₂ Rate μmol h ⁻¹	Total H ₂ μmol
82.5	17.5	17.9±1.7 after 6.2 h	138.3±2.6	3.4±0.4 after 4.7 h	43.2±3.7
72.5	27.5	21.3±2.8 after 6.5 h	160.8±15.9	4.8±0.1 after 3.9 h	36.4±3.2
62.5	37.5	24.4±2.1 after 7.8 h	166.0±7.0	4.9±0.6 after 2.6 h	38.0±3.4
50	50	11.5±2.3 after 10.4	70.1±17.8	5.43±2.4 after 2.6 h	36.6±12.2
37.5	62.5	>0.1±0.1 after 14.2 h	0.2±0.1	7.5±1.1 after 1.3 h	42.3±8.4
25	75	>0.1±0.1 after 14.2 h	0.4±0.3	7.4±0.1 after 1.3	44.4±0.6
0	100			7.5±0.6 after 1.3 h	50.1±5.1

The total H₂ produced by Pt/NCN-CN_x also shows that performance can be increased with the use of the redox mediator MV²⁺. It should also be noted that as the reaction proceeds, the H₂ evolution reaction rate slows, which may be attributed to the decay of the MV²⁺ redox mediator.³⁸ To highlight this, 2 mM of MV²⁺ was added part-way through an experiment to reline-based samples containing NCN-CN_x. Samples were irradiated with MV²⁺ for 17 hours, and then further MV²⁺ was added. It was observed that the production rate of H₂ increased upon the addition of this supplementary MV²⁺, with MV^{•+} visibly observed to have been generated *in situ* (Figure 2.13).

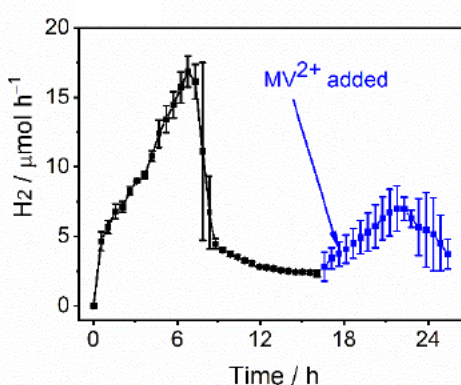


Figure 2.13. Effect of MV²⁺ on the photocatalytic H₂ production rate in reline DES. Samples were irradiated with MV²⁺ for 17 h then further methyl viologen was added, indicated by the portion of the curve in blue in reline-based solvent. Conditions: NCN-CN_x (2.0 mg), H₂PtCl₆ (0.05 mg Pt), TEOA (0.4 M), MV²⁺ (2 mM), H₂O (12.5% vol.) in reline (2.00 mL), AM 1.5G, 1 sun, 40 °C, constant N₂ purge. A further 0.05 mL of 7.8 mM aqueous MV²⁺ solution was added after 17 h.

A series of experiments were performed to understand the phenomenon of increasing rate with the addition of redox mediator in the deep eutectic solvents tested, and likewise the suppression of activity when MV^{2+} is used in water. As previously mentioned, addition of MV^{2+} to act as a redox mediator has been shown to suppress H_2 evolution performance when there exists good electron transfer between the photocatalyst and co-catalyst. While this is true in aqueous solutions tested, the beneficial effect of MV^{2+} in DESs suggests a poorer electron transfer between the light absorbing $NCN-CN_x$ and co-catalytic Pt. To showcase this, recycling experiments were performed in which the catalyst was separated from the reaction medium through centrifugation. Reline and water were compared for their ability to facilitate binding of co-catalytic Pt from H_2PtCl_6 to the $NCN-CN_x$ surface. This was done by briefly irradiating two sets of samples featuring $NCN-CN_x$ with co-catalytic Pt with one set in water and the other in reline. After 4 hours of irradiation of the $Pt/NCN-CN_x$, the photocatalyst was separated from its respective supernatant. The catalyst was collected and re-suspended in fresh solutions without additional Pt. This was to ensure the only Pt partaking in the reaction was that which had been previously deposited on the photocatalyst. Figure 2.14 shows that activity of the $Pt/NCN-CN_x$ is not affected by resuspension in an aqueous solution which indicates that Pt is deposited on the photocatalyst surface in an aqueous environment. Meanwhile, the photocatalytic H_2 evolution by the resuspended $NCN-CN_x$ in the reline-based solution is drastically lowered, suggesting that the Pt in DESs possesses poor immobilisation to the $NCN-CN_x$ surface. This likely arises from the differences in solvation of Pt particles in solution going from an aqueous medium to a more organic-based solvent.³⁹⁻⁴¹

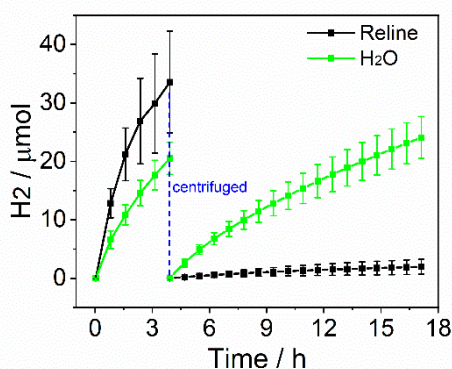


Figure 2.14. Study of the influence of the solvent on co-catalyst attachment. Photocatalytic H₂ generation at Pt/NCN-CN_x was performed under standard conditions in water and reline (2.0 mg NCN-CN_x, 0.05 mg Pt as H₂PtCl₆, 0.4 M TEOA in 2.0 mL water pH 7 or reline with 12.5% vol. water; AM 1.5G, 1 sun, 40 °C, continuous N₂ purge). After 4 h irradiation, samples were centrifuged, and the separated precipitate was re-suspended in fresh solution (0.4 M TEOA in 2.0 mL water pH 7 or reline with 12.5% vol. water) without added H₂PtCl₆ before irradiation was continued.

The carbon nitride material was also collected post-catalysis to determine the effect of the solvent on catalyst functionalisation. It has been shown in previous work that the cyanamide signal in the FT-IR can decrease significantly as the photocatalytic H₂ evolution reaction proceeds in an aqueous solution.³³ It was necessary to determine the effect, if any, the reline DES had on cyanamide groups. Figure 2.15 shows the IR spectra of NCN-CN_x collected post-catalysis versus pristine NCN-CN_x. Photocatalysts analysed this way were washed with water and ethanol, collected by centrifugation, and dried overnight prior to spectroscopic measurements. The FTIR spectra show no shift in wavenumber of the cyanamide functionality, and the relative intensity of the cyanamide functionality is higher from the NCN-CN_x sample recovered from 72.5% vol. reline. Some spectra show pronounced peaks close to 3500 cm⁻¹ which is attributed to excess water in the powders.

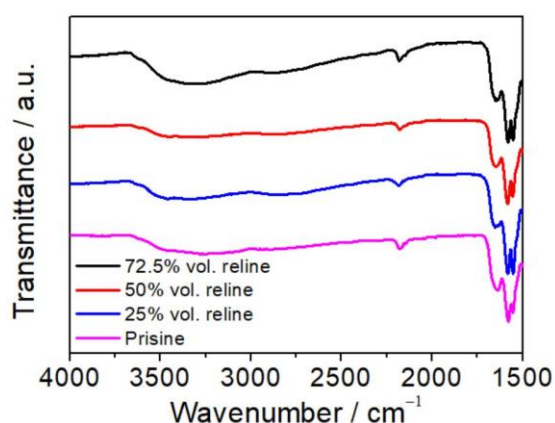


Figure 2.15. FT-IR spectra of NCN-CN_x photocatalysts post-irradiation in various concentrations of reline DES versus pristine, unused NCN-CN_x.

2.5.5. Photocatalytic H₂ Evolution in Glyceline-based Solvents with NCN-CN_x

Another popular DES glyceline was also tested in varying concentrations as a reaction medium for photocatalytic H₂ evolution. Glyceline, similar to reline was synthesised via a procedure in the literature, heating choline chloride and glycerol in a 1 : 2 molar ratio at 80 °C for 1 hour until a homogenous solution had formed.⁴² Pt/NCN-CN_x in 82.5% vol. glyceline with the redox mediator MV²⁺ showed notable activity, with 58.7±3.5 μmol_{H₂} produced after 14 hours (Figure 2.16). Decreasing the glyceline concentration to 72.5% vol. allowed the photocatalytic system to retain its performance and activity for H₂ production of 55.3±5.4 μmol_{H₂}. 65.4±3.4 μmol_{H₂} was produced after 14 hours in 62.5% vol. glyceline while 50% vol. glyceline-TEOA yielded a photocatalytic H₂ evolution rate of 8.2±0.6 μmol_{H₂} h⁻¹ with a total of 59.3±3.0 μmol_{H₂} observed after 14 hours irradiation.

Further decrease of the glyceline concentration in the reaction medium hampers photocatalytic H₂ evolution, with Pt/NCN-CN_x exhibiting behaviour similar to aqueous conditions, with 0.5±0.1 μmol_{H₂} and 0.9±0.1 μmol_{H₂} produced in 37.5% vol. glyceline and 25% vol. glyceline solutions, respectively. Again, it appears strong binding of the Pt co-catalyst to the NCN-CN_x surfaces facilitates MV²⁺ reduction over proton reduction, lowering availability of photogenerated charge carriers for proton reduction and inhibiting H₂ production.

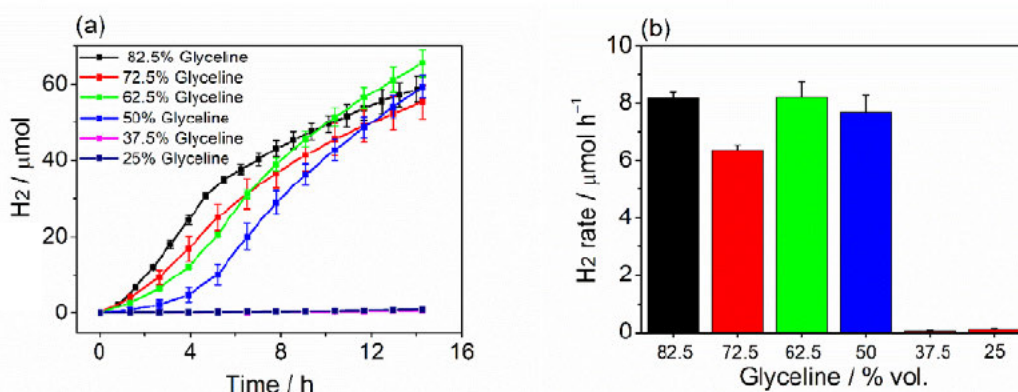


Figure 2.16 Cumulative photocatalytic H₂ generation at Pt/NCN-CN_x with added redox mediator in varying concentrations of glyceline in 2.0 mL (a) and maximum H₂ production rate observed at Pt/NCN-CN_x in various % vol. glyceline (b). Conditions: NCN-CN_x (2.0 mg) H₂PtCl₆ (0.05 mg Pt), MV²⁺ (2.0 mM), TEOA (0.4 M), 2.0 mL, 0.4 M TEOA, AM 1.5G, 1 sun, 40 °C, constant N₂ purge.

When no redox mediator is used, there is a notable difference in the H₂ evolution trends for the glyceline-based solutions. As the glyceline concentration is decreased from 82.5% vol to 72.5% vol., 62.5% vol and 50% vol., the total H₂ produced by Pt/NCN-CN_x was found to be 13.4±0.4 μmol_{H2}, 36.8±1.8 μmol_{H2}, 40.3±3.2 μmol_{H2}, and 60.7±0.6 μmol_{H2} respectively (Figure 2.17, Table 2.05). Further decrease in the glyceline concentration yields total H₂ production values by Pt/NCN-CN_x similar to those seen in H₂O. 57.4±6.3 μmol_{H2}, and 55.0±18.9 μmol_{H2} was produced in 37.5% vol. glyceline and 25% vol. glyceline, respectively.

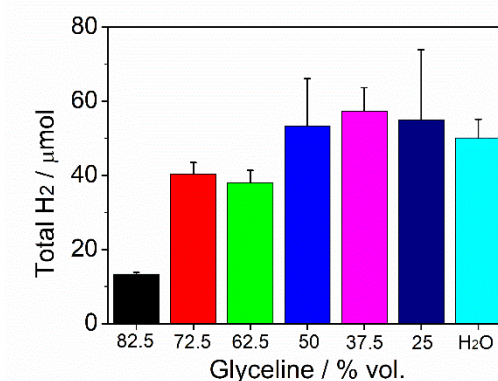


Figure 2.17. Cumulative photocatalytic H₂ generation at Pt/NCN-CN_x of varying glyceline concentrations in the absence of a redox mediator. Conditions: NCN-CN_x (2.0 mg), H₂PtCl₆ (0.05 mg Pt), TEOA (0.4 M), 2,0 mL, AM 1.5G, 1 sun, 40 °C, constant N₂ purge.

Pt/NCN-CN_x in higher concentrations of glyceline shows increase in performance when MV²⁺ is used. As with Pt/NCN-CN_x in reline, 2 mM of MV²⁺ was added part-way through an experiment to an 82.5% vol. glyceline-based solution containing NCN-CN_x irradiated in the presence of MV²⁺ with further MV²⁺ added after 17 hours. This supplementary MV²⁺, with MV^{•+} visibly generated *in situ*, increased the H₂ production rate at the Pt/NCN-CN_x catalyst (Figure 2.18).

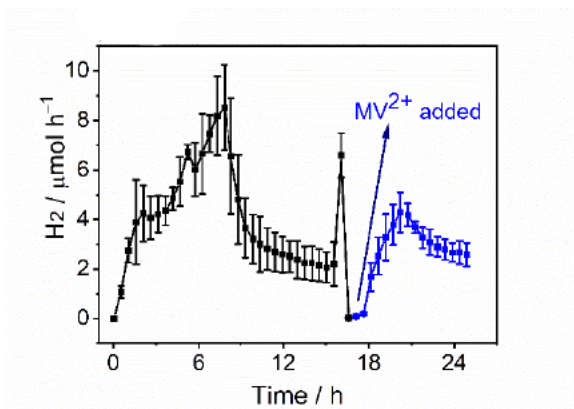


Figure 2.18. Effect of MV^{2+} on the photocatalytic H_2 production rate in glyceline DES. Samples were irradiated with MV^{2+} for 17 h then further methyl viologen was added, indicated by the portion of the curve in blue in glyceline-based solvent. Conditions: NCN-CN_x (2.0 mg), H_2PtCl_6 (0.05 mg Pt), TEOA (0.4 M), MV^{2+} (2 mM), H_2O (12.5% vol.) in reline (2.00 mL), AM 1.5G, 1 sun, 40 °C, constant N_2 purge. A further 0.05 mL of 7.8 mM aqueous MV^{2+} solution was added after 17 h.

This highlights that, even when the water content of the glyceline-based solvent exceeds 50%, H_2 evolution activity is not suppressed in the absence of MV. When the concentration of water in solution is greater than glyceline concentration, comparable performance to Pt/NCN-CN_x in pure H_2O is seen with a reaction profile comparable to a pure H_2O system (Figure 2.19). This is a result of DES-water mixtures with a higher water content essentially resembling an aqueous solvent, as the DES structure and components can no longer function.

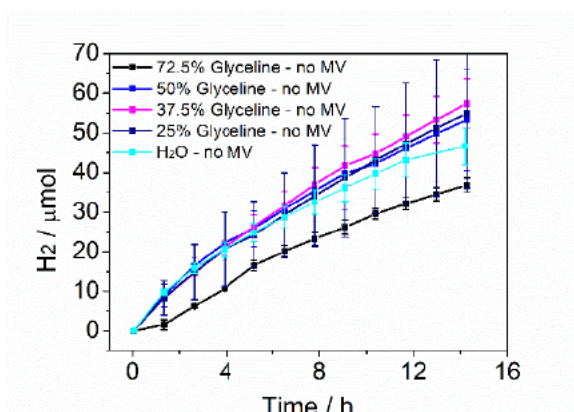


Figure 2.19. Cumulative photocatalytic H_2 generation at Pt/NCN-CN_x in glyceline with various glyceline concentrations in the absence of a redox mediator. Conditions: NCN-CN_x (2.0 mg), H_2PtCl_6 (0.05 mg Pt) TEOA (0.4 M) 2.0 mL, AM 1.5G, 1 sun, 40 °C, constant N_2 purge.

From this, it can be rationalised that at high glyceline concentrations, in the absence of a redox mediator, the hydrogen production is determined by the photocatalyst

and Pt interaction. In 82.5% vol. glyceline, where viscosity is high and solvation of Pt can be affected notably by the DES, Pt does not efficiently bind to NCN-CN_x to, and it is possible Pt is suspended in solution rather than bound to the photocatalyst. This causes issues with electron extraction at the NCN-CN_x conduction band, limiting availability of electrons at Pt for the reduction of protons. Addition of a redox mediator can aid in H₂ generation as the MV²⁺ is reduced it can shuttle electrons to Pt.

The addition of a redox mediator in DESs may increase activity through increasing electron transport in the DES solvent. If Pt is deposited on the NCN-CN_x surface then a redox mediator is not required to shuttle electrons in the system, as the deposited Pt will remove electrons from the photoexcited NCN-CN_x, otherwise Pt needs to move to the NCN-CN_x which will be affected by diffusion. A redox mediator is much smaller and can diffuse much more rapidly than the Pt, improving the electron transport and hence the rate of H₂ evolution.

Table 2.05. Photocatalytic H₂ generation by Pt/NCN-CN_x in glyceline-based solutions and H₂O in inert conditions with Total H₂ values after 14 h irradiation. NCN-CN_x (2.0 mg), H₂PtCl₆ (0.05 mg Pt) in 2.0 mL, 0.4 M TEOA, AM 1.5G, 1 sun, 40 °C, N₂ purge gas at 4 mL min⁻¹.

Glyceline % vol.	H ₂ O % vol.	With added MV ²⁺		Without added MV ²⁺	
		Max. H ₂ Rate μmol h ⁻¹	Total H ₂ μmol	Max. H ₂ Rate μmol h ⁻¹	Total H ₂ μmol
82.5	17.5	8.2±0.2 after 3.9 h	58.7±3.5	1.3±0.5 after 10.1 h	13.4±0.4
72.5	27.5	6.4±0.2 after 5.2 h	55.3±4.4	4.9±0.25 after 1.3 h	40.3±3.2
62.5	37.5	8.2±0.6 after 6.5 h	65.4±3.7	4.9±0.6 after 2.6 h	38.0±3.4
50	50	7.7±0.6 after 6.5 h	59.3±3.0	8.1±0.5 after 1.3 h	60.7±0.6
37.5	62.5	>0.1±0.1 after 14.2 h	0.5±0.1	6.4±0.1 after 1.3 h	60.8±3.2
25	75	>0.1±0.1 after 14.2 h	0.9±0.1	6.4±3.3 after 1.3 h	55.0±18.9
0	100			7.5±0.6 after 1.3 h	50.1±5.1

Again, NCN-CN_z powders subject to solar irradiation with glyceline DES were collected, washed with water and ethanol, and FT-IR spectroscopy was performed to visualise any effect on the cyanamide functionality of the photocatalyst post-irradiation (Figure 2.20). The FTIR spectra show no shift in wavenumber of the cyanamide functionality, as well as a higher intensity for the photocatalyst

recovered from the solvent with higher concentration of glyceline, relative to the solvents with lower glyceline concentration.

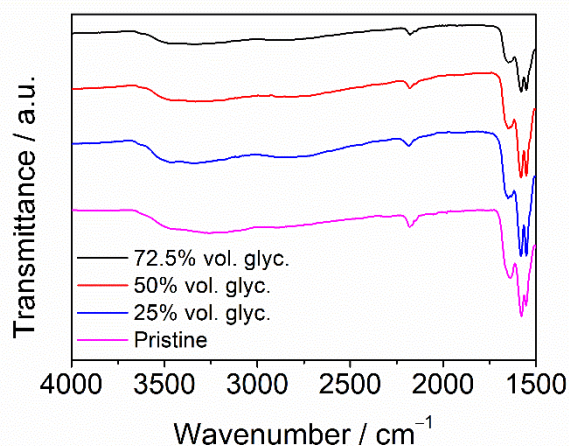


Figure 2.20. FT-IR spectra of NCN-CN_x photocatalysts post-irradiation in various concentrations of glyceline DES versus pristine, unused NCN-CN_x.

2.5.6. Photocatalytic H₂ Evolution in Ethaline-based Solvents with NCN-CN_x

In a similar manner, the activity of H₂ production by the NCN-CN_x photocatalyst with a Pt co-catalyst was examined in the well-known DES ethaline. In an 82.5% vol. ethaline solution with the redox mediator MV²⁺, Pt/NCN-CN_x produced 105.1±8.6 μmol_{H2} after 14 hours irradiation, with a maximum H₂ production rate of 15.9±1.4 μmol_{H2} h⁻¹ (Figure 2.21). Pt/NCN-CN_x immersed in solvents containing a 72.5% vol. and a 62.5% vol. ethaline solution showed very similar performance, with 95.7±5.3 μmol_{H2} and 95.3±6.6 μmol_{H2} detected, respectively. The Pt/NCN-CN_x became hindered as the ethaline content decreased, with 88.6±11.7 μmol_{H2} produced in a 50% vol. ethaline with a maximum H₂ production rate of 12.5±0.4 μmol_{H2} h⁻¹. The more aqueous-based solutions, similar to the photocatalytic behaviour observed in reline and glyceline, created a dramatic drop in H₂ production – 22.6±4.7 μmol_{H2} after 14 hours irradiation was detected when Pt/NCN-CN_x was immersed in 37.5% vol. ethaline. While the total H₂ production is much higher in comparison to water, it was noted that the deep blue colour created by the MV^{•+} radical upon initial irradiation had faded. This yielded a yellow solution indicative of the fully reduced

MV⁰ species, suggesting a degradation of the redox mediator, allowing charge carriers to react with available protons to evolve H₂ rather than being scavenged by MV²⁺. Such behaviour was not seen in 25% vol. ethaline and the presence of the MV^{•+} species was notable even after 14 hours irradiation. As such, much lower H₂ evolution was noted, with 1.4±0.5 μmol_{H₂} produced and so it appears the limit to which MV²⁺ may be beneficial as a redox mediator can alter between the solvents and is dependent on the DES concentration in the solution.

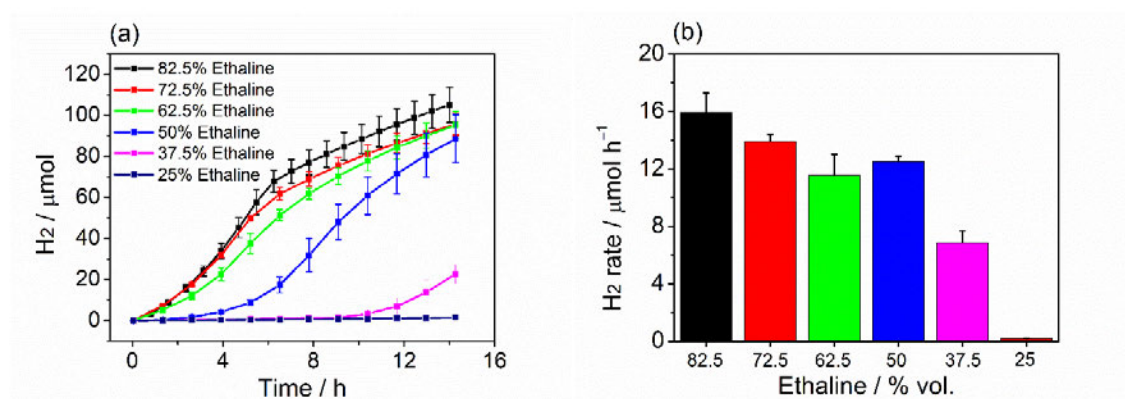


Figure 2.21. Cumulative photocatalytic H₂ generation at Pt/NCN-CN_x in varying concentrations of ethaline (a) and maximum H₂ production rate at Pt/NCN-CN_x in ethaline with varying concentration of ethaline (b). Conditions: NCN-CN_x (2.0 mg), H₂PtCl₆ (0.05 mg Pt), MV²⁺ (2.0 mM) TEOA (0.4 M), 2.0 mL, AM 1.5G, 1 sun, 40°C, constant N₂ purge.

Without the use of a redox mediator, there is little difference in H₂ evolution activity for solvents at high DES concentrations. Figure 2.22 shows Pt/NCN-CN_x in 72.5% vol. ethaline produced 57.6±6.3 μmol_{H₂} h⁻¹ while 58.6±4.1 μmol_{H₂} and 58.4±7.8 μmol_{H₂} was detected in 67.5% vol. ethaline and 55.0% vol. ethaline respectively. 51.7±5.9 μmol_{H₂} and 54.9±5.8 μmol_{H₂} was also produced in the same 14-hour irradiation period, which again compares favourably with a purely aqueous solution. This suggests that increasing H₂O concentration in the ethaline DES does not significantly alter photocatalytic performance. Again, the total H₂ as a function of time, shown in Figure 2.22 indicates the stability of the photocatalyst in the presence of ethaline.

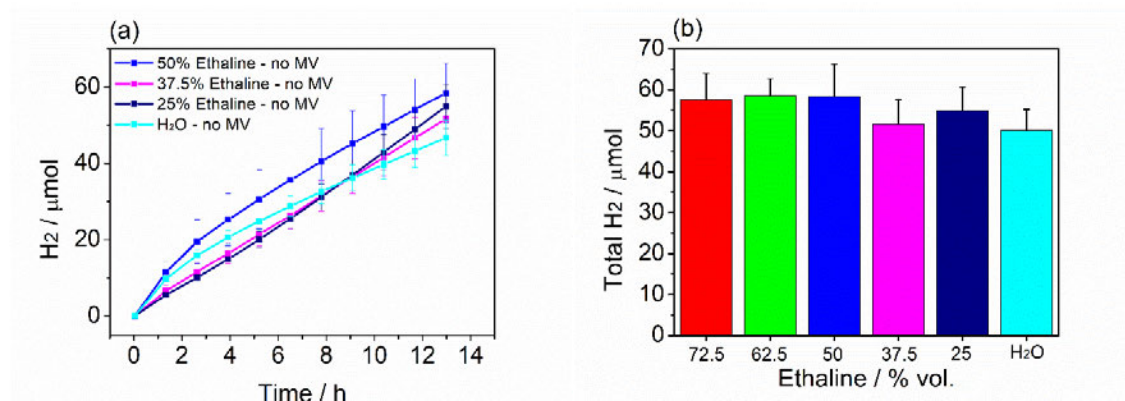


Figure 2.22. Cumulative photocatalytic H₂ generation at Pt/NCN-CN_x in ethaline with varying concentration of ethaline in the absence of a redox mediator. (a) and total H₂ produced at Pt/NCN-CN_x in varying % vol. ethaline and H₂O after 14 h irradiation (b) Conditions: NCN-CN_x (2.0 mg), H₂PtCl₆ (0.05 mg Pt) TEOA (0.4 M), 2.0 mL AM 1.5G, 1 sun, 40°C, constant N₂ purge.

Table 2.06. Photocatalytic H₂ generation by Pt/NCN-CN_x in ethaline-based solutions and H₂O in inert conditions with Total H₂ values after 14 h irradiation. NCN-CN_x (2.0 mg), H₂PtCl₆ (0.05 mg Pt), TEOA (0.4 M), 2.0 mL, AM 1.5G, 1 sun, 40 °C, N₂ purge gas at 4 mL min⁻¹.

		With added MV ²⁺		Without added MV ²⁺	
Ethaline % vol.	H ₂ O % vol.	Max. H ₂ Rate μmol h ⁻¹	Total H ₂ μmol	Max. H ₂ Rate μmol h ⁻¹	Total H ₂ μmol
82.5	17.5	15.9±1.3 after 5.5 h	105.1±8.6	2.5±1.3 after 0.8 h	21.6±1.3
72.5	27.5	21.3±2.8 after 6.5 h	160.8±15.9	8.0±2.5 after 1.3 h	57.6±6.3
62.5	37.5	11.6±1.4 after 6.5 h	95.4±6.6	10.3±0.7 after 1.3 h	58.6±4.1
50	50	11.1±3.4 after 7.8 h	88.6±11.7	8.9±2.2 after 1.3 h	58.4±7.8
37.5	62.5	6.8±0.8 after 14.2 h	22.6±4.7	5.1±1.1 after 1.3 h	51.7±5.9
25	75	0.2±0.1 after 14.2 h	1.4±0.5	4.2±0.3 after 1.3 h	54.9±5.8
0	100			7.5±0.6 after 1.3 h	50.1±5.1

2.5.7. Photocatalytic H₂ Evolution in DESs in the Absence of TEOA

As the DESs tested here are composed of organic compounds (urea, glycerol, and ethylene glycol for reline, glyceline, and ethaline respectively) it was necessary to determine the H₂ evolution in the absence of sacrificial TEOA. DESs are often viewed favourably for their stability and shelf life but have never been tested for the purposes of photocatalytic solar fuel production until this work. Due to the nature

of the components of the DESs studied in this work they can potentially contribute to sacrificial H₂ evolution through oxidation. Figure 2.23 shows the H₂ evolution by Pt/NCN-CN_x in 87.5% vol. DES, co-catalytic Pt in the form of H₂PtCl₆, and with added MV²⁺. No additional sacrificial reducing agent was applied for these reactions. Here, photogenerated positive holes are required to oxidise either water or the components of the DESs. As the oxidation of ethylene glycol, glycerol, and urea is more thermodynamically favourable than H₂O, it is highly likely that water splitting does not occur.

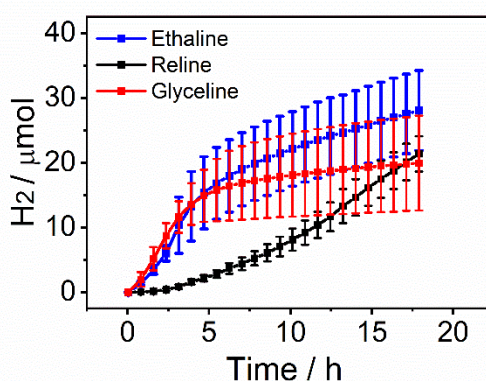


Figure 2.23. Photocatalytic H₂ production by NCN-CN_x in DESs in the absence of TEOA. Conditions: NCN-CN_x (2.0 mg), H₂PtCl₆ (0.05 mg Pt), MV₂₊ (2 mM), TEOA (0.4 M), H₂O (12.5% vol.) in ethaline, reline or glyceline (2.0 mL), AM 1.5G, 1 sun, 40°C, constant N₂ purge.

The Pt/NCN-CN_x photocatalyst produced 25.2±5.9 μmol_{H2} after 14 hours irradiation in the ethaline-based solution, as well as 19.2±6.9 μmol_{H2} and 14.7±2.8 μmol_{H2} in glyceline-based and reline-based solutions, respectively. It should be noted that the activity in the reline DES is very slow to begin with which is likely due to the difficulty of oxidation of urea in comparison to ethaline and glycerol.⁴³⁻⁴⁵ However, as the reaction proceeds and more urea is oxidised, Pt⁴⁺ is more likely to be reduced to Pt⁰ through the quenching of positive holes, preventing recombination. A slow electron supply slows the rate at which Pt is reduced, and so oxidising more urea allows more electrons to be generated. Electrons in the conduction band are then more readily available for the reduction of Pt and subsequently protons to hydrogen.

The oxidation of DES constituents is visible through photocatalytic hydrogen generation, as they can act as sacrificial reagents. However, when TEOA is employed to act as a sacrificial electron donor in conjunction with DESs, it is unlikely that the

organic DES constituents are oxidised by the photogenerated holes in NCN-CN_x due to the high oxidation potential of the TEOA in the system.⁴⁶

2.5.8. Homogenous Photocatalytic H₂ Evolution in DESs with Eosin Y

For any solvent to be considered as a suitable reaction medium, it should show diversity in its applications. Homogenous photocatalytic H₂ evolution using organic dyes is different from heterogenous photocatalysis, as the reaction components – light absorber, sacrificial reagent, and protons, are in the same state. This aids in increasing the rate of the reaction as kinetic limitations are not as prevalent. Another favourable aspect of using organic dyes is that they are cheap and readily available. Eosin Y as a light absorber has been investigated thoroughly in the literature, but solvent effects on its photocatalytic properties are not as prevalent.⁴⁷

Commercially available Eosin Y, as the disodium salt Na₂EY, was investigated as a light absorber in the organic DESs reline, glyceline, and ethaline, as well as H₂O under inert conditions with visible light by using a 400 nm cut-off filter ($\lambda > 400$ nm). EY was tested with co-catalytic Pt colloids and TEOA as a sacrificial quencher (Figure 2.24). In H₂O, the total H₂ production was determined to be $23.4 \pm 2.9 \mu\text{mol}_{\text{H}_2} \text{mM}^{-1}\text{EY}$ after 4.7 h, where the H₂ produced per mole of EY can be stated as the turnover number (TON). The H₂ production was also steady over the short period of irradiation.

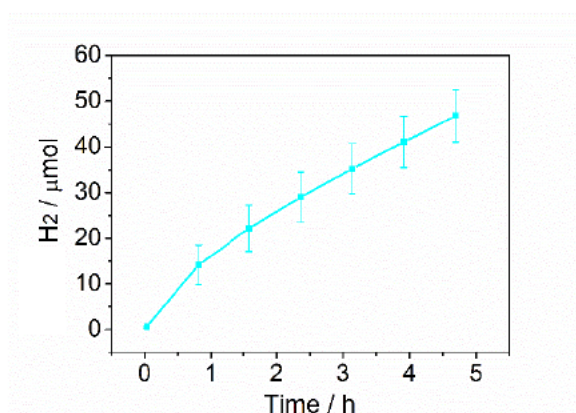


Figure 2.24. Photocatalytic H₂ production by Pt/EY in water after 4.7 h irradiation. Conditions: EY (2.0 mM), Pt colloids (0.05 mg), TEOA(0.4 M), 2.0 mL, $\lambda > 400$ nm, 40°C, constant N₂ purge.

The Pt/EY system was investigated with ethaline DES, and the water content of the ethaline was systematically varied. Pt/EY in 82.5% vol. ethaline showed a higher activity versus water, with $30.8 \pm 1.2 \mu\text{mol}_{\text{H}_2} \text{mM}^{-1}_{\text{EY}}$ after 4.7 h (Figure 2.25). The performance of Pt/EY in 72.5% vol. ethaline, 62.5% vol. reline, and 50% vol. reline was very similar, with $30.9 \pm 2.6 \mu\text{mol}_{\text{H}_2} \text{mM}^{-1}_{\text{EY}}$, $28.2 \pm 2.2 \mu\text{mol}_{\text{H}_2} \text{mM}^{-1}_{\text{EY}}$ and $29.6 \pm 2.3 \mu\text{mol}_{\text{H}_2} \text{mM}^{-1}_{\text{EY}}$ observed, respectively. Again, the stability even after 6.5 h irradiation can be observed, with almost linear H_2 production over time.

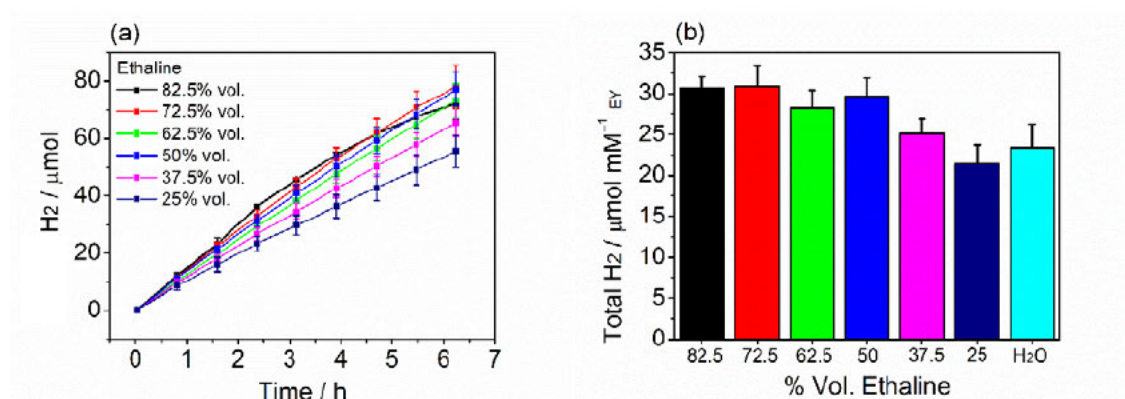


Figure 2.25. (a) Photocatalytic H_2 generation at Pt/EY in varying concentrations of ethaline over time and (b) TON of Pt/EY after 4.7 h irradiation. Conditions: EY (2 mM) Pt colloids (0.05 mg), TEOA (0.4 M), $\lambda > 400 \text{ nm}$, 40°C , 2.0 mL, constant N_2 purge.

Interestingly, the H_2 production activity by the photocatalyst drops slightly, with decreasing concentration of ethaline, as a 37.5% vol. and 25% vol. reline solution produced $25.1 \pm 1.8 \mu\text{mol}_{\text{H}_2} \text{mM}^{-1}_{\text{EY}}$ and $21.4 \pm 2.3 \mu\text{mol}_{\text{H}_2} \text{mM}^{-1}_{\text{EY}}$, respectively. The activity of the catalyst in these conditions more closely resembles water than the other solvents containing reline, which indicates that increase in ethaline concentration can aid the photocatalytic activity.

Some interesting observations are noted for the photocatalytic H_2 production by the same Pt/EY catalyst in glyceline (Figure 2.26). In 82.5% vol. and 72.5% vol. glyceline solutions, H_2 production is notably decreased in comparison to water, with a total H_2 production of $19.8 \pm 0.1 \mu\text{mol}_{\text{H}_2}$ and $34.5 \pm 5.4 \mu\text{mol}_{\text{H}_2}$, respectively. Notably, the catalytic activity slows down after 3 hours in both solvents. Performance of Pt/EY increases when the concentration of glyceline decreases, with 62.5% vol., 50% vol., 37.5% vol., and 25% vol. solutions of glyceline producing total H_2 amounts of $49.4 \pm 8.0 \mu\text{mol}_{\text{H}_2}$, $43.4 \pm 20 \mu\text{mol}_{\text{H}_2}$, $51.3 \pm 4.4 \mu\text{mol}_{\text{H}_2}$, and $49.0 \pm 2.6 \mu\text{mol}_{\text{H}_2}$,

respectively. Increase in water content shows activity more comparable to the performance in water as the solvent.

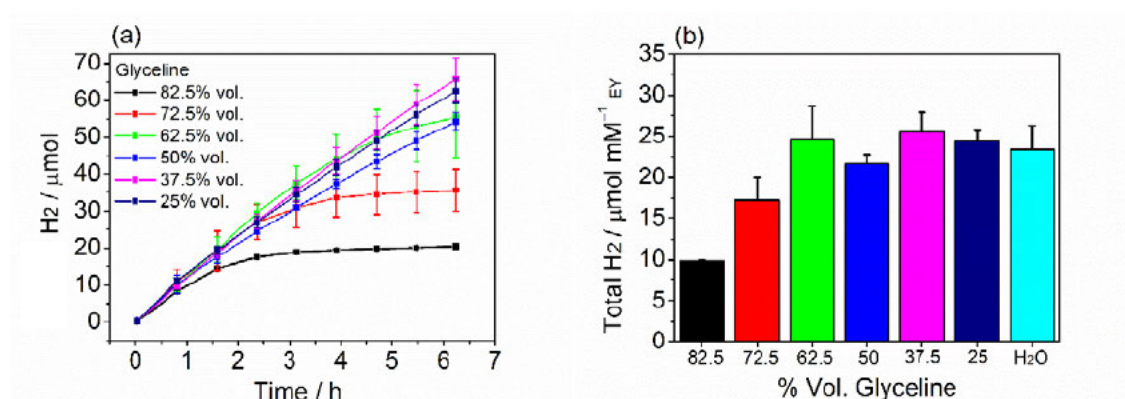


Figure 2.26. (a) Photocatalytic H₂ generation at Pt/EY in varying concentrations of glyceline over time and (b) TON of Pt/EY after 4.7 h irradiation. Conditions: EY (2 mM), Pt colloids (0.05 mg), TEOA (0.4 M), 2.0 mL, $\lambda > 400$ nm, 40°C, constant N₂ purge.

Pt/EY was also tested in the presence of reline for its photocatalytic H₂ evolution performance (Figure 2.27). Like glyceline, PT/EY shows low performance in 82.5% vol. reline, with 29.2 ± 5.5 μmol_{H₂} after 4.7 h irradiation in visible light. Decrease in the concentration of reline shows an increase in performance with PT-EY in 72.5% vol. reline, 62.5% vol. reline, and 50% vol. reline producing 56.7 ± 5.3 μmol_{H₂}, 64.0 ± 4.5 μmol_{H₂}, and 62.9 ± 7.3 μmol_{H₂} respectively.

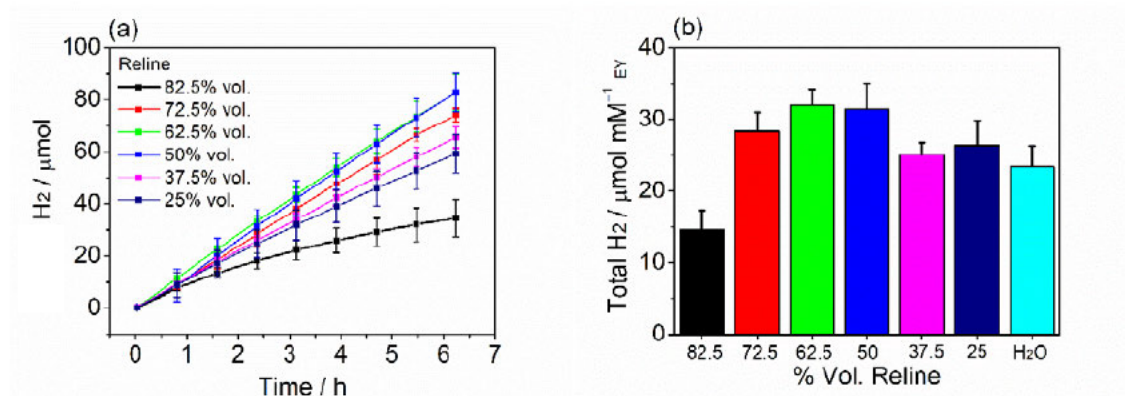


Figure 2.27. (a) Photocatalytic H₂ generation at Pt/EY in varying concentrations of reline over time and (b) TON of Pt/EY after 4.7 h irradiation. Conditions: EY (2 mM), Pt colloids (0.05 mg), TEOA (0.4 M), 2.0 mL, $\lambda > 400$ nm, 40°C, constant N₂ purge.

Similar activity of PT/EY is observed in water when 37.5% vol. reline and 25% vol. reline were applied as the solvent with 50.3 ± 3.3 μmol_{H₂} and 52.7 ± 7.1 μmol_{H₂} observed after 4.7 hours irradiation, respectively. Some conclusions may be drawn

from this data. First, at higher reline concentrations, diffusion of solid Pt may result in a lower H₂ evolution. This is because Pt must first withdraw excited electrons from EY*, and high concentrations of DES may affect the diffusion of large Pt particles. At high concentrations of ethaline (Figure 2.25) this phenomenon may not occur due to ethaline's naturally lower viscosity. As more H₂O is added to the reline DES, viscosity decreases and subsequently increases mobility in the solvent. This may also explain the lower H₂ production activity of Pt/EY in high concentrations of glyceline, as glyceline is a more viscous than the ethaline solvent.

Notably lower DES concentrations show similar behaviour in terms of stability, activity, and reaction profile to water. It can be inferred then that the DES structure possesses some effect on the reaction reagents. Eosin Y, when excited quickly converts to an excited triplet state. This triplet state undergoes reductive quenching by TEOA present in solution to yield the EY*⁻ species.⁴⁸ This EY*⁻ species is known to be highly reactive and can induce self-bleaching.⁴⁹ It is not unconceivable that the ions and intermolecular interactions between the solvent and excited Eosin Y can augment its lifetime, lowering the self-bleaching process and, as a result, the efficiency and utilization of excited dye species and photoinduced H₂ evolution could be improved.

2.6. Discussion

The work presented in this chapter is to date the only use of DESs as solvents for photocatalytic H₂ evolution. Most reaction systems use aqueous buffers at a certain pH to maximise the efficiency of the sacrificial electron donor. For example, EDTA has been shown to act as an electron donor at pH 6, while TEOA is normally used at pH 7.0.^{48, 50} TEOA is typically used at this pH as at an acidic pH, the lone pair of TEOA is protonated which lowers its oxidation potential.^{51, 52} (Figure 2.28). TEOA also has the added benefit of being irreversibly oxidised after quenching photogenerated holes, and the process of electron donation to the light absorber is kinetically and thermodynamically favourable.^{53, 54}

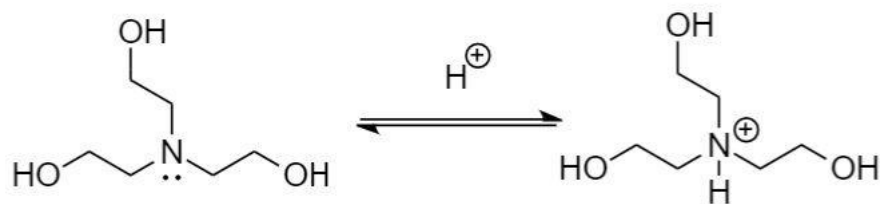


Figure 2.28. Schematic of TEOA protonation. When protonated, the lone pair on the N atom of TEOA is no longer able to partake in sacrificial electron donation to photoexcited light absorbers.

As TEOA is a base with a pKa 7.7, it induces an alkaline environment. The reduction of protons is more challenging in an alkaline environment due to the potential shift of the proton reduction half reaction to a more negative potential.⁵⁵ This can be seen experimentally- In water at pH 7.0 with 0.4 M TEOA, the Pt/NCN-CN_x produced 86.1±5.4 μmol_{H₂} with a maximum production rate of 13.0±1.4 μmol_{H₂} h⁻¹ after 14 hours irradiation (Figure 2.08), while in water with the same concentration of TEOA without pH adjustment produced 50.1±5.1 μmol_{H₂}. All solutions containing DESs contained “neat” TEOA i.e., no pH adjustment was done on the samples. While this may not yield the optimal conditions for proton reduction in given conditions the photocatalysts in the solvents tested compete or even outcompete water given identical reaction systems, highlighting the effectiveness of DESs as a solvent.

The intrinsic difference in photocatalytic behaviour of photocatalytic systems, both homogenous and heterogenous, is something which remains elusive, although can be speculated. Heterogenous systems involving semiconducting powders are dependent on the suspension of the photocatalysts, and their surface interactions with the solvent. It is possible that the photocatalyst experiences different surface phenomena in different solvents. As the solvents themselves are highly charged and contain ions, it is possible they aid in stabilising the various charged species in the reaction system, such as MV^{•+} and the electron intermediates in the system.

2.7. Conclusions

DESs have shown to provide an alternative and competitive solvent for photocatalytic H₂ evolution using both homogenous and heterogenous

photocatalysts. The redox mediator methyl viologen plays an important role for the performance of the photocatalytic system in DESs, particularly in cases when DES concentration is high. This is attributed to the reduction of Pt^{4+} in H_2PtCl_6 in DESs occurring in the solvent medium rather than on the photocatalyst surface, which is observed in water. Pt particles in solution require an electron shuttle to enable more efficient H_2 production. Addition of the redox mediator MV^{2+} partway through a reaction after the decomposition of MV^{2+} when DESs are used as a solvent can aid in increasing catalytic activity. However, the redox mediator can also hinder photocatalytic H_2 evolution performance by reacting with excited electrons in a more aqueous environment. Various other components are necessary for a high rate of photocatalytic H_2 production in the DESs, particularly a small quantity of water to arguably provide a more labile proton source, and TEOA as a sacrificial reagent. DESs can undergo oxidation to provide some photocatalytic performance, with the trends in activity reflected in the oxidation potential of the HBD component of the DES.

The water content of the DES is shown to greatly influence activity. It is proposed that in solutions where the content of DES is less than 50%, a solvent more closely resembling an aqueous environment dominates in terms of solvent properties, which can be seen from the photocatalytic trends in H_2 production. Notably, DESs do not compromise the long-term stability or compromise key structures in the NCN-CN_x photocatalyst, with the N=C=N^- cyanamide functionality responsible for catalytic activity as seen in post-irradiation IR analysis of the catalyst.

DESs show they are versatile by exhibiting photocatalytic activity with the homogenous organic dye Eosin Y as a light absorber. Photocatalytic activity can actually be increased relative to water, however the reasons for this increase in performance is not well understood, with possible investigations into the absorbance or fluorescence behaviour of the EY photoabsorber in DESs leading to an understanding of the reaction system.

2.8. Materials and Methods

Chemical Reagents: All chemical reagents used for this work were used as purchased and without further purification. Choline chloride (>99%), urea (analytical grade, 99.5%), ethylene glycol (>99%), glycerol (>99%), dicyandiamide (DCDA, 99%), potassium thiocyanate (99+%, analytical grade), triethanolamine (>98%), dihydrogen hexachloroplatinate hexahydrate, methyl viologen dichloride hydrate (98+%), Eosin Y (disodium salt, certified pure) and dihydrogen potassium phosphate (>99%) were all purchased from Fisher Scientific. 18.2 m Ω water was used throughout the experiments.

Synthesis of Deep Eutectic Solvents : Reline, glyceline and ethaline were prepared in accordance with literature procedures by stirring choline chloride with urea, glycerol, and ethylene glycol, respectively in a 1:2 molar ratio at 80 °C until a homogenous liquid had formed.^{2, 17}

Synthesis of NCN-CN_x: Graphitic carbon nitride was synthesised according to a literature procedure, whereby DCDA (5 g) was weighed into an alumina crucible, covered, and then heated in a muffle furnace at 550°C in air for 4 hours (10°C min⁻¹).⁵⁶ After cooling to room temperature, the yellow mass denoted DCDA-CN_x was thoroughly ground in a mortar and pestle (2.33 g). NCN-CN_x was synthesised according to a slightly modified literature procedure,³³ whereby DCDA-CN_x (1.0 g) was ground in a mortar and pestle with KSCN (2.0 g). The yellow powder was then dried overnight under vacuum at 140°C, before being placed in an open alumina crucible followed by heating in a muffle furnace to 400°C for 1 hour (10 °C min⁻¹) under N₂ (4 L min⁻¹) and a further heating step under N₂ at 500°C for 30 minutes (10 °C min⁻¹). An olive-green mass remained after cooling to room temperature, which was ground in a mortar and pestle, followed by tip sonication in a phosphate buffer for 10 minutes (0.1 M, pH 4.5). The resulting suspension was filtered and washed with water and ethanol, and the solid was collected and then dried under vacuum overnight at 50°C (0.76 g).

Treatment of Data: All photocatalysis, dye degradation and electrochemistry measurements were performed in triplicate and are given as the unweighted mean \pm standard deviation (σ). σ of a measured value was calculated using equation

(2.07), where n is the number of repeated measurements, x is the value of a single measurement and \bar{x} is the unweighted mean of the measurements.

$$\sigma = \sqrt{\frac{\sum(x - \bar{x})^2}{n - 1}} \quad (2.07)$$

Photocatalytic H₂ Generation in DESs: NCN-CN_x (2.0 mg, unless otherwise stated) was transferred into a glass sample vial (Chromacol 10-SV, Fisher) along with the reagent solution (2.0 mL unless otherwise stated). Samples were capped with rubber septa, vortexed briefly, and agitated in a sonic bath for 20 minutes prior to irradiation. Samples analysed under N₂ were purged for 10 minutes prior to irradiation to de-aerate the solution. Samples were irradiated using a solar light simulator (Thermo Oriel 92194-1000) equipped with an AM 1.5G filter (Newport) with an intensity of 1 sun. Samples were mounted in a water bath maintained at 40 °C and stirred at 700 RPM. The sample headspace was subject to a constant purge of N₂ at a rate of 4.0 mL min⁻¹ controlled by a mass flow controller (Bronkhorst). H₂ evolution was monitored by gas chromatography (Shimadzu Nexis 2030) using an auto-sampler programmed to inject 2 mL of the selected headspace stream. Experiments using Eosin Y were performed in the same manner using Eosin Y (2.0 mM) instead of NCN-CN_x.

Resuspension Experiment: Photocatalytic H₂ generation was performed by the standard procedure in reline (2.0 mg NCN-CN_x, 0.05 mg Pt as H₂PtCl₆, 0.38 M TEOA in 2.0 mL reline with 12.5% vol. water) and water (2.0 mg NCN-CN_x, 0.05 mg Pt as H₂PtCl₆, 0.4 M TEOA in 2.0 mL water pH 7) under inert conditions. After 4 h irradiation (AM 1.5G, 1 sun, 40 °C, continuous N₂ purge), samples were removed from the light and centrifuged using a Sigma 1-14 Microfuge (10,000 RPM, 10 min). The supernatant was decanted, and the precipitate was re-suspended in a fresh solution made up from the same solvent, but without added H₂PtCl₆ (0.4 M TEOA in 2.0 mL reline with 12.5% vol. water or 0.4 M TEOA in 2.0 mL water pH 7). The samples were purged again, and irradiation was continued (AM 1.5G, 1 sun, 40 °C, continuous N₂ purge).

Physical Measurements

Powder X-Ray Diffraction (PXRD): PXRD was performed on a Bruker D8 X-Ray Diffractometer with Cu K α ($\lambda=1.54056 \text{ \AA}$). The materials undergoing analysis were mounted and tightly packed on a zero-background spinner and diffraction patterns measured with Bragg-Brentano geometry between 10° and 80° with a step size of 0.02° for 45 minutes.

Fourier Transform Infrared Spectroscopy (FT-IR): FT-IR spectroscopy of materials was conducted with a Perkin Elmer Spectrum-Two FT-IR Spectrometer equipped with a UATR accessory.

UV/Vis Spectroscopy: UV/Vis absorption spectra were recorded on a Perkin Elmer Lambda 365 spectrometer using a Quartz UV/Vis cuvette with a path length of 1 cm.

DR-UV Spectroscopy and Band gap Determination: UV/Vis reflectance spectra were recorded on a Perkin Elmer Lambda 365 spectrometer using a diffuse reflectance accessory and with BaSO $_4$ as a reference material. Reflectance spectra were recorded and converted to Kubelka-Munk using the relationship:⁵⁷

$$\frac{k}{s} = \frac{(1 - R)^2}{2R} \quad (2.08)$$

where k is the absorption coefficient and s is the scattering coefficient of the sample. The energy of a photon is given by:

$$E = \frac{hc}{\lambda} \quad (2.09)$$

where h is Planck's Constant ($6.626 \times 10^{-34} \text{ J s}$), c is the speed of light ($3 \times 10^8 \text{ m s}^{-1}$) and λ is the wavelength (nm). Given that $1 \text{ eV} = 1.6 \times 10^{-19} \text{ J}$, Equation (2.09) can be converted to:

$$E = \frac{1240 \text{ (eV nm)}}{\lambda \text{ (nm)}} \quad (2.10)$$

The Tauc relationship is given by the Tauc and Davis-Mott relationship:⁵⁸

$$(\alpha h\nu)^n = B(h\nu - E_g) \quad (2.11)$$

where h is the Planck constant, ν is the photon's frequency, E_g is the band gap energy, and B is a constant. The coefficient n factor depends on the nature of the electron transition and is equal to 1/2 or 2 for the direct and indirect transition band gaps, respectively.^{59, 60} The region in the Tauc plots shown in Figure 2.05 showing steep linear increase of light absorption with increasing energy can be fitted linearly, and when $(\alpha h\nu)^n = 0$, the band gap energy E_g can be estimated.

Sample Analysis by Gas Chromatography (GC): Gas chromatography was performed on a Shimadzu Nexis GC-2030 gas chromatograph equipped with a barrier-discharge ionisation detector (BID) and a molecular sieve column. The total run time of the method was 5 minutes. The GC was calibrated using calibration gas (2000 ppm H₂, BOC), diluted with N₂ at different ratios using a set of mass flow controllers (Bronkhorst) to provide known concentrations of H₂. Gas samples were programmed to auto-inject into the GC via a multiport stream selector valve directing the selected sample purge gas stream through a 2 mL sample loop before injection. H₂ evolution rates were calculated from the measured H₂ concentration in the purge gas and the purge gas flow rate. Cumulative H₂ production was calculated from the H₂ evolution rate and time passed since the previous measurement, assuming a constant H₂ evolution rate between time points. All samples were performed in triplicate (unless otherwise stated).

2.9. References

1. P. T. Anastas and J. C. Warner, *Green Chemistry: Theory and Practice*, Oxford University Press, New York, 1998.
2. A. P. Abbott, G. Capper, D. L. Davies, R. K. Rasheed and V. Tambyrajah, *Chem. Commun.*, 2003, 70-71.
3. E. L. Smith, A. P. Abbott and K. S. Ryder, *Chem. Rev.*, 2014, **114**, 11060-11082.
4. B. B. Hansen, S. Spittle, B. Chen, D. Poe, Y. Zhang, J. M. Klein, A. Horton, L. Adhikari, T. Zelovich, B. W. Doherty, B. Gurkan, E. J. Maginn, A. Ragauskas, M. Dadmun, T. A. Zawodzinski, G. A. Baker, M. E. Tuckerman, R. F. Savinell and J. R. Sangoro, *Chem. Rev.*, 2021, **121**, 1232-1285.
5. T. Beyersdorff, T. J. S. Schubert, U. Welz-Biermann, W. Pitner, A. P. Abbott, K. J. McKenzie, and K. S. Ryder in *Electrodeposition from Ionic Liquids*, ed. F. Endres D. MacFarlane and A.P. Abbott, Wiley-VHC, Weinheim, 1st edn, 2008, vol. 1, ch. 2, pp. 15-46.
6. J. S. Wilkes and M. J. Zaworotko, *J. Chem. Soc., Chem. Commun.*, 1992, 965-967.
7. F. Endres and S. Zein El Abedin, *Phys. Chem. Chem. Phys.*, 2006, **8**, 2101-2116.
8. J.-Z. Yang, P. Tian, L.-L. He and W.-G. Xu, *Fluid Phase Equilib.*, 2003, **204**, 295-302.

9. S.-I. Hsiu, J.-F. Huang, I. W. Sun, C.-H. Yuan and J. Shiea, *Electrochim. Acta*, 2002, **47**, 4367-4372.
10. A. P. Abbott, G. Capper, D. L. Davies and R. Rasheed, *Inorg. Chem.*, 2004, **43**, 3447-3452.
11. M. S. Sitze, E. R. Schreiter, E. V. Patterson and R. G. Freeman, *Inorg. Chem.*, 2001, **40**, 2298-2304.
12. I. Skarmoutsos, D. Dellis, R. P. Matthews, T. Welton and P. A. Hunt, *J. Phys. Chem. B*, 2012, **116**, **16**, 4921-4933
13. Y.-F. Lin and I. W. Sun, *Electrochim. Acta*, 1999, **44**, 2771-2777.
14. O. S. Hammond, D. T. Bowron and K. J. Edler, *Green Chem.*, 2016, **18**, 2736-2744.
15. A. K. Halder and M. N. D. S. Cordeiro, *ACS Sustain. Chem. Eng.*, 2019, **7**, 10649-10660.
16. A. Shishov, A. Bulatov, M. Locatelli, S. Carradori and V. Andrich, *Microchem. J.*, 2017, **135**, 33-38.
17. A. P. Abbott, D. Boothby, G. Capper, D. L. Davies and R. K. Rasheed, *J. Am. Chem. Soc.*, 2004, **126**, 9142-9147.
18. J. D. Mota-Morales, M. C. Gutiérrez, I. C. Sanchez, G. Luna-Bárcenas and F. del Monte, *Chem. Commun.*, 2011, **47**, 5328-5330.
19. H. Wang, Y. Jing, X. Wang, Y. Yao and Y. Jia, *J. Mol. Liq.*, 2011, **163**, 77-82.
20. A. Hayyan, F. S. Mjalli, I. M. AlNashef, Y. M. Al-Wahaibi, T. Al-Wahaibi and M. A. Hashim, *J. Mol. Liq.*, 2013, **178**, 137-141.
21. R. Stefanovic, M. Ludwig, G. B. Webber, R. Atkin and A. J. Page, *Phys. Chem. Chem. Phys.*, 2017, **19**, 3297-3306.
22. C. R. Ashworth, R. P. Matthews, T. Welton and P. A. Hunt, *Phys. Chem. Chem. Phys.*, 2016, **18**, 18145-18160.
23. B. Ozturk, C. Parkinson and M. Gonzalez-Miquel, *Sep. Purif. Technol.*, 2018, **206**, 1-13.
24. A. P. Abbott, G. Capper, D. L. Davies, H. L. Munro, R. K. Rasheed and V. Tambyrajah, *Chem. Commun.*, 2001, 2010-2011.
25. Q. Xu, L. Y. Qin, Y. N. Ji, P. K. Leung, H. N. Su, F. Qiao, W. W. Yang, A. A. Shah and H. M. Li, *Electrochim. Acta*, 2019, **293**, 426-431.
26. A. P. Abbott, *ChemPhysChem*, 2004, **5**, 1242-1246.
27. A. P. Abbott, G. Capper and S. Gray, *ChemPhysChem*, 2006, **7**, 803-806.
28. C. D'Agostino, R. C. Harris, A. P. Abbott, L. F. Gladden and M. D. Mantle, *Phys. Chem. Chem. Phys.*, 2011, **13**, 21383-21391.
29. D. J. G. P. van Osch, C. H. J. T. Dietz, J. van Spronsen, M. C. Kroon, F. Gallucci, M. van Sint Annaland and R. Tuinier, *ACS Sustain. Chem. Eng.*, 2019, **7**, 2933-2942.
30. B. O'Regan and M. Grätzel, *Nature*, 1991, **353**, 737-740.
31. Y. Shen, X. He and F. R. Hung, *J. Phys. Chem. C*, 2015, **119**, 24489-24500.
32. C. L. Boldrini, N. Manfredi, F. M. Perna, V. Trifiletti, V. Capriati and A. Abboto, *Energy Technol.*, 2017, **5**, 345-353.
33. V. W.-h. Lau, I. Moudrakovski, T. Botari, S. Weinberger, M. B. Mesch, V. Duppel, J. Senker, V. Blum and B. V. Lotsch, *Nat. Commun.*, 2016, **7**, 12165.
34. X. Li, Y. Dai, Y. Ma, S. Han and B. Huang, *Phys. Chem. Chem. Phys.*, 2014, **16**, 4230-4235.
35. E. Reisner, D. J. Powell, C. Cavazza, J. C. Fontecilla-Camps and F. A. Armstrong, *J. Am. Chem. Soc.*, 2009, **131**, 18457-18466.
36. Y. Xie, H. Dong, S. Zhang, X. Lu and X. Ji, *J. Chem. Eng. Data*, 2014, **59**, 3344-3352.
37. C. Ma, A. Laaksonen, C. Liu, X. Lu and X. Ji, *Chem. Soc. Rev.*, 2018, **47**, 8685-8720.
38. M. Heyrovský, *J. Chem. Soc., Chem. Commun.*, 1987, 1856-1857.
39. Y. Borodko, P. Ercius, D. Zherebetsky, Y. Wang, Y. Sun and G. Somorjai, *J. Phys. Chem. C*, 2013, **117**, 26667-26674.
40. N. Steinfeldt, *Langmuir*, 2012, **28**, 13072-13079.
41. J. Quinson and K. M. Ø. Jensen, *Adv. Colloid Interface Sci.*, 2020, **286**, 102300.
42. Y. Wang, C. Ma, C. Liu, X. Lu, X. Feng and X. Ji, *J. Chem. Eng. Data*, 2020, **65**, 2446-2457.

43. S.-K. Geng, Y. Zheng, S.-Q. Li, H. Su, X. Zhao, J. Hu, H.-B. Shu, M. Jaroniec, P. Chen, Q.-H. Liu and S.-Z. Qiao, *Nat. Energy*, 2021, **6**, 904-912.
44. R. B. de Lima, V. Paganin, T. Iwasita and W. Vielstich, *Electrochim. Acta*, 2003, **49**, 85-91.
45. L. Roquet, E. M. Belgsir, J. M. Léger and C. Lamy, *Electrochim. Acta*, 1994, **39**, 2387-2394.
46. M. J. Berr, P. Wagner, S. Fischbach, A. Vaneski, J. Schneider, A. S. Susha, A. L. Rogach, F. Jäckel and J. Feldmann, *Appl. Phys. Lett.*, 2012, **100**, 223903.
47. L. Wang, H. Zhao, Y. Chen, R. Sun and B. Han, *Opt. Commun.*, 2016, **370**, 122-126.
48. T. Lazarides, T. McCormick, P. Du, G. Luo, B. Lindley and R. Eisenberg, *J. Am. Chem. Soc.*, 2009, **131**, 9192-9194.
49. S. Min and G. Lu, *J. Phys. Chem. C*, 2012, **116**, 19644-19652.
50. C. A. Caputo, M. A. Gross, V. W. Lau, C. Cavazza, B. V. Lotsch and E. Reisner, *Angew. Chem. Int. Ed.*, 2014, **53**, 11538-11542.
51. Y. Pellegrin and F. Odobel, *C. R. Chim.*, 2017, **20**, 283-295.
52. R. N. Sampaio, D. C. Grills, D. E. Polyansky, D. J. Szalda and E. Fujita, *J. Am. Chem. Soc.*, 2020, **142**, 2413-2428.
53. A. Rodenberg, M. Oraziotti, B. Probst, C. Bachmann, R. Alberto, K. K. Baldrige and P. Hamm, *Inorg. Chem.*, 2015, **54**, 646-657.
54. K. Kalyanasundaram, J. Kiwi and M. Grätzel, *Helv. Chim. Acta*, 1978, **61**, 2720-2730.
55. S. Horvath, L. E. Fernandez, A. M. Appel and S. Hammes-Schiffer, *Inorg. Chem.*, 2013, **52**, 3643-3652.
56. S. Cao, J. Low, J. Yu and M. Jaroniec, *Adv. Mater.*, 2015, **27**, 2150-2176.
57. P. Kubelka and F. Munk, *Z. Tech. Phys.*, 1931, **12**, 193.
58. E. Davis and N. Mott, *Philos. Mag.*, 1970, **22**, 0903-0922.
59. J. I. Pankove, *Optical Processes in Semiconductors*, Dover Publications Inc., New York, 1975.
60. P. Makuła, M. Pacia and W. Macyk, *J. Phys. Chem. Lett.*, 2018, **9**, 6814-6817.

Chapter 3

Deep Eutectic Solvents as a Reaction Medium for Aerobic Hydrogen Evolution

3.1. Introduction

Progress in photocatalytic solar fuel generation and research into materials and conditions has received a large amount of attention in the scientific community as we aim to develop methods of alleviating dependence on fossil fuels. Benchmark photocatalytic systems should be implemented for their feasibility in real world applications, as well as showcasing desirable properties such as high performance and stability.

In the literature, a large issue that remains relatively unexplored is the effect of O_2 on artificial photosynthesis, with the vast majority of reactions investigated for solar fuel production being performed in anaerobic / inert conditions. These anaerobic conditions are often achieved through the purging of reaction systems with N_2 or Ar gas. While this is beneficial to increasing photocatalyst performance anaerobic conditions are costly to maintain on an industrial level scale, and many highly active photocatalysts have not been investigated for their ability to perform in the presence of atmospheric O_2 . In full water splitting reactions, water when oxidised yields O_2 even under inert conditions. Therefore, catalysts need to perform O_2 -tolerant H_2 evolution, and O_2 tolerance of the catalyst is necessary to improve overall water splitting processes. Exposure of proton reduction catalysts to O_2 is therefore almost unavoidable.

3.2. Principles of O_2 Reduction

O_2 reduction, in the context of an artificial photosynthetic system, is an often-undesirable reaction for a variety of reasons. At neutral pH, the reduction of protons to molecular H_2 occurs at a theoretical potential = -0.42 V vs. NHE, while the

reduction of O₂ possesses numerous pathways all of which are deemed to be thermodynamically favourable in comparison to proton reduction.¹ (Figure 3.01)

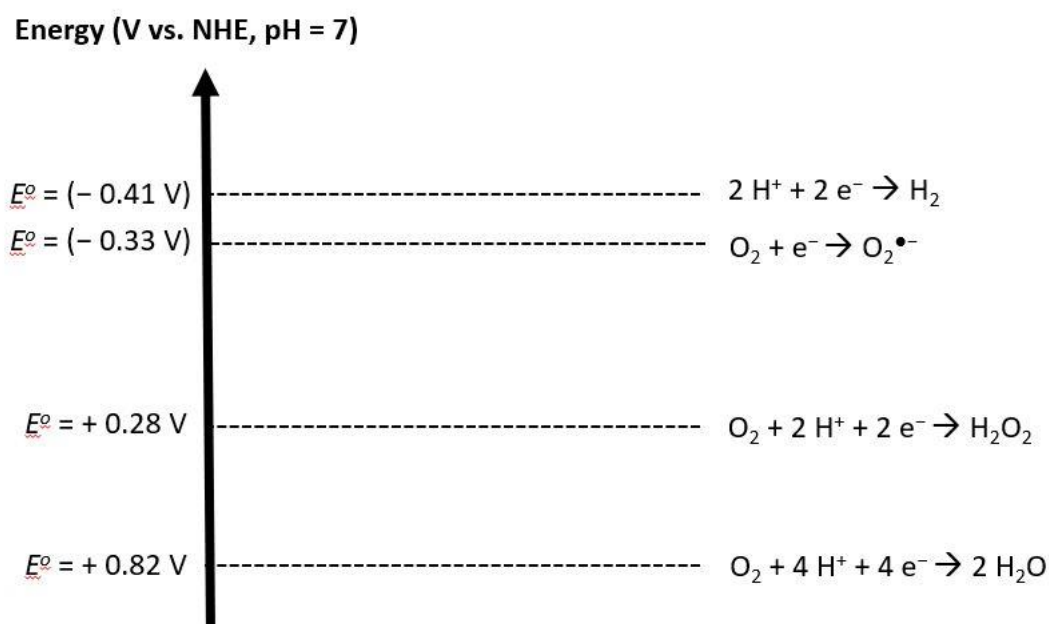


Figure 3.01. Potential energy diagram for possible O₂ reduction reactions at pH 7. Schematic adapted from information in REF 1.

At neutral pH, O₂ can be reduced to water provided enough electrons are available to facilitate the reaction. Of the reduction reactions presented, water is the most thermodynamically stable product but is difficult to obtain due to the difficulty associated with cleaving the O=O double bond. In addition, the reduction one mole of molecular O₂ to water requires four protons and four electrons – this multi-phase and multi-step process is kinetically hindered compared to other O₂ reduction reactions.² As a result, O₂ is often incompletely reduced, forming products such as H₂O₂ or superoxide radicals O₂^{•-}, which are often called reactive oxygen species (ROSs). ROSs formed during reductive processes can be damaging to catalysts and components of the reaction system.³ Photoexcited catalysts and light absorbers are generally reactive towards O₂ and developing systems which protect photoexcited catalysts is highly favourable for reaction systems.⁴

It should be noted that the incomplete reduction products can themselves be further reduced to thermodynamically stable water from the following reactions:





The processes required to facilitate the O₂ reduction processes showcased here all compete with proton reduction in a photocatalytic system. As such, H₂ evolution catalysts will also react with O₂ if present. O₂, if present, can act as a photocatalytic quencher through the uptake of photoexcited electrons, or O₂ can be reduced at the co-catalytic surface, again competing with protons for photoexcited electrons. It has been observed in the literature that highly active photocatalysts can bind O₂ from air onto their surface, inducing undesired stress on the crystal structure of the photocatalyst causing photocorrosion.⁵ The presence and reduction of O₂ therefore in many cases diminishes the performance of photocatalysts employed for photocatalytic H₂ evolution.

3.3. O₂ Tolerant Photocatalysis

The accepted definition of O₂ tolerant photocatalysis describes the maintenance of activity of a catalyst in the presence of O₂ - however some considerations must be made if this definition is accepted. Catalysts which show activity towards proton reduction in the presence of O₂ are said to be O₂ tolerant.⁶ It is not clear if a catalytic system in which 1% of activity is retained in the presence of O₂ should be considered O₂ tolerant. Furthermore, it is difficult to draw meaningful conclusions about reaction systems which exhibit a high retention of photocatalytic activity at a minimal O₂ concentration, and meaningful conclusions about the suitability of a photocatalyst under real-world operating conditions are elusive as a result. Some liberties are taken in the literature when aerobic H₂ production is concerned, which may be a result of the sheer lack of O₂ tolerant systems. However, it is generally accepted that catalysts which can reduce the O₂ diffused to the active sites without being irreversibly damaged are stated to be O₂ tolerant.

O₂ tolerance of a photocatalyst is an important factor that is often unreported in reaction systems, despite its importance when considering a practical device. H₂ evolution systems will unavoidably be exposed to O₂. This may be through the

formation of O_2 *in situ* from water splitting, or through a leakage in the reaction cell (Figure 3.02).^{6,7}

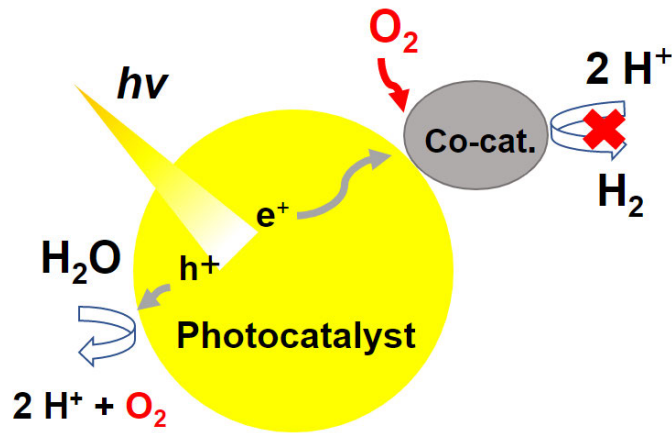


Figure 3.02. Depiction of possible routes of O_2 presence in photocatalysis

O_2 tolerance also plays an important role in electrolyzers / photoelectrochemical (PEC) cells. These systems contain two electrodes with O_2 evolved at the anode and H_2 evolved at the cathode separated by a proton exchange membrane to facilitate proton transfer from the anodic chamber to the cathode, and to prevent mixing the two evolved gases (Figure 3.03).⁸ O_2 produced at the anode and the proton reducing cathode can still occur through O_2 leakage from the atmosphere into the electrochemical cell or from the anodic chamber after membrane degradation.^{7, 9} The mixing of O_2 with the cathodic chamber can occur even with pristine membranes if low electrolyzer loads are used and when electrolyzers are operated under pressure. Upon mixing, the interaction between cathode and O_2 becomes inevitable without additional protection of the catalyst.

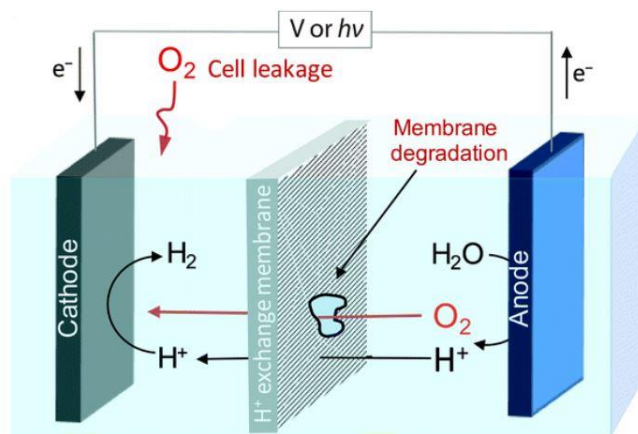


Figure 3.03. Schematic of a PEC cell, showing the potential routes through which a proton reducing catalyst at the cathode could be exposed to O₂. Reprinted with permission from REF 6. Copyright 2015, Royal Society of Chemistry

In situations like this, the O₂ available is more favourably reduced versus protons, which lowers quantum efficiencies and the solar-to-hydrogen efficiency of photocatalysts. In reaction systems involving molecular and heterogenous photocatalysts, O₂ can act as a quencher for photoexcited electrons before the electron can be transported to a co-catalyst.¹⁰⁻¹³ Notably, the formation of reactive oxygen species – ROSs – such as peroxides and radicals can lead to undesirable reactions that may induce damage to photocatalytic components or to photocatalysts themselves. In cases where biological co-catalysts (hydrogenases) are used, O₂ can irreversibly react with the active site, creating a permanently oxidised co-catalyst incapable of harvesting electrons for proton reduction.^{14, 15}

3.4. Methods of Oxygen-Tolerant Photocatalysis

Methods of inducing O₂ tolerance is an area which is largely unexplored in the literature in comparison to other research areas such as material development, although work has been done in this area. Inducing O₂ tolerance is primarily focussed on preventing O₂ from competing with proton reduction sites on catalysts. This is because any electrons which are used in O₂ reduction processes over proton reduction lower the quantum efficiency for photocatalysts and the Faradaic efficiency of electrocatalysts, as charge carriers do not participate in fuel production.^{16, 17} Highly active materials which are capable of reducing protons and incoming O₂ have been investigated with the focus on Co molecular catalysts.^{18, 19} Indeed, being able to fully reduce O₂ present to harmless water, all the while reducing protons may not be so disadvantageous, however issues would remain with lower overall efficiencies as described above. Using antioxidant species in reaction systems can also aid in increasing O₂ tolerance. The electroreduction of ROSs has been reported by synthetic hydrogenases deposited on carbon electrodes. The issues of stability of the catalyst remain however, as the hydrogenase mimic works only in a neutral pH region and is an expensive component of the electrolysis set-up.²⁰

A rather neat method of inducing O₂ tolerance involves the use of “blocking layers” on catalytic materials. This can be done using a redox-active hydrogel, as has been shown by and Plumeré et al., with an understanding of the mechanism proposed by Fourmound et al.^{21, 22} The former’s work focussed on developing a polymer constructed from redox-active monomers, which showed that electron transfer between the polymer-bound redox mediator functionalities controls the potential applied to the active site of the hydrogenase and thus insulates the enzyme from excessive oxidative stress.²² It was found that the polymer upon exposure to O₂ has a fully *reversible* effect on the catalytic H₂-oxidation current, showing that the catalyst can reduce incoming O₂ after performing H₂ oxidation through electron transfer, thus providing self-activated protection from O₂.²¹ This can be viewed as a chemical approach to inducing O₂ tolerance, where a physical approach of introducing a literal O₂ barrier has been achieved by coating polymers with a nanosized-oxygen-barrier, where O₂ impermeable polymers can decrease the rate at which O₂ permeates to thin coatings of metal oxides.²³ While this work had no bearing on photocatalytic or electrocatalytic performance, it highlights the possibility of offering a layer of protection to materials which are sensitive to O₂.

This was realised in work by Domen and co-workers on photocatalytic particles for water splitting. Here, particles consisting of a (Ga_{1-x}Zn_x)(N_{1-x}O_x) photocatalyst loaded with Rh were investigated – Rh is capable of catalysing the formation of water i.e., the reverse of water splitting.²⁴ This back reaction could be prevented through the addition of a Cr₂O₃ layer on the Rh co-catalyst, as the Cr₂O₃ blocked O₂ from diffusing to the Rh surface.^{25, 26} This mechanism is highlighted in Figure 3.04 below. Proton reduction was still active in the material despite the Cr₂O₃ layer blocking some catalytic sites on the Rh. This was confirmed through IR spectroscopy, which illustrated that protons were able to penetrate the Cr₂O₃ to reach a catalytic Pt surface. Selectively allowing proton reduction over oxygen reduction has also been studied using ammonium tetrathiomolybdate tethered to Au, whereby proton reduction catalysis was observed after water splitting without O₂ interference.²⁷ Thus a catalytic system may be devised that can utilize a ligand-based diffusion mechanism to permit hydrogen evolution selectively in the presence of O₂.

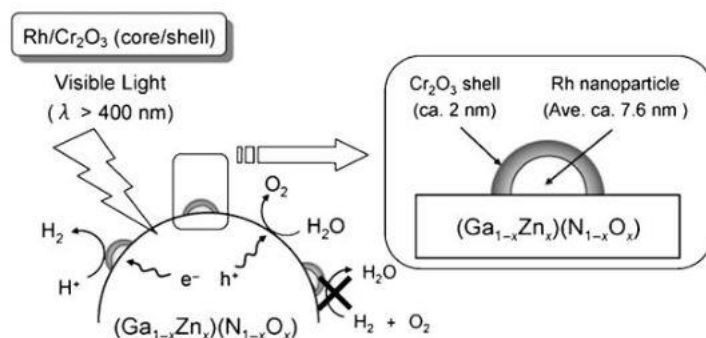


Figure 3.04. Schematic representation of O_2 exclusion by a Cr_2O_3 layer loaded on a Rh cocatalyst for photocatalytic H_2 production.^{25, 28} Reprinted with permission from REF 25. Copyright 2006, WILEY-VCH.

It should be noted that heterogenous particles in general exhibit higher O_2 tolerances relative to molecular catalysts and hydrogenases, presumably as a result of the absence of organic frameworks. Moreover, proton reducing surfaces are also active for the O_2 reduction processes as has been shown for MoS_2 particles and Au nanoparticles.^{29, 30} Another interesting approach is by using O_2 present as a method of “self-repair.” This was obtained with a $CuRhO_2$ photoelectrode for water splitting with visible light.³¹ In this example, H_2 evolution was observed at low overpotentials in solution saturated with atmospheric levels of O_2 , while in an inert atmosphere H_2 production was not as efficient. This was attributed to the reduction of the semiconductor forming Cu^0 . However, in the presence of air or O_2 , Cu^0 was not detected, implying that $CuRhO_2$ is “self-healing” (Figure 3.05).

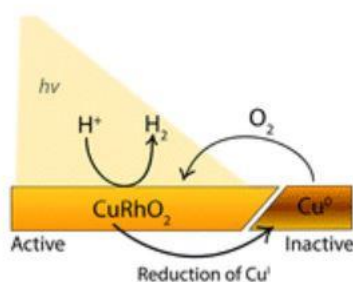


Figure 3.05. Illustration of O_2 -driven self-repair after photocorrosion of a $CuRhO_2$ photoelectrode to form inactive Cu^0 .³¹ Reprinted with permission from REF 6. Copyright 2015, Royal Society of Chemistry.

A similar approach has also been observed for CdS quantum dots (QDs), where the QDs in a highly alkaline environment showed good photocatalytic activity, but low stability.³² The reaction proceeded with the formation of Cd^0 , indicated by a black

precipitate in conjunction with loss of CdS absorption peak in the UV/Vis spectrum. The CdS/Cd⁰ particles were then subject to irradiation in an aerobic environment with atmospheric levels of O₂ and it was shown that catalytic activity could be regained. This was credited to O₂ providing an easily reduced secondary substrate (due to the facile nature of O₂ reduction) in the photoreactor that precludes the accumulation of Cd⁰ and thereby maintains the stability of the particle during photocatalysis.³² This work also showed that in some given reaction conditions, H₂ evolution in air was lower relative to N₂ as a result of the consumption of photogenerated charge carriers by O₂.

To date, solvent effects on the O₂ tolerance, and indeed on photocatalytic solar fuel production processes themselves remain largely unreported in the scientific literature despite the fact that photocatalytic components and reagents are in constant contact with the reaction solvent.

It has been reported that deep eutectic solvents allow for the stabilisation of O₂-sensitive radicals formed from chemical, electrochemical and photochemical methods, even after 6 months of initial radical formation.³³ The stabilisation is thought to arise from the unique nanostructure of DESs, shielding the species from O₂ present in the surrounding environment allowing them to possess a longer lifetime versus a conventional aqueous solvent in the presence of air. In addition, they have shown capability for producing products from air-sensitive organic syntheses with O₂ present, notably the reaction of Grignard addition on aldehydes to ketones.^{34, 35}

This chapter focusses on utilising DESs as a medium for O₂-tolerant photocatalytic hydrogen evolution. O₂ tolerance was determined by comparing photocatalytic activity for H₂ evolution in both the presence and absence of atmospheric O₂ in reaction samples, with the O₂ tolerance measured used as an overall indicator of performance. Photocatalysts which are viewed as O₂ intolerant were used without any structural redesigns or modifications, and to show that O₂ tolerance can be induced simply through solvent tuning. The added benefit of investigating solvent effects to induce O₂ tolerance lies in the fact that DESs are highly tunable and functionable through the choice of hydrogen bond donor and acceptor. This allows

the exploration solely on the effect of the solvent on O₂ tolerance, rather than introducing costly redesigns to the photocatalyst materials.

3.5. Results

3.5.1. Solar Hydrogen Evolution of NCN-CN_x Photocatalyst in Aerobic Conditions

The performance in an aerobic atmosphere of the as previously synthesised NCN-CN_x photocatalyst was investigated in an aqueous solution containing 0.4 M TEOA at pH 7 and co-catalytic platinum. Figure 3.06 shows the total H₂ produced from the Pt/NCN-CN_x catalyst during irradiation in both the presence and absence of a redox mediator. Pt/NCN-CN_x produced 0.3±0.1 μmol_{H₂} after 15.5 hours of irradiation when 2 mM of methyl viologen as a redox mediator was added. Similar to anaerobic conditions, performance increased when no methyl viologen was used, with 7.6±1.2 μmol_{H₂} after 15.5 hours of irradiation and a maximum activity of 0.75±0.15 μmol_{H₂} h⁻¹ g⁻¹_{cat.}. The total hydrogen and maximum activity of the Pt/NCN-CN_x is vastly diminished in aerobic conditions in comparison to an inert environment, with the O₂ tolerance of the photocatalyst calculated to be 1.7±0.7% with methyl viologen and 8.7±1.5% without methyl viologen. (Figure 3.07).

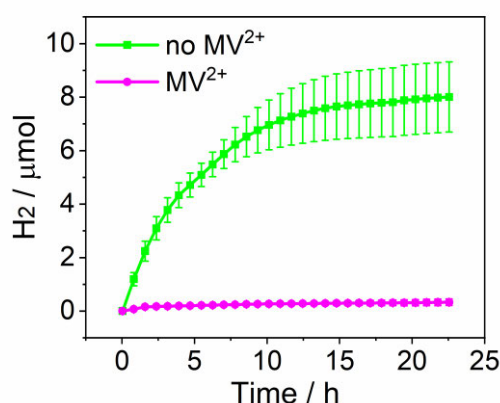


Figure 3.06. Effect of methyl viologen on hydrogen evolution at Pt/NCN-CN_x in air. Conditions: NCN-CN_x (2.0 mg), H₂PtCl₆ (0.05 mg Pt), MV²⁺ (2 mM – purple trace), TEOA (0.4 M), pH 7 (2.0 mL), AM 1.5G, 1 sun, 40 °C, constant air purge.

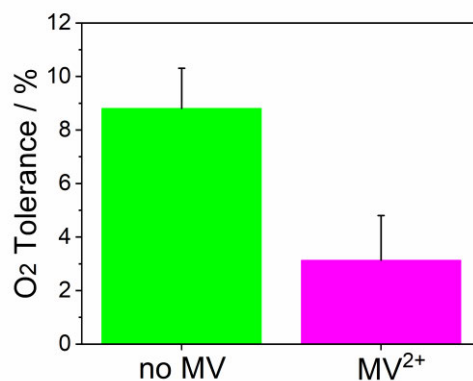


Figure 3.07. O₂ tolerance of Pt/NCN-CN_x with and without methyl viologen after 14 hours of irradiation.

The O₂ tolerance as a percentage was calculated using

$$\text{O}_2 \text{ Tolerance (\%)} = \frac{\text{Total H}_2 \text{ in air after } t}{\text{Total H}_2 \text{ in N}_2 \text{ after } t} \times 100 \quad (3.03)$$

where t = time. An interesting observation can be made for the photocatalyst in an aerobic environment, whereby upon irradiation the typical turquoise-blue colour associated with the reduced state of the material in an aerobic environment is not observed. This intuitively shows that the photoexcited electrons in the trapped states of the NCN-CN_x photocatalyst responsible for the change in colour upon irradiation are no longer present, which in turn suggests that these excited electrons in the photocatalyst are quenched by molecular O₂ present and cause a lowering of the H₂ evolution performance. The comparison of the NCN-CN_x photocatalyst in inert and aerobic conditions are shown in Figure 3.08. The O₂ tolerance of the catalyst decreases further over time, with almost no activity observed for H₂ evolution after 10 hours.

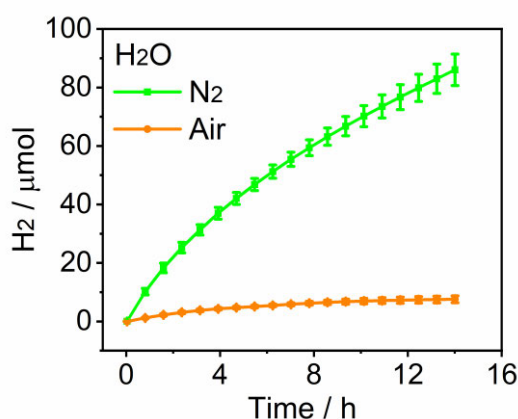


Figure 3.08. Photocatalytic H₂ evolution of Pt/NCN-CN_x photocatalyst in nitrogen (green) and air (orange). Conditions: NCN-CN_x (2.0 mg), H₂PtCl₆ (0.05 mg Pt), MV²⁺ (2 mM), TEOA (0.4 M), pH 7 (2.0 mL), AM 1.5G, 1 sun, 40 °C, constant N₂ or air purge.

The photocatalyst was then investigated for aerobic hydrogen evolution in deep eutectic solvents without any modifications to the catalyst. Atmospheric levels of O₂ were used, with all samples subject to a constant purge of air during solar irradiation. In an 82.5% vol. reline solution tested, the Pt/NCN-CN_x showed much higher performance versus water in the presence of air. It was observed that after 14 hours irradiation, 123.5±8.1 μmol_{H₂} was detected in a reline-based solvent, with a maximum activity of 8.9±0.9 μmol_{H₂} h⁻¹ g⁻¹_{cat} (Figure 3.09). The reaction profile shows very similar behaviour to the same catalyst in an inert atmosphere, highlighting the retention of Pt/NCN-CN_x performance. The O₂ tolerance for the photocatalyst at certain points in the reaction can also be calculated. Nearly 100% of photocatalytic activity is retained after 4.7 h irradiation, and the catalyst shows exceptional O₂ tolerance throughout the reaction, with 89.3±6.1% of the original activity retained versus inert conditions.

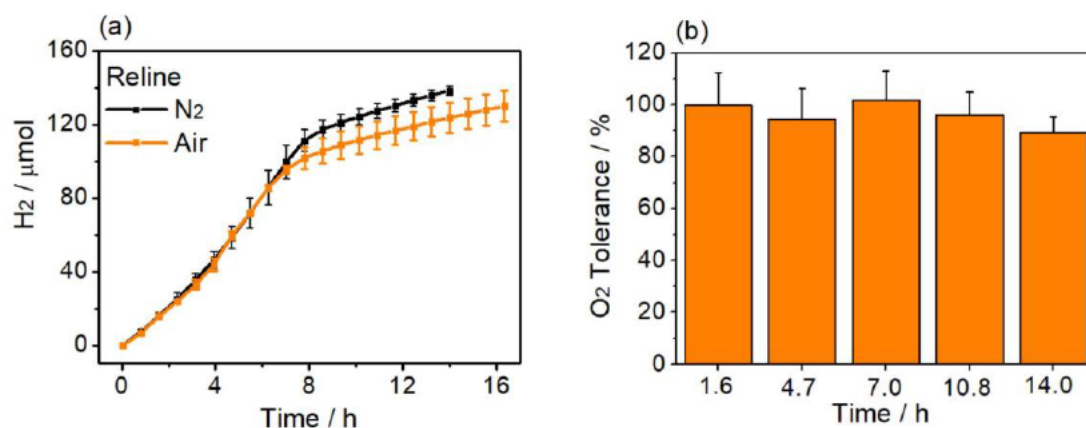


Figure 3.09. Photocatalytic H₂ generation in 82.5% reline at Pt/NCN-CN_x in N₂ and atmospheric levels of O₂ (a) and calculated O₂ tolerance of Pt/NCN-CN_x at given time points during the course of the reaction (b). Conditions: NCN-CN_x (2.0 mg), H₂PtCl₆ (0.05 mg Pt), in 82.5% vol. reline, TEOA (0.4 M), MV²⁺ (2 mM), AM 1.5G, 1 sun, 40 °C, constant N₂ or air purge.

The apparent quantum yield (AQY) was calculated for the Pt/NCN-CN_x photocatalyst to determine the fate of photoexcited electrons in the system. AQY was measured at a monochromatic wavelength of 405 nm, in the region where NCN-CN_x can absorb visible light. The monochromatic filter was placed in front of samples to prevent any other wavelength of light interacting with the reaction. The results from the AQY

measurements in both inert and aerobic conditions are shown in Table 3.01. The AQY for H₂ evolution in aerobic reline was determined at 3.9±0.3% after 20 hours of irradiation which is within error identical to the AQY observed in anaerobic conditions. This indicates that charge carriers in the reaction system are not quenched or are limited in their interaction with O₂ in the samples. The retention of quantum efficiency shows that photogenerated electrons at the catalyst surface are more readily used for proton reduction over O₂ reduction.

Table 3.01. Apparent quantum yield (AQY) determination for anaerobic and aerobic photocatalytic H₂ evolution in 82.5% vol. reline. Conditions: NCN-CN_x (2.0 mg), H₂PtCl₆ (0.05 mg Pt), TEOA (0.4 M), 40 °C, constant N₂ or air purge. A = 2.5 cm², λ = 405 nm in N₂, I = 2.69 mW cm⁻² in N₂ and 2.69 mW cm⁻² in air

Time h	n(H₂) - N₂ μmol	QE - N₂ %	n(H₂) - Air μmol	QE - Air %
1.1	1.7±0.7	3.9±1.6	1.4 1.4±0.6	3.2±1.5
2.1	2.4±1.0	2.9±1.1	2.0±0.6	2.3±0.7
3.1	3.2±1.1	2.5±0.8	3.0±1.0	2.3±0.8
4.2	4.2±1.5	2.6±0.9	3.9±1.1	2.4±0.7
5.2	5.4±1.2	2.6±0.6	5.3±1.0	2.6±0.5
10.1	13.1±4.7	3.1±1.2	14.7±2.0	3.5±0.5
15.1	21.7±9.3	3.5±1.5	23.4±2.6	3.8±0.4
20.0	30.8±12.6	3.7±1.5	32.2±2.9	3.9±0.3

The O₂ tolerance of the Pt/NCN-CN_x catalyst was also measured in the presence of glyceline. The total H₂ produced in air by Pt/NCN-CN_x after 14.0 h solar irradiation was 53.0±3.4 μmol_{H₂} (Figure 3.10). Again, the photocatalyst is observed to be very stable in terms of H₂ production activity in 21% O₂ with good retention of photocatalytic activity. After 14.0 h irradiation, the O₂ tolerance was observed to be 90.4±7.8%.

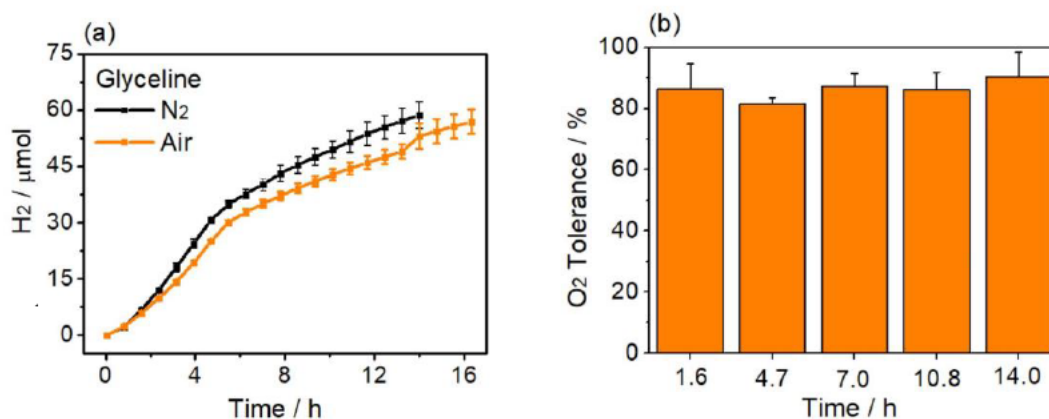


Figure 3.10. Photocatalytic H₂ generation in 82.5% glyceline at Pt/NCN-CN_x in N₂ and atmospheric levels of O₂ (a) and calculated O₂ tolerance of Pt/NCN-CN_x at given time points during the course of the reaction (b). Conditions: NCN-CN_x (2.0 mg), H₂PtCl₆ (0.05 mg Pt), in 82.5% vol. glyceline, TEOA (0.4 M) MV²⁺ (2 mM), 2.0 mL, AM 1.5G, 1 sun, 40 °C, constant N₂ or air purge.

The O₂ tolerance and photocatalytic behaviour was also determined in an 82.5% vol. ethaline solution, with the results shown in Figure 3.11. The results show that in atmospheric levels of O₂ Pt/NCN-CN_x produced 77.3±6.9 μmolH₂ after 14.0 h irradiation under a constant air purge. Comparison of the performance in inert conditions by the same catalyst in otherwise identical conditions showed that the catalyst exhibited an O₂ tolerance of 73.6±9.0%

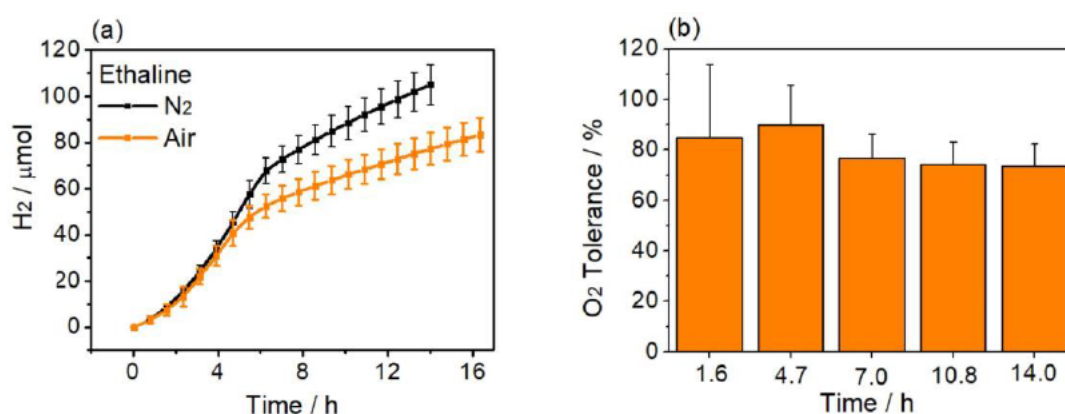


Figure 3.11. Photocatalytic H₂ generation in 82.5% ethaline at Pt/NCN-CN_x in N₂ and atmospheric levels of O₂ (a) and calculated O₂ tolerance of Pt/NCN-CN_x at given time points during the course of the reaction (b). Conditions: NCN-CN_x (2.0 mg), H₂PtCl₆ (0.05 mg Pt), in 82.5% vol. ethaline, TEOA (0.4 M), MV²⁺ (2 mM), AM 1.5G, 1 sun, 40 °C, constant N₂ or air purge.

It is evident the DESs allow for the maintenance of high activity of the photocatalyst for H₂ evolution in the presence of O₂. Figure 3.12 shows the total H₂ produced in each of the DESs tested in an inert and aerobic environment. This indicates the

photocatalyst exhibits a similar reaction profile in the DESs in air and nitrogen as well as a high degree of stability and performance.

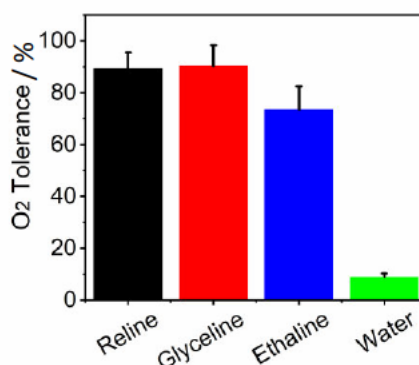


Figure 3.12. O₂ tolerance of Pt/NCN-CN_x in DES-based solutions and water. Values taken after 14.0 hours of irradiation in aerobic and anaerobic conditions.

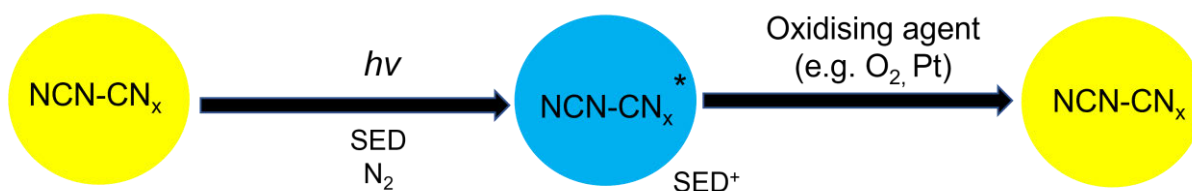
These results show that O₂ tolerance can be induced simply from changing the solvent media, and solvent properties can aid in augmenting photocatalytic hydrogen evolution in the presence of O₂.

3.5.2. Investigating Solvent Effects on Photocatalytic Properties

Having identified that a change in solvent can alter O₂ tolerance, it was necessary to gain an understanding of the behaviour of the photocatalyst material in the DES-based solvents to highlight their applicability in aerobic photocatalytic systems.

As previously mentioned, and has been shown in the literature, the NCN-CN_x photocatalyst can accumulate photogenerated electrons in trapped states upon irradiation, providing photogenerated holes are sufficiently quenched.^{36, 37} The accumulated electrons give rise to a notable colour change on the material, from yellow to turquoise blue. This state is often called “reduced” carbon nitride, denoted as NCN-CN_x^{*}. In an inert atmosphere, NCN-CN_x^{*} is readily observed in all solvents investigated in the results shown here. It has also been shown that the excited electrons located in the NCN-CN_x^{*} material can be quenched allowing the

photocatalyst to revert to its original colour. This mechanism is highlighted in Scheme 3.01.³⁷



Scheme 3.01. Mechanistic depiction of the formation of reduced NCN-CN_x^* under an inert atmosphere during solar photoirradiation with a sacrificial electron donor (SED). The SED becomes oxidised in the process to generate the NCN-CN_x^* reduced species, which can then be oxidised by O_2 or Pt to realise the original photocatalyst.

In water, the NCN-CN_x^* state can also be isolated and examined provided an inert atmosphere is maintained, as the reduced photocatalyst is quenched upon exposure to air. Interestingly, the reduced photocatalyst can be maintained in both an inert and aerobic atmosphere in the DES-based solutions, with removal of the electrons from the reduced NCN-CN_x^* photocatalyst prevented. This allows the characterisation and detection using diffuse reflectance UV-Vis spectroscopy. NCN-CN_x^* shows an absorption band at 680 nm in an aerobic atmosphere in the DES-based solvent post irradiation using sacrificial TEOA as a hole scavenger. This band is not detected for the photocatalyst in an aerobic atmosphere in an aqueous solution, as the NCN-CN_x^* catalyst is not maintained. (Figure 3.13).

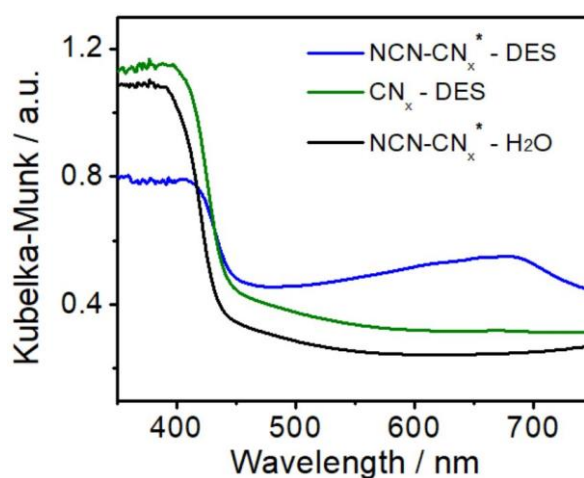


Figure 3.08. Kubelka-Munk function of the diffuse reflectance UV-Vis spectra of NCN-CN_x in a DES-TEOA solution (green trace) and aqueous TEOA solution (black trace) prior to irradiation with simulated solar light.

These spectra were recorded in anaerobic conditions. NCN-CN_x* absorption spectrum in a DES-TEOA solution (blue) was recorded in air after irradiation.

From determining that the NCN-CN_x* species can be isolated without being quenched by molecular O₂, it was necessary to gain an understanding of the chemical properties of the solvents which hinder the quenching of the photocatalyst.

Microwire chronoamperometry is an electroanalytical technique that can be used to simultaneously determine the concentration of dissolved O₂ and the diffusion coefficient of O₂ in solution.³⁸ Using a microcylindrical electrode (defined as a working electrode with a dimension smaller than 50 μm),³⁹ transient decays of experimental currents obtained from potential step chronoamperometry can be fitted to the theoretical Shoub-Szabo Equation.⁴⁰ In a single step chronoamperometry experiment, the potential applied to the working electrode is stepped from a value where no reaction occurs, to one where reduction (or oxidation) occurs at a mass transport-controlled rate. The current measured is explained by:

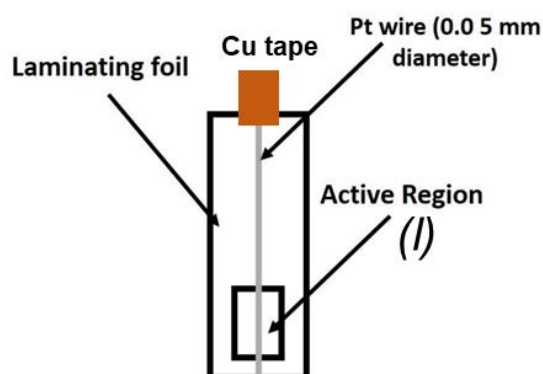
$$I_{\text{theo}}(t) = nFIDc \times \left(\frac{\pi \times e^{-\frac{2}{5} \times \sqrt{\pi \frac{Dt}{16r^2}}}}{4 \sqrt{\pi \frac{Dt}{16r^2}}} + \frac{\pi}{\ln \left[\sqrt{\left(64 \times e^{-0.5772 \times \frac{Dt}{16r^2}} \right) + e^{\frac{5}{3}}} \right]} \right) \quad (3.04)$$

where I_{theo} is the measured current in amperes, F is Faraday's constant, r is the microwire electrode radius in metres, n is the number of electrons participating in the reduction or oxidation reaction and c and D are the concentration and diffusion coefficient of the analyte, respectively. Microelectrodes allow this phenomenon to occur due to their large diffusion layers relative to the electrode surface. Mass transport of the electroactive species is varied from the linear diffusion to steady state diffusion over short time periods, and the switch in diffusion regime allows unknown variables in the equation to be determined.³⁸ Moreover, when electrodes are miniaturised currents become smaller but result in an increase in the current density, and the mass transport of electroactive species is changed from traditional linear diffusion to multi-dimensional diffusion.³⁹ The properties of microelectrodes therefore allows them to be employed in non-traditional solvents. In conventional

electrolytes, the polar nature of the solvent ensures high conductivity with little ohmic resistance in the solution. When nonpolar solvents are used, the ohmic resistance drastically increases. However, the properties of microelectrodes reduces the ohmic resistance in extremely diminished electrolytic solutions, with studies showing that at diffusion controlled currents the ohmic potential drop is no longer dependent on the size and geometry of the microelectrode, but solely on the properties of the electrolyte.⁴¹⁻⁴⁴

Microelectrodes and the theory derived from them has previously been applied to determine the electrochemical behaviour of ferrocene in glyceline and ethaline, and found that the diffusion of the ferrocenium ion in glyceline was an order of magnitude lower glyceline than in ethaline ($3.2 \times 10^{-8} \text{ m}^2 \text{ s}^{-1}$ versus $3.9 \times 10^{-9} \text{ m}^2 \text{ s}^{-1}$, respectively), which was attributed to glyceline's higher viscosity.⁴⁵ Microdisc electrodes have also been applied for the simultaneous determination of the diffusion coefficient and concentration of O_2 in ionic liquids which showed that the diffusivity of O_2 generally increases as the viscosity of the IL decreases.⁴⁶ Microwire chronoamperometry has never been employed to determine the diffusion coefficient and concentration of O_2 in deep eutectic solvents. As photocatalysts which are air-sensitive can exhibit tolerance to O_2 and perform photocatalytic proton reduction in the presence of O_2 , it was necessary to gain an understanding of the chemical behaviour of O_2 in the solvents tested for photocatalysis.

The Pt microwire electrode used in this work was fabricated at the University of Bath by Professor Frank Marken. A Pt microwire electrode was fabricated according to a literature procedure, whereby Pt wire with a known diameter ($50 \mu\text{m}$) was placed between laminating paper with a rectangular window cut out to expose the wire.^{38,47} (See Methods and Materials for full experimental information). A schematic of the electrode is presented below (Scheme 3.02).



Scheme 3.02. Schematic depicting the as-constructed microwire Pt electrode. The active region with unknown length (l) is the only section of the Pt wire which is exposed to the electrolyte. The microwire electrode was made by Professor Frank Marken at the University of Bath.

When constructed, the precise length (l) of the active region was unknown and had to be calibrated electrochemically using aqueous $K_4[Fe(CN)_6]$ (see Materials and Methods for full experimental procedure). Using a three electrode setup with the microwire Pt electrode as a working electrode, Ag/AgCl as a reference electrode and Pt mesh as a counter electrode, cyclic voltammetry (CV) was used to determine the stability and efficiency of the working electrode. The voltammogram in Figure 3.14 shows both a reduction and an oxidation wave, which is attributed to the well-known redox couple of the $[Fe(CN)_6]^{4-}$ and $[Fe(CN)_6]^{3-}$ ions.

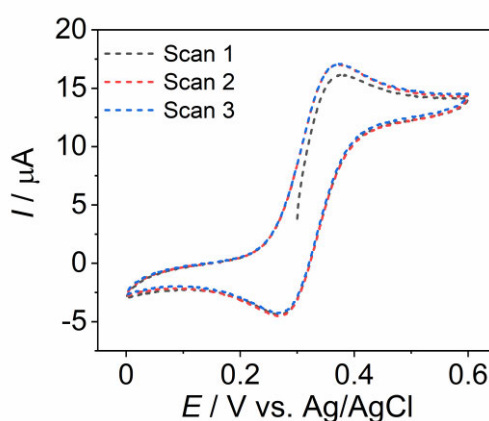


Figure 3.14. Cyclic voltammogram of 5.0 mM $K_4[Fe(CN)_6]$ in 1 M NaCl. Conditions: Pt microwire working electrode, Ag/AgCl reference electrode, Pt mesh counter electrode, 25 °C, scan rate = 50 mV s⁻¹

An aqueous solution containing a known concentration of $K_4[Fe(CN)_6]$ and NaCl to act as an electrolyte is used to calibrate the length of the electrode as the diffusion

coefficient of the $[\text{Fe}(\text{CN})_6]^{4-}$ ion in water is known to be $6.5 \times 10^{-8} \text{ m}^2 \text{ s}^{-1}$ at $25 \text{ }^\circ\text{C}$.⁴⁸ From this, the only unknown variable of the Shoup-Szabo equation is l . As such, potential step chronoamperometry was used to determine the current decay at the Pt microwire electrode. The potential was stepped from 0.0 V to $0.6 \text{ V vs. Ag/AgCl}$ to ensure enough energy was supplied to counteract overpotential effects. The current decay observed with the experimentally obtained current was fitted to the theoretical equation in equation (3.04) to optimise the value of l . Chronoamperograms were recorded 3 times and the concatenated fit of the three scans to the equation to the current decay is shown in Figure 3.15.

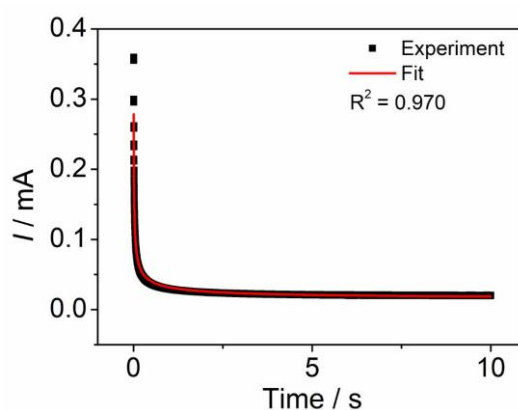


Figure 3.15. Experimental ferricyanide oxidation current decay from stepped-potential chronoamperometry at Pt microwire electrode (black trace) and concatenated fit with Equation 3.04 for determination of electrode length (red trace). Conditions: $\text{K}_4[\text{Fe}(\text{CN})_6]$ (5 mM), NaCl (1 M), Pt microwire working electrode, Ag/AgCl reference electrode, Pt mesh counter electrode, potential step from 0.0 V to $0.6 \text{ V vs. Ag/AgCl}$ after 10 seconds. with 2 ms sampling time, $25 \text{ }^\circ\text{C}$

From the optimised fitting of the unknown length parameter, the length can be determined with great approximation – in this case the length of the active region of the Pt microwire electrode was found to be 3.80 cm.

After determining the length, the electrode could then be used to find unknown values of the diffusion coefficients and concentrations of analytes in solution, namely the diffusion and concentration of O_2 in the DESs tested for photocatalysis.

3.5.3. Simultaneous Determination of Diffusion Coefficient and Concentration of Oxygen in DESs.

In a similar manner to electrode length calibration, the unknown values of the diffusion coefficient, D , and concentration, c , were found using potential step chronoamperometry. First, CV was performed in the solvents identical to those tested for photocatalysis in aerobic conditions to find the reduction potential of O_2 . The CV recorded in 82.5% vol. reline shows the reduction of O_2 in Figure 3.16. After determining the reduction potential, potential step chronoamperometry was then employed and the current traces fitted to find the values of D and c for O_2 .

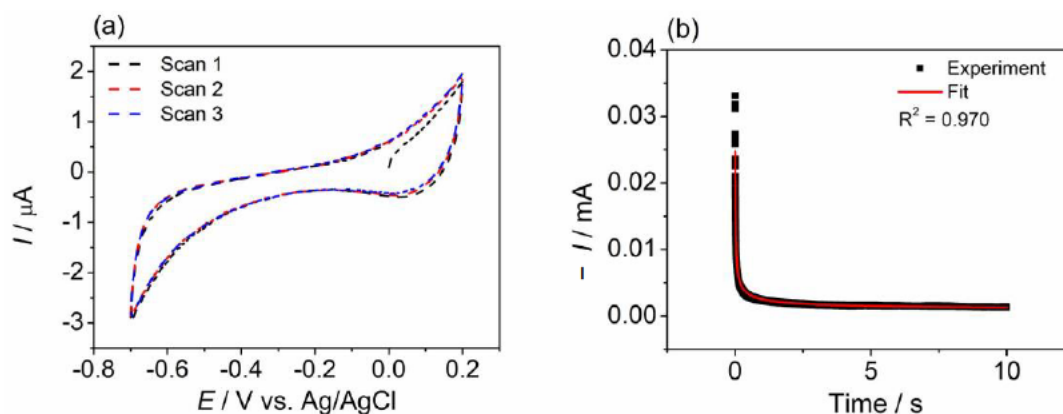


Figure 3.16. (a) Cyclic voltammogram of O_2 at Pt microwire electrode in 82.5% vol. reline containing 0.4 M TEOA, identical to photocatalytic solvent conditions. Conditions: 82.5% vol. reline, 0.4 M TEOA, 15.0 mL, Pt microwire working electrode, Ag/AgCl reference electrode, Pt mesh counter electrode, 40 °C, scan rate = 50 mV s⁻¹. (b) Experimental current decay of O_2 from potential step chronoamperometry at Pt microwire electrode (black trace) in 82.5% vol. reline containing 0.4 M TEOA and concatenated fit of 3 experimental chronoamperograms to Eqn. 3.04 for determination of diffusion coefficient and concentration of dissolved O_2 . Conditions: 82.5% vol. reline, TEOA (0.4 M), 15.0 mL, Pt microwire working electrode, Ag/AgCl reference electrode, Pt mesh counter electrode, potential step from 0.2 V to (-0.8) V vs. Ag/AgCl after 10 seconds with 2 ms sampling time, 40 °C.

Optimising fitting of the diffusion coefficient and concentration parameters of the Shoub-Szabo equation to the experimentally observed current produced values for both D and c of dissolved O_2 in the solution, which were found to be $2.93 \pm 0.02 \times 10^{-10} \text{ m}^2 \text{ s}^{-1}$ and $168 \pm 0.91 \text{ } \mu\text{M}$. It should be noted that the potential step applied at the electrode is a reducing step from 0.2 V to -0.8 V vs. Ag/AgCl which yielded a negative current. The current trace shown here is the experimentally obtained values multiplied by (-1) to yield an inverted current trace. This was done to simplify

fitting of the concatenated current traces to the equation. To accurately fit the experimental current, it was necessary to discard the first 40 ms of the obtained current trace for all chronoamperograms (first 20 datapoints). This was done to mitigate the double layer charging effects perturbing the current at initial timepoints, and to remove datapoints on the current trace associated with the reduction of protons, as these will appear earliest in the current trace (due to the final applied potential).³⁸

The same procedure was then repeated for the other DES-based solvents tested for air-tolerant photocatalysis, with the cyclic voltammograms of the Pt microwire electrode recorded in 82.5% vol. ethaline and 82.5% vol. glyceline, both containing 0.4 M TEOA. Again, these solvent compositions were those tested for air-tolerant photocatalysis. The results of the cyclic voltammetry experiments and the potential step chronoamperometry are shown in Figure 3.17 and Figure 3.18, respectively.

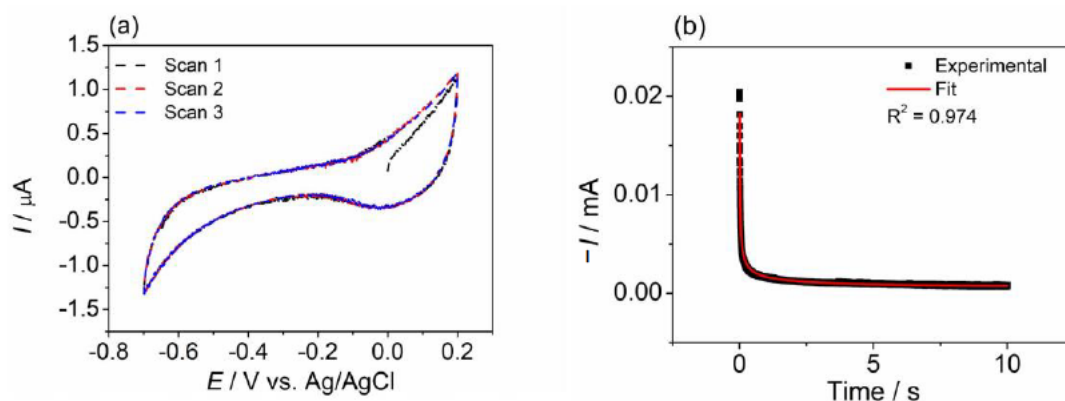


Figure 3.17. (a) 3 scan cyclic voltammogram at Pt microwire electrode in 82.5% vol. glyceline with 0.4 M TEOA, identical to photocatalytic conditions. Conditions: 82.5% vol. glyceline, 0.4 M TEOA, 15.0 mL, Pt microwire working electrode, Ag/AgCl reference electrode, Pt mesh counter electrode, 40 °C, scan rate = 50 mV s⁻¹ (b) Experimental current decay from potential step chronoamperometry at Pt microwire electrode (black trace) in 82.5% vol. glyceline with 0.4 M TEOA and concatenated fit of 3 experimental chronoamperograms to the Shoup-Szabo equation for determination of diffusion coefficient and concentration of dissolved O₂. Conditions: 82.5% glyceline, TEOA (0.4 M), 15.0 mL Pt microwire working electrode, Ag/AgCl reference electrode, Pt mesh counter electrode, potential step from 0.2 V to (-0.8) V vs. Ag/AgCl after 10 seconds with 2 ms sampling time, 40 °C.

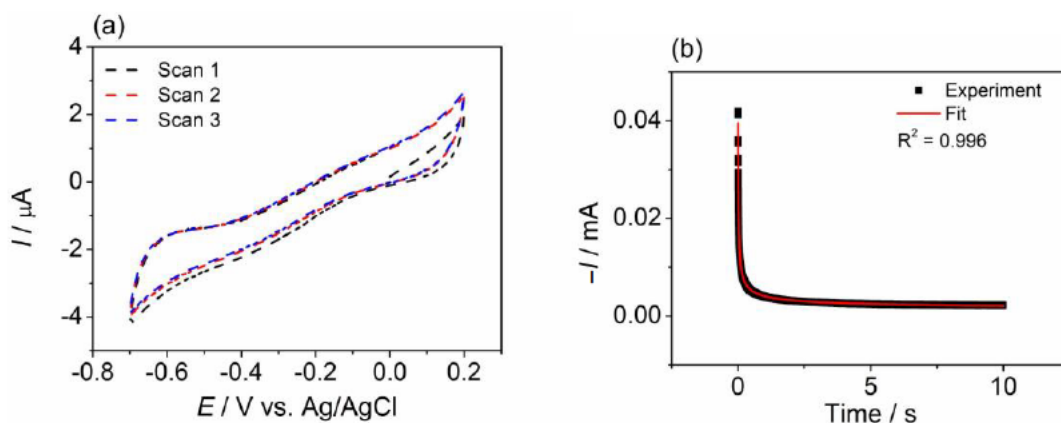


Figure 3.18. (a) 3 scan cyclic voltammogram at Pt microwire electrode in 82.5% vol. ethaline with 0.4 M TEOA, identical to photocatalytic conditions. Conditions: 82.5% vol. ethaline, 0.4 M TEOA, Pt microwire working electrode, Ag/AgCl reference electrode, Pt mesh counter electrode, 40 °C, scan rate = 50 mV s⁻¹ (b) Experimental current decay from potential step chronoamperometry at Pt microwire electrode (black trace) in 82.5% vol. ethaline with 0.4 M TEOA and concatenated fit of 3 experimental chronoamperograms to the Shoup-Szabo equation for determination of diffusion coefficient and concentration of dissolved O₂. Conditions: 82.5% vol. ethaline, TEOA (0.4 M), 15.0 mL, Pt microwire working electrode, Ag/AgCl reference electrode, Pt mesh counter electrode, potential step from 0.2 V to (-0.8) V vs. Ag/AgCl after 10 seconds. with 2 ms sampling time, 40 °C.

For an aqueous 0.4 M TEOA pH = 7.0 solution, the diffusion coefficient and concentration of O₂ was also determined to show the comparison of the behaviour of O₂ in DESs to water. Figure 3.19 shows the CV and the chronoamperometric current decay resulting from the potential step obtained in water.

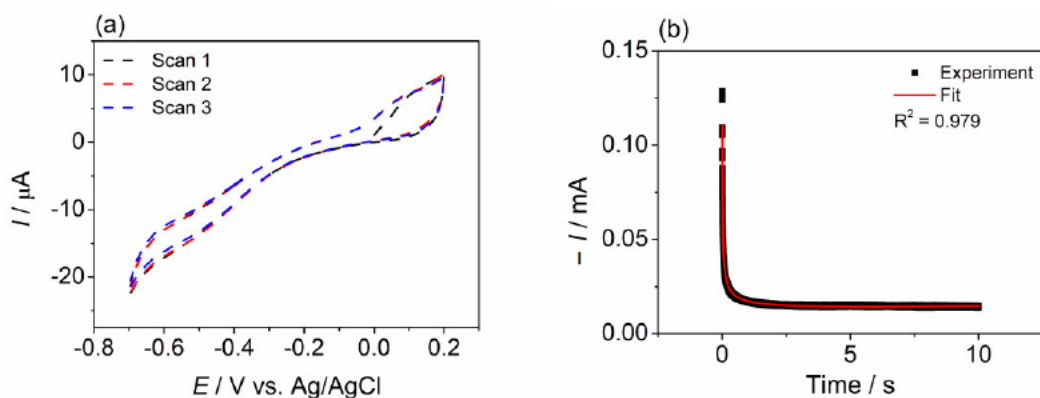


Figure 3.19. (a) 3 scan cyclic voltammogram at Pt microwire electrode in 0.4 M TEOA pH 7.0, identical to photocatalytic conditions. Conditions: 0.4 M TEOA pH 7.0, 15.0 mL, Pt microwire working electrode, Ag/AgCl reference electrode, Pt mesh counter electrode, 40 °C, scan rate = 50 mV s⁻¹ (b) Experimental current decay from potential step chronoamperometry at Pt microwire electrode (black trace) in 0.4 M TEOA pH 7.0, and c concatenated fit of 3 experimental chronoamperograms to theoretical equation for determination of diffusion coefficient and concentration of dissolved O₂. Conditions: 0.4 M TEOA pH 7.0, 15.0 mL, Pt microwire working electrode, Ag/AgCl reference electrode, Pt mesh counter electrode, potential step from 0.2 V to (-0.8) V vs. Ag/AgCl after 10 seconds. with 2 ms sampling time, 40 °C.

From the current decay profile resulting from potential step chronoamperometry, the D and c values obtained are the optimal values to fit the concatenated experimental chronoamperometric scans. The results from the optimised D and c parameters are shown in Table 3.02.

Table 3.02. O_2 solubility and diffusivity in different solvents determined by microwire chronoamperometry and observed O_2 tolerance during photocatalytic H_2 generation in these solvents. Conditions: DES (82.5% vol. DES, 0.4 M TEOA, 2 mM MV) or water (0.4 M TEOA, pH 7), 40 °C; photocatalysis: NCN-CN_x (2.0 mg), H_2PtCl_6 (0.05 mg Pt) in 2.0 mL solvent, (AM 1.5G, 1 sun, constant air or N_2 purge)

Solvent	$c(O_2)$ μM	$D(O_2)$ $m^2 s^{-1}$	O_2 Tolerance %
Reline	167.8±0.9	$2.93 \pm 0.02 \times 10^{-10}$	89.3±6.1
Glyceline	218.8±2.0	$9.52 \pm 0.01 \times 10^{-11}$	90.4±7.9
Ethaline	250.7±0.4	$3.32 \pm 0.01 \times 10^{-10}$	73.5±9.0
H_2O	223.5±0.4	$2.94 \pm 0.02 \times 10^{-9}$	8.8±1.5

It is evident that all DESs were electrochemically determined to have O_2 diffusion coefficients about an order magnitude lower than that of water. This can be thought of as a result of the much higher viscosities of DESs, slowing the transport of O_2 in solution. It can be seen, from comparing trends of the diffusion coefficient to the O_2 tolerance, the much slower diffusivity of O_2 in the DESs enhances the O_2 tolerance of the photocatalyst for solar H_2 evolution. In addition, the concentration of dissolved O_2 also has an effect on the O_2 tolerance as evidenced from concentration of O_2 in reline and ethaline – while these solvents possess comparable diffusivities of molecular O_2 , reline shows a much lower concentration of dissolved O_2 which is thought to enhance O_2 tolerance, as a lower concentration of O_2 infers less O_2 available to compete with protons for photogenerated electrons. Moreover, while reline and glyceline exhibit similar O_2 tolerances, there is a notable difference in concentration and diffusivity between the solvents, with glyceline possessing a slower diffusivity. Diffusion of O_2 *in situ* will obviously impact photocatalytic O_2 tolerance, as a slower transport of O_2 in the solution to catalytically active sites prevents O_2 from interacting and reacting with the sites in question. As such, O_2

tolerance can both be controlled by tuning the concentration and diffusivity of dissolved O₂.

The concentration of O₂ can be tuned through the ionic strength of a solution. Because the choline chloride based DESs used here are constructed through the interaction of a chloride ion to a hydrogen bond network, the number of ions present in solution is high which can lower the concentration of dissolved O₂ through a phenomenon known as the salting out effect. By increasing the ionic strength through the salt concentration, the amount of dissolved analytes in solution, particularly gases, can be lowered.⁴⁹ From knowing that the concentration of O₂ influences photocatalytic O₂ tolerance it was necessary to perform experiments to corroborate the influence of *c* and *D* on the O₂ tolerance.

Saline water is known to have a lower concentration of dissolved O₂ as a result of the salting out effect.⁵⁰ As such, a series of NaCl solutions of varying concentrations were tested as reaction media with NCN-CN_x for photocatalytic H₂ evolution (Figure 3.20). NCN-CN_x in 1 M NaCl using sacrificial TEOA with a redox mediator was irradiated in both an inert and aerobic atmosphere. In an inert atmosphere, NCN-CN_x produced 26.9±3.4 μmol_{H2} after 14 hours whilst the same catalyst produced 3.7±0.8 μmol_{H2} in air, correlating to a photocatalytic O₂ tolerance of 13.9±3.3%. Further increasing the NaCl concentration further increased the O₂ tolerance and aerobic H₂ evolution performance. NCN-CN_x in a 2 M NaCl and 4 M NaCl solution under nitrogen produced 29.0±1.3 μmol_{H2} and 29.3±0.9 μmol_{H2} respectively after 14 hours continuous irradiation, whilst an aerobic atmosphere yielded 6.9±3.0 μmol_{H2} in 2 M NaCl and 10.0±1.3 μmol_{H2} in 4 M NaCl.

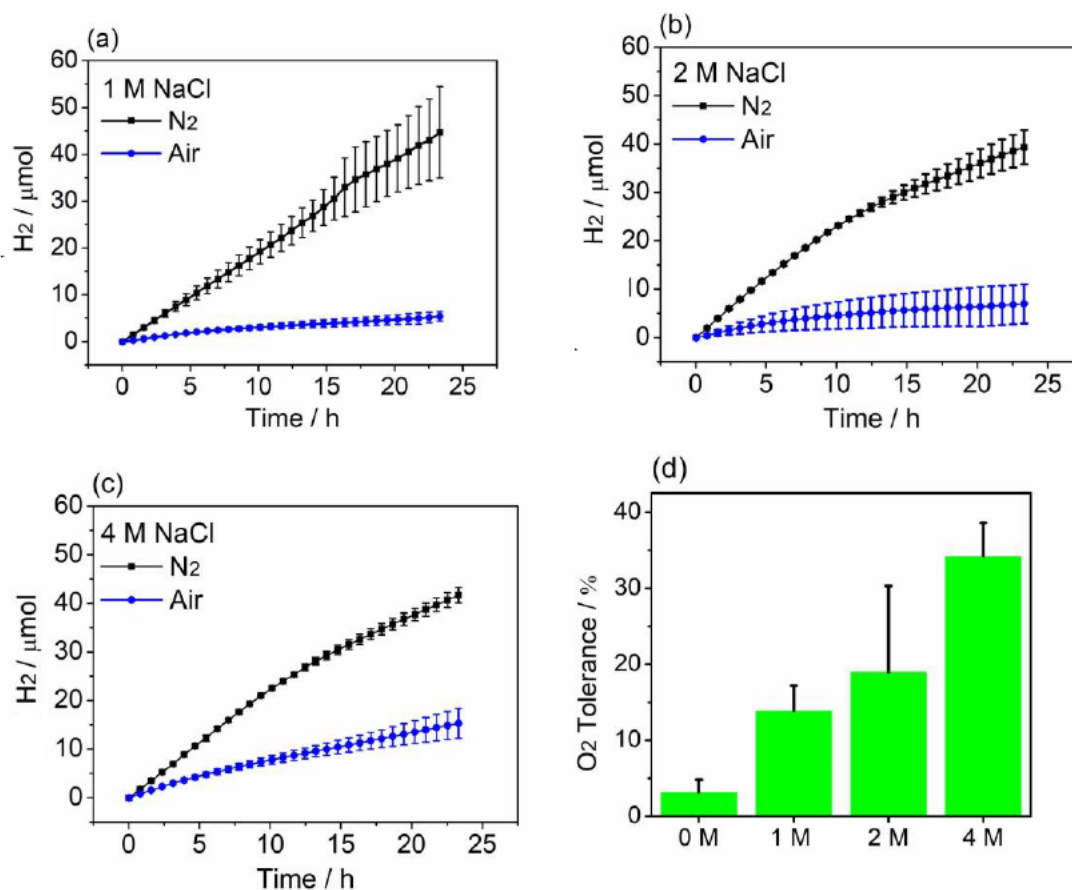


Figure 3.20. Photocatalytic H₂ production in brine solutions of varying concentrations examined under inert and aerobic atmospheres, (a) 1 M NaCl (b) 2 M NaCl and (c) 4 M NaCl and O₂ tolerance of NCN-CN_x after 14 hours irradiation. Conditions: NCN-CN_x (2.0 mg), H₂PtCl₆ (0.05 mg Pt), TEOA (0.4 M), methyl viologen (2 mM), NaCl (1, 2 or 4 M), in H₂O (2.00 mL, pH 7.0), AM 1.5G, 1 sun, 40 °C, constant N₂ or air purge.

Knowing that increasing NaCl concentration increased photocatalytic O₂ tolerance, the saline solutions were also tested to electrochemically ascertain concentration and diffusion coefficients of O₂ using microwire chronoamperometry. Shown in Table 3.03 are the optimised values of *D* and *c* to create the non-linear fit for the experimental chronoamperometric current traces.

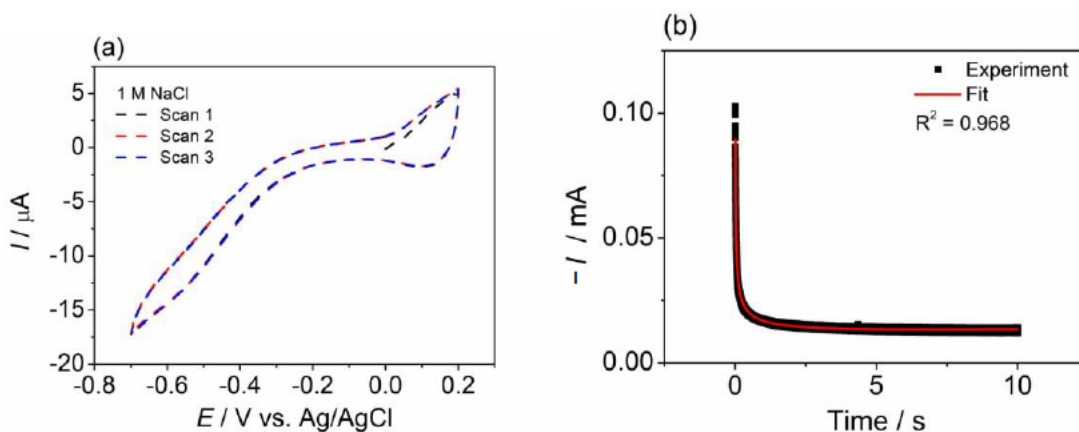


Figure 3.21. (a) 3 scan cyclic voltammogram at Pt microwire electrode in 1 M NaCl identical to photocatalytic conditions. Conditions: NaCl (1 M), TEOA (0.4 M), pH 7.0, 15.0 mL, Pt microwire working electrode, Ag/AgCl reference electrode, Pt mesh counter electrode, 40 °C, scan rate = 50 mV s⁻¹. (b) Experimental current decay from potential step chronoamperometry at Pt microwire electrode (black trace) and c concatenated fit of 3 experimental chronoamperograms to the Shoup-Szabo equation for determination of diffusion coefficient and concentration of dissolved O₂. Conditions: NaCl (1 M) 0.4 M TEOA pH 7.0, 15.0 mL, Pt microwire working electrode, Ag/AgCl reference electrode, Pt mesh counter electrode, potential step from 0.2 V to (-0.8) V vs. Ag/AgCl after 10 seconds. with 2 ms sampling time, 40 °C.

Table 3.03. O₂ solubility and diffusivity in brines of different concentration and observed O₂ tolerance during photocatalytic H₂ generation. Conditions: NCN-CN_x (2.0 mg), H₂PtCl₆ (0.05 mg Pt) in 2.0 mL water (0.4 M TEOA, pH 7, 2 mM MV); (AM 1.5G, 1 sun, 40 °C, constant nitrogen and air purge)

Solvent	c(O ₂) μM	D(O ₂) m ² s ⁻¹	O ₂ Tolerance %
0 M NaCl	223±0.4	2.94±0.01 × 10 ⁻⁹	3.1±1.7
1 M NaCl	265±0.6	2.30±0.01 × 10 ⁻⁹	13.9±3.3
2 M NaCl	165±0.2	1.55±0.01 × 10 ⁻⁹	19.0±11.4
4 M NaCl	128±0.3	1.13±0.02 × 10 ⁻⁹	34.2±4.4

These results show that diminishing the diffusivity of O₂ aids in increasing O₂ tolerance, with diffusivity and concentration decreasing by around 50%. Moreover, whilst increasing salinity can decrease the diffusivity notably, the diffusion coefficients in aqueous solutions here are still ~10 times higher than those seen in DESs. This indicates lowering diffusivity of molecular O₂ in the solution is a key physical property for solvents to aid in augmenting aerobic photocatalytic O₂ tolerance. It is apparent from the results that pairing low diffusivity with low O₂

concentration is decisive when considering reaction conditions for hydrogen evolution in aerobic conditions.

3.5.4. Rationalising Oxygen Tolerance from a Mechanistic Perspective

Having identified that a low concentration and a low diffusion coefficient aid in increasing photocatalytic H₂ evolution in aerobic conditions, it is necessary to understand the role which both concentration and diffusion play in the mechanism at the photocatalyst.

The rate of hydrogen generation, R_{H2} is assumed to be a function of the available charge carriers, assuming all available charge carriers are used to generate hydrogen:

$$R_{H_2} = R_{hv} \quad (3.05)$$

An O₂ tolerance of unity is obtained when all available charge carriers can generate hydrogen in the presence of O₂. Therefore, O₂ tolerance can be expressed as:

$$O_2 \text{ Tolerance} = 1 \times \frac{R_{H_2}}{R_{hv}} \quad (3.06)$$

If O₂ is available to interact with charge carriers, charge carriers will more favourably be quenched by O₂ than be used for H₂ generation. The rate at which O₂ quenches available charge carriers, R_{O2}, therefore determines how many charge carriers are left for H₂ generation:

$$R_{H_2} = R_{hv} - R_{O_2} \quad (3.07)$$

If the rate of hydrogen generation decreased assuming a constant rate of charge carrier generation, O₂ tolerance will decrease. Substituting R_{H2} in equation (3.07) for equation (3.06) yields the expression:

$$O_2 \text{ Tolerance (\%)} = 100 \times \frac{R_{hv} - R_{O_2}}{R_{hv}} \quad (3.08)$$

$$O_2 \text{ Tolerance (\%)} = 100 \times \left(1 - \frac{R_{O_2}}{R_{hv}}\right) \quad (3.09)$$

The rate of charge carrier quenching by O₂ at the photocatalyst surface can be quantitatively assessed by treating a photocatalyst particle as a spherical electrode at which O₂ is electrochemically reduced under diffusion limitation with the following equation:⁴¹

$$R_{O_2} = 4\pi \times n \times r \times D_{O_2} \times c_{O_2} \quad (3.10)$$

where R_{O₂} is the rate of O₂ reduction, n is the number of electrons quenched per molecule of O₂, r is the particle radius, and D_{O₂} and c_{O₂} are the diffusion coefficient and concentration of O₂, respectively.

Substituting R_{O₂} in equation (3.10) for equation (3.09) shows how O₂ tolerance can be expressed as a function of D_{O₂} and c_{O₂}:

$$O_2 \text{ Tolerance (\%)} = 100 \times \left(1 - \frac{4\pi \times n \times r \times D_{O_2} \times c_{O_2}}{R_{hv}}\right) \quad (3.11)$$

$$O_2 \text{ Tolerance (\%)} = 100 - \frac{4\pi nr}{R_{hv}} (D_{O_2} \times c_{O_2}) \quad (3.12)$$

Equation (3.12) can be plotted as a linear equation, with O₂ tolerance as a function of D_{O₂} and c_{O₂}.

From the electrochemically obtained D_{O₂} and c_{O₂} values of the solvents, and the photocatalytically obtained O₂ tolerances, a graph can be plotted which emphasises the effect of low values D_{O₂} and c_{O₂}. This is highlight in Figure 3.22 below.

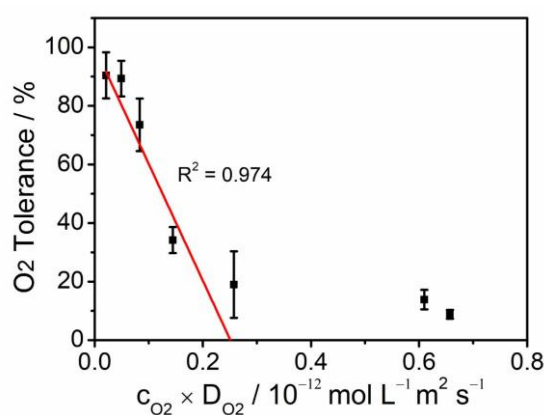


Figure 3.22. Plot of the O₂ tolerance for H₂ evolution versus the product of D_{O₂} and c_{O₂} in the respective reaction medium fitted according to equation (3.12).

This plot shows that decreasing the diffusion coefficient and concentration of O_2 in solution leads to an increase in O_2 tolerance. Intuitively, this makes sense – when no O_2 is present in solution ($c_{O_2} = 0$) the “tolerance” of the catalyst to O_2 is unity. Likewise, if O_2 in solution does not diffuse ($D_{O_2} = 0$) to the catalyst, the dissolved O_2 will not interact with photogenerated charge carriers on the photocatalyst surface, enabling the catalyst to reduce protons and evolve hydrogen. Figure 3.22 also shows that the experimentally obtained O_2 tolerances coincide well with the mathematical model proposed, with those values with low O_2 tolerances – and therefore high c and D parameters – not considered part of the fit. This is interpreted as a result of the different nature of O_2 flux in the solutions. At low values of c and D for O_2 , the O_2 tolerance can be thought of as being diffusion controlled. This is because diffusion is the limiting factor in this situation as any O_2 which is dissolved in solution is not mobile enough to interact with the photogenerated charge carriers. At high values of c and D , where O_2 tolerance is low, the O_2 tolerance can be thought of as being kinetically controlled, meaning Equation 3.10 (and therefore Equation 3.12) no longer applies. In this case, the limiting cause of O_2 tolerance results from the redox processes associated with O_2 reduction and the kinetic challenges associated with O_2 reduction. For this model to be true, we also consider that proton flux is not limited in the solutions due to the smaller size of protons.

3.6. Discussion

From showing that low diffusivity and concentration, particularly coupled together in tandem, can enhance photocatalytic hydrogen evolution in the presence of air, it is possible to rationalise conditions which are applicable to other reaction systems and photocatalysts. Tuning the solvent medium rather than catalyst re-design to enhance photocatalysis may be achieved using some key criteria, based on eqn. 12.

- Increasing the rate of charge carrier flux
- Lowering the diffusivity and concentration of dissolved O_2
- Decreasing the particle radius r

Some considerations should be made for these criteria. Increasing the charge carrier flux to the particle surface can be produced from a few methods, namely by

enhancing charge separation. The rate of charge carrier flux may also be enhanced through an increase in light intensity. Lowering the diffusivity may be realised through increasing viscosity, but a further increase in viscosity may result in lowering of proton flux, decreasing the H₂ evolution activity. The decrease in particle size may also lead to an increase in the bandgap of the semiconductor as a result of quantum confinement.

The results show that O₂ tolerance can be increased simply through solvent tuning. As has been discussed, a high degree of focus on increasing the O₂ tolerance comes from catalyst engineering and introducing constructs / layers onto catalysts which can increase the cost and limit scalability for solar fuel production. Some work in the literature where H₂ was produced in both inert and aerobic conditions is shown in Table 3.04. Despite some high values obtained for the O₂ tolerances for some materials, considerations must be given to the experimental setup. A Ni₂P/CdS photocatalyst was tested in inert and aerobic conditions for H₂ evolution, and after 3 hours showed an O₂ tolerance of 46.1%.⁵¹ Co-catalytic MoS₂ nanosheets on a CdS photocatalyst was shown to exhibit an O₂ tolerance of 61.9%, while a highly active CoP/CdS photocatalyst was stated to retain 79.8% of its original photocatalytic H₂ production activity in air versus N₂.^{52, 53} These photocatalysts are known to be very active for H₂ evolution and were carried out using potent hole scavengers, which aids in increasing activity. Moreover, the reactions were carried out in closed reaction chambers. This indicates that any O₂ present will be reduced irreversibly and not be replenished. Any O₂ reduced depletes the O₂ concentration, and so once O₂ has been consumed, charge carriers are free to reduce protons. A molecular system of CoP/EY also showed O₂ tolerance of 70±4% in a closed reaction chamber.⁵⁴ RuP/CoP co-catalysts have also been tested for their O₂ tolerance coupled to a TiO₂ light absorber, with a low O₂ tolerance of 17% reported for the catalytic system.⁵⁵ Other molecular systems containing Ru as the photosensitiser have also reported values for O₂ tolerance. Zhao and co-workers reported [Ru(bpy)₃]²⁺ coupled to a Co complex with a DPA-Bpy ligand showed O₂ tolerance of 40%.⁵⁶ Rau and co-workers showed that a Ru(imidazolium) chromophore and a cobaloxime catalyst in tandem, called Ru(mmip)[PF₆]₃/ Co(dmgh)₂ was active in air for photocatalytic H₂ evolution – the photocatalyst first reduced O₂ in situ and then

showed proton reduction performance.⁵⁷ The same group reported similar behaviour for [Ru(dnbpy)(tbbpy)₂](PF₆)₂/ [Co(dmgh)₂], whereby O₂ reduction in a closed chamber occurred before the onset of proton reduction.⁵⁸ The novelty of the work presented in this chapter shows that even when O₂ is continuously applied to the reaction system, H₂ evolution can still occur at a high rate versus completely inert conditions. This demonstrates that solvent effects can themselves act as a barrier for photocatalytic systems and there is no need for catalyst modifications to render them O₂ tolerant, and O₂ tolerance can be induced through simple solvent design. This also showcases to date the only example of O₂ tolerance of a carbon nitride photocatalyst in the literature.

Table 3.04. Examples of O₂-tolerant photocatalysts for H₂ evolution in the literature

Photocatalyst	O ₂ Tolerance	Flow Type	Reference number
CdS	167.8±0.9	Sealed Chamber	5
Ni ₂ /CdS	46,1%	Closed Chamber	51
MoS ₂ /CdS	61.9%	Closed Chamber	52
CoP/CdS	79.5%	Closed Chamber	53
CoP/EY	70±4%	Closed Chamber	54
RuP/CoP/TiO ₂	17%	Closed Chamber	55
[Ru(bpy ₃)] ²⁺ /[Co(DPA-bpy)(H ₂ O)](PF ₆) ₃	40%	Closed chamber	56
Ru(mmip)[PF ₆] ₃ /Co(dmgh) ₂	n/a	Closed chamber O ₂ reduction occurred in situ	57
[Ru(dnbpy)(tbbpy) ₂](PF ₆) ₂ /[Co(dmgh) ₂]	n/a	Closed chamber O ₂ reduction occurred in situ	58

3.7. Conclusions

DEs have shown to provide a suitable reaction medium for solar H₂ evolution at a Pt/NCN-CN_x photocatalyst in aerobic conditions. This catalyst is known to be intolerant to O₂ and H₂ evolution in water under aerobic conditions shows this. The photocatalytic H₂ production in air can be increased in the type III DEs tested with a >90% retention of activity in air versus N₂ in some cases. The O₂ tolerance is shown to occur over prolonged irradiation periods. The reduced photocatalytic state can be maintained in an aerobic environment in DEs, without being quenched by atmospheric O₂ as a result of the solvent, and this reduced state can be probed with UV-Vis spectroscopy. Microwire chronoamperometry can be used to electrochemically analyse the DEs to simultaneously determine the diffusion coefficient and concentration of dissolved O₂ in the solvents. Analyses was carried out with a Pt microwire electrode, which was shown to have been successfully made, with the length of the electrode determined through potential step chronoamperometry. Potential step chronoamperometry also shows that the DEs possess a much lower O₂ diffusion coefficient relative to water, with some DEs also showing a lower dissolved O₂ concentration. By comparing trends in the diffusion coefficient and concentration of O₂ to the photocatalytically observed O₂ tolerance, it can be rationalised that low concentrations and diffusion coefficients aid in increasing the aerobic H₂ evolution activity of the catalyst. Through this, solvents can be designed to have low O₂ diffusion and concentration – this was achieved through saline solutions of varying NaCl concentration. By increasing the salinity, and subsequently lowering the O₂ diffusion and concentration, the O₂ tolerance of the photocatalyst was also shown to increase. From this, a mechanistic model was constructed which showed that O₂ tolerance as a function of diffusion and concentration of O₂ was in good agreement with experimentally observed photocatalytic O₂ tolerances. This mechanistic model also aids suggests design criteria for realising systems with enhanced O₂ tolerance to aid in producing hydrogen under aerobic conditions without any catalytic modifications.

3.8. Methods and Materials

Chemical Reagents

All chemical reagents used for this work were used as purchased and without further purification. Choline chloride (>99%), urea (analytical grade, 99.5%), ethylene glycol (>99%), glycerol (>99%), Titanium (iv) oxide (P25, Aeroxide®) triethanolamine (>98%), Eosin Y, disodium salt (certified pure), sodium chloride (>99%), potassium ferrocyanide trihydrate (crystalline, certified pure), hydrochloric acid (37.0% w/w, extra pure) were all purchased from Fisher Scientific. 18.2 mΩ water was used throughout the experiments. Pt microwire ($d = 50 \mu\text{m}$, 99.99%) was purchased from Advent UK.

Photocatalytic H₂ Generation in DESs in Inert and Aerobic Conditions

NCN-CN_x (2.0 mg, unless otherwise stated) was transferred into a glass sample vial (Chromacol 10-SV, Fisher) along with the reagent solution (2.0 mL unless otherwise stated). Samples were capped with rubber septa, briefly vortexed, and agitated in a sonic bath for 20 minutes. Samples analysed under N₂ were purged for 10 minutes prior to irradiation to de-aerate the solution. Samples were irradiated using a solar light simulator (Thermo Oriel 92194-1000) equipped with an AM 1.5G filter (Newport) with an intensity of 1 sun. Samples were mounted in a water bath maintained at 40 °C and stirred at 800 RPM. The sample headspace was subject to a constant purge of N₂ or air at a rate of 4 mL min⁻¹ controlled by a mass flow controller (Bronkhorst). H₂ evolution was monitored by gas chromatography (Shimadzu Nexis 2030) using an auto-sampler programmed to inject 2 mL of the selected headspace stream. Experiments using Eosin Y were performed in the same manner using Eosin Y (2 mM) instead of NCN-CN_x.

Synthesis of Deep Eutectic Solvents

Reline, glyceline and ethaline were prepared in accordance with literature procedures, by stirring choline chloride with urea, glycerol, and ethylene glycol, respectively in a 1:2 molar ratio at 80 °C until a homogenous liquid had formed.^{59, 60}

Treatment of data

All photocatalysis, dye degradation and electrochemistry measurements were performed in triplicate and are given as the unweighted mean \pm standard deviation (σ). σ of a measured value was calculated using equation (3.13), where n is the number of repeated measurements, x is the value of a single measurement and \bar{x} is the unweighted mean of the measurements.

$$\sigma = \sqrt{\frac{\sum(x - \bar{x})^2}{n - 1}} \quad (3.13)$$

Physical Measurements

Sample Analysis by Gas Chromatography (GC). Gas chromatography was performed on a Shimadzu Nexis GC-2030 gas chromatograph equipped with a barrier-discharge ionisation detector (BID) and a molecular sieve column. The total run time of the method was 5 minutes. The GC was calibrated using calibration gas (2000 ppm H₂, BOC), diluted with N₂ at different ratios using a set of mass flow controllers (Bronkhorst) to provide known concentrations of H₂. Gas samples were programmed to auto-inject into the GC via a multiport stream selector valve directing the selected sample purge gas stream through a 2 mL sample loop before injection. H₂ evolution rates were calculated from the measured H₂ concentration in the purge gas and the purge gas flow rate. Cumulative H₂ production was calculated from the H₂ evolution rate and time passed since the previous measurement, assuming a constant H₂ evolution rate between time points. All samples were performed in triplicate (unless otherwise stated).

Apparent Quantum Yield (AQY): Photocatalysis samples were prepared as stated above using a glass sample vial (Chromacol 10-SV, Fisher) as the photoreactor with an irradiated area $A = 2.5 \text{ cm}^2$. Samples were purged with N₂ or air continuously during irradiation with monochromatic light ($\lambda = 405 \text{ nm}$, $I = 2.7 \text{ mW cm}^{-2}$). Hydrogen was quantified by GC using the process described above. AQY was calculated according to Equation (3.14):

$$\text{AQY (\%)} = \frac{2n \times N_A \times h \times c}{t_{\text{irr}} \times I \times A \times \lambda} \quad (3.14)$$

here n is the total H_2 produced per unit time, N_A is Avogadro's Constant, h is Planck's Constant, c is the speed of light, t_{irr} is the irradiation time, I is the irradiation intensity and A is the irradiated area.

Electrochemistry

Electrochemical experiments were carried out in a thermostatic Pyrex beaker held at 40 °C using an EmStat 3+ Potentiostat (PalmSens). A three-electrode setup was used with a BASi Ag/AgCl 3 M KCl (BASi) reference electrode, a 50 μ m diameter Pt microwire working electrode and a Pt mesh counter electrode. 15.0 mL of electrolyte was used for each electrochemical experiment. All potentials are referenced versus Ag/AgCl.

Microelectrode Preparation.

The Pt microwire electrode was prepared by Professor Frank Marken at the University of Bath. A Pt microwire electrode was fabricated according to a literature procedure.^{38, 47} A rectangular window (approx. 1×3 cm) was cut out of a strip of laminating plastic foil (approx. 3×10 cm). A length of Pt microwire (50 μ m diameter, Advent UK) was inserted between the laminating sheets so to expose part of the Pt wire through the window. The laminating foil was first sealed with a domestic iron, and then additionally sealed with epoxy resin to prevent the Pt wire inside the foil from coming into contact with the electrolyte.

Electrode Length Determination.

The Pt microwire working electrode length was accurately determined in a 5 mM potassium ferrocyanide solution in 0.1 M aqueous NaCl (pH not adjusted). Cyclic voltammetry (CV, $v = 50 \text{ mV s}^{-1}$) was performed to determine the potential step parameters for chronoamperometry. A potential step chronoamperogram was recorded (sampling rate 2 ms), holding at 0.0 V for 10 s before stepping to +0.6 V vs. Ag/AgCl and holding for another 10 s. A simulated current (I_{theo}) was calculated by applying the ferrocyanide concentration (5 mM) and diffusion coefficient ($6.5 \times 10^{-10} \text{ m}^2 \text{ s}^{-1}$) to Equation (3.04).⁴⁰ The fitting was optimised in Origin Lab software, giving a calibrated electrode length of $3.802 \pm 0.003 \text{ cm}$.

$$I_{\text{theo}}(t) = nFDc \times \left(\frac{\pi \times e^{-\frac{2}{5} \times \sqrt{\pi \frac{Dt}{16r^2}}}}{4 \sqrt{\pi \frac{Dt}{16r^2}}} + \frac{\pi}{\ln \left[\sqrt{\left(64 \times e^{-0.5772 \times \frac{Dt}{16r^2}} \right) + e^3} \right]} \right) \quad (3.04)$$

Where I is the current, n is the number of transferred electrons, F is Faraday's constant, l is the electrode length, D is the O₂ diffusion coefficient, c is the O₂ concentration, t is the time, and r is the electrode radius.

O₂ Concentration Determination in DESs.

The O₂ diffusion coefficient and the concentration of dissolved O₂ in the different DESs were determined by O₂ reduction at the Pt microwire working electrode in an analogous manner to the electrode length determination. CVs were performed in each DES (scan rate = 50 mV s⁻¹) to determine the potential step parameters E_1 and E_2 . A potential step chronoamperogram was recorded (sampling time 2 ms) by holding at E_1 for 10 s before stepping to E_2 and holding for another 10 s. A simulated current (I_{theo}) was calculated by applying the calibrated electrode dimensions ($l=3.802$ cm, $r=25$ μm) to Equation (3.04). Values for c and D were obtained from fitting experimental currents to Equation (3.04) using the Origin programme, using a concatenated fit of 3 individual measurements per solvent.

3.9. References

1. P. M. Wood, *Biochem. J.*, 1988, **253**, 287-289.
2. J. Wang, C.-X. Zhao, J.-N. Liu, D. Ren, B.-Q. Li, J.-Q. Huang and Q. Zhang, *Nano Mater. Sci.*, 2021, **3**, 313-318.
3. K. Das and A. Roychoudhury, *Front. Environ. Sci.*, 2014, **2**.
4. W. T. Eckenhoff and R. Eisenberg, *Dalton Trans.*, 2012, **41**, 13004-13021.
5. L. Ma, M. Liu, D. Jing and L. Guo, *J. Mater. Chem. A*, 2015, **3**, 5701-5707.
6. D. W. Wakerley and E. Reisner, *Energy Environ. Sci.*, 2015, **8**, 2283-2295.
7. M. Danilczuk, F. D. Coms and S. Schlick, *J. Phys. Chem. B*, 2009, **113**, 8031-8042.
8. C.-Y. Lin, Y.-H. Lai, D. Mersch and E. Reisner, *Chem. Sci.*, 2012, **3**, 3482-3487.
9. L. Ghassemzadeh, K.-D. Kreuer, J. Maier and K. Müller, *J. Phys. Chem. C*, 2010, **114**, 14635-14645.
10. S. Ji, W. Wu, W. Wu, P. Song, K. Han, Z. Wang, S. Liu, H. Guo and J. Zhao, *J. Mater. Chem.*, 2010, **20**, 1953-1963.
11. J. Olmsted, *Chem. Phys. Lett.*, 1974, **26**, 33-36.
12. A. P. Gerola, J. Semensato, D. S. Pelloso, V. R. Batistela, B. R. Rabello, N. Hioka and W. Caetano, *J. Photochem. Photobiol., A*, 2012, **232**, 14-21.
13. P. Du and R. Eisenberg, *Energy Environ. Sci.*, 2012, **5**, 6012-6021.

14. S. T. Stripp, G. Goldet, C. Brandmayr, O. Sanganas, K. A. Vincent, M. Haumann, F. A. Armstrong and T. Happe, *Proc. Natl. Acad. Sci. U.S.A.*, 2009, **106**, 17331-17336.
15. H. Ogata, S. Hirota, A. Nakahara, H. Komori, N. Shibata, T. Kato, K. Kano and Y. Higuchi, *Structure*, 2005, **13**, 1635-1642.
16. B. Mondal and A. Dey, *Chem. Commun.*, 2017, **53**, 7707-7715.
17. D. W. Wakerley and E. Reisner, *Phys. Chem. Chem. Phys.*, 2014, **16**, 5739-5746.
18. A. Mahammed, B. Mondal, A. Rana, A. Dey and Z. Gross, *Chem. Commun.*, 2014, **50**, 2725-2727.
19. B. Mondal, K. Sengupta, A. Rana, A. Mahammed, M. Botoshansky, S. G. Dey, Z. Gross and A. Dey, *Inorg. Chem.*, 2013, **52**, 3381-3387.
20. S. Dey, A. Rana, D. Crouthers, B. Mondal, P. K. Das, M. Y. Darensbourg and A. Dey, *J. Am. Chem. Soc.*, 2014, **136**, 8847-8850.
21. V. Fourmond, S. Stapf, H. Li, D. Buesen, J. Birrell, O. Rüdiger, W. Lubitz, W. Schuhmann, N. Plumeré and C. Léger, *J. Am. Chem. Soc.*, 2015, **137**, 5494-5505.
22. N. Plumeré, O. Rüdiger, A. A. Oughli, R. Williams, J. Vivekananthan, S. Pöller, W. Schuhmann and W. Lubitz, *Nature Chem.*, 2014, **6**, 822-827.
23. Y. Leterrier, *Prog. Mater. Sci.*, 2003, **48**, 1-55.
24. K. Maeda and K. Domen, *J. Phys. Chem. Lett.*, 2010, **1**, 2655-2661.
25. K. Maeda, K. Teramura, D. Lu, N. Saito, Y. Inoue and K. Domen, *Angew. Chem. Int. Ed.*, 2006, **45**, 7806-7809.
26. K. Maeda, K. Teramura, D. Lu, N. Saito, Y. Inoue and K. Domen, *J. Phys. Chem. C*, 2007, **111**, 7554-7560.
27. S. Chatterjee, K. Sengupta, S. Dey and A. Dey, *Inorg. Chem.*, 2013, **52**, 14168-14177.
28. M. Yoshida, K. Takanahe, K. Maeda, A. Ishikawa, J. Kubota, Y. Sakata, Y. Ikezawa and K. Domen, *J. Phys. Chem. C*, 2009, **113**, 10151-10157.
29. T. Wang, D. Gao, J. Zhuo, Z. Zhu, P. Papakonstantinou, Y. Li and M. Li, *Chem.--Eur. J.*, 2013, **19**, 11939-11948.
30. Y. Wang, E. Laborda, K. Tschulik, C. Damm, A. Molina and R. G. Compton, *Nanoscale*, 2014, **6**, 11024-11030.
31. J. Gu, Y. Yan, J. W. Krizan, Q. D. Gibson, Z. M. Detweiler, R. J. Cava and A. B. Bocarsly, *J. Am. Chem. Soc.*, 2014, **136**, 830-833.
32. D. W. Wakerley, K. H. Ly, N. Kornienko, K. L. Orchard, M. F. Kuehnel and E. Reisner, *Chem.--Eur. J.*, 2018, **24**, 18385-18388.
33. J. A. McCune, M. F. Kuehnel, E. Reisner and O. A. Scherman, *Chem*, 2020, **6**, 1819-1830.
34. C. Vidal, J. García-Álvarez, A. Hernán-Gómez, A. R. Kennedy and E. Hevia, *Angew. Chem. Int. Ed.*, 2014, **53**, 5969-5973.
35. D. Arnodo, S. Ghinato, S. Nejrotti, M. Blangetti and C. Prandi, *Chem. Commun.*, 2020, **56**, 2391-2394.
36. W. Yang, R. Godin, H. Kasap, B. Moss, Y. Dong, S. A. J. Hillman, L. Steier, E. Reisner and J. R. Durrant, *J. Am. Chem. Soc.*, 2019, **141**, 11219-11229.
37. V. W.-h. Lau, D. Klose, H. Kasap, F. Podjaski, M.-C. Pignié, E. Reisner, G. Jeschke and B. V. Lotsch, *Angew. Chem. Int. Ed.*, 2017, **56**, 510-514.
38. J. Weber, A. J. Wain and F. Marken, *Electroanalysis*, 2015, **27**, 1829-1835.
39. K. Aoki, *Electroanalysis*, 1993, **5**, 627-639.
40. A. Szabo, D. K. Cope, D. E. Tallman, P. M. Kovach and R. M. Wightman, *J. Electroanal. Chem. Interfacial Electrochem.*, 1987, **217**, 417-423.
41. J. Heinze, *Angew. Chem. Int. Ed. Engl.*, 1993, **32**, 1268-1288.
42. K. B. Oldham, *J. Electroanal. Chem. Interfacial Electrochem.*, 1987, **237**, 303-307.
43. S. Bruckenstein, *Anal. Chem.*, 1987, **59**, 2098-2101.
44. A. M. Bond, D. Luscombe, K. B. Oldham and C. G. Zoski, *J. Electroanal. Chem. Interfacial Electrochem.*, 1988, **249**, 1-14.

45. L. Bahadori, N. S. Abdul Manan, M. H. Chakrabarti, M. A. Hashim, F. S. Mjalli, I. M. AlNashef, M. A. Hussain and C. T. J. Low, *Phys. Chem. Chem. Phys.*, 2013, **15**, 1707-1714.
46. A. R. Neale, P. Li, J. Jacquemin, P. Goodrich, S. C. Ball, R. G. Compton and C. Hardacre, *Phys. Chem. Chem. Phys.*, 2016, **18**, 11251-11262.
47. A. Neudeck and L. Kress, *J. Electroanal. Chem.*, 1997, **437**, 141-156.
48. R. N. Adams, A. J. Bard, *Electrochemistry at Solid Electrodes*, Marcel Dekker Inc., New York, 1969.
49. F. J. Millero, F. Huang and A. L. Laferiere, *Mar. Chem.*, 2002, **78**, 217-230.
50. S. L. Clegg and P. Brimblecombe, *Geochim. Cosmochim. Acta*, 1990, **54**, 3315-3328.
51. Z. Sun, H. Zheng, J. Li and P. Du, *Energy Environ. Sci.*, 2015, **8**, 2668-2676.
52. D. A. Reddy, H. Park, S. Hong, D. P. Kumar and T. K. Kim, *J. Mater. Chem. A*, 2017, **5**, 6981-6991.
53. S. Cao, Y. Chen, C.-J. Wang, X.-J. Lv and W.-F. Fu, *Chem. Commun.*, 2015, **51**, 8708-8711.
54. F. Lakadamyali, M. Kato, N. M. Muresan and E. Reisner, *Angew. Chem. Int. Ed. Engl.*, 2012, **51**, 9381-9384.
55. F. Lakadamyali, M. Kato, N. M. Muresan and E. Reisner, *Angew. Chem. Int. Ed.*, 2012, **51**, 9381-9384.
56. W. M. Singh, T. Baine, S. Kudo, S. Tian, X. A. Ma, H. Zhou, N. J. DeYonker, T. C. Pham, J. C. Bollinger, D. L. Baker, B. Yan, C. E. Webster and X. Zhao, *Angew. Chem. Int. Ed. Engl.*, 2012, **51**, 5941-5944.
57. L. Petermann, R. Staehle, M. Pfeifer, C. Reichardt, D. Sorsche, M. Wächtler, J. Popp, B. Dietzek and S. Rau, *Chem.–Eur. J.*, 2016, **22**, 8240-8253.
58. R. Staehle, S. Losse, M. R. Filipovic, I. Ivanović-Burmazović, J. G. Vos and S. Rau, *ChemPlusChem*, 2014, **79**, 1614-1621.
59. A. P. Abbott, D. Boothby, G. Capper, D. L. Davies and R. K. Rasheed, *J Am Chem Soc*, 2004, **126**, 9142-9147.
60. A. P. Abbott, G. Capper, D. L. Davies, R. K. Rasheed and V. Tambyrajah, *Chem. Commun.*, 2003, 70-71.

Chapter 4

Augmenting Performance of Hydrogenase Enzymes for Photocatalytic Hydrogen Evolution via Solvent Tuning

4. Introduction

4.1. Co-catalysts and Enzymes

Co-catalysts are an essential component of photocatalytic systems as they aid in charge separation by acting as harvesters of photoexcited electrons from the conduction band of semiconductors, or from the lowest unoccupied molecular orbital of a molecular light absorber.¹ For the production of hydrogen from sunlight, co-catalysts are employed for their stability, their low proton to catalyst (adsorbate-surface) binding energies, and their ability to lower overpotentials of chemical reactions.² As previously discussed, Pt is conventionally recognised as the ideal co-catalyst. However due to the cost associated with Pt, research into other co-catalysts for photocatalytic H₂ production systems is an area of interest. While efficient noble metal free catalysts have been developed which are thought to be competitive with Pt, the use of these co-catalysts requires a high degrees of tuning and functionality, with synthesis methods to produce these co-catalysts are likely not suitable for larger scale systems.³⁻⁵

Enzymes are biological co-catalysts which are essential for all life on earth. Enzymes vary in function, with some enzymes evolved to work in harsh reaction conditions. There exists a branch of enzymes called *hydrogenases* (H₂ases) which can efficiently catalyse both the forward and back reactions of proton reduction i.e. enzymes can work to both evolve hydrogen and oxidise hydrogen at the enzyme active site.^{6, 7} These enzymes come in a variety of forms with a variety of active sites and have been used in reaction systems with impressive results, which will be discussed in

depth. H₂ases act in the same way as conventional proton reduction co-catalysts in photocatalysis by utilising photoexcited electrons to evolve hydrogen at remarkably low overpotentials.⁸ The benefit of enzymes is their ubiquitous nature, and that they can be extracted and purified from biological sources to allow a much greener method of solar hydrogen production.⁹

4.2. H₂ase Chemistry

Three classes of H₂ases are known to exist which catalyse the interconversion of molecular hydrogen and protons. While differing in protein structure and sequence, all H₂ases are known to possess active sites consisting of metal carbonyls.^{10, 11} The most common H₂ases are those named [FeFe]- and [NiFe]-H₂ase according to the metals which constitute the active site. Characteristically, these H₂ases feature CO and CN⁻ coordinating ligands as well as having the bimetallic centres bridged with sulfur.¹² The sulfur atoms creating a bridge at the metal centre results from the amino acid cysteine found in the protein structure.¹¹ The orientation and coordination of the ligands and the surrounding protein structure create a free coordination site on one of the metals to generate a binding site for H₂ and protons.

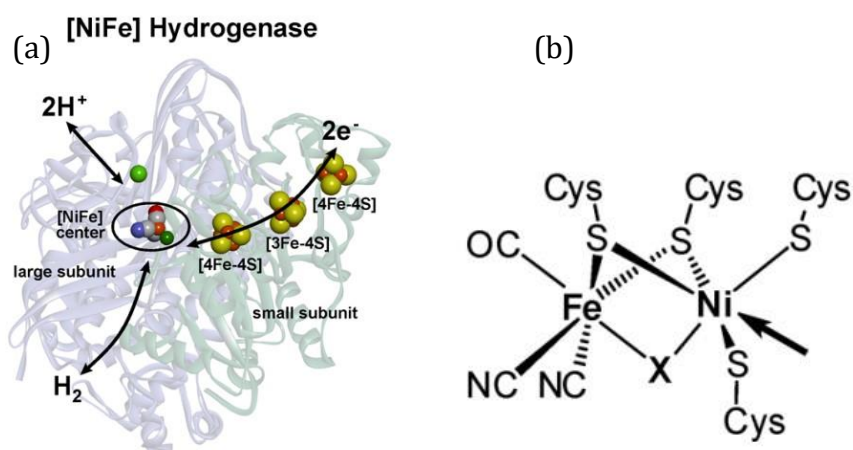


Figure 4.01. Structure of [NiFe]-H₂ase from *Desulfovibrio vulgaris*. The electron transport chain composed of Fe-S clusters is shown along with proton and H₂ mobility pathways (a) and chemical structure of the [NiFe]-H₂ase active site, with the arrow indicating a free coordination site. X indicates the coordination of molecular oxygen or a hydroxyl group. Reprinted with permission from REF 14. Copyright 2014, American Chemical Society.

These H₂ases are found in the periplasm or the cytoplasm of cells as solubilised or membrane-bound components.^{11, 13} H₂ases in nature have a primary role of energy

provision through H₂ oxidation and to balance the redox potential of the cell, but may also be involved in establishing proton gradients across cell membranes to regulate the pH.¹⁴ Electrons can be consumed through proton reduction or produced through the oxidation of H₂, with the H₂ase location within the cell giving them a preferential role as H₂ producers or consumers. However, many purified catalytically active H₂ases have bidirectional properties and can act to uptake or produce H₂ depending on the cell's physiological context.¹⁵

The catalytic sites of [NiFe]- and [FeFe]-H₂ases are buried inside the enzyme's protein structure, and so chemical components are required to shuttle over several nanometres between the metal site and the surface.¹⁶ It is believed electrons use the Fe-S clusters as relays, which occurs through the redox centre's highly structured arrangement and proximity of around 1.0 nm.¹⁷ This spatial arrangement favours the fast transfer of electrons through space or through bonded orbitals.¹⁸ Theoretical studies conducted by McCullagh and Voth have suggested that the electron transport process can activate hydrophilic channels in the protein structure, which allows protons to be more easily supplied to the active site.¹⁹ This research shows a favourable property of enzymes, in that they are highly ordered and have evolved such chemical mechanisms to maximise efficiency for redox processes.

[NiFe]-H₂ase enzymes are the most common variety of H₂ases and can be sourced and purified from a variety of different bacteria, including *E. Coli*, *Salmonella Choleraesuis*, *Pyrococcus furiosus*, and various *Desulfovibrionales*.^{7, 20} [NiFe]-H₂ases have a Mg²⁺ cation found at the end of the amino acid chain in the larger protein structure which is bonded to water and three amino acids electrostatically – the presence of Mg²⁺ aids in stabilising solvent-free regions of the protein.²¹ In addition, as the Mg²⁺ is located 1.3 nm (13 Å) from the [NiFe] cluster, it is thought to connect the catalytically active site to a hydrogen bonding network to serve as a proton transfer pathway. As such, this helps lower overpotential associated with diffusion of protons and to provide a lower activation energy for proton reduction.

The mechanism of redox process on [NiFe]-H₂ases is debated. Using crystallographic and spectroscopic data, it was shown that Fe in the metal site does not change its oxidation state – it is instead Ni which participates in redox

chemistry.^{22, 23} The Ni metal can exist in what is commonly called a “ready” state and an “unready” state (Ni-B and Ni-A, respectively).^{22, 24} While the terminology may seem confusing, both the ready and unready state are the oxidised forms of the active site, with both becoming catalytically active upon a mono-reduction step in conjunction with proton transfer. Ni-B is known to return to its catalytically active state quicker than Ni-A, hence the term “ready,” with the Ni³⁺ cation reduced to Ni²⁺.^{25, 26} The reason for this disparity in activation kinetics between Ni-A and Ni-B was proposed to be a result of the difference in bridging ligands between the two different redox states.²⁷

To convert the Ni-B ready structure to one which can efficiently act as a redox catalyst, a highly reducing environment is often required to cleave oxygen and hydroxyl groups bound to the Ni²⁺.²⁸ Likewise, the reverse is possible – when exposed to an aerobic environment, the Ni²⁺ cation in the metal cluster reverts to the catalytically inactive Ni-B state, which is detectable using linear sweep voltammetry.²⁷ In fact, upon purification, the active site is found most commonly as the Ni-B ready state, with bound oxygen located on the Ni metal, generating the Ni³⁺ species.²⁹ As such, [NiFe]-H₂ases should be carefully considered due to their low oxygen tolerance and their inability to re-activate unless exposed to an extreme reducing environment.

4.3. [NiFeSe]-H₂ases

There exists a subgroup of [NiFe]-H₂ases which possess a Se atom on a selenocysteine amino acid located close to the Ni-Fe cluster. Due to the difference in genetic translation mechanisms available to most bacteria, the incorporation of the selenocysteine amino acid into the protein structure often comes at a high energetic cost to the bacteria.³⁰ Despite this, the structures of the active sites of [NiFe]-H₂ases and [NiFeSe]-H₂ases are very similar, except for the replacement of a terminally coordinated cysteine residue by selenocysteine. In addition, electron paramagnetic resonance (EPR) spectroscopy shows the minimal presence of inactive Ni-A and Ni-B states. It has been reported that [NiFeSe]-H₂ase isolated aerobically exhibits only low-intensity EPR signals which can be attributed to the inactive Ni-A and Ni-B states.^{31, 32} Moreover, research has shown that light-induced reactivation of the

metal cluster occurs approximately 5 times faster for [NiFeSe]-H₂ase compared to [NiFe]-H₂ase.³¹

Due to the replacement of a S atom with Se, the chemical behaviour of the enzyme is altered in a number of ways. Se is a much larger atom than S and is therefore conducive to a more acidic, weaker bound proton on the atom in question. Due to its lower pK_a, it is thought that Se can more readily donate protons to create a more reducing environment, and so leading to an increase in H₂ production.^{33, 34} In fact, proton-deuterium exchange experiments featuring [NiFeSe]-H₂ase have shown that the activity of the enzyme for H₂ and H-D production is larger than H₂ and H-D production by [NiFe]-H₂ase.^{24, 35} Moreover, in the presence of molecular O₂, the Se-O bond should be weaker than that of a S-O bond, resulting in any oxygen-bound states present in a [NiFeSe]-H₂ase to be more quickly removed which may act to preserve the enzyme's active site and induce O₂ tolerance.^{36, 37}

In [NiFe]-H₂ases studied in the literature to date, conventionally [NiFe]-H₂ases are viewed as oxygen sensitive and intolerant which is thought to arise from the nature and behaviour of three Fe-S clusters found in the enzyme's small subunit.^{14, 38} These Fe-S clusters constitute the electron transport chain linking the enzyme's active site to the protein surface, and are called the proximal cluster, the medial cluster, and the distal cluster due to their distance from the active site. In [NiFe]-H₂ases the proximal and distal clusters are [Fe₄S₄] whereas the medial cluster is known to have a [Fe₃S₄] subunit.^{14, 39-41} In [NiFeSe]-H₂ases, all three clusters have the [Fe₄S₄] composition.^{23, 42, 43} The difference in confirmation may be essential for tuning the electronic properties of the enzymes.⁴⁴

The mechanism of H₂ transport has also been proposed for the [NiFeSe]-H₂ase purified from the bacterium *Desulfomicrobium baculatum*. Molecular dynamic simulations performed on the enzyme highlighted the H₂ partition coefficient between the enzyme active site and the surrounding solution is much higher compared to a [NiFe]-H₂ase as well as having a H₂ diffusion pathway which allows the accommodation of a greater concentration of H₂ at the active site.^{45, 46} These structural differences are thought to have an impact on enzymatic activity and its inhibition by H₂, as a build-up of H₂ around the active site slows enzymatic activity.

In addition to its electronic and structural properties, [NiFeSe]-H₂ases are shown to possess an increase in their tolerance towards O₂. Electrochemical measurements using *Desulfomicrobium baculatum* [NiFeSe]-H₂ase have shown that the inactivation i.e., the formation of the oxidised Ni-B and Ni-A states, does not occur at positive (oxidising) potentials in an anaerobic environment in sufficient levels of H₂.⁴⁷ In fact, cyclic voltammetry showed that, in the presence of O₂, a mix of two inactive states form which are distinguishable by the difference in electrochemical potentials which are thought to be “reactivating” – one of these states is preferentially found in a reducing, H₂ rich atmosphere and can be reactivated at the same potential as the anaerobically inactivated H₂ase, which indicates this state of re-activation is most likely a result of kinetic limitations on the active site.⁴⁷ The inactive site formed in an aerobic atmosphere is reactivated very quickly at potentials close to the proton reduction potential shown again electrochemically.

Many factors are thought to contribute to the relative O₂ tolerance of the [NiFeSe]-H₂ase. Crystallographic results from the aerobically purified enzyme show the presence of oxidised Se.⁴² Oxidation of Se is more favourable versus sulfur when substituted in the cysteine amino acid i.e., selenocysteine is easier to oxidise than normal cysteine.^{48, 49} The oxidation of Se in these structures indicate that the active site is afforded certain levels of oxidative attack through protection via chemical tuning. In addition, Se is a much larger atom than that of S and so presence of selenium may therefore sterically block and chemically protect the nickel centre from O₂. Oxidised species of Se are also much easier to reduce, which is in accordance with the rapid reduction of the deactivated, oxidised [NiFeSe]-H₂ases. This also comes in conjunction with full active site recovery and H₂ production upon O₂ removal.⁴⁷ As such, the bulkier Se and the ease with which selenocysteine is oxidized and reduced back to the active form could explain the increased O₂ tolerance of [NiFeSe]-H₂ases. These properties allow these enzymes to be investigated for their H₂ production performance both electrochemically and photochemically, as it has been shown that in some instances of deactivated highly reduced Ni¹⁺ states, light can aid in cleaving species bound to the Ni¹⁺ cation.⁵⁰

4.4. The Experimental O₂ Tolerance of [NiFeSe]-H₂ase

Electrochemical experiments conducted by Parkin et al. attempted to rationalise the activity of [NiFeSe]-H₂ase from the bacteria *Desulfomicrobium baculatum*. Protein film voltammetry, an electrochemical technique used to examine the behaviour of proteins on electrodes, showed some key findings. It was demonstrated that at reducing potentials [NiFeSe]-H₂ase was a good producer of H₂ in an anaerobic inert environment, with steep intersection across the zero-current axis showing that H⁺ reduction occurs with minimal overpotential.⁴⁷ The high activity is explained by stronger kinetic bias towards H₂ production.^{51, 52} Gas mixing experiments, showed that the [NiFeSe]-H₂ase also retained 17% of its electrochemical activity in an atmosphere containing 1% O₂ at 30 °C.⁴⁷ [NiFeSe]-H₂ases in their oxidised, deactivated state can also be reduced to their active state at low redox potential, another characteristic of O₂ tolerance.⁵³ This behaviour was also examined, whereby reactivation of the enzyme occurred at cathodic potentials following injection with an electrolyte saturated with O₂ and subsequent purging of the headspace with H₂.⁴⁷

While [NiFe]- and [NiFeSe]-H₂ases are commonly called “O₂ tolerant,” there lies distinctions in the nature of O₂ tolerance, and its kinetic reactivation upon reduction of the enzyme active site. With [NiFe]-H₂ases, the inactive oxidised Ni³⁺ state can be induced upon exposure to O₂ or through application of an anodic potential to the enzyme.^{54, 55} Ni³⁺ can be reduced to Ni²⁺ either chemically or electrochemically, and the rapid or slow kinetics of this reduction process dictate the O₂ tolerance of the active site. However, Ni³⁺ has not been detected in [NiFeSe]-H₂ase, and while the enzyme can be oxidised this is often thought to arise from the oxidation of the selenocysteine.^{24, 31, 35, 52, 56}

Importantly, [NiFeSe]-H₂ase has been shown to act as a co-catalyst in photocatalytic H₂ evolution experiments, in both aerobic and anaerobic conditions. The first of these experiments utilised dye-sensitised TiO₂ attached with the enzyme.⁵⁷ [NiFeSe]-hydrogenase has a large number of surface-exposed glutamate and aspartate residues in close proximity to the distal [4Fe4S] cluster which may act as natural anchor sites, via the carboxylate, to TiO₂. Excitation of a ruthenium dye by

visible light causes an electron to be injected into the conduction band of TiO_2 – this electron is then transferred to $[\text{NiFeSe}]\text{-H}_2\text{ase}$ where catalytic proton reduction to hydrogen occurs. The stability of the enzyme towards O_2 was measured by exposing the enzyme to air, followed by addition of TiO_2 and Ru dye to the enzyme solution. The cell was then purged with N_2 and irradiated. 50% activity of the enzyme was reportedly lost.⁵⁷

Aerobic photocatalytic H_2 evolution was also probed using Eosin Y as a light absorber and $[\text{NiFeSe}]\text{-H}_2\text{ase}$ under varying levels of O_2 .⁵⁸ After 1 h visible light irradiation, known levels of O_2 were injected into the solution, with atmospheric levels of O_2 (21%) showed that enzyme activity had dropped by 90% compared to anaerobic conditions. (Figure 4.02)

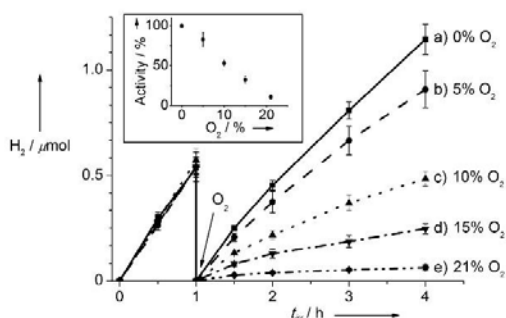


Figure. 4.02. Photocatalytic H_2 production at EY- H_2ase in varying levels of O_2 under visible light. Conditions: Eosin Y (1 μmol), H_2ase (10 pmol), aqueous TEOA (2.25 mL, 0.15 M, pH 7.0) at 25 °C. The EY-hydrogenase system was exposed to different O_2 headspace concentrations after 1 h of irradiation under 2% CH_4/N_2 . Reproduced with permission from REF 58. Copyright 2013, Wiley-VCH.

While these experiments show the potential of aerobic H_2 evolution by $[\text{NiFeSe}]\text{-H}_2\text{ase}$, it is evident that the presence of O_2 greatly hinders proton reduction activity. This chapter aims to show that simple solvent tuning involving DESs can increase enzymatic activity for H_2 evolution in atmospheric levels of O_2 , and the oxygen tolerance of the enzyme tethered to a TiO_2 photocatalyst can be sustained over long irradiation periods, with prolonged H_2 production.

4.5. Results

4.5.1 H₂ Evolution Performance by [NiFeSe]-H₂ase – TiO₂ in Water

To first test the performance of the enzyme, a model photocatalyst system containing [NiFeSe]-H₂ase purified from *Desulfomicrobium baculatum* was established in aqueous conditions. The [NiFeSe]-H₂ase enzyme was purified by Dr. Christine Cavazza Université Grenoble Alpes and was kindly donated by Dr. Alan le Goff to aid in this work. 21 pmol of [NiFeSe] co-catalytic H₂ase was added to a 2.0 mL 0.4 M TEOA pH = 7.0 aqueous solution alongside 5.0 mg TiO₂ to act as the light absorber (full experimental details in Materials and Methods). A notable performance of the [NiFeSe]-H₂ase – TiO₂ system was observed, with 74.8±6.5 μmol_{H₂} produced in an inert environment after 24 hours (Figure 4.03), with a turnover number (TON) of the enzyme of (3.56±0.31 × 10⁶) mol_{H₂} per mol_{Hase}. A maximum turnover frequency (TOF) of 0.4±0.02 × 10⁶ h⁻¹ was observed after 0.8 hours. The reaction profile shows a steady production of H₂ from [NiFeSe]-H₂ase – TiO₂, with a slower but still steady production after 20 hours, which shows the stability of the enzyme for proton reduction.

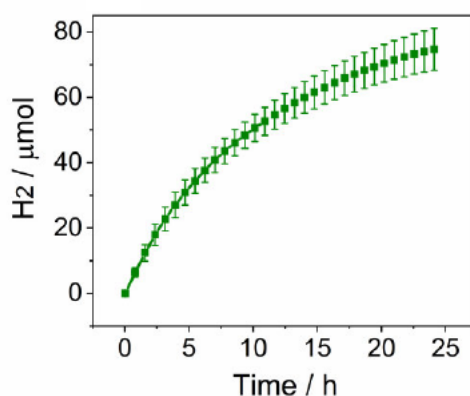


Figure 4.03. Photocatalytic H₂ evolution in aqueous 0.4 M TEOA pH = 7.0 by [NiFeSe]-TiO₂ (a) under nitrogen after 24.1 hours. Conditions: TiO₂ (5.0 mg), [NiFeSe]-H₂ase (21 pmol), 0.4 M TEOA pH 7 (2.0 mL), AM 1.5G, 1 sun, 40 °C, constant N₂ purge.

An important chemical property of reaction systems with enzymes is the pH. A pH too high or low can cause denaturation of the protein structure. Enzymes adopt a

certain structure to maximise/minimise hydrophilic/hydrophobic interactions with its external environment. Changes in pH and temperature can alter this protein structure and cause the enzyme to cease functioning. On further looking at pH and its effect on enzyme activity, the total H₂ at [NiFeSe]-H₂ase – TiO₂ was investigated in water, with 0.4 M TEOA adjusted to pH 7.2 (Figure 4.04). The results show that approximately 13% of activity is lost when shifting the pH by 0.2 units higher. As the efficiency of TEOA as an electron donor is actually improved in alkaline conditions, the lower activity in pH 7.2 by [NiFeSe]-H₂ase – TiO₂ can be attributed to the enzyme's inherent sensitivity to pH.

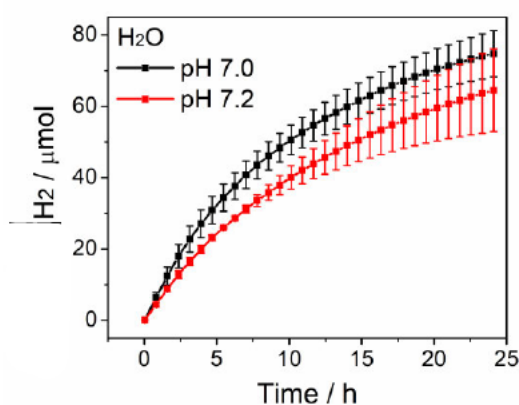


Figure 4.04. Photocatalytic H₂ evolution in H₂O pH = 7.0 by [NiFeSe]-TiO₂ (black trace) and H₂O pH = 7.2 (red trace). Conditions: TiO₂ (5.0 mg), [NiFeSe]-H₂ase (21 pmol), TEOA (0.4 M), AM 1.5G, 1 sun, 40 °C, constant N₂ purge.

4.5.2. H₂ Evolution Performance by [NiFeSe]-H₂ase – TiO₂ in Reline

Subsequently, the activity the same photocatalytic system of [NiFeSe]-H₂ase – TiO₂ in DES was investigated in reline. [NiFeSe]-H₂ase – TiO₂ in 80% vol. reline produced 1.93±0.6 μmol_{H₂} correlating to a TON of 92,000±29,000 (TOF_{H₂ase} = 6900±3900 h⁻¹). It should be noted the remaining volume was made up to 2.0 mL with an aqueous TEOA solution with initial concentration of 1.95 M adjusted to pH = 7.0. This ensured the final concentration of TEOA in the DES-based solution was 0.4 M. The initial TEOA concentrations added to the DESs prior to photocatalytic H₂ evolution are presented in Table 4.01.

Table 4.01. Aqueous TEOA concentrations added to DESs. The final TEOA concentration after pH adjustment was 0.4 M.

Initial TEOA Concentration M	Initial pH	Volume added mL	Concentration of aq. TEOA % vol.
1.947	7.0	0.38	20%
1.27	7.0	0.58	30%
0.949	7.0	0.78	40%
0.755	7.0	0.98	50%
0.627	7.0	1.18	60%
0.536	7.0	1.38	70%
0.47	7.0	1.58	80%
0.416	7.0	1.78	90%

Increasing the aqueous content in the reline-based solvents increases the performance notably. The same photocatalytic system in 70% vol. reline, 60% vol. reline and 50% vol. reline produced $13.6 \pm 1.4 \mu\text{mol}_{\text{H}_2}$, $21.6 \mu\text{mol}_{\text{H}_2}$, $28.3 \pm 3.2 \mu\text{mol}_{\text{H}_2}$ respectively. An even further increase in activity was observed in both the 40% vol. reline and 30% vol. reline, with total H_2 amounts of $45.6 \mu\text{mol}_{\text{H}_2}$ and 52.8 ± 4.7 produced after 21.8 hours, respectively. Upon further increase of the water content of the solvents to make 20% vol. reline and 10% vol. reline, [NiFeSe]-H₂ase produced $56.1 \pm 4.9 \mu\text{mol}_{\text{H}_2}$ and $61.5 \pm 16.8 \mu\text{mol}_{\text{H}_2}$ respectively. The total H_2 and TON of the enzyme in reline-based solvents are summarised in Table 4.02. Therefore, increasing water content in the solution in the reline-based solutions enhances H_2 evolution performance increases. The low performance in the high reline concentrations may be attributed to high viscosity of the solution. In addition, the solutions with lower reline content show a similar reaction profile to the aqueous control without any DES present. Therefore, the higher reline content may lower enzymatic activity or induce difficulty of [NiFeSe]-H₂ase tethering to TiO_2 *in situ*.

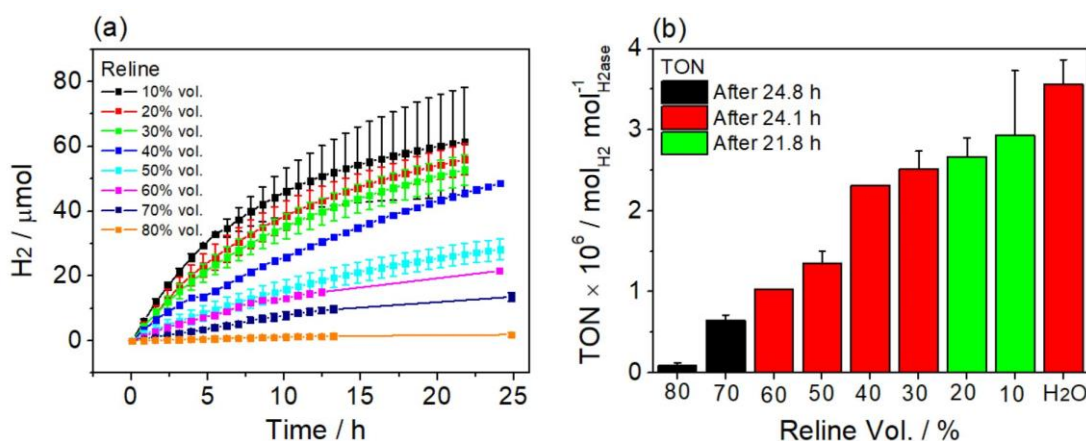


Figure 4.05. Photocatalytic H₂ evolution in DESs of varying reline concentration by [NiFeSe]-TiO₂ (a) and turnover of H₂ase after certain time periods in varying reline concentration and H₂O (b). Conditions: TiO₂ (5.0 mg) TEOA (0.4 M), [NiFeSe]-H₂ase (21 pmol), 2.0 mL, AM 1.5G, 1 sun, 40 °C, constant N₂ purge

Table 4.02. Conditions and H₂ evolution performance by [NiFeSe]-H₂ase – TiO₂ in varying reline concentration. Values obtained after 24.1 h. * denotes total H₂ values after 21.8 h. Conditions: TiO₂ (5.0 mg), TEOA (0.4 M), 2.0 mL, 40 °C, AM1.5G, constant N₂ purge.

Reline % Vol.	H ₂ O – TEOA vol. mL	Total H ₂ μmol	TON mol _{H₂} mol ⁻¹ _{H₂ase}	TOF _{max} mol _{H₂} mol ⁻¹ _{H₂ase s⁻¹}
80	0.4	1.9±0.6	9.2±2.9 × 10 ⁴	1.9±1.1 after 3.9 h
70	0.6	13.6±1.4	6.4±0.7 × 10 ⁵	18.9±7.4 after 7.8 h
60	0.8	21.6	1.0 × 10 ⁶	27.9 after 1.6 h
50	1	28.3±3.2	1.3±0.2 × 10 ⁶	22.0±4.8 after 1.6 h
40	1.2	48.6	2.3 × 10 ⁶	54.7 after 0.8 h
30	1.4	52.8±4.7*	2.5±0.2 × 10 ⁶ *	76.3±10.5 after 0.8 h
20	1.6	56.1±4.9*	2.7±0.2 × 10 ⁶ *	74.7±21.6 after 0.8 h
10	1.8	61.5±16.8*	2.9±0.8 × 10 ⁶ *	103.1±10.2 after 0.8 h

4.5.3. H₂ Evolution Performance by [NiFeSe]-H₂ase – TiO₂ in Ethaline

The same photocatalytic system of [NiFeSe]-H₂ase – TiO₂ was tested in ethaline-based solvents, with the ethaline content varied to determine photocatalytic behaviour and performance. In high concentrations of ethaline, H₂ evolution performance was notably low, with [NiFeSe]-H₂ase – TiO₂ in 80% vol. ethaline, 70% vol. ethaline, and 60% vol. ethaline producing 2.9±0.1 μmol_{H₂}, 10.3±2.1 μmol_{H₂}, and

29.9±1.2 $\mu\text{mol}_{\text{H}_2}$ respectively after 24.1 h irradiation. Upon increasing the water concentration, and decreasing the DES-like nature of the solvent, photocatalytic performance for H_2 evolution was increased, with 50% vol. ethaline exhibiting 55.4±3.1 $\mu\text{mol}_{\text{H}_2}$ also after 24.1 h. Further decrease in ethaline concentration led to H_2 evolution by the photocatalytic system to be comparable to that of water, with the photocatalyst in 40% vol. ethaline and 30% ethaline producing 62.1±4.9 $\mu\text{mol}_{\text{H}_2}$ and 63.8 $\mu\text{mol}_{\text{H}_2}$, respectively. Only one sample of [NiFeSe]-H₂ase – TiO₂ was tested in 30% vol. ethaline, and so no experimental error was recorded. Photocatalytic performance found to be greater in 20% vol. ethaline and 10% vol. ethaline with total H_2 produced determined to be 63.1±27.5 $\mu\text{mol}_{\text{H}_2}$ and 65.2±25.6 after 20.9 h irradiation, respectively. The turnover frequency was also highest in 10% vol. ethaline, with the enzyme showing a maximum TOF_{max} of 74.9±22.6 s⁻¹.

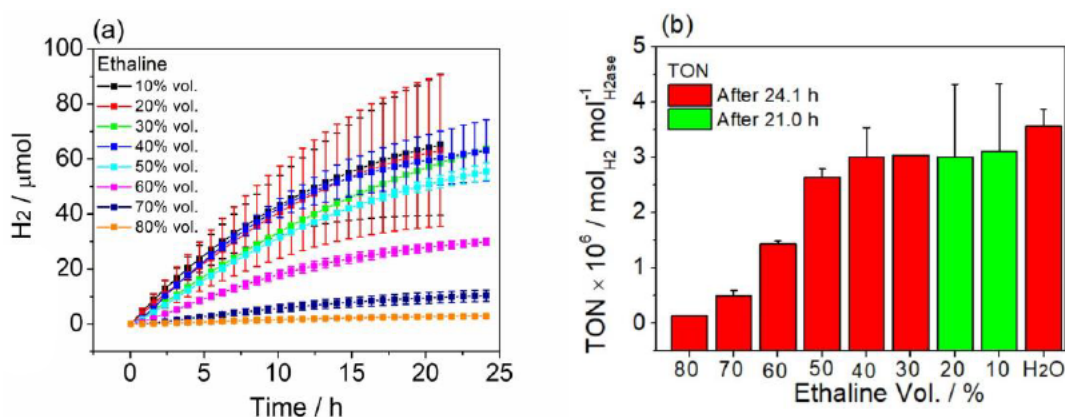


Figure 4.06. Photocatalytic H_2 evolution in DESs of varying ethaline concentration by [NiFeSe]-TiO₂ (a) and TON of H₂ase after certain time periods in varying concentration of ethaline and H₂O solvents (b). Conditions: TiO₂ (5.0 mg), TEOA (0.4 M) [NiFeSe]-H₂ase (21 pmol), 2.0 mL, AM 1.5G, 1 sun, 40 °C, constant N₂ purge

Table 4.03. Conditions and H_2 evolution performance by [NiFeSe]-H₂ase – TiO₂ in varying % vol. ethaline. Values observed after 24.1 h. * denotes total H_2 values after 20.9 h. Conditions: TiO₂ (5.0 mg), 0.4 M TEOA, 2.0 mL 40 °C, AM1.5G, constant N₂ purge.

Ethaline % Vol.	H ₂ O – TEOA vol. mL	Total H ₂ μmol	TON $\text{mol}_{\text{H}_2} \text{mol}^{-1}_{\text{H}_2\text{ase}}$	TOF _{max} $\text{mol}_{\text{H}_2} \text{mol}^{-1}_{\text{H}_2\text{ase}} \text{s}^{-1}$
80	0.4	2.9±0.1	$1.4 \pm 0.1 \times 10^5$	2.7±0.2 after 3.9 h
70	0.6	10.3±2.1	$4.9 \pm 1.0 \times 10^5$	9.6±2.4 after 3.9 h
60	0.8	29.9±1.2	$1.4 \pm 0.1 \times 10^6$	27.8±2.8 after 3.9 h
50	1	55.4±3.1	$2.6 \pm 0.1 \times 10^6$	47.8±4.6 after 3.1 h
40	1.2	62.1±4.9	$3.0 \pm 0.5 \times 10^6$	59.6±2.3 after 3.1 h
30	1.4	63.8	3.0×10^6	48.8 after 2.4 h

20	1.6	63.1±27.5*	3.0±1.3 × 10 ⁶ *	63.2±33.3 after 0.8 h
10	1.8	65.2±25.6*	3.1±1.2 × 10 ⁶ *	74.9±22.6 after 0.8 h

4.5.3. H₂ Evolution Performance by [NiFeSe]-H₂ase – TiO₂ in Glyceline

[NiFeSe]-H₂ase – TiO₂ was also tested for its H₂ evolution performance in solvents containing the DES glyceline with favourable results versus the other solvents tested. Even in high % volumes of glyceline, H₂ evolution performance was modest, with the photocatalytic system producing 24.9±0.6 μmol_{H₂} after 24.9 h solar irradiation in 80% vol. glyceline, and 59.5±5.3 μmol_{H₂} in 60% vol. glyceline after 24.1 h. Lower % volumes of glyceline were comparable to water in terms of overall H₂ produced, with the total H₂ produced in 40% vol. glyceline and 30% vol. glyceline determined to be 68.1±3.0 μmol_{H₂} and 72.4±2.0 μmol_{H₂} respectively after 24.1 h. The photocatalyst in solutions containing 20% vol. glyceline and even outcompeted water as a solvent, with 91.4±12.0 μmol_{H₂} produced and a maximum TOF of 122.4±10.1. A solution containing 10% vol. glyceline showed photocatalytic performance comparable within error of 20% vol. glyceline, with 85.7±10.5 μmol_{H₂}. Under the given conditions, it appears glyceline offers competition as a candidate to increase enzymatic performance towards H₂ evolution.

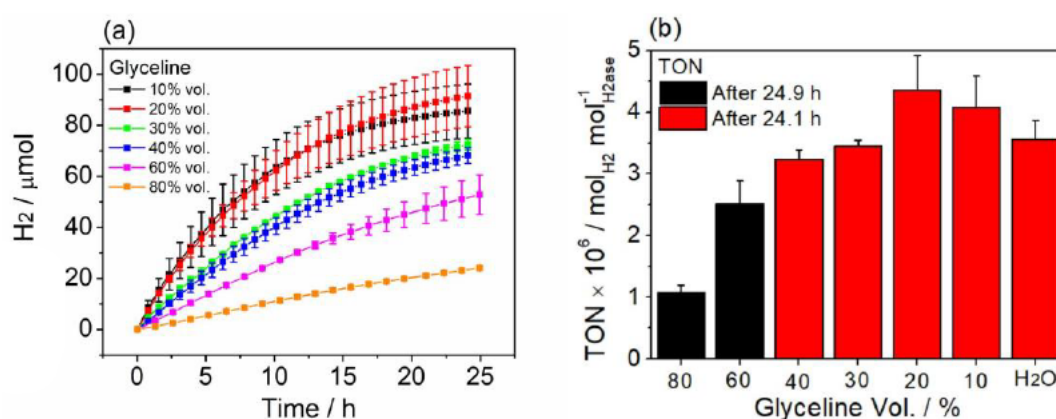


Figure 4.07. Photocatalytic H₂ evolution in DESs of varying glyceline % volumes by [NiFeSe]-TiO₂ (a) and turnover of H₂ase after certain time periods in hours varying percentage volumes of glyceline and H₂O (water) solvents (b). Conditions: TiO₂ (5.0 mg), TEOA (0.4 M), [NiFeSe]-H₂ase (21 pmol), 2.0 mL, AM 1.5G, 1 sun, 40 °C, constant N₂ purge

Table 4.04. Conditions and H₂ evolution performance by [NiFeSe]-H₂ase – TiO₂ in varying % vol. glyceline. Values observed after 24.1 h. * denotes total H₂ values after 24.9 h. Conditions: TiO₂ (5.0 mg), TEOA (0.4 M), [NiFeSe]-H₂ase (21 pmol), 2.0 mL 40 °C, AM1.5G, constant N₂ purge.

Glyceline % Vol.	H ₂ O – TEOA vol. mL	Total H ₂ μmol	TON mol _{H₂} mol ⁻¹ _{H₂ase}	TOF _{max} mol _{H₂} mol ⁻¹ _{H₂ase} s ⁻¹
80	0.4	24.9±0.6*	1.1±0.1 × 10 ⁶ *	14.1±2.2 after 5.2 h
60	0.8	59.5±5.3*	2.8±0.2 × 10 ⁶ *	54.2±1.7 after 1.6 h
40	1.2	68.1±3.0	3.2±0.1 × 10 ⁶	56.8±6.8 after 2.4 h
30	1.4	72.4±2.0	3.4±0.1 × 10 ⁶	78.3±3.0 after 0.8 h
20	1.6	91.4±12.0	4.4±0.5 × 10 ⁶	122.4±10.1 after 0.8 h
10	1.8	85.7±10.5	4.1±0.5 × 10 ⁶	144.7±45.8 after 0.8 h

To test the viability of glyceline as a solvent, the H₂ase-TiO₂ system was irradiated over a 3-day period continuously and the total H₂ evolution performance monitored (Figure 4.08). In a 60% vol. glyceline solution, after 72 h the H₂ evolution performance was relatively stable and continuous, with 83.2±12.7 μmol_{H₂} in total detected. While the TOF slowed after 24 h, the continuous H₂ production shows that the performance of the enzyme can be efficiently employed even in high % volumes of organic DESs. The enzymes used for photocatalytic purposes often require solvents suited to maintain their protein structure, namely the hydrophobic outer shell, with the channels which aid in moving H₂ to and from the active site said to be hydrophobic too.^{59, 60} Despite the organic nature of the glyceline DES, enzyme performance is still maintained, but conclusions on the effect of the DES itself on the enzyme structure and subunits should be speculated.

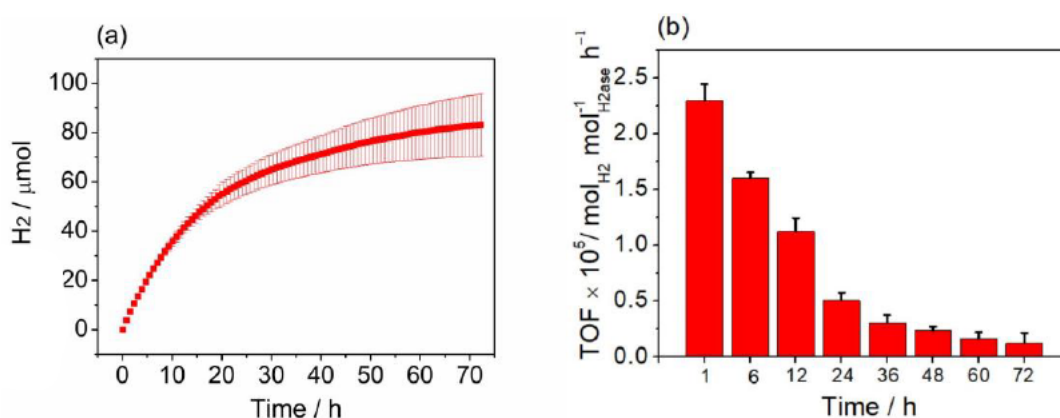


Figure 4.08. H₂ evolution by [NiFeSe]-H₂ase – TiO₂ in 60% vol glyceline after 3 days irradiation (a) and turnover frequency of [NiFeSe]-H₂ase per hour recorded at time periods over 3-day irradiation period (b). Conditions:

TiO₂ (5.0 mg), TEOA (0.4 M), 2.0 mL (60% vol. glyceline), 21 pmol [NiFeSe]-H₂ase, 40 °C, AM1.5G, constant N₂ purge.

To determine the effect of glyceline on [NiFeSe]-H₂ase binding to TiO₂, resuspension experiments were performed in varying concentrations of glyceline. 21 pmol of [NiFeSe]-H₂ase was added to 2.0 mL solutions containing 5 mg TiO₂. These solutions were stirred in an inert atmosphere for 30 minutes. Following stirring, the solutions were centrifuged, with the resulting supernatant containing any H₂ase not attached to TiO₂ pipetted out, and fresh solution added without any H₂ase. The TiO₂ pellets in fresh supernatant were then tested for their H₂ evolution performance. (Figure 4.09). The H₂ evolution by the TiO₂ pellets in this fresh solvent was compared to TiO₂ pellets where the supernatant pipetted out was then re-added i.e., the original solvent where the enzyme was added before centrifugation was investigated as a reaction medium. These experiments helped determine how much enzyme attached to the TiO₂ surface.

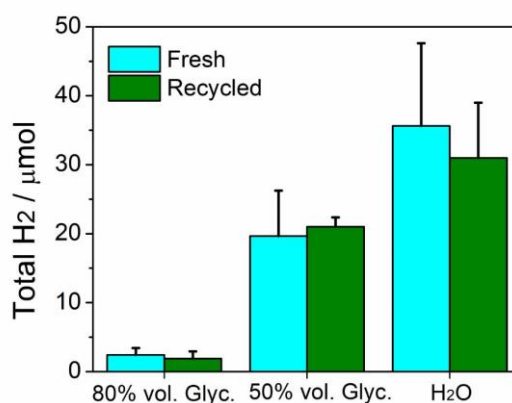


Figure 4.09. H₂ produced by [NiFeSe]-H₂ase – TiO₂ in fresh and resuspended solutions containing varying concentrations of glyceline after 9.3 h irradiation. Conditions. TiO₂ (5.0 mg), TEOA (0.4 M) 2.0 mL (fresh or resuspended), 40 °C, AM1.5G, constant N₂ purge.

The centrifuged TiO₂ catalyst produced 2.4±1.0 µmol_{H₂} after 9.3 h irradiation when fresh 80% vol. glyceline was used, and 1.9±1.0 µmol_{H₂} when the original supernatant was used to resuspend the centrifuged TiO₂ pellet. In fresh and recycled 50% vol. glyceline, TiO₂ showed higher performance with 19.6±6.6 µmol_{H₂} and 21.0±1.4 µmol_{H₂} detected respectively. In a purely aqueous solution, centrifuged TiO₂ resuspended in fresh H₂O produced 35.6±12.0 µmol_{H₂} while in re-used original supernatant the total H₂ evolved was comparable with 31.0±8.0 µmol_{H₂} produced.

It has been shown in the literature that the attachment of [NiFeSe]-H₂ase to TiO₂ in an aqueous solution is efficient, with transfer of electrons from TiO₂ to the enzyme outcompeting the transfer of electrons from a redox mediator relay.⁵⁷ This is confirmed by the results in Figure 4.09, whereby after mixing TiO₂ with [NiFeSe]-H₂ase and removal of the solution to add in a fresh solution without any enzyme, the photocatalytic performance is maintained. This trend is also observed in 80% vol. glyceline and 50% vol. glyceline, indicating that enzyme tethering to the TiO₂ surface is favourable despite the presence of DES. In addition, control experiments using TiO₂ without any co-catalytic enzyme irradiated in 80% vol. glyceline produced limited H₂, with 0.5 μmol_{H₂} detected after 24.1 h (Figure 4.10). The resuspension experiments highlight that at least some enzyme attaches to the TiO₂ surface even through the viscous DES.

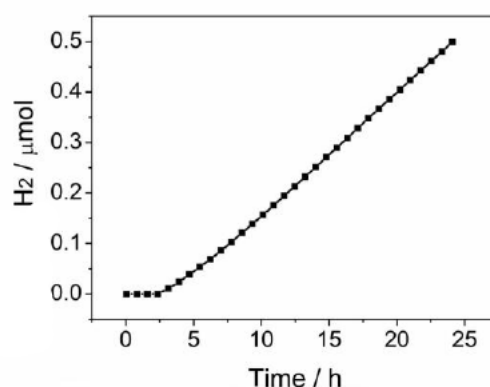


Figure 4.10. Control experiment showing H₂ evolution by TiO₂ without [NiFeSe]-H₂ase in 80% vol. glyceline. Conditions: TiO₂ (5.0 mg), 0.4 M TEOA, 2.0 mL, 40 °C, AM1.5G, constant N₂ purge.

4.5.4 Oxygen Tolerance of [NiFeSe]-H₂ase – TiO₂ in DESs

After highlighting the performance of [NiFeSe]-H₂ase – TiO₂ in organic-based DESs and having previously highlighted the ability of DESs to increase oxygen tolerance of photocatalysts for H₂ evolution, the [NiFeSe]-H₂ase – TiO₂ photocatalytic system was tested for aerobic photocatalytic H₂ evolution in the presence of DESs in comparison to water.

Figure 4.11 shows the total H₂ evolution by [NiFeSe]-H₂ase – TiO₂ in water under a continuous inert and aerobic purge. Under aerobic conditions, with an O₂ level of 21% the activity of the photocatalyst is almost completely quenched relative to its inert counterpart, with 2.7±1.3 μmol_{H₂} produced after 24.1 h irradiation (TON = 1.3±0.6 × 10⁵). This correlates to an overall O₂ tolerance of 3.6±1.7%, showing that while the enzyme does exhibit some oxygen tolerance as reported in the literature, the constant presence of O₂ shows the need for maintaining a suitable, highly reducing environment to realise the enzyme’s performance for aerobic H₂ evolution in water.

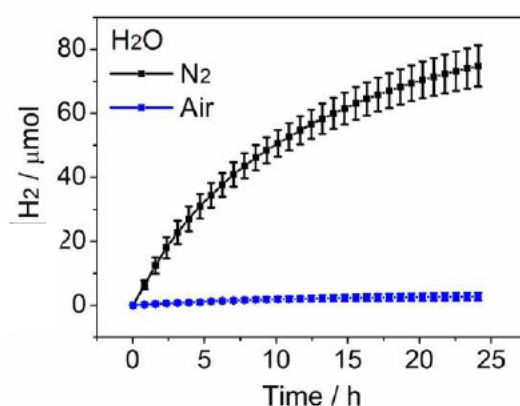


Figure 4.11. H₂ evolution by [NiFeSe]-H₂ase – TiO₂ in water in inert and aerobic conditions. Conditions: TiO₂ (5.0 mg), 21 pmol H₂ase, 0.4 M TEOA pH = 7.0, 2.0 mL, 40 °C, constant N₂ or air purge

The photocatalytic O₂ tolerance for the [NiFeSe]-H₂ase – TiO₂ system was also determined in solvents containing glyceline, as DESs have been shown to augment aerobic H₂ evolution versus water. As demonstrated in water, the catalytic activity is almost entirely quenched in aerobic conditions and so it was necessary to view the effect that simply changing solvent had on photocatalytic H₂ generation. The total H₂ produced when [NiFeSe]-H₂ase – TiO₂ is irradiated in varying concentration of glyceline in air and N₂ is shown in Figure 4.12. Moderate amounts of H₂ are produced in 80% vol. glyceline and 60% vol. glyceline relative to the total H₂ by the same catalyst in inert conditions, with 21.3±3.0 μmol_{H₂} (TON = 1.1±0.1 × 10⁶) and 34.0±6.0 μmol_{H₂} after 24.9 h respectively. The oxygen tolerance exhibited correlates to 88.5±12.7% and 64.4±14.8%. (Figure 4.12). The oxygen tolerance and total H₂ noticeably decreases as the glyceline content also decreases, with [NiFeSe]-H₂ase in 40% vol. glyceline, 30% vol. glyceline and 20% glyceline produced total H₂ amounts

of $13.9 \pm 2.1 \mu\text{mol}_{\text{H}_2}$, $11.6 \pm 4.9 \mu\text{mol}_{\text{H}_2}$ and $6.4 \pm 1.1 \mu\text{mol}_{\text{H}_2}$ respectively. This also relates to a lowered oxygen tolerance of the photocatalyst. The photocatalyst in 10% vol. glyceline exhibits performance and O_2 tolerance similar to water, with $3.0 \pm 2.8 \mu\text{mol}_{\text{H}_2}$ produced after 24.1 h with an O_2 tolerance of $3.5 \pm 3.3\%$.

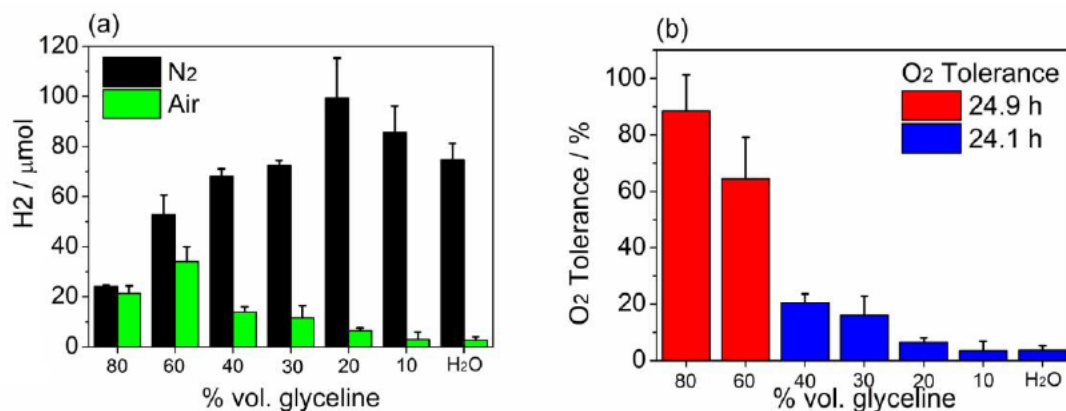


Figure 4.12. H₂ evolution of [NiFeSe]-H₂ase – TiO₂ in varying glyceline concentration and H₂O after 24.9 h (80% vol. glyceline, 60% vol glyceline) and 24.1 h (a) and oxygen tolerance calculated from total H₂ produced by [NiFeSe]-H₂ase – TiO₂ in in varying glyceline concentration and H₂O after 24.9 h (red) and 24.1 h (blue). Conditions: TiO₂ (5.0 mg), 0.4 M TEOA, 2.0 mL, 21 pmol H₂ase, 40 °C, AM1.5G, constant N₂ or air purge.

The photocatalytic O₂ tolerance values for [NiFeSe]-H₂ase – TiO₂ are summarised in Table 4.05. It is evident that decreasing the glyceline concentration aids in increasing photocatalytic performance under an inert atmosphere and shows similar behaviour to that of the photocatalyst in water. This suggests the enzyme favours a more aqueous environment for proton reduction. However, at high glyceline concentrations, aerobic H₂ production is higher in comparison to those solutions with little or no DES, and that tolerance of the enzyme for oxygen can be increased by increasing the glyceline concentration. Therefore, simply changing and tuning the solvent environment can aid to increase the photocatalytic performance for the [NiFeSe]-H₂ase enzyme under air.

Table 4.05. Summary of oxygen tolerance calculated from total H₂ produced by [NiFeSe]-H₂ase – TiO₂ in in varying glyceline concentration. Conditions: TiO₂ (5.0 mg), TEOA (0.4 M), H₂ase (21 pmol) 2.0 mL, 40 °C, AM1.5G, constant N₂ or air purge.

Glyceline Conc.	Total H ₂ – N ₂	Total H ₂ – air	O ₂ Tolerance
% Vol.	μmol	μmol	%
80	24.9±0.6	21.3±3.0	88.5±12.7 after 24.9 h
60	59.5±5.3	34.0±6.0	64.3±14.8 after 24.9 h

40	68.1±3.0	13.9±2.1	20.5±3.2 after 24.1 h
30	72.4±2.0	11.6±4.9	16.0±6.8 after 24.1 h
20	91.4±12.0	6.4±1.1	6.5±1.5 after 24.1 h
10	85.7±10.5	3.0±2.8	3.5±3.3 after 24.1 h

The apparent quantum yield (AQY) was calculated for the [NiFeSe]-H₂ase – TiO₂ photocatalyst in a 60% vol. glycine solution to examine the activity under monochromatic light. AQY was measured at a monochromatic wavelength of 405 nm, with the monochromatic filter placed in front of samples to prevent any other wavelength of light interacting with the reaction. The results from the AQY measurements for the photocatalyst in both inert and aerobic conditions are shown in Table 4.06. The AQY for H₂ evolution in aerobic reline was determined at 3.9±0.3% after 20 hours of irradiation which is within error identical to the AQY observed in anaerobic conditions. This indicates that charge carriers in the reaction system are not quenched or are limited in their interaction with O₂ in the samples, The retention of quantum efficiency shows that photogenerated electrons at the catalyst surface are more readily used for proton reduction over O₂ reduction.

Table 4.06 Apparent Quantum Yield (AQY) determination for anaerobic and aerobic photocatalytic H₂ evolution in 60% vol. glycine. Conditions: TiO₂ (5.0 mg) [NiFeSe]-H₂ase (21 pmol) 0.4 M TEOA, 2.0 mL, 40 °C, constant N₂ or air purge. $I = 5.29 \text{ mW cm}^{-2}$, $A = 2.5 \text{ cm}^2$, $\lambda = 405 \text{ nm}$ in N₂, $I = 5.33 \text{ mW cm}^{-2}$, $A = 2.5 \text{ cm}^2$, $\lambda = 405 \text{ nm}$ in air

Time h	n(H ₂) – N ₂ μmol	QE – N ₂ %	n(H ₂) – Air μmol	QE – Air %
1.1	1.7±0.1	2.3±0.2	1.7±0.3	2.3±0.4
2.1	3.6±0.2	2.2±0.3	3.3±0.5	1.9±0.2
3.1	5.4±0.3	2.1±0.3	4.5±0.6	1.7±0.4
4.2	7.1±0.5	2.2±0.4	6.2±0.8	1.5±0.4
5.2	8.9±0.6	2.0±0.4	7.3±0.8	1.4±0.3
10.1	15.5±1.3	1.5±0.2	11.0±1.3	0.7±0.3
15.3	21.3±1.9	1.3±0.2	13.2±2.1	0.4±0.3
23.9	29.1±2.9	1.0±0.1	15.5±3.8	0.4±0.3

The AQY results are in good agreement with the total H₂ produced in the 60% vol. glyceline solvent, with slow decay in catalytic activity in both inert and aerobic conditions and show a high degree of retention of quantum efficiency during the first few hours of irradiation with decrease over time, which can be attributed to the slower catalytic performance as the reaction is allowed to proceed.

This phenomenon of solvent tuning to increase photocatalytic oxygen tolerance was also observed when Eosin Y was used as a light absorber used in conjunction with 10 pmol [NiFeSe]-H₂ase. Notably the total H₂ evolution was much lower than heterogenous systems featuring TiO₂. 0.5 mM Eosin Y was irradiated in visible light by employing a UV cut-off filter ($\lambda > 400$ nm) in both water and solutions featuring glyceline. In water, the homogenous [NiFeSe]-H₂ase – EY catalyst produced 1.1±0.2 $\mu\text{mol}_{\text{H}_2}$ (TON = $1.0 \pm 0.2 \times 10^4$) after 4.7 h under inert conditions, and 0.5±0.1 $\mu\text{mol}_{\text{H}_2}$ with an experimentally observed photocatalytic oxygen tolerance of 44.6±9.0% (Figure 4.13). In the presence of glyceline, the [NiFeSe]-H₂ase – EY activity for H₂ evolution was much lower in comparison to water. In 60% vol. glyceline, [NiFeSe]-H₂ase – EY produced 0.07±0.02 $\mu\text{mol}_{\text{H}_2}$ in inert conditions, and 0.06±0.01 $\mu\text{mol}_{\text{H}_2}$ in the presence of air. In 30% vol. glyceline, the same photocatalyst produced 0.6±0.1 $\mu\text{mol}_{\text{H}_2}$ in nitrogen and 0.3±0.1 $\mu\text{mol}_{\text{H}_2}$. The lower catalytic H₂ evolution performance by Eosin Y in the presence of glyceline may be explained via the fact that direct electron transfer by the Eosin Y to the enzyme is limited from a diffusional aspect, whereby the more viscous solution does not allow for favourable interaction of the dye with the enzyme. Also, which has been previously discussed is the quenching effect of glycerol on excited Eosin Y, which can lower the lifetime of the excited state.⁶¹ As glyceline concentration decreases, H₂ production increases. However, again with increasing glyceline concentration, photocatalytic O₂ tolerance increases highlighting the strength of the DESs effect on limiting O₂ diffusion to compete with proton reduction. The catalytic activity of the Eosin Y ceases after 4 hours, which may be attributed to the quenching effect of air on photoexcitation processes occurring in Eosin Y.

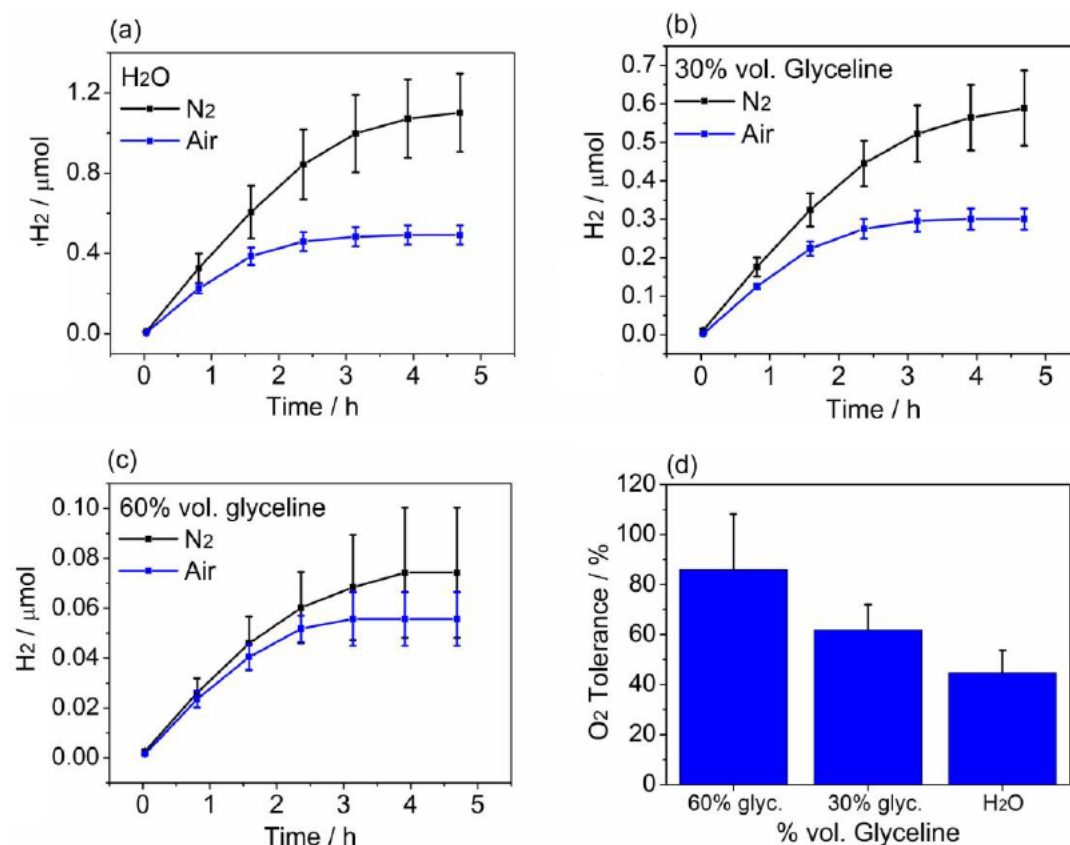


Figure 4.13. H₂ evolution of [NiFeSe]-H₂ase - Eosin Y after 4.7 h under inert conditions (black trace) and aerobic conditions (blue trace) in H₂O (a) 30% vol. glycine (b) 60% vol. glycine (c) and oxygen tolerance calculated from total H₂ produced by [NiFeSe]-H₂ase - Eosin Y after 4.7 h (d). Conditions: Eosin Y (0.5 mM), TEOA (0.4 M), pH 7, 2.0 mL, 10 pmol H₂ase, 40 °C, visible light irradiation ($\lambda > 400$ nm), constant N₂ or air purge.

4.5.5. Proton Mobility in DESs - Rationalising Enzymatic Performance

The diffusion coefficient and concentration of protons can be determined electrochemically using the technique of potential step microwire chronoamperometry. It can be hypothesised that the mobility and diffusion of protons to the enzyme impacts proton reduction in the enzyme active site. Limiting the availability of protons for the enzyme could possibly limit the H₂ production. Proton mobility has been studied before in a series of ILs, with potential step chronoamperometry at a Pt microdisc electrode in hydroxyl functionalized imidazolium ILs showing greater proton mobility than non-hydroxyl functionalised ILs.⁶² However, the diffusion of protons in choline chloride based DESs remains

unexplored and for this work it is important to understand the chemical behaviour of protons in DESs to rationalise H₂ production by the [NiFeSe]-H₂ase enzyme.

The microwire electrode used in this work was prepared by Professor Frank Marken at the University of Bath. A Pt microwire electrode was fabricated according to a literature procedure, with the same process followed in Chapter 3. Similar to the electrode used for the reduction of dioxygen in DESs, constructed, the precise length (*l*) of the active region was unknown and had to be calibrated electrochemically (see Materials and Methods for full experimental procedure). Using a three electrode setup with the microwire Pt electrode as a working electrode, Ag/AgCl as a reference electrode and Pt mesh as a counter electrode, cyclic voltammetry was used to determine the potentials at which the K₄[Fe(CN)₆] was oxidised and reduced (Figure 4.14). Since the diffusion coefficient in water is known the only unknown variable of the Shoup-Szabo equation is *l*. The procedure for determining the electrode length was the same as the procedure employed in Chapter 3, with the current decay at the Pt microwire electrode obtained from chronoamperometry fitted to the theoretical equation to optimise the value of *l*.

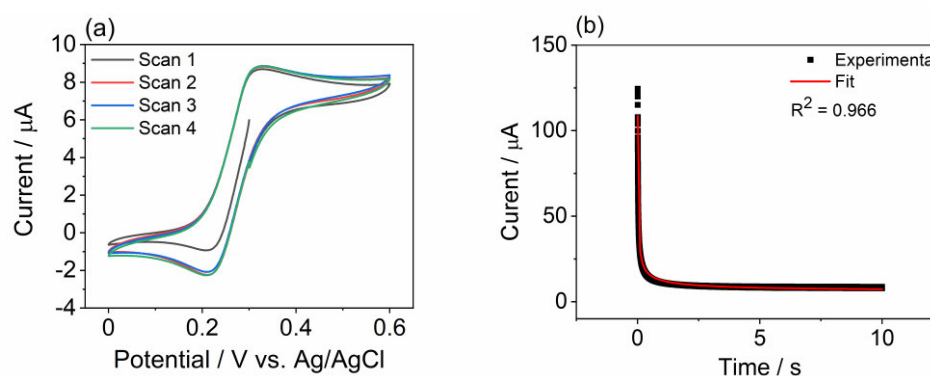


Figure 4.14. Cyclic voltammogram of 5.0 mM K₄[Fe(CN)₆] in 1 M NaCl (a) Experimental ferricyanide oxidation current decay from potential step chronoamperometry at a Pt microwire electrode (black trace) and fit of theoretical chronoamperogram for determination of electrode length (red trace). (b) Conditions: Pt microwire working electrode, Ag/AgCl reference electrode, Pt mesh counter electrode, 25 °C, scan rate = 50 mV s⁻¹ for CV, potential step from 0.0 V to 0.6 V vs. Ag/AgCl after 10 seconds. with 2 ms sampling time for chronoamperometry.

From the optimised fitting, the length can be determined with great approximation – in this case the length of the active region of the Pt microwire electrode was found to be 1.48 cm. The electrode could then be used to find the unknown values of the diffusion coefficients and concentrations of protons in the DESs.

The potential step for the reduction of protons had to be probed under inert conditions, as the intrinsic presence of dioxygen would disturb the current observed at the microwire electrode. Moreover, different potential steps were investigated to find the optimal values for the diffusion and concentration of protons in the solvents tested. First, in water with 1.0 M NaCl to act as an electrolyte, cyclic voltammetry was performed on the microwire Pt electrode, with a Ag/AgCl reference electrode and a Pt mesh counter electrode (Figure 4.15).

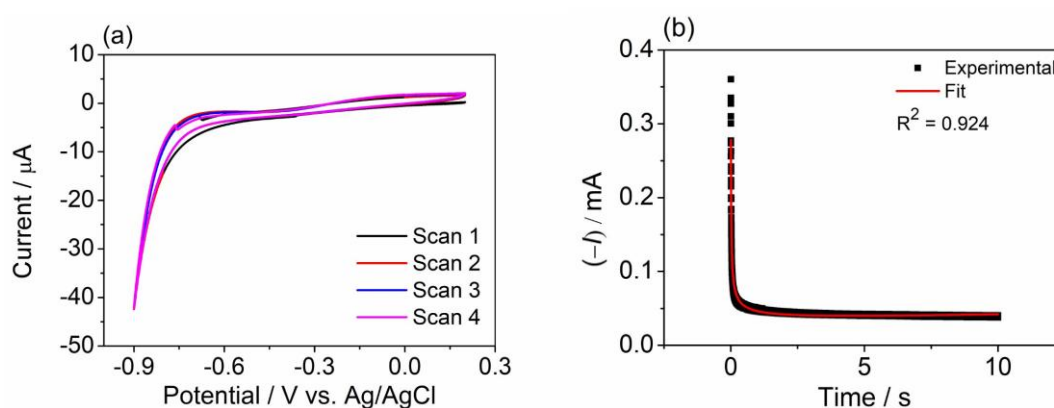


Figure 4.15. (a) Cyclic voltammogram of proton reduction at Pt microwire electrode in 1.0 M NaCl. Conditions: Pt microwire working electrode, Ag/AgCl reference electrode, Pt mesh counter electrode, 100 mL 40 °C, scan rate = 50 mV s⁻¹ (b) Experimental current decay from potential step chronoamperometry at Pt microwire electrode (black trace) in 1.0 M NaCl and fit of Shouh-Szabo equation for determination of diffusion coefficient and concentration of protons. Conditions: Pt microwire working electrode, Ag/AgCl reference electrode, Pt mesh counter electrode, potential step from 0.2 V to (-0.9) V vs. Ag/AgCl after 10 seconds, 100 mL, 40 °C

The diffusion coefficient and concentration of protons in 1.0 M NaCl was found to be $3.7 \pm 0.1 \times 10^{-9} \text{ m s}^{-1}$ and the concentration $5 \times 10^{-3} \text{ M}$, which is in line with results found in the literature.⁶³ Subsequently, cyclic voltammetry was performed in solvents of varying glyceline concentrations to view proton reduction at the Pt microwire electrode in inert conditions (Figure 4.16). The current is observed to increase with decreasing glyceline concentration – notably in 80% vol. glyceline the potential is notably shifted by 0.1 V versus the other DESs, indicating proton reduction is perhaps hindered in these conditions. The oxidation sweeps in the voltammograms highlight possible oxidation processes, which is most likely the oxidation of hydrogen formed during the reduction sweep. The same solutions were subject to potential step chronoamperometry to determine the diffusion coefficient and proton concentration, with Figure 4.17 and Table 4.07 showing the results of

the simultaneous fitting of the D and c parameters of the theoretical current to the experimentally observed current.

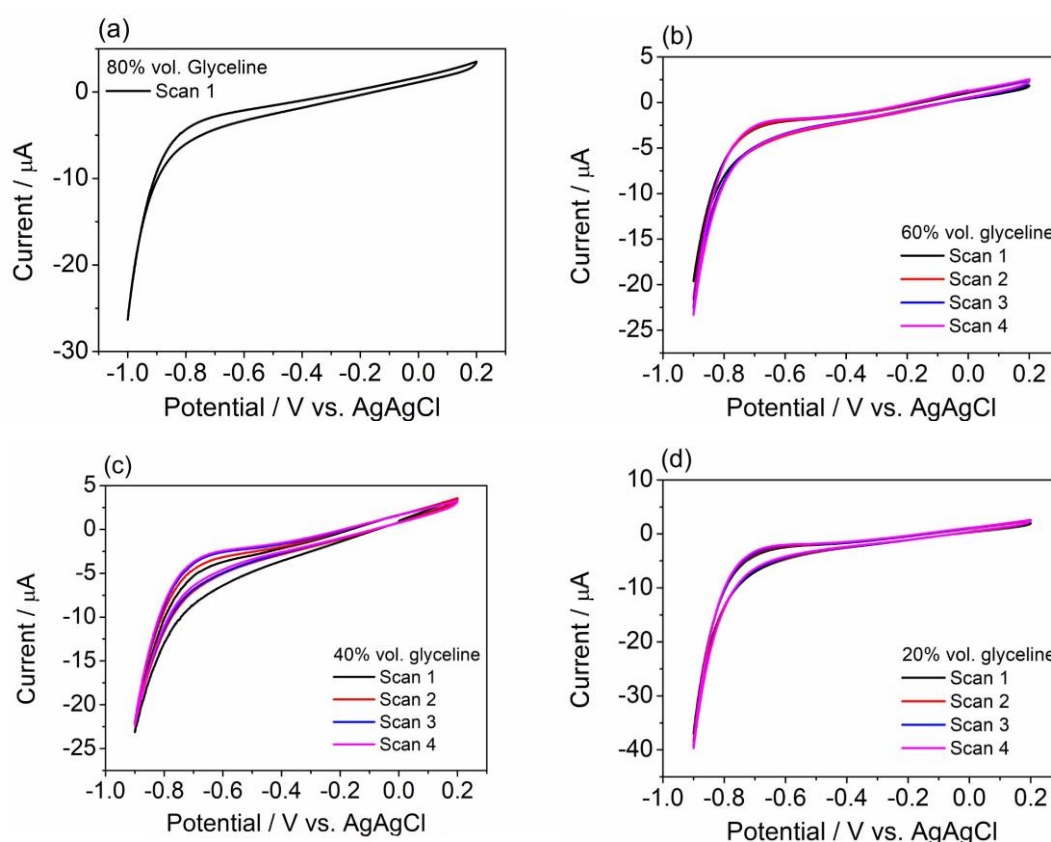


Figure 4.16. Cyclic voltammogram of proton reduction under inert conditions at Pt microwire electrode in (a) 80% vol. glyceline (b) 60% vol. glyceline (c) 40% glyceline and (d) 20% glyceline. Conditions: Pt microwire working electrode, Ag/AgCl reference electrode, Pt mesh counter electrode, 100 mL, 40 °C, 1.0 M NaCl, scan rate = 50 mV s^{-1}

Some interesting observations can be made from the chronoamperometric traces and the fitting of D and c values for understanding proton behaviour in the presence of DESs. 80% vol. glyceline showed optimal fitting when $D = 5.75 \pm 0.1 \times 10^{-9} \text{ m}^2 \text{ s}^{-1}$ and $c = 2.42 \pm 0.01 \times 10^{-3} \text{ M}$ with a potential step from 0.2 V to (-1.0) V vs. Ag/AgCl. Similar values are obtained when fitting D and c to the current trace observed in 60% vol. glyceline, with D calculated as $5.30 \pm 0.1 \times 10^{-9} \text{ m}^2 \text{ s}^{-1}$ and $c = 2.70 \pm 0.1 \times 10^{-3} \text{ M}$. The diffusion of protons is found to be slower with decreasing glyceline concentration, as D was determined to be $3.46 \pm 0.5 \times 10^{-9} \text{ m}^2 \text{ s}^{-1}$ and $3.58 \pm 0.1 \times 10^{-9} \text{ m}^2 \text{ s}^{-1}$ in 40% vol. glyceline and 20% vol. glyceline respectively. The opposite trend was observed with the proton concentration, as an increase in proton concentration was conducive to a decrease in glyceline concentration, with $4.07 \pm 1.0 \times 10^{-3} \text{ M}$ and

$5.97 \pm 1.3 \times 10^{-3}$ M calculated in 40% vol. glyceline and 20% vol. glyceline respectively.

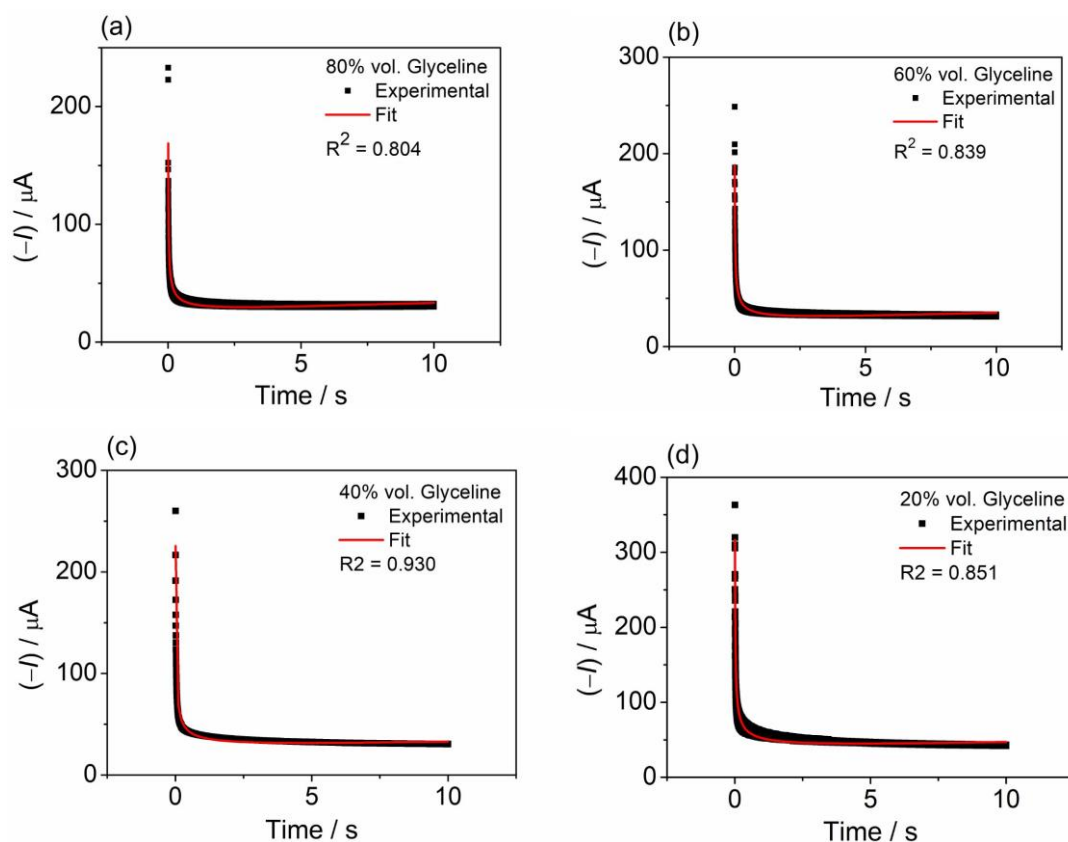


Figure 4.17. Experimental current decay from potential step chronoamperometry at Pt microwire electrode (black trace) and fit of Shouub-Szabo equation (red trace) for simultaneous determination of diffusion coefficient and concentration of protons in (a) 80% vol. glyceline (b) 60% vol. glyceline, (c) 40% vol. glyceline and (d) 20% glyceline. Conditions: Pt microwire working electrode, Ag/AgCl reference electrode, Pt mesh counter electrode, NaCl (1.0 M), potential step from 0.2 V to (-1.0) V vs. Ag/AgCl after 10 seconds, 100 mL, 40 °C

Table 4.07. Proton concentration and diffusion coefficient in solvents of varying glyceline concentration, determined by potential step chronoamperometry at a Pt microwire electrode.

Glyceline % vol.	$c(H^+)$ M	$D(H^+)$ $m^2 s^{-1}$
80	$2.42 \pm 0.01 \times 10^{-3}$	$5.75 \pm 0.1 \times 10^{-9}$
60	$2.70 \pm 0.1 \times 10^{-3}$	$5.30 \pm 0.1 \times 10^{-9}$
40	$4.07 \pm 1.0 \times 10^{-3}$	$3.46 \pm 0.5 \times 10^{-9}$
20	$5.97 \pm 1.3 \times 10^{-3}$	$3.58 \pm 0.1 \times 10^{-9}$
0 (H ₂ O)	5.0×10^{-3}	$3.70 \pm 0.1 \times 10^{-9}$

Solvents containing less glyceline exhibit almost double the number of protons, with the general trend observed as a lower DES concentration leads to an increase in available protons. This may be a result of the increased protons available through the addition of water in the solutions – as water is a protic solvent, the likelihood of free protons dissociating and becoming reduced is likely to occur. It has already been discussed that above a certain water content, DESs tend to lose their properties and adopt those resembling aqueous solutions. This may also lead to an explanation as an increase in H₂ evolution, as solvents which show the higher proton concentrations also show the higher photocatalytic activity.

The diffusion of protons in the glyceline-based solvents shows an interesting relationship. It appears that proton diffusion is inversely proportional to photocatalytic H₂ production, with the solvents invoking a more active environment for photocatalysis showing slower proton diffusion. The increase in glyceline concentration may increase the proton diffusion through the vast array of hydrogen bonds present, as it has been shown previously that proton mobility via the Grotthus mechanism increases in hydroxyl functionalised ILs increase.⁶² It can be argued that the alcoholic hydroxyl group of the glycerol present in glyceline can serve as both proton acceptor and proton donor, thus enabling the formation of hydrogen bonding networks.⁶⁴

Interestingly this is also observed in an ethaline-based solution - a 60% vol. ethaline was subject to potential step chronoamperometry using the same Pt microwire electrode to determine the mobility and concentration of protons (Figure 4.18). Optimised simultaneous fitting of the diffusion coefficient and concentration of protons yielded values of $3.46 \pm 0.3 \times 10^{-9} \text{ m}^2 \text{ s}^{-1}$ and $1.80 \pm 0.3 \times 10^{-3} \text{ M}$. Cyclic voltammetry at the electrode when tested showed the presence of a small amount of oxygen, highlighted by a drop in the reduction current, as well as possessing a wave concurrent with O₂ reduction at around 0.5 V vs Ag/AgCl. The solution was then purged again to remove any excess O₂ prior to potential step chronoamperometric measurements.

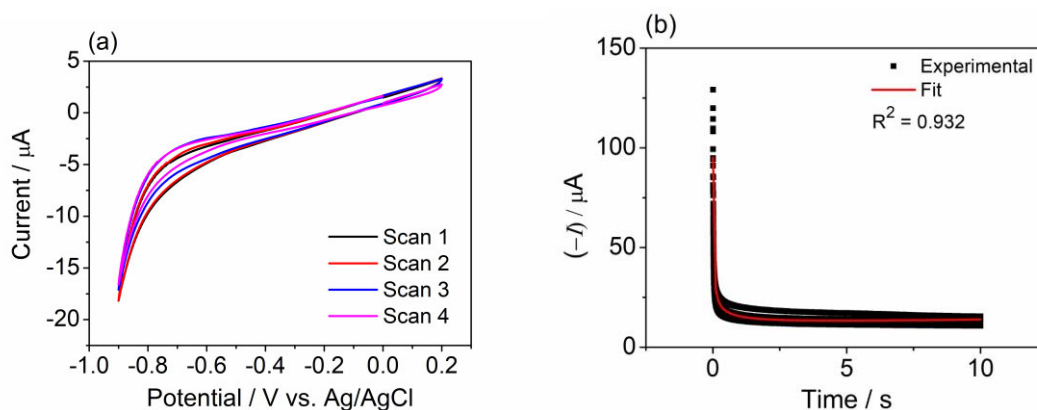


Figure 4.18. Cyclic voltammogram of 60% vol. ethaline (a) Experimental current decay from stepped-potential chronoamperometry at Pt microwire electrode (black trace) and fit of Shoub-Szabo equation for simultaneous determination of diffusion and concentration of protons (red trace). (b) Conditions: Pt microwire working electrode, Ag/AgCl reference electrode, Pt mesh counter electrode, NaCl (1 M), 100 mL 40 °C, scan rate = 50 mV s⁻¹ for CV, potential step from 0.2 V to (-0.9) V vs. Ag/AgCl after 10 seconds. with 2 ms sampling time for chronoamperometry.

Upon comparison of the D and c values obtained in 60% vol. ethaline and 60% vol. glyceline, the mobility of protons appears to be slightly lower in 60% vol. ethaline compared to 60% vol. glyceline, as well as a lower proton concentration. The observed total H₂ produced photocatalytically is almost double in 60% vol glyceline versus 60% ethaline, and so it may be concluded that proton mobility as well as the availability of protons in the solvent are determining factors for maximum performance of the enzyme.

However, it is apparent that creating an environment where protons are more mobile does not lead to an increase in the proton reduction rate of the enzyme. In cases where proton mobility is high, we assume that the enzyme's activity is not limited by proton diffusion. It can be rationalised then that activity where proton mobility is high is limited by the proton reduction kinetics at the enzyme's active site. In cases when the diffusion of protons is deemed to be slower i.e., in more aqueous-based solvents, diffusion is rate limiting. Further studies to decipher the relationship between proton mobility and photocatalytic activity may also show changes in conformation of the enzyme or DES components interacting with chemical features of the enzyme. The oxygen tolerance of the enzyme is still governed by the diffusion and concentration of dissolved oxygen in the solution,

whereby in higher DES concentrations, the diffusion and concentration of oxygen is smaller in comparison to water.

4.5.6. Electrochemical Studies of a [NiFeSe]-H₂ase Electrode in the Presence of Glycine

Studying enzymes on electrode surfaces is an effective way of determining electrode-protein electron transfer kinetics, with the focus on recording the transfer of electrons and subsequent catalytic activity.^{11, 65} It is important to ensure that enzymes when undergoing electrochemical studies are electronically bound to the electrode substrate, as the electron exchange between the electrode and enzyme in solution provides inconclusive results about the true nature of the electron transfer capabilities.^{11, 66}

These experiments were performed by Thomas Pichon and Alan Le Goff at Université Grenoble Alpes. To view the electrocatalytic performance of [NiFeSe]-H₂ase in the presence of glycine, a multiwalled carbon nanotube (MWCNT) electrode saturated with [NiFeSe]-H₂ase was employed as the working electrode (see Materials and Methods for full experimental information). MWCNTs offer enlarged surface areas versus conventional glassy carbon electrodes, allowing more enzyme to be absorbed onto the electrode, as well as exposing more of the electrode to the electrolyte. The activity of the MWCNT-H₂ase electrode was studied with cyclic voltammetry, swept from 0.0 V to (-0.75 V) at a scan rate of 0.01 V s⁻¹, with varying glycine concentration (Figure 4.19). The reference electrode for electrochemical analyses was a saturated calomel electrode (SCE). The activity of the [NiFeSe]-H₂ase – MWCNT was also compared to a standard aqueous pH 6.5 phosphate buffer.

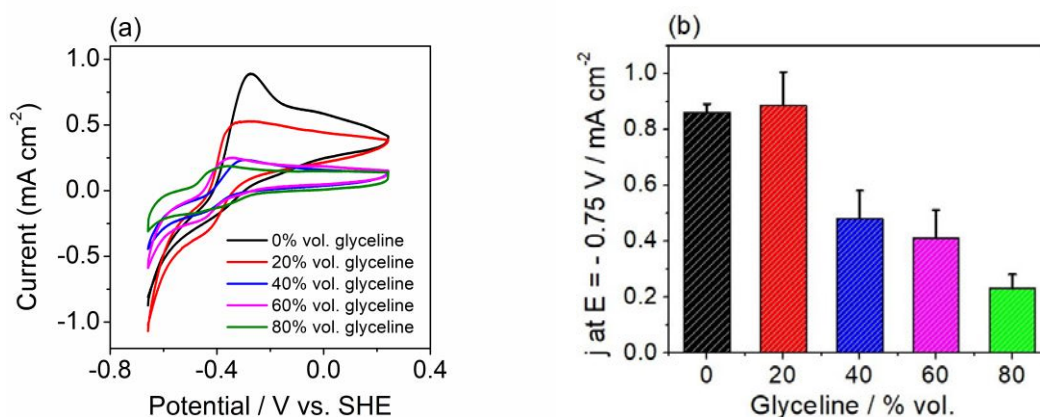


Figure 4.19. (a) Cyclic voltammogram from 0.0 V to (-0.75 V) vs. SHE of [NiFeSe]-H₂ase – MWCNT electrode in K₂HPO₄ phosphate pH 6.5 (black trace) and glyceline of varying concentrations. Red trace indicates water with no additional glyceline. Conditions: [NiFeSe]-H₂ase – MWCNT working electrode, saturated calomel reference electrode (SCE), Pt rod counter electrode, TEOA (0.4 M) pH 7.0, 25 °C, 0.01 V s⁻¹ scan rate, de-aerated (O₂ free) solution. The electrochemical measurements were performed By Thomas Pichon and Alan le Goff at Université Grenoble Alpes

The voltammograms show decreasing current with decreasing glyceline concentration and oxidative sweeps show an onset of an oxidation process at around (-0.3 V) vs. SHE which is attributed to H₂ oxidation formed during the reduction sweep. Notably, 20% vol. glyceline (red trace) shows almost similar electrochemical activity to the pH 6.5 phosphate buffer highlighted by the same current detected at (-0.75 V) vs. SHE. The current density shows quite neatly a near linear decrease with increasing glyceline concentration, similar in behaviour to the [NiFeSe]-H₂ase activity in photocatalysis.

4.6. Discussion

There are many factors to consider when utilising enzymes in photocatalytic solar fuel reaction systems. Hydrogenases, and enzymes in particular, are inherently sensitive to pH. A pH too high or low can cause denaturation of the protein structure. Enzymes adopt a certain structure to maximise/minimise hydrophilic/hydrophobic interactions with its external environment. Changes in pH and temperature can alter this protein structure and cause the enzyme to cease functioning.

The pH of DESs and their effect on enzyme structure has not thoroughly been touched on in this chapter and leaves room for interpretation and rationality. The solvents used for experimental purposes contain a controlled quantity of water,

which in turn contains a certain concentration of TEOA to ensure the final TEOA concentration is 0.4 M. The TEOA added to the DES solution is adjusted to pH 7.0 using HCl and measured with a pH probe prior to mixing. Not much is known about the final pH of the solution containing water, TEOA and DES, or the pH properties of DESs in general with the pH determined for a vast array of DESs determined computationally.⁶⁷ Some results in the literature show that choline chloride : fructose DESs all show a slight acidity (pH ~ 6) with an increase to more alkaline with increasing temperature.⁶⁸ Dilute solutions of DESs have also been studied using a conventional pH probe, where the DES concentration was 0.5 M in water, which showed that the pH of ethaline and glyceline at 25 °C were both between 4.5 and 5.0.⁶⁹ This slight acidity is attributed to the fact that the HBD component for ethaline and glyceline – ethylene glycol and glycerol, respectively – are both weak acids as they possess hydroxyl groups. In solution, when the water concentration is larger than the DES concentration, the DES largely becomes dissociated and forms individual species dissolved in situ, and so this acidity likely arises from free ethylene glycol and glycerol.

It is also unclear what effect the DES has on the pH 7.0 TEOA solution. It is possible that the pH of the TEOA solution is altered when mixed with a DES. In fact, due to the acidic nature of the HBD in ethaline in glyceline, in high concentrations of DES the TEOA may experience a more acidic shift. The shift of pH on TEOA away from neutrality is known to hinder its performance as a sacrificial electron donor, and a lower pH suggests that more TEOA becomes protonated. This lowers the kinetic potential of electron donation to quench photogenerated positive holes in the TiO₂. This in turn lowers the H₂ evolution activity in semiconductor-based photocatalytic systems. As shown, the photocatalytic activity in a high concentration of DES shows limited activity in comparison to those solvents containing more water. The high DES concentration inducing protonation on the TEOA may be a contributing factor to the decrease in activity.

However, potential step chronoamperometry allows us to calculate with good approximation the proton concentration in solution. As pH is a function of proton concentration, the experimentally obtained proton concentration values can be applied to Equation (4.05):

$$\text{pH} = -\log_{10}[\text{H}^+] \quad (4.05)$$

Table 4.08. Proton concentration and pH in solvents of varying glyceline concentration, determined by potential step chronoamperometry at a Pt microwire electrode.

Glyceline % vol.	c(H⁺) M	pH
80	$2.42 \pm 0.01 \times 10^{-3}$	2.6
60	$2.70 \pm 0.1 \times 10^{-3}$	2.6
40	$4.07 \pm 1.0 \times 10^{-3}$	2.4
20	$5.97 \pm 1.3 \times 10^{-3}$	2.2
0 (H ₂ O)	5.0×10^{-3}	2.3

The concentration and pH's shown here, particularly of those in more aqueous solutions show acidity which is significantly lower from that presented in the literature and also show a strange result in that water has an acidic pH. This result may arise from the incomplete reduction of protons in the solutions, and so the concentration determined is only the apparent concentration. To investigate this, the potential step at the Pt microwire electrode should be increased. Systematically increasing the potential step to where the diffusion coefficient no longer changes while the concentration does change would indicate the potential is in the range for reduction of protons in solution. This is because the diffusion regime for the Shoub-Szabo equation is in the time domain for the current decay (where the tails off and gradually reaches zero), and so no change in the diffusion coefficient means current decay measured is dependent on concentration of the analyte. Moreover, as the glyceline and ethaline HBD components themselves contain protons, it is possible that at more negative, highly reducing potentials, protons from the HBD could become reduced, which would interfere with the current transients observed at the working electrode.

The pH of the solvents could also be estimated from the cyclic voltammograms obtained from the [NiFeSe]-H₂ase MWCNT electrode. Where the voltammogram intercepts when current = 0.0 mA, the equilibrium potential for the 2H⁺/H₂ couple can be estimated by extrapolating the intercept to the x-axis. By determining the

potential in this manner, the concentration of protons can be estimated and from this, a pH deduced.^{47,70}

4.7. Conclusion

A [NiFeSe]-H₂ase has been shown to be photocatalytically and electrocatalytically active in organic DESs. Organic solvents are not normally suitable for enzyme applications due to their hydrophobic nature. However, tuning the DES through optimising water content, and indeed through tuning the solvents themselves through selection of HBD component can alter photocatalytic activity of the [NiFeSe]-H₂ase on a TiO₂ light absorber. [NiFeSe]-H₂ase exhibits good affinity for the TiO₂ photocatalyst as shown through resuspension experiments, which highlight the suitability of DESs as reaction solvents. The effect of DESs on enzyme structure could be studied to better understand redox processes at the enzyme active site. pH has an effect on the photocatalytic H₂ performance, arguably as a result of shifting away from optimal functioning pH for the [NiFeSe]-H₂ase. The enzymatic activity is high even after long irradiation periods, achieving high TONs and TOFs even after 24 hours and 72 hours irradiation in DES-based solvents. The O₂ tolerance of the photocatalytic system can also be increased, again through tuning the solvent conditions with high DES concentrations showing higher O₂ tolerances vs. water which likely arises through the lower O₂ diffusivity and O₂ concentration arising from the DES. As a result, AQYs of the [NiFeSe]-H₂ase – TiO₂ photocatalyst are retained, again even after lengthy irradiation periods. The tuning of the DES solvent can also augment the photocatalytic activity for homogenous photocatalysts, with glyceline aiding in increasing the O₂ tolerance of [NiFeSe]-EY versus water.

Microwire chronoamperometric determination of proton concentration and mobility was successfully carried out with a homemade Pt microwire electrode. This Pt microwire was used to perform cyclic voltammetry and potential step chronoamperometry in solutions containing DES. Through optimisation of the diffusion coefficient and concentration parameters, theoretical chronoamperometric current traces were fitted with success to experimental current traces using the Shoub-Szabo equation to enable the determination of proton concentration and diffusion coefficient in solvents containing DES.

A MWCNT electrode was coated with [NiFeSe]-H₂ase and used as a working electrode to successfully show the relationship between decreasing current with increasing glyceline concentration. This approach also shows that electrochemical analysis can be used to rationalise the proton reduction ability of materials tested for photocatalytic proton reduction. Studying the reaction environment and tuning / functionalising solvents to envision catalytic behaviour can be transferred to different fields of chemistry, and shows how electrochemistry and photocatalysis can work in tandem to investigate novel reaction conditions.

4.8. Materials and Methods

Chemical Reagents

All chemical reagents used for this work were used as purchased and without further purification. Choline chloride (>99%), urea (analytical grade, 99.5%), ethylene glycol (>99%), glycerol (>99%), Titanium (iv) oxide (P25, Aeroxide®) triethanolamine (>98%), Eosin Y, disodium salt (certified pure), sodium chloride (>99%), potassium ferrocyanide trihydrate (crystalline, certified pure), hydrochloric acid (37% w/w, extra pure) were all purchased from Fisher Scientific. 18.2 mΩ water was used throughout the experiments. Pt microwire ($d = 50 \mu\text{m}$, 99.99%) was purchased from Advent UK.

Synthesis of Deep Eutectic Solvents

Reline, glyceline and ethaline were prepared in accordance with literature procedures, by stirring choline chloride with urea, glycerol, and ethylene glycol, respectively in a 1:2 molar ratio at 80 °C until a homogenous liquid had formed.^{71,72}

Purification of [NiFeSe]-H₂ase

[NiFeSe]-H₂ase was purified from the bacterium *Desulfomicrobium baculatum* according to a literature procedure.⁷³ The enzyme was prepared in the lab of Dr. Christine Cavazza at Université Grenoble Alpes, and was a kind gift from Dr. Alan le Goff (September 2021). The initial concentration of [NiFeSe]-Tris stock was 34 μM.

Treatment of data

All photocatalysis, dye degradation and electrochemistry measurements were performed in triplicate and are given as the unweighted mean \pm standard deviation (σ). σ of a measured value was calculated using equation (4.06), where n is the number of repeated measurements, x is the value of a single measurement and \bar{x} is the unweighted mean of the measurements.

$$\sigma = \sqrt{\frac{\sum(x - \bar{x})^2}{n - 1}} \quad (4.06)$$

Preparation of Samples

All samples used in the experiments were prepared in the following manner unless otherwise stated. TiO₂ powder (5.0 mg) was weighed into a glass sample vial (Chromacol, 10-SV) along with 2.0 mL of solvent and a stir bar. Samples were briefly vortexed and then sonicated in a sonic bath for 20 minutes. The solutions were capped with a rubber septum and purged with N₂ gas from MFCs (Bronkhorst) with a flow rate of 20 mL min⁻¹ for 10 minutes to de-aerate the solutions. The samples were then introduced into a glovebox under an inert atmosphere (Saffron, O₂ level < 5.0 ppm) as well as an aliquot of [NiFeSe]-H₂ase at a concentration of 2.1 $\times 10^{-3}$ mM. The septa were removed from the sample, and 0.01 mL of this enzyme stock was added to each sample, giving a final number of moles of enzyme at 21 pmol. Samples were then re-sealed in the glovebox and irradiated in a solar simulator (Newport Oriel) upon removal from the glovebox at an intensity of 1 sun for a given period of time. For samples containing Eosin Y, 1 μ mol (0.5 mM) of Eosin Y was used instead of TiO₂ and 10 pmol of enzyme was the molar enzyme quantity.

Resuspension Experiments

Samples were prepared as above with TiO₂, and [NiFeSe]-H₂ase was added as described above in the glovebox. Once the enzyme was added, samples were briefly stirred in the glovebox for 30 minutes at 600 rpm. These solutions containing enzyme and TiO₂ were decanted into centrifuge tubes in the glovebox and then sealed. The centrifuge tubes were removed from the glovebox and centrifuged on a benchtop centrifuge at 5000 rpm. Pellets of TiO₂ were recovered by removal of the supernatant in the glovebox, and the pellets were then resuspended in a fresh solution of the same nature as the decanted supernatant but without hydrogenase.

For samples with recycled supernatant, the supernatant originally decanted off after initial centrifugation was added again (to account for any losses during decanting) and used to resuspend the TiO₂ pellets.

Physical Measurements

Sample Analysis by Gas Chromatography (GC). Gas chromatography was performed on a Shimadzu Nexis GC-2030 gas chromatograph equipped with a barrier-discharge ionisation detector (BID) and a molecular sieve column. The total run time of the method was 5 minutes. The GC was calibrated using calibration gas (2000 ppm H₂, BOC), diluted with N₂ at different ratios using a set of mass flow controllers (Bronkhorst) to provide known concentrations of H₂. Gas samples were programmed to auto-inject into the GC via a multiport stream selector valve directing the selected sample purge gas stream through a 2 mL sample loop before injection. H₂ evolution rates were calculated from the measured H₂ concentration in the purge gas and the purge gas flow rate. Cumulative H₂ production was calculated from the H₂ evolution rate and time passed since the previous measurement, assuming a constant H₂ evolution rate between time points. All samples were performed in triplicate (unless otherwise stated).

Microelectrode Preparation.

The microwire electrode used in this work was prepared by Professor Frank Marken at the University of Bath. A Pt microwire electrode was fabricated according to a literature procedure.^{63, 74} A rectangular window (approx. 1×3 cm) was cut out of a strip of laminating plastic foil (approx. 3×10 cm). A length of Pt microwire (50 μm diameter, Advent UK) was inserted between the laminating sheets so to expose part of the Pt wire through the window. The laminating foil was first sealed with a domestic iron, and then additionally sealed with epoxy resin to prevent the Pt wire inside the foil from coming into contact with the electrolyte.

Electrode Length Determination.

The length of the Pt microwire electrode was accurately determined in a 5 mM potassium ferrocyanide solution containing 1.0 M aqueous NaCl (pH not adjusted). Cyclic voltammetry (CV, $v = 50 \text{ mV s}^{-1}$) was performed to determine the potential

step parameters for chronoamperometry. A potential step chronoamperogram was recorded (sampling rate 2 ms), holding at 0.0 V for 10 s before stepping to +0.6 V vs. Ag/AgCl and holding for another 10 s. A simulated current (I_{theo}) was calculated by applying the ferrocyanide concentration (5 mM) and diffusion coefficient ($6.5 \times 10^{-10} \text{ m}^2 \text{ s}^{-1}$) to Equation (4.03).⁷⁵ The fitting was optimised in Origin Lab software, giving a calibrated electrode length of $1.4804 \pm 0.002 \text{ cm}$.

$$I_{\text{theo}}(t) = nFDc \times \left(\frac{\pi \times e^{-\frac{2}{5} \times \sqrt{\pi \frac{Dt}{16r^2}}}}{4 \sqrt{\pi \frac{Dt}{16r^2}}} + \frac{\pi}{\ln \left[\sqrt{\left(64 \times e^{-0.5772 \times \frac{Dt}{16r^2}} \right) + e^{\frac{5}{3}}} \right]} \right) \quad (4.03)$$

Where I is the current, n is the number of transferred electrons, F is Faraday's constant, l is the electrode length, D is the O_2 diffusion coefficient, c is the O_2 concentration, t is the time, and r is the electrode radius.

Proton Mobility and Concentration Determination in DESs.

The O_2 diffusion coefficient and the concentration of dissolved O_2 in the different DESs were determined by O_2 reduction at the Pt microwire working electrode in an analogous manner to the electrode length determination. CVs were performed in each DES (scan rate = 50 mV s^{-1}) to determine the potential step parameters E_1 and E_2 . A potential step chronoamperogram was recorded (sampling time 2 ms) by holding at E_1 for 10 s before stepping to E_2 and holding for another 10 s. A simulated current (I_{theo}) was calculated by applying the calibrated electrode dimensions ($l=1.4804 \text{ cm}$, $r=25 \text{ }\mu\text{m}$) to Equation (4.03). Values for c and D were obtained by a least squares refinement using the Origin programme, using a concatenated fit of 3 individual measurements per solvent.

[NiFeSe]-H₂ase – MWCNT Electrode Preparation

The [NiFeSe]-H₂ase – MWCNT electrodes were prepared in the lab by Dr. Alan le Goff and Thomas Pichon at Université Grenoble Alpes (May 2022).

N-methyl-2-pyrrolidone (NMP) dispersions of MWCNTs were prepared by 30 min sonication of 5 mg MWCNTs dispersed in 1 mL NMP until a homogeneous black suspension was obtained. Then 20 μL of the MWCNTs solution were drop-casted on

a glassy carbon electrode and NMP was removed under vacuum leaving a 5- μm -thick film on the GCE. MWCNT-modified electrodes were soaked for 1 h in DMF solution containing 10 mM of 1-pyrenebutyric acid adamantyl amide and thoroughly washed with DMF and distilled water. The functionalized electrodes were then incubated with 20 μL of the enzymatic solution (1.5 mg mL^{-1}) in 50 mM sodium phosphate buffer at pH 7.6 for 1 hour at room temperature. The electrodes were finally washed with buffer and stored in the respective buffer when not in use.

[NiFeSe]-H₂ase – MWCNT Electrochemical Setup

The electrochemical measurements were performed by Thomas Pichon and by Dr. Alan le Goff at Université Grenoble Alpes (May 2022).

The electrochemical experiments were carried out in a three-electrode electrochemical cell using a Biologic VMP3 Multi Potentiostat. The MWCNT bioelectrodes were used as working electrodes. Pt wire was used as counter electrode and the Saturated Calomel Electrode (SCE) served as reference electrode. The experiments were conducted at room temperature. All current densities are normalized towards the geometrical surface of the glassy carbon electrode (0.071 cm^2). Prior to experiments, the hydrogenase-modified electrodes were activated by poisoning the electrode at -1 V vs SCE for ten minutes.

4.9. References

1. J. Yang, H. Yan, X. Zong, F. Wen, M. Liu and C. Li, *Philos. Trans. R. Soc. London, Ser. A*, 2013, **371**, 20110430.
2. H.-L. Chou, B.-J. Hwang and C.-L. Sun, in *New and Future Developments in Catalysis*, ed. S. L. Suib, Elsevier, Amsterdam, 2013, 1st edn., vol. 1, ch. 9, pp. 217-270.
3. B. Hinnemann, P. G. Moses, J. Bonde, K. P. Jørgensen, J. H. Nielsen, S. Horch, I. Chorkendorff and J. K. Nørskov, *J. Am. Chem. Soc.*, 2005, **127**, 5308-5309.
4. Y.-J. Yuan, H.-W. Lu, Z.-T. Yu and Z.-G. Zou, *ChemSusChem*, 2015, **8**, 4113-4127.
5. W. Wang, T. Li, S. Komarneni, X. Lu and B. Liu, *J. Colloid Interface Sci.*, 2022, **608**, 1553-1575.
6. P. M. Vignais, B. Billoud and J. Meyer, *FEMS Microbiol. Rev.*, 2001, **25**, 455-501
7. P. M. Vignais and B. Billoud, *Chem. Rev.*, 2007, **107**, 4206-4272.
8. V. Engelbrecht and T. Happe, in *Methods Enzymology*, ed. F. Armstrong, Academic Press, Massachusetts, 2018, 1st edn., vol. 613, ch 8, pp. 203-230.
9. J. W. Peters, W. N. Lanzilotta, B. J. Lemon and L. C. Seefeldt, *Science*, 1998, **282**, 1853-1858.
10. Y. Nicolet, C. Piras, P. Legrand, C. E. Hatchikian and J. C. Fontecilla-Camps, *Structure*, 1999, **7**, 13-23.

11. K. A. Vincent, A. Parkin and F. A. Armstrong, *Chem. Rev.*, 2007, **107**, 4366-4413.
12. R. D. Bethel and M. Y. Darensbourg, *Nature*, 2013, **499**, 40-41.
13. L. F. Wu and M. A. Mandrand, *FEMS Microbiol. Rev.*, 1993, **10**, 243-269.
14. W. Lubitz, H. Ogata, O. Rüdiger and E. Reijerse, *Chem. Rev.*, 2014, **114**, 4081-4148.
15. J. R. Lancaster, *The Bioinorganic Chemistry of Nickel*, Wiley-VCH, Weinheim, 1988.
16. C. C. Page, C. C. Moser, X. Chen and P. L. Dutton, *Nature*, 1999, **402**, 47-52.
17. C. C. Moser, C. C. Page, R. Farid and P. L. Dutton, *J. Bioenerg. Biomembr.*, 1995, **27**, 263-274.
18. J N Onuchic, D N Beratan, a. J R Winkler and H. B. Gray, *Annu. Rev. Biophys. Biomol. Struct.*, 1992, **21**, 349-377.
19. M. McCullagh and G. A. Voth, *J. Phys. Chem. B*, 2013, **117**, 4062-4071.
20. M. L. K. Sanchez, C.-H. Wu, M. W. W. Adams and R. B. Dyer, *Chem. Commun.*, 2019, **55**, 5579-5582.
21. Y. Higuchi, T. Yagi and N. Yasuoka, *Structure*, 1997, **5**, 1671-1680.
22. H. Ogata, W. Lubitz and Y. Higuchi, *Dalton Trans.*, 2009, 7577-7587.
23. E. Garcin, X. Vernede, E. C. Hatchikian, A. Volbeda, M. Frey and J. C. Fontecilla-Camps, *Structure*, 1999, **7**, 557-566.
24. M. Teixeira, G. Fauque, I. Moura, P. A. Lespinat, Y. Berlier, B. Prickril, H. D. Peck, Jr., A. V. Xavier, J. Le Gall and J. J. Moura, *Eur. J. Biochem.*, 1987, **167**, 47-58.
25. V. M. Fernandez, E. C. Hatchikian and R. Cammack, *Biochim. Biophysic. Acta, Protein Struct. Mol. Enzymol.*, 1985, **832**, 69-79.
26. S. Kurkin, S. J. George, R. N. Thorneley and S. P. Albracht, *Biochemistry*, 2004, **43**, 6820-6831.
27. S. E. Lamle, S. P. J. Albracht and F. A. Armstrong, *J. Am. Chem. Soc.*, 2004, **126**, 14899-14909.
28. V. M. Fernandez, E. C. Hatchikian, D. S. Patil and R. Cammack, *Biochim. Biophysic. Acta, Gen. Subj.*, 1986, **883**, 145-154.
29. J. C. Fontecilla-Camps, A. Volbeda, C. Cavazza and Y. Nicolet, *Chem. Rev.*, 2007, **107**, 4273-4303.
30. S. Yoshizawa and A. Böck, *Biochim. Biophysic. Acta, Gen. Subj.*, 2009, **1790**, 1404-1414.
31. M. Medina, E. Claude Hatchikian and R. Cammack, *Biochim. Biophys. Acta, Bioenerg.*, **1275**, 227-236.
32. M. Teixeira, G. Fauque, I. Moura, P. A. Lespinat, Y. Berlier, B. Prickril, H. D. Peck Jr, A. V. Xavier, J. Le Gall and J. J. G. Moura, *Eur. J. Biochem.*, 1987, **167**, 47-58.
33. E. S. Arnér, *Exp. Cell Res.*, 2010, **316**, 1296-1303.
34. C. Wombwell, C. A. Caputo and E. Reisner, *Acc. Chem. Res.*, 2015, **48**, 2858-2865.
35. F. M. A. Valente, A. S. F. Oliveira, N. Gnadat, I. Pacheco, A. V. Coelho, A. V. Xavier, M. Teixeira, C. M. Soares and I. A. C. Pereira, *J. Biol. Inorg. Chem.*, 2005, **10**, 667-682.
36. R. J. Hondal and E. L. Ruggles, *Amino Acids*, 2011, **41**, 73-89.
37. S. W. Benson, *Chem. Rev.*, 1978, **78**, 23-35.
38. J. Fritsch, P. Scheerer, S. Frielingsdorf, S. Kroschinsky, B. Friedrich, O. Lenz and C. M. T. Spahn, *Nature*, 2011, **479**, 249-252.
39. A. Volbeda, M. H. Charon, C. Piras, E. C. Hatchikian, M. Frey and J. C. Fontecilla-Camps, *Nature*, 1995, **373**, 580-587.
40. J. C. Fontecilla-Camps, A. Volbeda, C. Cavazza and Y. Nicolet, *Chem. Rev.*, 2007, **107**, 4273-4303.
41. H. Ogata, P. Kellers and W. Lubitz, *J. Mol. Biol.*, 2010, **402**, 428-444.
42. M. C. Marques, R. Coelho, A. L. De Lacey, I. A. C. Pereira and P. M. Matias, *J. Mol. Biol.*, 2010, **396**, 893-907.
43. A. Volbeda, P. Amara, M. Iannello, A. L. De Lacey, C. Cavazza and J. C. Fontecilla-Camps, *Chem Commun*, 2013, **49**, 7061-7063.

44. M. C. Marques, R. Coelho, I. A. C. Pereira and P. M. Matias, *Int. J. Hydrogen Energy*, 2013, **38**, 8664-8682.
45. C. S. Baltazar, V. H. Teixeira and C. M. Soares, *J. Biol. Inorg. Chem.*, 2012, **17**, 543-555.
46. O. Gutiérrez-Sanz, M. C. Marques, C. S. Baltazar, V. M. Fernández, C. M. Soares, I. A. Pereira and A. L. De Lacey, *J. Biol. Inorg. Chem.*, 2013, **18**, 419-427.
47. A. Parkin, G. Goldet, C. Cavazza, J. C. Fontecilla-Camps and F. A. Armstrong, *J. Am. Chem. Soc.*, 2008, **130**, 13410-13416.
48. O. Skaff, D. I. Pattison, P. E. Morgan, R. Bachana, V. K. Jain, K. I. Priyadarsini and M. J. Davies, *Biochem. J.*, 2012, **441**, 305-316.
49. B. Cardey and M. Enescu, *J. Phys. Chem. A*, 2007, **111**, 673-678.
50. H. Ogata, Y. Mizoguchi, N. Mizuno, K. Miki, S.-i. Adachi, N. Yasuoka, T. Yagi, O. Yamauchi, S. Hirota and Y. Higuchi, *J. Am. Chem. Soc.*, 2002, **124**, 11628-11635.
51. K. A. Vincent, A. Parkin and F. A. Armstrong, *Chem. Rev.*, 2007, **107**, 4366-4413.
52. J. Riethausen, O. Rüdiger, W. Gärtner, W. Lubitz and H. S. Shafaat, *ChemBioChem*, 2013, **14**, 1714-1719.
53. A. L. De Lacey, C. Gutiérrez-Sánchez, V. M. Fernández, I. Pacheco and I. A. Pereira, *J. Biol. Inorg. Chem.*, 2008, **13**, 1315-1320.
54. A. L. De Lacey, V. M. Fernandez, M. Rousset and R. Cammack, *Chem. Rev.*, 2007, **107**, 4304-4330.
55. K. A. Vincent, A. Parkin, O. Lenz, S. P. J. Albracht, J. C. Fontecilla-Camps, R. Cammack, B. Friedrich and F. A. Armstrong, *J. Am. Chem. Soc.*, 2005, **127**, 18179-18189.
56. M. Teixeira, I. Moura, G. Fauque, M. Czechowski, Y. Berlier, P. A. Lespinat, J. Le Gall, A. V. Xavier and J. J. Moura, *Biochimie*, 1986, **68**, 75-84.
57. E. Reisner, D. J. Powell, C. Cavazza, J. C. Fontecilla-Camps and F. A. Armstrong, *J. Am. Chem. Soc.*, 2009, **131**, 18457-18466.
58. T. Sakai, D. Mersch and E. Reisner, *Angew. Chem. Int. Ed.*, 2013, **52**, 12313-12316.
59. J. C. Fontecilla-Camps, P. Amara, C. Cavazza, Y. Nicolet and A. Volbeda, *Nature*, 2009, **460**, 814-822.
60. Y. Montet, P. Amara, A. Volbeda, X. Vernede, E. C. Hatchikian, M. J. Field, M. Frey and J. C. Fontecilla-Camps, *Nat Struct Biol*, 1997, **4**, 523-526.
61. H. Feldman, M. A. Iron, D. Fixler, S. Moshkov, N. Zurgil, E. Afrimzon and M. Deutsch, *Photochem. Photobiol. Sci.*, 2021, **20**, 1397-1418.
62. Y. Li, Y. Hu, G. Chen, Z. Wang and X. Jin, *Sci. China, Ser. B Chem.*, 2017, **60**, 734-739.
63. J. Weber, A. J. Wain and F. Marken, *Electroanalysis*, 2015, **27**, 1829-1835.
64. K. D. Kreuer, *Solid State Ionics*, 1997, **94**, 55-62.
65. K. A. Vincent and F. A. Armstrong, *Inorg. Chem.*, 2005, **44**, 798-809.
66. C. Léger, S. J. Elliott, K. R. Hoke, L. J. C. Jeuken, A. K. Jones and F. A. Armstrong, *Biochemistry*, 2003, **42**, 8653-8662.
67. T. Lemaoui, F. Abu Hatab, A. S. Darwish, A. Attoui, N. E. H. Hammoudi, G. Almustafa, M. Benaicha, Y. Benguerba and I. M. Alnashef, *ACS Sus. Chem. Eng.*, 2021, **9**, 5783-5808.
68. A. Hayyan, F. S. Mjalli, I. M. AlNashef, T. Al-Wahaibi, Y. M. Al-Wahaibi and M. A. Hashim, *Thermochim. Acta*, 2012, **541**, 70-75.
69. S. A. A. Russ, M. Jablonsky, J. Sima, *BioRes.* 2018, **3**, 5042- and 5051.
70. P. Rodriguez-Maciá, A. Dutta, W. Lubitz, W. J. Shaw and O. Rüdiger, *Angew. Chem. Int. Ed.*, 2015, **54**, 12303-12307.
71. A. P. Abbott, D. Boothby, G. Capper, D. L. Davies and R. K. Rasheed, *J Am Chem Soc*, 2004, **126**, 9142-9147.
72. A. P. Abbott, G. Capper, D. L. Davies, R. K. Rasheed and V. Tambyrajah, *Chem. Commun.*, 2003, 70-71.

73. E. C. Hatchikian, M. Bruschi and J. Le Gall, *Biochem. Biophys. Res. Commun.*, 1978, **82**, 451-461.
74. A. Neudeck and L. Kress, *J. Electroanal. Chem.*, 1997, **437**, 141-156.
75. A. Szabo, D. K. Cope, D. E. Tallman, P. M. Kovach and R. M. Wightman, *J. Electroanal. Chem. Interfacial Electrochem.*, 1987, **217**, 417-423.

Chapter 5

Summary and Outlook

5.1. Thesis Summary

This thesis has highlighted the first use of type III deep eutectic solvents as an effective medium for solar hydrogen production using both heterogenous and homogenous photocatalysts. By tuning the solvent properties through the addition and removal of water and by selecting appropriate constituents of the solvent i.e., by varying the HBD component, different catalytic properties and trends can be realised. Spectroscopic techniques such as FT-IR and DR-UV, as well as analytical techniques show that the solvents do not compromise the stability of the photocatalyst. In fact, given certain conditions DESs can outperform standard aqueous solutions. Some insight is given to this, such as the nature of the deposition of co-catalytic Pt on the photocatalyst surface, aiding the functionality of a redox mediator. In aqueous solutions, the NCN-CN_x photocatalyst shows a strong affinity for Pt, and through resuspension experiments it is believed the Pt is deposited directly on NCN-CN_x. This phenomenon is not observed in DESs, and it is observed that activity is high when a redox mediator is used. This is a result of the redox mediator shuttling excited electrons from the photocatalyst to the Pt in solution, where H₂ evolution occurs. Without the use of a redox mediator, Pt/NCN-CN_x in DESs still show good activity for solar hydrogen production versus water in otherwise identical reaction conditions. Tuning DESs is the ideal way for optimising H₂ production activity and the work presented in this thesis shows that simply changing the reaction media can lead to increases in photocatalytic H₂ production performance without any costly catalyst modifications or reactor re-design.

The chemical properties of DESs also allow them to be viewed as reaction conditions for aerobic hydrogen evolution. In aqueous solutions, the photocatalytic activity of heterogenous photocatalysts is hindered drastically, likely resulting from a high O₂ concentration and O₂ mobility in the solvent. The H₂ production performance in aerobic conditions by the same photocatalytic system shows much higher performance in type III DESs. This higher performance arises from the low diffusion

of O₂ in the solvent, as well as a relatively low O₂ concentration. This enables photocatalysts which are typically intolerant to oxygen to retain up to 90% of its activity relative to an inert atmosphere. Again, simply changing the solvent allows this to occur. Electroanalysis using a homemade Pt microwire electrode (made and provided by Professor Frank Marken at the University of Bath) in the solvents has shown that variations in the diffusion and concentration values of O₂ varies between the DESs tested, and that both parameters play an important role in understanding the increase in photocatalytic O₂ tolerance. By showing that limiting diffusion and concentration of O₂ in the solution, solvents can be rationally designed to increase the O₂ tolerance. This thesis has shown that potential step chronoamperometry can determine the diffusion and concentration of O₂ in salinated solutions, with an increase in salinity conducive to a lower O₂ concentration and diffusion. Through realising that diffusion and concentration play an important role in the photocatalytic O₂ tolerance, a mathematical model can be applied to photocatalysts based on the flux of O₂ at a spherical electrode. The rate of O₂ flux is a function of diffusion and concentration, as well as particle size. This model allows the design of appropriate reaction conditions to aid in increasing O₂ tolerance, through using solvents with low O₂ diffusivities and concentrations, as well as increasing charge carrier generation and decreasing particle size.

Using the findings from these results, the photocatalytic O₂ tolerance of a [NiFeSe]-H₂ase was investigated which has been previously shown in the literature to exhibit low H₂ evolution activity in air relative to an inert atmosphere. Through solvent tuning, the work presented in this thesis shows that the [NiFeSe]-H₂ase coupled to a TiO₂ light absorber can perform favourably in organic type III DESs, which again has not been shown in the literature prior. DESs can aid to increase H₂ evolution in both inert and aerobic conditions, and through resuspension experiments show that the enzyme tethering to the TiO₂ is not affected by the solvent. Moreover, a heterogenous photocatalyst Eosin Y when used with [NiFeSe]-H₂ase shows similar behaviour in terms of O₂ tolerance in DESs, where low DES concentrations exhibit low O₂ tolerance and vice versa. Again, electrochemical analysis of the solvents provides some insight into the trends in photocatalytic H₂ evolution, whereby the electrochemically determined diffusion and concentration of protons in the solvents

likely play an important role in mediating the photocatalytic performance. This thesis also shows that electrocatalytic methods can rationalise the activity of photocatalysis in identical solvents, and provides an insight into the effect of the solvent on H₂ production.

5.2. Outlook

This thesis hopes to showcase a new alternative class of solvents for photocatalytic purposes. Due to the sheer number of possible DESs available through the choice of hydrogen bond acceptor and donor components, the scope and research into solvent effects on solar fuel generation is limitless. As a result of their cost and ease of preparation, this thesis hopes to showcase the viability of DESs in new reaction systems and with further understanding of solvent behaviour and characteristics, it may be possible to rationalise which solvents are appropriate for energy applications through their chemical nature.¹ Through the work presented in this thesis, it is hoped that more consideration is given to photocatalytic oxygen tolerance when investigating reaction systems for solar fuel generation. Indeed, oxygen tolerance does not necessarily mean that catalyst modifications need to be performed, but simply tuning and changing the solvent can increase performance.² Through rational solvent design, it is hoped that new research is opened up for catalytic oxygen tolerance, and that catalytic materials and solvents are optimised in such a way so that catalysts can become fully tolerant to oxygen. This would pave the way for larger scale water splitting systems, where catalysts are not necessarily deactivated in the presence of oxygen, and that photocatalytic reaction systems will someday no longer view oxygen as an inconvenience to maximise the solar hydrogen evolution performance.³

The research presented in this thesis also highlights that further research into the nature of catalytic activity. Varying reaction parameters such as the amount of co-catalytic Pt and methyl viologen concentration would highlight the effect of such reagents on catalytic rate. Studies into the behaviour of the solvent during photocatalysis could also show the effect of the solvent on catalytic processes, and if DESs are broken down or react with charge carriers.⁴⁻⁶ Some liquid chromatography studies would enable the detection of compounds formed during

photocatalytic reactions. Further spectroscopic studies could also be performed, particularly for homogenous photocatalysis. For example, UV-Vis and photoluminescence studies could provide insight into the behaviour of EY, its degradation and change in optical and fluorescent properties in different DES.⁷⁻¹¹ In addition, if viscosity is a limiting factor for high glyceline and reline concentrations with EY, a redox mediator could be used to aid in shuttling electrons from the photoexcited EY* to Pt in solution.

Other reaction conditions could be used to determine the hypothesis for the mechanism of diffusion controlled O₂ tolerance. The proposed equation is dependent on light intensity (and charge carrier flux), as well as particle size. By using solvents with known diffusion coefficients and concentrations of dissolved O₂, the O₂ tolerance could be investigated for its dependence on particle size or light intensity. A ball mill could be used to create photocatalyst particles of a defined size, and O₂ tolerant hydrogen production could be performed and the photocatalytic O₂ tolerance determined as a function of particle size.¹²⁻¹⁴

The use of DESs may also be used for other photochemical reactions, such as the reduction of CO₂ into useful fuels. Some DESs based on choline chloride have proven capable of CO₂ capture.¹⁵ Coupling CO₂ capture and reduction systems enables a more functionable device to be constructed for solar fuel production.^{16, 17} Moreover, the use of DESs as reaction media does not need to be limited to photocatalysis, as this work has also shown that electrocatalysis can be viable in the solvents tested. An emerging class of deep eutectic solvents called “aqueous salt hydrates” are formed from eutectic mixtures of salt and ice.¹⁸ Due to their nature, these solvents are much easier to handle than the type III DESs used in this work, as they are much less viscous. Research into these solvents is in its infancy but have been investigated as electrolytes in energy storage devices.^{19, 20} These solvents possess naturally high salinities, and so would make for interesting reaction solvents for photocatalytic hydrogen evolution in aerobic conditions.

Further electrochemical studies for the determination of proton mobility in DESs would provide a more wholistic understanding on the chemical processes occurring at the hydrogenase. It is not inconceivable that the diffusion of protons, particularly

at low values, affects the hydrogen production. An extremely low proton mobility would prevent protons from reaching active sites of photocatalytic particles lowering the hydrogen evolution activity. Hydrogenases are dependent on the rate of which they are supplied substrates, as their overpotentials for redox processes are extremely low. As such, a better understanding of the chemical behaviour of protons in solvents is necessary to develop reaction systems which utilise hydrogenases, particularly those which are sensitive to O₂. In addition, a better understanding of the effects of solvent on the structure of hydrogenases are important to aid in maximising enzymatic TON. The polarity and hydrophobicity of solvents and their effect on photocatalytic hydrogenase activity could be researched to investigate their respective effects on enzyme behaviour. There may arise difficulties in purification and characterisation of the enzyme once it has been employed in a photocatalytic reaction system however, and so studies in this area should be carefully considered and managed for optimal results.

Overall, characterisation, spectroscopic, and analytical studies of photocatalysts and the photocatalytic components (co-catalysts and redox mediators) should be more intensively researched for a better understanding of processes occurring *in situ*. Through these investigations, it would be ideal to decipher favourable mechanisms which aid in increasing photocatalytic activity for the production of solar fuels as products for energy challenges.

5.3. References

1. S. Azmi, M. F. Koudahi and E. Frackowiak, *Energy Environ. Sci.*, 2022, **15**, 1156-1171.
2. M. G. Allan, M. J. McKee, F. Marken and M. F. Kuehnel, *Energy Environ. Sci.*, 2021, **14**, 5523-5529.
3. H. Nishiyama, T. Yamada, M. Nakabayashi, Y. Maehara, M. Yamaguchi, Y. Kuromiya, Y. Nagatsuma, H. Tokudome, S. Akiyama, T. Watanabe, R. Narushima, S. Okunaka, N. Shibata, T. Takata, T. Hisatomi and K. Domen, *Nature*, 2021, **598**, 304-307.
4. J.-J. Duan, X.-X. Zheng, H.-J. Niu, J.-J. Feng, Q.-L. Zhang, H. Huang and A.-J. Wang, *J. Colloid Interface Sci.*, 2020, **560**, 467-474.
5. X. Yu, E. C. dos Santos, J. White, G. Salazar-Alvarez, L. G. M. Pettersson, A. Cornell and M. Johnsson, *Small*, 2021, **17**, 2104288.
6. B. Zhu, Z. Liang and R. Zou, *Small*, 2020, **16**, 1906133.
7. H. Feldman, M. A. Iron, D. Fixler, S. Moshkov, N. Zurgil, E. Afrimzon and M. Deutsch, *Photochem Photobiol Sci*, 2021, **20**, 1397-1418.
8. A. Kadyan, S. Juneja and S. Pandey, *J. Phys. Chem. B*, 2019, **123**, 7578-7587.

9. Y. Murakami, S. K. Das, Y. Himuro and S. Maeda, *Phys. Chem. Chem. Phys.*, 2017, **19**, 30603-30615.
10. C. R. Wright, L. VandenElzen and T. A. Hopkins, *J. Phys. Chem. B*, 2018, **122**, 8730-8737.
11. C. L. Boldrini, N. Manfredi, F. M. Perna, V. Capriati and A. Abbotto, *Chem. Eur. J.*, 2018, **24**, 17656-17659.
12. Z. Zhang, C.-C. Wang, R. Zakaria and J. Y. Ying, *J. Phys. Chem. B*, 1998, **102**, 10871-10878.
13. K. Kočí, L. Obalová, L. Matějová, D. Plachá, Z. Lacný, J. Jirkovský and O. Šolcová, *Appl. Catal. B*, 2009, **89**, 494-502.
14. S. Chaudhuri, A. Ghosh and S. K. Chattopadhyay, in *Green Synthetic Approaches for Biologically Relevant Heterocycles*, ed. G. Brahmachari, Elsevier, Amsterdam, 2021, 2nd ed., vol. 1, ch. 14, pp. 617-653.
15. A. Krishnan, K. P. Gopinath, D.-V. N. Vo, R. Malolan, V. M. Nagarajan and J. Arun, *Environ. Chem. Lett.*, 2020, **18**, 2031-2054.
16. J. F. Brennecke and B. E. Gurkan, *J. Phys. Chem. Lett.*, 2010, **1**, 3459-3464.
17. K. Wei, H. Guan, Q. Luo, J. He and S. Sun, *Nanoscale*, 2022, **14**, 11869-11891.
18. Y. Marcus, *ACS Sus. Chem. Eng.*, 2017, **5**, 11780-11787.
19. T. Sun, S. Zheng, H. Du and Z. Tao, *Nano-Micro Letters*, 2021, **13**, 204.
20. Y. Sun, B. Liu, L. Liu and X. Yan, *Adv. Funct. Mater.*, 2022, **32**, 2109568.